

## Revealing the Fate of Photo-Generated Charges in Metal Halide Perovskites

Hutter, Eline

**DOI**

[10.4233/uuid:f8e21539-bd26-4694-b170-6d0641e4c31a](https://doi.org/10.4233/uuid:f8e21539-bd26-4694-b170-6d0641e4c31a)

**Publication date**

2018

**Document Version**

Final published version

**Citation (APA)**

Hutter, E. (2018). *Revealing the Fate of Photo-Generated Charges in Metal Halide Perovskites*. [Dissertation (TU Delft), Delft University of Technology]. <https://doi.org/10.4233/uuid:f8e21539-bd26-4694-b170-6d0641e4c31a>

**Important note**

To cite this publication, please use the final published version (if applicable).  
Please check the document version above.

**Copyright**

Other than for strictly personal use, it is not permitted to download, forward or distribute the text or part of it, without the consent of the author(s) and/or copyright holder(s), unless the work is under an open content license such as Creative Commons.

**Takedown policy**

Please contact us and provide details if you believe this document breaches copyrights.  
We will remove access to the work immediately and investigate your claim.

# Revealing the Fate of Photo-Generated Charges in Metal Halide Perovskites

Proefschrift

ter verkrijging van de graad van doctor  
aan de Technische Universiteit Delft,  
op gezag van de Rector Magnificus prof. dr. ir. T. H. J. J. van der Hagen,  
voorzitter van het College voor Promoties,

in het openbaar te verdedigen op  
19 juni 2018 om 12:30 uur  
door  
Eline Mathilde HUTTER

Master of Science in de Chemische Wetenschappen,  
Universiteit Utrecht, Nederland  
geboren te Breda, Nederland

<http://repository.tudelft.nl>

*Live, as if you were to die tomorrow*

*Learn, as if you were to live forever*

~ Mahatma Gandhi ~



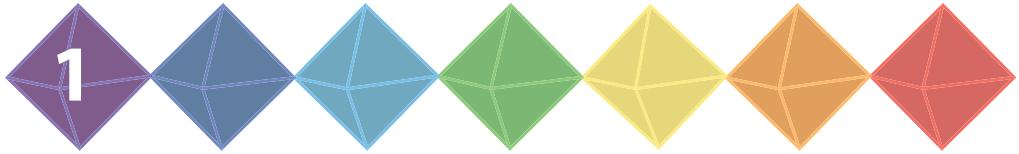


# Table of Contents

<b>Chapter 1</b>	<b>1</b>
Introduction	
<b>Chapter 2</b>	<b>13</b>
Background Information and Methodology	
<b>Chapter 3</b>	<b>29</b>
Charge Carriers in Thin Films and Macroscopic Crystals of Methylammonium Lead Iodide Perovskites	
<b>Chapter 4</b>	<b>53</b>
Interfacial Kinetics of Charge Transfer from Methylammonium Lead Iodide Perovskites to Organic Transport Materials	
<b>Chapter 5</b>	<b>75</b>
Temperature-Dependent Recombination Pathways in Tetragonal and Orthorhombic Phases of Methylammonium Lead Iodide Perovskites	
<b>Chapter 6</b>	<b>97</b>
The Role of the Monovalent Cation on the Recombination Kinetics in Lead Iodide Perovskites	
<b>Chapter 7</b>	<b>121</b>
Band-Like Charge Transport in Antimony-Bismuth Alloyed $\text{Cs}_2\text{AgBi}_{1-x}\text{Sb}_x\text{Br}_6$ Halide Double Perovskites	
Summary	<b>139</b>
Samenvatting	<b>143</b>
Dankwoord	<b>147</b>
Curriculum Vitae	<b>151</b>
List of Publications	<b>153</b>
List of Presentations	<b>157</b>



# Introduction



In the past few years, metal halide perovskite (MHP) semiconductors have received tremendous attention in the solar cell research community. This is mainly due to the rapid rise in power conversion efficiency of MHP-based solar cells, which, starting at 3.8% in 2009,<sup>1</sup> already reached values exceeding 22% in 2017.<sup>2</sup> Additionally, MHP-based devices can also be used as top cells in two-cell configurations with bottom cells based on silicon (Si), thereby having the potential to boost the efficiencies of commercial Si-based solar cells up to 30%.<sup>3</sup> More recently, the application of MHPs was further extended to X-ray detectors and light-emitting diodes (LEDs).<sup>4–6</sup> Considering their wide range of applications and the fact that these can be easily deposited from solution,<sup>7</sup> MHPs are promising low-cost alternatives to established technologies such as (multi-)crystalline Si and gallium arsenide (GaAs). This chapter introduces MHPs in general and provides some background information on the fascinating optoelectronic properties of these materials. Additionally, this chapter describes the motivations and (past) challenges that have led to the research presented in this thesis. Finally, some recommendations for future research directions are given. In view of the excessive pace with which this research field has moved forward, this thesis can be considered as a timeline of MHP research from 2014 to early 2018.

### 1.1 The promise of metal halide perovskites for photovoltaic applications

In general, *perovskites* represent a class of crystals that share the formula  $ABX_3$ , in which A and B are cations (A larger than B) and X an anion.<sup>7</sup> A schematic representation of the cubic perovskite crystal structure is shown in **Figure 1.1a**. In the case of metal halide perovskites, a divalent metal such as lead ( $Pb^{2+}$ ) or tin ( $Sn^{2+}$ ) occupies the B-site and is surrounded by halides, *e.g.* iodide ( $I^-$ ), bromide ( $Br^-$ ) or chloride ( $Cl^-$ ), at the X-site. A small monovalent organic cation such as methylammonium (MA:  $CH_3NH_3^+$ ), formamidinium (FA:  $CH_2(NH_2)_2^+$ ) or the inorganic cesium ( $Cs^+$ ) then fills up the voids in the three-dimensional inorganic framework built from corner-sharing metal halide octahedra. Methylammonium lead iodide ( $MAPbI_3$ ) and methylammonium lead bromide ( $MAPbBr_3$ ) were the first reported MHPs to be successfully used as light-absorbing layers in photovoltaic devices.<sup>1,8</sup> These materials are semiconductors with

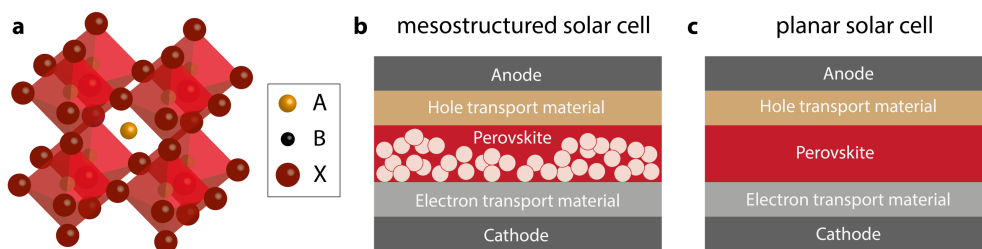


**Figure 1.1:** (a) Schematic representation of the cubic perovskite crystal structure, in which A and B are cations (A larger than B) and X an anion. (b-c) Perovskite-based solar cell in meso-structured (b) or planar (c) configuration.

bulk bandgaps of around 1.6 and 2.3 eV, respectively.<sup>9,10</sup> This difference in bandgap can be understood considering that the energy levels at the band edges originate from the orbitals of the metal halide octahedra.<sup>11</sup> Consequently, changing the halide and/or the divalent metal can be used to manipulate the absorption onset and emission wavelength. Interestingly, on mixing for instance bromide and iodide in  $\text{MAPbX}_3$ , any bandgap value intermediate to  $\text{MAPbI}_3$  and  $\text{MAPbBr}_3$  can be obtained. Furthermore, although the energy levels of the monovalent cation do not contribute to either the conduction band minimum or valence band maximum, the nature of the cation actually does affect the bandgap. That is, both the distances and angles between the metal halide octahedra depend on the size of the cation and hence, changing the cation can be used as another tool to tune the properties of MHPs.<sup>12,13</sup> This tunability of the bandgap is one of the key properties of MHPs, since it enables design of materials with desired bandgaps, for instance close to 1.35 eV for a single junction solar cell, or any other value desired for their use in multiple-junction (tandem) configurations.

The first MHP-based solar cell architectures were so-called meso-structured solar cells, consisting of MHPs infiltrated into a mesoporous scaffold of either electron-accepting titania ( $\text{TiO}_2$ ) or insulating alumina ( $\text{Al}_2\text{O}_3$ ) particles, see **Figure 1.1b**.<sup>8</sup> Eventually, the best performing devices were obtained using planar heterojunction configurations in which a few hundred nanometer thick MHP film is sandwiched between electron- and hole-selective transport materials (see **Figure 1.1c**).<sup>14–16</sup> Currently, a substantial number of research groups is able to reach power conversion efficiencies in between 15 and 20%, using MHPs with bandgaps of 1.6 to 1.7 eV. Though less frequently reported, record efficiencies close to 23% have also been obtained.<sup>17</sup> Although these numbers are exceptionally high in comparison with other non-commercialized solar cell technologies, the power conversion efficiencies are still not at their theoretical limits. That is, assuming that planar pin-junctions based on MHPs behave according to the Shockley-Queisser limit (defined for pn-junction solar cells),<sup>18</sup> their maximum efficiency is around 30.5% in the case of a 1.6 eV bandgap, and should be able to reach 33.7% if the bandgap is around 1.35 eV.

## 1.2 Factors limiting performance of MHP-based solar cells

One of the questions that naturally arises is:

*What are factors limiting the efficiency of MHP-based solar cells?*

To answer this question, we should first consider some processes that in general, govern the efficiency of a solar cell:

- Generation of free charges in the perovskite layer on light absorption
- Transport of charges to the perovskite-transport material interface
- Extraction of charges by charge-selective transport materials
- Collection of these charges at the opposite electrodes

The generation of free charges from light in any semiconductor is highly dependent on its wavelength-dependent absorption coefficient and exciton binding energy. If the latter is lower than the thermal energy, the absorption of light results in free negatively charged electrons in the conduction band, leaving positively charged holes in the valence band of the semiconductor. These electrons and holes need to be collected at the opposite electrodes. Note that charge generation mainly depends on intrinsic material properties of MHPs. On the other hand, as also indicated by the fact that device efficiencies vary from researcher to researcher, the transport of photo-generated charges through the perovskite and their extraction and collection are very sensitive to processing conditions. This can be partially understood considering that there might be unintentional defects inside MHP crystallites or at their surfaces, which act as traps to either electrons or holes and hence, prevent the charges from being extracted. Additionally, electrons and holes can recombine with each other instead of reaching the perovskite-transport material interface. The time between the generation and trapping or recombination of a charge is defined as the charge carrier lifetime. Obviously, charges with longer lifetimes are more likely to reach the interface and get extracted by the transport material than short-lived charges. Another crucial parameter for transport is the charge carrier mobility, which is a measure for the speed at which a charge moves. Together, the charge carrier lifetime and mobility determine the average distance over which charges diffuse. This distance is also known as the charge carrier diffusion length, which is closely related to the collection probability of charges.<sup>19</sup>

### 1.3 Transport and extraction of photo-generated charges in MHPs

In order to find answers to the above question, we first of all investigate the relationship between the preparation route of MHPs and the diffusion of electrons and holes, which is shown in **Chapter 3**. Here, we use a unique approach to experimentally determine both mobilities and lifetimes of free charges, using a combination of Time-Resolved Microwave Conductivity (TRMC) measurements and modelling of experimental data. The working principle of the TRMC technique is similar to more widely known THz spectroscopy, but the measurement conditions in TRMC experiments are more suitable to access light intensity regimes that are relevant to solar cells. In addition, we have used complementary Time-Resolved Photoluminescence (TRPL) measurements, which probes the emission of photons on recombination of electrons and holes. Although the latter is frequently used to determine charge carrier lifetimes in MHPs, TRPL measurements alone actually give very limited insight in the dynamics of free charges. Given that TRMC directly probes free, mobile charge carriers, this is a more preferable technique to determine charge carrier lifetimes. In **Chapter 2**, we detail how the above techniques can be used to study the generation and diffusion of free charges. In addition, **Chapter 2** provides some theory behind generation and transport of free charges in periodic solid semiconductors such as MHPs.

Importantly, recombination *via* trap states that originate from defects is a loss mechanism that could in principle be eliminated. Therefore, it is very important that the quality of

MHP crystals and their surfaces is optimized to contain minimum numbers of defects. On modelling the experimental TRMC and TRPL data, as shown in **Chapter 3**, we can directly get information on the trap density as function of the preparation route, sample morphology or composition. Hence, we observe that trap densities in MAPbI<sub>3</sub> perovskites typically range from 10<sup>14</sup> to 10<sup>16</sup> cm<sup>-3</sup>. Considering that these numbers are on the same order of magnitude as the charge carrier densities in a solar cell under operating conditions, trapping of photo-excited charges might be in competition with extraction at the electrodes. To further investigate whether this is indeed, a limiting factor for device performance, we deposit transport materials on top of MAPbI<sub>3</sub> perovskites and study the extraction of charges. The results are shown in **Chapter 4**. From here, we find that holes can be efficiently extracted from MAPbI<sub>3</sub>, while electrons can instead get stuck into trap states. The latter potentially impedes the extraction of electrons and hence, lowers the device efficiency. However, we also find that the trap densities of 10<sup>14</sup> cm<sup>-3</sup> observed in high quality MHP layers are actually low enough not to hamper electron extraction, so that electron losses due to trapping are less substantial than expected.

In contrast to frequently used TRPL measurements, our TRMC experiments allow us to study the fate of the non-extracted charges, provided that these have sufficient mobility. Hence, we can get distinctive insights in the kinetics at the interface between the MHP layer and the transport material. Surprisingly, we find that a number of state-of-the-art transport materials, including the fullerene derivative [6,6]-phenyl-C<sub>61</sub>-butyric acid methyl ester (PCBM), suffer from substantial interfacial recombination. That is, not only the electrons are efficiently extracted by PCBM, but also the holes get immobilized at the MHP-PCBM interface instead of remaining in the MHP layer. Therefore, we conclude that most charge carrier losses actually occur on the perovskite-transport material interface, which we believe to be one of the main future challenges when it comes to boosting the efficiencies of MHP-based solar cells to their theoretical limits.

#### 1.4 Fundamental properties of lead iodide perovskite semiconductors

As mentioned above, the first studies presented in this thesis were related to investigating factors limiting the efficiency of MHP-based solar cells, which we found to be losses due to interfacial recombination and in addition, to a lesser extent, trapping of free electrons in the MHP layer itself. In spite of the enormous research efforts on improving experimental procedures to optimize device performance, there is surprisingly little fundamental knowledge about these semiconductor materials. Although the trap densities are in a relevant order of magnitude for an operating solar cell, the densities are still exceptionally low. That is, if each unintentional defect led to one trap state, a trap density on the order of 10<sup>15</sup> cm<sup>-3</sup> would roughly correspond to only one defect for every ten million unit cells. From this point of view, it is thus quite fascinating that such high quality semiconductors can be made relatively easily using wet chemical processing routes. The exceptionality of MHPs is further reflected in the fact that highly luminescent perovskite quantum dots were synthesized with seemingly little effort,<sup>20,21</sup> again indicating that high quality MHPs can be obtained with relative ease compared to



other technologies.

*The relative ease with which high quality MHPs can be prepared illustrates that these semiconductors are very interesting materials not only for applications, but also from a more fundamental point of view.*

Therefore, in **Chapters 5 and 6** we aim at gaining more fundamental insights in charge carrier generation and recombination processes in bulk MHPs. Studying the charge dynamics in MAPbI<sub>3</sub> as function of temperature in **Chapter 5** leads us to reveal a striking feature of MHPs, namely that the recombination between free electrons and holes is thermally activated (at least for charge densities below 10<sup>17</sup> cm<sup>-3</sup>). Because of its high absorption coefficient, MAPbI<sub>3</sub> is conventionally seen as a direct bandgap semiconductor. However, since its enhanced electron-hole recombination with temperature is more typical for indirect semiconductors, we propose that the energy levels at the band edges in MAPbI<sub>3</sub> are actually characterized by a combination of direct and indirect transitions. Importantly, the concept of a direct-indirect character of the bandgap enables a semiconductor to combine the favorable absorption properties of direct transitions with the slow recombination of an indirect transition. While some research groups have attributed the relatively slow recombination in MAPbI<sub>3</sub> to the dipolar organic cation, we show in **Chapter 6** that the transport of charges and their temperature-dependent recombination in fully inorganic CsPbI<sub>3</sub> perovskites are nearly identical to MAPbI<sub>3</sub>. Therefore, these results suggest that optoelectronic properties of MHPs are mainly dictated by the lead iodide framework rather than the monovalent cation.

Although not experimentally confirmed, it seems likely that the trap density in MHPs does not directly correspond to the density of crystallographic defects. It has been theoretically proposed that only a few types of defects result in intra-bandgap states, while other defect states are located in either the valence or conduction band and do therefore, not act as trap states.<sup>11</sup> The precise influence of defects, and their competition or synergy with the direct–indirect bandgap character, could be the subject of important future work within the research community.

### 1.5 Toxicity concerns of lead-based solar cells

One of the major drawbacks that hampers commercialization of perovskite-based solar cells is the use of poisonous Pb<sup>2+</sup>, which has, in view of its relatively high water-solubility, a larger potential environmental impact than *e.g.* cadmium telluride (CdTe) or metallic lead.<sup>22</sup> The question is:

*Can lead be replaced with non-toxic alternatives while preserving the favorable transport properties of lead-based perovskites?*

Here, favorable transport properties include sufficiently high charge carrier mobilities and long lifetimes due to low trap densities and relatively slow electron-hole

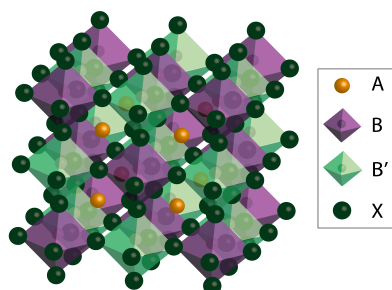


**Figure 1.2:** Schematic representation of the halide double perovskite (*i.e.* elpasolite) crystal structure.

recombination. In the first attempts to replace lead, the most obvious alternatives from the same group, *i.e.*  $\text{Sn}^{2+}$  and  $\text{Ge}^{2+}$ , were used. Unfortunately, these ions appeared to be sensitive to further oxidation into  $\text{Sn}^{4+}$  and  $\text{Ge}^{4+}$ , respectively.<sup>23</sup> This oxidation leads to defects in the crystal and electronic doping of the MHP,<sup>24</sup> which drastically reduces the overall device performance and stability.<sup>25</sup> An alternative approach is to replace  $\text{Pb}^{2+}$  with a mixture of monovalent and trivalent metal ions, for instance using one  $\text{Ag}^+$  and one  $\text{Bi}^{3+}$  ion for every two  $\text{Pb}^{2+}$  ions.<sup>27–29</sup> Together with  $\text{Cs}^+$  at the A-site and  $\text{Br}^-$  or  $\text{Cl}^-$  at the X-site, these ions yield so-called halide double perovskites (HDPs). Double perovskites are also known as elpasolites, a class of materials sharing the general formula  $\text{A}_2\text{BB}'\text{X}_6$  (see **Figure 1.2**)<sup>28</sup>, with a symmetry analogous to the  $\text{ABX}_3$  perovskite (**Figure 1.1a**). The recently reported HDPs  $\text{Cs}_2\text{AgBiBr}_6$  and  $\text{Cs}_2\text{AgBiCl}_6$  absorb less sunlight than  $\text{MAPbI}_3$  due to their larger and indirect bandgaps of 2.2 and 2.8 eV, respectively.<sup>27</sup> However, the general observation that a mixture of mono- and trivalent metals can be used instead of divalent metals opens up a whole new platform for designing non-toxic materials with desirable bandgaps for single- or multiple-junction solar cells.

In **Chapter 7**, we investigate the optoelectronic properties of several HDPs. Starting from the previously reported  $\text{Cs}_2\text{AgBiBr}_6$ , we replace controlled amounts of  $\text{Bi}^{3+}$  with  $\text{Sb}^{3+}$ , which interestingly gradually reduces the bandgap, reaching values close to 1.6 eV if 40% of the  $\text{Bi}^{3+}$  is replaced with  $\text{Sb}^{3+}$ . Remarkably, although the absolute mobilities are lower, we find that the temperature dependence of the mobility in these HDPs follows the exact same trend as observed for their lead-based analogues (*i.e.*  $\text{CsPbBr}_3$ ).<sup>30</sup> The tunability of the absorption onset in combination with band-like charge transport in antimony-bismuth alloyed HDPs makes these compounds promising candidates for future applications implementing lead-free perovskites. As a first step toward HDP-based solar cells with tunable bandgaps, we report a route to make thin films of  $\text{Cs}_2\text{AgBi}_{1-x}\text{Sb}_x\text{Br}_6$  with  $x$ -values ranging from 0 to 0.4. Thus far, the charge transport properties of these films are not as favorable as observed for *e.g.*  $\text{MAPbI}_3$ . However, only the future will tell whether this is an intrinsic limitation of antimony-bismuth alloyed HDPs or if optimizing synthesis routes will improve the quality to levels competitive

with lead-based perovskites.

## 1.6 Outline of this thesis

**Chapter 2** provides a theoretical background of semiconductors and the spectroscopic techniques that are used throughout this thesis. Most importantly, the working principles of the TRMC technique are explained and how this is used to get information about free charges generated by light in semiconductor materials. Additionally, a kinetic model is introduced that we use in **Chapters 3 to 6** to get quantitative information from our time-resolved spectroscopy measurements.

In **Chapter 3**, we start with configurations used in the first MHP-based solar cells, which are polycrystalline thin films of the perovskite  $\text{MAPbI}_3$ . The techniques and analysis methods introduced in **Chapter 2** are used to reveal the transport properties of light-generated free charges as function of the morphology of  $\text{MAPbI}_3$ . We find that in planar thin films, charges can diffuse over distances on the order of a micrometer. From here, we conclude that the diffusion length of charges in  $\text{MAPbI}_3$  can be large enough to overcome the film thickness that is needed to absorb a substantial amount of sunlight. Finally, repeating these experiments with millimeter-sized  $\text{MAPbI}_3$  crystals, we find that the diffusion length can be at least one order of magnitude larger if the dimensions of charge transport are no longer affected by the size of the crystalline domains.

In an operating solar cell, the charges generated by light in the  $\text{MAPbI}_3$  layer eventually need to be collected at the electrodes. A crucial step here is the extraction of free charges by transport layers, that connect the perovskite to the electrodes. In **Chapter 4**, we use TRMC measurements to investigate how effectively organic transport materials can extract the light-generated charges from a thin  $\text{MAPbI}_3$  film. In order to study this, we deposit different materials on top of the  $\text{MAPbI}_3$  that extract either free electrons from its conduction band or free holes (*i.e.*, missing electrons) from its valence band. The kinetic model used in **Chapter 3** is extended to account for the additional processes occurring on the interface between  $\text{MAPbI}_3$  and the organic layer. Most importantly, we find that holes can be efficiently extracted from the  $\text{MAPbI}_3$ , whereas electrons can be either extracted or immobilized into a trap state in the  $\text{MAPbI}_3$ . Finally, conditions are proposed under which the extraction efficiency should reach unity.

The fact that diffusion of electrons and holes in  $\text{MAPbI}_3$  is sufficient to enable efficient extraction of both, is one of the main reasons behind the success of MHPs. Micrometer-long diffusion lengths can be reached thanks to relatively slow recombination between free electrons and holes. In **Chapter 5**, we perform an in-depth study of the generation and recombination dynamics in  $\text{MAPbI}_3$ . We observe that there is a barrier for recombination between electrons and holes, which can be overcome by thermal energy. In order to explain these findings, we propose that electron-hole recombination is momentum-forbidden, which drastically slows down recombination.

Many properties of  $\text{MAPbI}_3$ , such as the mobilities and lifetimes of free charges, have been attributed to rotational freedom of the dipolar organic cation.<sup>31,32</sup> In **Chapter 6**, we investigate whether the favorable optoelectronic properties of  $\text{MAPbI}_3$  are indeed,

unique to MA-based perovskites. Therefore, we start with developing a method to prepare high-quality thin films of CsPbI<sub>3</sub> perovskites, in which the cation is inorganic and does not have a dipole moment. Importantly, we find that both the generation and transport of charges in CsPbI<sub>3</sub> is definitely not inferior to MAPbI<sub>3</sub>. In fact, we find that replacing controlled amounts of the organic cation with inorganic cations actually improves charge transport properties. This not only explains why these mixed-cation MHPs have resulted in record-breaking solar cell efficiencies, but also illustrates how the optoelectronic properties of MHPs can be manipulated by changing their composition.

In order to commercialize MHPs, the poisonous lead should ideally be replaced by non-toxic alternatives. In **Chapter 7**, we prepare MHPs in which Pb<sup>2+</sup> is replaced with a mixture of the less poisonous metals silver (Ag<sup>+</sup>), bismuth (Bi<sup>3+</sup>) and antimony (Sb<sup>3+</sup>), yielding crystals with the general formula Cs<sub>2</sub>AgBi<sub>1-x</sub>Sb<sub>x</sub>Br<sub>6</sub>, and investigate their optoelectronic properties. Importantly, we find that the transport mechanism of charges in these compounds is not very different from lead-based perovskites, which makes them promising candidates for non-toxic MHP-based solar cells.

## 1.7 References

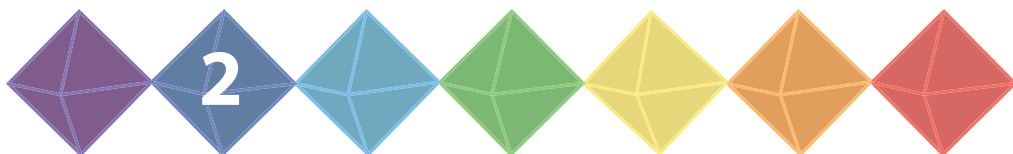
1. Kojima, A., Teshima, K., Shirai, Y. & Miyasaka, T. Organometal halide perovskites as visible-light sensitizers for photovoltaic cells. *J. Am. Chem. Soc.* **131**, 6050–6051 (2009).
2. Yang, W. S. *et al.* Iodide management in formamidinium-lead-halide-based perovskite layers for efficient solar cells. *Science* **356**, (2017).
3. McMeekin, D. P. *et al.* A mixed-cation lead mixed-halide perovskite absorber for tandem solar cells. *Science* **351**, 151–155 (2016).
4. Yakunin, S. *et al.* Detection of X-ray photons by solution-processed lead halide perovskites. *Nat. Photonics* **9**, 444–449 (2015).
5. Song, J. *et al.* Quantum Dot Light-Emitting Diodes Based on Inorganic Perovskite Cesium Lead Halides (CsPbX<sub>3</sub>). *Adv. Mater.* **27**, 7162–7167 (2015).
6. Stranks, S. D. & Snaith, H. J. Metal-halide perovskites for photovoltaic and light-emitting devices. *Nat. Nanotechnol.* **10**, 391–402 (2015).
7. Green, M. A., Ho-Baillie, A. & Snaith, H. J. The emergence of perovskite solar cells. *Nat. Photonics* **8**, 506–514 (2014).
8. Lee, M. M., Teuscher, J., Miyasaka, T., Murakami, T. N. & Snaith, H. J. Efficient hybrid solar cells based on meso-superstructured organometal halide perovskites. *Science* **338**, 643–647 (2012).
9. Jeon, N. J. *et al.* Compositional engineering of perovskite materials for high-performance solar cells. *Nature* **517**, 476–480 (2015).
10. Eperon, G. E. *et al.* Formamidinium lead trihalide: a broadly tunable perovskite for efficient planar heterojunction solar cells. *Energy Environ. Sci.* **7**, 982 (2014).
11. Yin, W.-J. W., Yang, J.-H. J., Kang, J., Yan, Y. & Wei, S.-H. Halide Perovskite Materials for Solar Cells: A Theoretical Review. *J. Mater. Chem. A* **3**, 8926–8942 (2015).
12. Amat, A. *et al.* Cation-induced band-gap tuning in organohalide perovskites: Interplay of spin-orbit coupling and octahedra tilting. *Nano Lett.* **14**, 3608–3616 (2014).
13. Filip, M. R. & Giustino, F. Steric engineering of metal-halide perovskites with tunable optical bandgaps. *Nat. Commun.* **5**, 1–19 (2014).
14. Ball, J. M. *et al.* Optical properties and limiting photocurrent of thin-film perovskite solar cells. *Energy Environ. Sci.* **8**, 602–609 (2015).
15. Zhou, H. *et al.* Interface engineering of highly efficient perovskite solar cells. *Science* **345**, 542–546 (2014).
16. Correa Baena, J. P. *et al.* Highly efficient planar perovskite solar cells through band alignment engineering. *Energy Environ. Sci.* **8**, 2928–2934 (2015).
17. <http://www.nrel.gov>.
18. Shockley, W. & Queisser, H. J. Detailed balance limit of efficiency of p-n junction solar cells. *J. Appl. Phys.* **32**,

- 510–519 (1961).
19. [www.pveducation.org](http://www.pveducation.org).
20. Yakunin, S. *et al.* Low-threshold amplified spontaneous emission and lasing from colloidal nanocrystals of caesium lead halide perovskites. *Nat. Commun.* **6**, 8056 (2015).
21. Protesescu, L. *et al.* Nanocrystals of Cesium Lead Halide Perovskites (CsPbX<sub>3</sub>, X = Cl, Br, and I): Novel Optoelectronic Materials Showing Bright Emission with Wide Color Gamut. *Nano Lett.* **15**, 3692–3696 (2015).
22. Slavney, A. H. *et al.* Chemical Approaches to Addressing the Instability and Toxicity of Lead–Halide Perovskite Absorbers. *Inorg. Chem.* **56**, 46–55 (2016).
23. Stoumpos, C. C., Malliakas, C. D., Kanatzidis, M. G. & G., K. M. Semiconducting tin and lead iodide perovskites with organic cations: phase transitions, high mobilities, and near-infrared photoluminescent properties. *Inorg. Chem.* **52**, 9019–9038 (2013).
24. Takahashi, Y., Hasegawa, H., Takahashi, Y. & Inabe, T. Hall mobility in tin iodide perovskite CH<sub>3</sub>NH<sub>3</sub>SnI<sub>3</sub>: Evidence for a doped semiconductor. *J. Solid State Chem.* **205**, 39–43 (2013).
25. Liao, W. *et al.* Lead-Free Inverted Planar Formamidinium Tin Triiodide Perovskite Solar Cells Achieving Power Conversion Efficiencies up to 6.22%. *Adv. Mater.* **28**, 9333–9340 (2016).
26. Frolova, L. A., Anokhin, D. V., Gerasimov, K. L., Dremova, N. N. & Troshin, P. A. Exploring the Effects of the Pb<sup>2+</sup> Substitution in MAPbI<sub>3</sub> on the Photovoltaic Performance of the Hybrid Perovskite Solar Cells. *J. Phys. Chem. Lett.* **7**, 4354–4357 (2016).
27. McClure, E. T., Ball, M. R., Windl, W. & Woodward, P. M. Cs<sub>2</sub>AgBiX<sub>6</sub> (X = Br, Cl): New Visible Light Absorbing, Lead-Free Halide Perovskite Semiconductors. *Chem. Mater.* **28**, 1348–1354 (2016).
28. Slavney, A. H., Hu, T., Lindenberg, A. M. & Karunadasa, H. I. A Bismuth–Halide Double Perovskite with Long Carrier Recombination Lifetime for Photovoltaic Applications. *J. Am. Chem. Soc.* **138**, 2138–2141 (2016).
29. Filip, M. R., Hillman, S., Haghighirad, A. A., Snaith, H. J. & Giustino, F. Bandgaps of the Lead-Free Halide Double Perovskites Cs<sub>2</sub>BiAgCl<sub>6</sub> and Cs<sub>2</sub>BiAgBr<sub>6</sub> from Theory and Experiment. *J. Phys. Chem. Lett.* **7**, 2579–2585 (2016).
30. Gélvez-Rueda, M. C. *et al.* Effect of Cation Rotation on Charge Dynamics in Hybrid Lead Halide Perovskites. *J. Phys. Chem. C* **120**, 16577–16585 (2016).
31. Motta, C. *et al.* Revealing the role of organic cations in hybrid halide perovskite CH<sub>3</sub>NH<sub>3</sub>PbI<sub>3</sub>. *Nat. Commun.* **6**, 7026 (2015).
32. Park, M. *et al.* Critical Role of Methylammonium Librational Motion in Methylammonium Lead Iodide (CH<sub>3</sub>NH<sub>3</sub>PbI<sub>3</sub>) Perovskite Photochemistry. *Nano Lett.* **17**, 4145–4157 (2017).





# Background Information and Methodology



## **Partially based on**

Eline M. Hutter, Tom J. Savenije, and Carlito S. Ponseca Jr., Time-Resolved Photoconductivity Measurements on Organo-Metal Halide Perovskites, *Perovskite Solar Cells*, 2017, 179-232, *World Scientific Publishing Co*

Eline M. Hutter, Giles E. Eperon, Samuel D. Stranks, Tom J. Savenije, Charge Carriers in Planar and Meso-Structured Organic-Inorganic Perovskites: Mobilities, Lifetimes, and Concentrations of Trap States, *J. Phys. Chem. Lett.*, 2015, 6, 3082–3090



## 2.1 Band diagrams of semiconductors

A bulk material can be considered as a huge molecule with an indefinite number of bonding and antibonding molecular orbitals.<sup>1</sup> In contrast with molecules however, the orbitals that are close in energy in a bulk material form a quasi-continuum of energy levels: an energy band. In between these bands, there are energy regimes at which there are no molecular orbitals, which are called forbidden bands. In a three-dimensional crystal, the arrangement of atoms and their interatomic distances are not necessarily the same in each direction. Therefore, the energies of both the allowed and forbidden bands are directional, which is often depicted in an energy ( $E$ ) versus  $k$ -space diagram. Here,  $k$  is an angular wavenumber related to momentum  $p$ :

$$k = \frac{p}{\hbar} \quad (2.1)$$

The following equation relates the energy to  $k$ :

$$E = \frac{\hbar^2 k^2}{2m} \quad (2.2)$$

with  $m$  the electron mass and  $\hbar$  the reduced Planck constant. In general, semiconductor materials are characterized by forbidden bands of less than a few eV between a band completely filled with electrons (the valence band) and an empty band (the conduction band). The energy difference between the valence band maximum (VBM) and the conduction band minimum (CBM) is defined as the bandgap value ( $E_g$ ). **Figures 2.1a** and **2.1b** show schematic representations of the energy diagrams in  $k$ -space of direct and indirect semiconductors, respectively.<sup>2</sup> For direct semiconductors, the VBM and CBM are at the same  $k$ -value and as a result, electrons can be thermally or optically excited from the VBM to the CBM with preservation of momentum (**Figure 2.1a**).

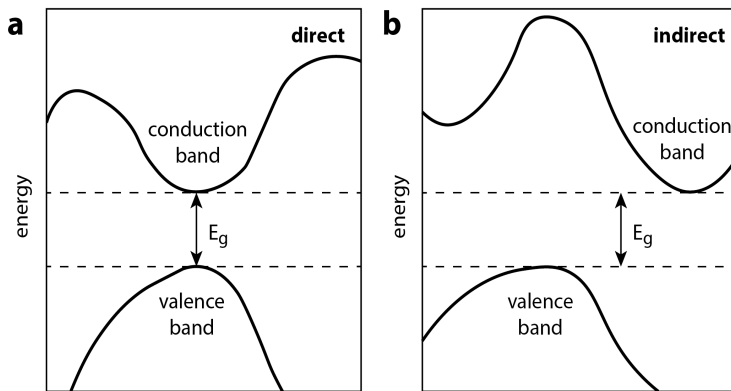


**Figure 2.1:** (a-b) Schematic representation of the energy diagrams in  $k$ -space of direct (a) and indirect (b) semiconductors.

On the other hand, in indirect semiconductors, the CBM is shifted in  $k$ -space with respect to the VBM, which requires a change in momentum. **Equation 2.2** shows that the curvature of the bands in the  $E$  versus  $k$  diagram is determined by  $k^2$  and  $1/m$ . The effective mass  $m^*$  of an electron in a crystal is often expressed as a fraction of the mass of a free electron  $m_0$ . The importance of the effective mass will be further highlighted in **Paragraph 2.3**.

## 2.2 Generation of charges from light

On illumination of semiconductors with photons of energies larger than the bandgap energy, electrons can be excited to the conduction band (CB), leaving a positive charge (hole) in the valence band (VB). Each absorbed photon initially forms one electron-hole pair, which is called an exciton. In an operating solar cell, electrons and holes need to be separately collected at opposite electrodes and therefore, it is desirable that excitons dissociate into free CB electrons and VB holes. The fraction of excitations resulting in free charges ( $x$ ) is related to the exciton binding energy  $E_B$  and the thermal energy  $k_B T$ , and can be calculated using the Saha equation<sup>3</sup>:

$$\frac{x^2}{1-x} = \frac{1}{n} \left( \frac{2\pi m^* k_B T}{h^2} \right)^{3/2} e^{-\frac{E_B}{k_B T}} \quad (2.3)$$

Here,  $\left( \frac{2\pi m^* k_B T}{h^2} \right)^{3/2}$  represents the density of states in the conduction band and  $n$  is the total excitation density. **Figure 2.2** shows  $x$  as function of temperature for  $n$  values ranging from  $10^{14}$  to  $10^{18} \text{ cm}^{-3}$ . The exciton binding energies of 5 meV (a) and 16 meV (b) correspond to the tetragonal and orthorhombic crystal phases, respectively, of methylammonium lead iodide (MAPbI<sub>3</sub>) perovskites.<sup>4</sup> This shows that the yield of exciton dissociation into free charges at room temperature will be close to unity for  $E_B$  values of a few meV, if the total charge density is below  $10^{16} \text{ cm}^{-3}$ .

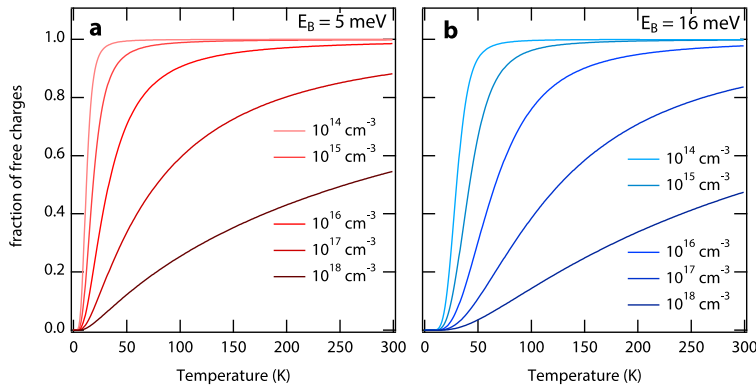


**Figure 2.2:** (a-b) Fraction of the initial charge carrier population leading to free charges as function of temperature for exciton binding energies of 5 meV (a) and 16 meV (b) and charge carrier densities in between  $10^{14}$  and  $10^{18} \text{ cm}^{-3}$ .

Throughout this thesis, time-resolved spectroscopy techniques are used to gain insight in the dynamics of excitons and free charges in MHPs, which are typically generated using short laser pulses with a single photon wavelength  $\lambda$ . In general, the penetration of light through a material varies with the photon energy and as a consequence, the charge carrier generation profile is highly dependent on the excitation wavelength. For a sample with thickness  $L$ , the light intensity transmitted ( $I_T$ ) by the sample is related to the incident intensity ( $I_0$ ) by the absorption coefficient  $\alpha$ :

$$\frac{I_T}{I_0} = e^{-\alpha L} \quad (2.4)$$

Note that this equation neglects reflection. For highly reflective materials such as MHP thin films,  $I_0$  has to be corrected for the reflected light ( $I_R$ ) and the light intensity in the sample at distance  $L$  ( $I_L$ ) from the surface should be calculated from:

$$\frac{I_L}{I_0 - I_R} = e^{-\alpha L} \quad (2.5)$$

**Figure 2.3a** shows the absorption coefficient,  $\alpha$  ( $\text{cm}^{-1}$ ) of a  $\text{MAPbI}_3$ , calculated from absorption and transmission spectra of thin (50 and 300 nm) films. These spectra are recorded with a spectrophotometer equipped with an integrating sphere: thin films are placed in front of the sphere to measure the fraction of transmitted light ( $F_T$ ) or inside the sphere to detect the total fraction of reflected and transmitted light ( $F_{R+T}$ ). The latter is used to calculate the fraction of absorbed light ( $F_A$ ):

$$F_A = 1 - F_{R+T} \quad (2.6)$$

The fraction of reflected light ( $F_R$ ) is determined by:

$$F_R = 1 - F_A - F_T \quad (2.7)$$

Analogous to **Equation 2.5**,  $\alpha$  is obtained from:

$$\frac{F_T}{1 - F_R} = e^{-\alpha L} \quad (2.8)$$

For thick ( $L > 300$  nm) perovskite films, the  $F_T$  at high excitation energies ( $\lambda < 500$  nm) is too small to accurately measure and therefore thinner ( $L > 50$  nm) layers are used to determine  $\alpha$  in this regime. On the other hand, thicker samples enable to resolve  $\alpha$  close to the absorption onset (see also **Figure 3.6b**). **Figure 2.3a** shows that  $\alpha$  is at least two orders of magnitude larger for  $\lambda = 400$  nm than  $\lambda = 800$  nm, which means that varying the excitation wavelength of the laser used in spectroscopy measurements changes the initial density profile of the charge carriers. This is plotted in **Figure 2.3b**, showing the

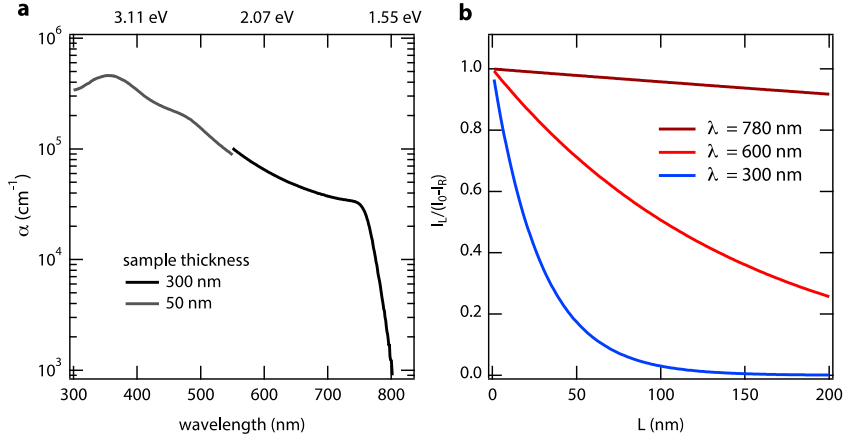


**Figure 2.3:** (a) Semi-logarithmic plot of the absorption coefficient of MAPbI<sub>3</sub>. (b) Initial charge carrier generation profile for different excitation wavelengths using the absorption coefficients from a:  $1.2 \times 10^4 \text{ cm}^{-1}$  for 780 nm,  $6.8 \times 10^4 \text{ cm}^{-1}$  for 600 nm and  $3 \times 10^4 \text{ cm}^{-1}$  for 405 nm. As detailed in **Equations 2.5** and **2.8**, the incident light is corrected for reflection.

penetration of light through MAPbI<sub>3</sub> for excitation wavelengths of 405, 600 and 780 nm, using **Equation 2.5**. This shows that, on illuminating MAPbI<sub>3</sub> at 405 nm, the majority of photo-excited charges is initially located within 100 nm of the surface, independent of the total sample thickness. On the other hand, higher excitation wavelengths result in a lower density, but more homogeneous distribution of charge carriers.

### 2.3 Charge carrier mobility and lifetime

In order to efficiently collect the light-generated electrons and holes, the average distance over which these diffuse has to be sufficient to overcome the thickness of the MHP. Therefore, their diffusion lengths  $L_D$  should ideally be larger than the material thickness required to absorb a substantial fraction of the solar spectrum. As mentioned in **Paragraph 1.2**,  $L_D$  is a function of both the mobility  $\mu$  and lifetime  $\tau$  of charge carriers:

$$L_D = \sqrt{\frac{k_B T}{e} \mu \tau} \quad (2.9)$$

where  $k_B$  is Boltzmann's constant,  $T$  the absolute temperature and  $e$  the electronic charge. In periodic solid materials, such as bulk MHPs, the mobility is a measure for the speed at which a charge moves through the solid in the presence of an electric field:

$$v_d = \mu E \quad (2.10)$$

with  $v_d$  the drift velocity and  $E$  the electric field strength. This net movement of charges

due to drift is possible if there are energy states available that are close in energy.<sup>2</sup> Note that this is different from a net displacement of charges due to random motion (diffusivity), which will only occur in the case of a concentration gradient. The mobility of an electron ( $\mu_e$ ) in the conduction band depends on its effective mass ( $m_e^*$ ), and is therefore different for each semiconductor. Similarly, the hole mobility ( $\mu_h$ ) scales with the effective mass ( $m_h^*$ ) in the valence band, and is therefore not necessarily equal to  $\mu_e$ . Another important factor is the scattering time  $\tau_{s,e}$  (or  $\tau_{s,h}$ ), which is defined as the time that an electron (hole) can travel until a collision. Therefore, electron and hole mobility are defined as:<sup>2</sup>

$$\mu_e = \frac{e\tau_{s,e}}{m_e^*} \quad (2.11)$$

$$\mu_h = \frac{e\tau_{s,h}}{m_h^*} \quad (2.12)$$

Examples of scattering events that reduce  $\mu_e$  or  $\mu_h$  include collisions with vibrating lattice atoms, also known as phonon scattering, and collisions with charged defects in the lattice, referred to as ionized impurity scattering. Information about the dominant scattering mechanism can be obtained from the temperature dependence of  $\mu$ . That is, enhanced thermal motion of atoms results in reduced phonon scattering times ( $\tau_{s,phonon}$ ), which decreases the mobility on increasing temperatures according to:<sup>2</sup>

$$\tau_{s,phonon}(T) \propto \mu_{phonon}(T) \propto T^{-3/2} \quad (2.13)$$

On the other hand, the temperature dependence of mobility due to ionized impurity scattering scales with:<sup>2</sup>

$$\tau_{s,impurity}(T) \propto \mu_{impurity}(T) \propto \frac{T^{3/2}}{N} \quad (2.14)$$

where  $N$  is the concentration of charged defects. The proportionality between temperature and the ionized impurity scattering time ( $\tau_{s,impurity}$ ) can be understood from the thermal velocity of charge carriers. Enhanced velocity of charges reduces their time spent in proximity of a charged defect and as a consequence, the ionized impurity scattering probability decreases with increasing temperatures. The total scattering time ( $\tau_s$ ) is a function of all scattering events:

$$\frac{1}{\tau_s} = \frac{1}{\tau_{phonon}} + \frac{1}{\tau_{impurity}} + \dots \quad (2.15)$$

Hence, the absolute values of  $\mu_e$  and  $\mu_h$  are highly dependent on intrinsic material properties such as the band structure, but may also vary per sample based on its defect chemistry.

Another crucial parameter for  $L_D$  is the charge carrier lifetime  $\tau$ , which is defined as the average time between the generation of a charge carrier and its decay. Charge carrier decay can occur *via* recombination between a conduction band electron and a valence band hole, while energy is released in the form of light or heat. In general, electron-hole recombination is faster in direct semiconductors than in indirect semiconductors, resulting in longer charge carrier lifetimes for the latter. In addition, photo-generated electrons and/or holes can get trapped into intra-bandgap states, which reduces their lifetime as a free charge and decreases their collection probability. Analogous to the mobility, the lifetimes of electrons ( $\tau_e$ ) and hole ( $\tau_h$ ) are thus a function of intrinsic properties such as the type of bandgap, but also highly sensitive to variable parameters like the nature and concentrations of defects in a material.

## 2.4 The Time-Resolved Microwave Conductivity technique

The Time-Resolved Microwave Conductivity (TRMC) technique can be used to study both the mobilities and lifetimes of photo-generated charge carriers in semiconductor materials with low background conductivities.<sup>5–8</sup> Additionally, extensive analysis of TRMC data provides insight in the recombination mechanisms and defect densities. The TRMC technique is based on the interaction between the electric field component of microwaves (GHz regime) and mobile charge carriers. Pulsed laser light is used to excite electrons from the VB to the CB of the semiconductor of interest. In the past decades, TRMC measurements have been extensively used to study charge carrier dynamics in organic systems, *e.g.* conjugated polymers,<sup>5,9</sup> in which electrons are excited from the highest occupied molecular orbital (HOMO) to the lowest unoccupied molecular orbital (LUMO). If photo-excitation of a material results in the generation of free, mobile charge carriers, the conductivity of the material is enhanced. By definition, electrical conductivity  $\sigma$  scales with the concentrations of free electrons  $n_e$ , free holes  $n_h$  and their mobilities according to:

$$\sigma = e(\mu_e n_e + \mu_h n_h) \quad (2.16)$$

With the TRMC technique, the change in conductivity between dark and after illumination, *i.e.*  $\Delta\sigma$ , is studied. From here, the photoconductance  $\Delta G$  can be determined, which will be described in more detail later in this chapter. Although an inhomogeneous excitation profile can result in a gradient in the conductivity throughout the sample, the TRMC technique probes the integrated change in conductivity over the film thickness. Therefore,  $\Delta G$  is proportional to the product of the total number of photo-induced free charges and their mobility (see also **Equation 2.22**). Absorption of microwaves by photo-induced charges reduces the microwave power  $P$  on the detector. This is

schematically depicted in **Figure 2.4**. The normalized reduction in microwave power  $P$  ( $\Delta P/P$ ) is related to  $\Delta G$  by:

$$\frac{\Delta P}{P} = -K\Delta G \quad (2.17)$$

where  $K$  is a sensitivity factor. Note that  $\Delta P$  is negative while  $\Delta G$  is positive.  $\Delta P$  is recorded as function of time after the laser pulse and thus, the TRMC technique can be used to determine both the mobility and time-dependent concentration (*i.e.* the lifetime) of photo-induced free charges. Considering that both electrons and holes contribute to the photoconductance,  $\Delta G$  is proportional to the sum of both their concentrations and mobilities (see **Figure 2.4**). This is similar to photoconductivity measured using THz spectroscopy,<sup>10–12</sup> but in contrast with frequently used time-resolved photoluminescence measurements, which specifically detects radiative recombination events. Therefore, the decays obtained with TRMC cannot be directly compared to PL transients, and careful data analysis is required. Additionally, PL does not necessarily originate from recombination between free mobile charges and therefore, the processes observed with TRMC can be different from those detected with PL.

**Figure 2.5** shows a representation of the TRMC set-up used in this thesis. Here, photo-excitation is realized by laser pulses of 3–5 ns full width at half maximum (FWHM) with a tunable wavelength at a repetition rate of 10 Hz. The maximum light intensity is on the

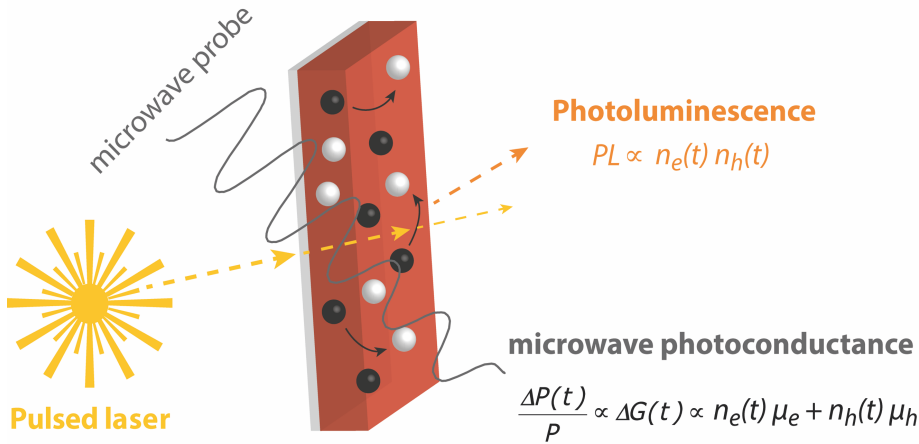


**Figure 2.4:** Representation of time-resolved photoluminescence (TRPL) and microwave conductance (TRMC) measurements on a thin semiconductor film. In both techniques, electrons (black spheres) are excited to the conduction band by a short laser pulse, leaving mobile holes (white spheres) in the valence band. TRMC is used to measure the photoconductance ( $\Delta G$ ), which scales with the time-dependent concentration and mobility  $\mu$ , of free electrons ( $n_e$ ) and holes ( $n_h$ ). The sinusoidal line represents the magnitude of the microwave electric field as it passes through the sample. Radiative recombination of these mobile electrons and holes is probed by TRPL. The latter is, if it originates from recombination between free electrons and holes, a function of the concentrations of electrons ( $n_e(t)$ ) and holes ( $n_h(t)$ ).

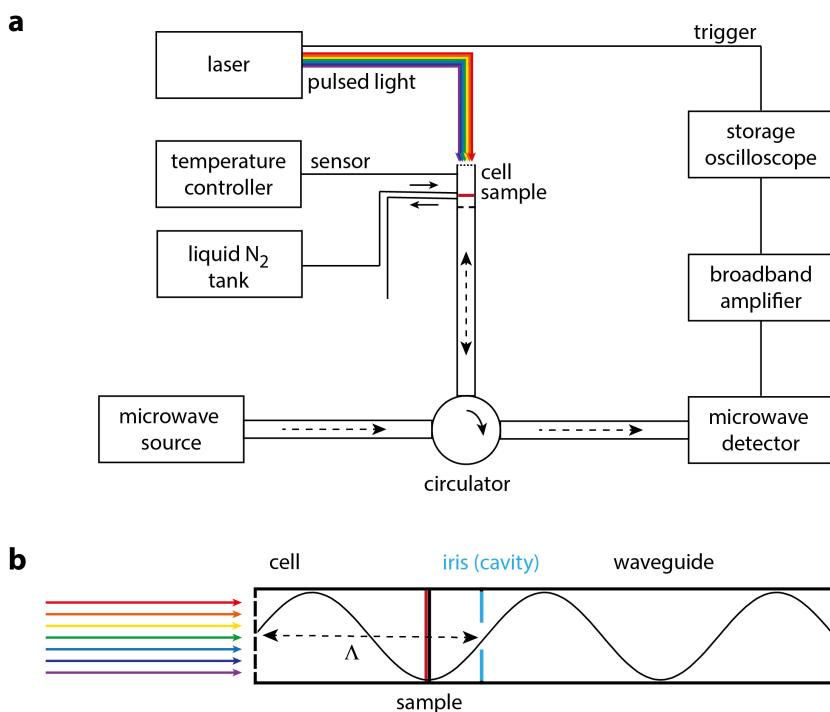


**Figure 2.5:** (a) Schematic representation of the TRMC set-up. Monochromatic microwaves are generated using a voltage-controlled oscillator (microwave source). The sample of interest is placed in a fully reflective microwave cell (b), at approximately  $\frac{3}{4}$  of cell length  $\Lambda$  to maximize overlap with the electric field of the microwaves with wavelength  $\Lambda$ . A circulator separates incident from the reflected microwaves.

order of  $10^{15}$  photons/cm<sup>2</sup> per pulse. Metallic, neutral density filters with different optical densities are placed in between the laser and the sample to vary the photon fluence and thereby the concentration of photo-induced charges. In addition, the set-up is equipped with a cryostat, which enables us to measure at controlled temperatures in between 77 K and 400 K. Monochromatic microwaves with a frequency in the range of 8.2 to 12.4 GHz are generated using a voltage-controlled oscillator. The sample of interest is placed in a microwave cell that ends with a metal grating (see **Figure 2.5b**), which fully reflects the microwaves. This cell is made from a gold-plated X-band waveguide. The sample is placed at  $\frac{3}{4}$  of the cell length  $\Lambda$  so that its position corresponds to the maximum electric field strength for microwaves with wavelength  $\Lambda$ . A quartz window is glued on top of the grating to seal the cell and avoid air exposure of the sample. The millimeter-sized openings of the grating transmit approximately 80% of the laser light.

Most importantly, if the laser pulse induces free charges in the material, its conductivity increases and the total microwave reflection is reduced ( $\Delta P$ ). The cell is connected to a



microwave source and detector *via* X-band waveguides, see **Figure 2.5a**. A microwave circulator is incorporated to separate the incident from the reflected microwaves. The diode detector converts the microwave power into a direct current (DC), generating a voltage of 0.5-1.0 V when dropped across a resistor. Typically,  $\Delta P$  is several orders of magnitude smaller than  $P$ . Therefore, an offset regulator is used to subtract the DC part, which leaves the laser-induced alternating current (AC) signal undisturbed. This AC signal is then amplified ( $26\times$ ) and stored as function of time using a digital oscilloscope with a sampling rate of 4 GHz (every 0.25 ns). The trigger input of the oscilloscope is connected to a fast optical sensor that is illuminated by each laser pulse to start the acquisition of a microwave trace. Typically, the TRMC traces are averaged over  $10^2$  pulses.

As mentioned above, the  $\Delta G$  is directly calculated from  $\Delta P/P$  using the sensitivity factor  $K$ . The magnitude of  $K$  depends on the dimensions of the microwave cell, the dielectric properties of all the media in the cell and the microwave frequency. To determine  $K$  for a given sample, the following approach is used. First, the microwave reflection of a loaded microwave cell,  $P$  is calculated by numerically solving the Maxwell equations, using the characteristics of the cell itself and the dielectric properties of the media inside (sample, substrate and gas). Then, the reflected microwave power  $P'$  of the sample in the same cell is calculated, but now the sample has a small specific conductivity,  $\sigma$ . By definition, a change in conductance is related to the change in conductivity according to:

$$\Delta G = \frac{\Delta \sigma A}{b} = \frac{\Delta \sigma a L}{b} = \Delta \sigma \beta L \quad (2.18)$$

Here,  $A$  is the area of the sample perpendicular to the electric field vector of the microwaves  $E_{mic}$  and  $b$  is the width of the sample in the direction of  $E_{mic}$ . For a sample with thickness  $L$ ,  $A$  is given by  $a \times L$ , where  $a$  is the sample height. Replacing the ratio of  $a$  and  $b$  by  $\beta$ , the change in conductance can be calculated from the change in conductivity, the inner dimensions of the cell ( $\beta$ ) and  $L$ . The sensitivity factor  $K$  can now be found by:

$$\frac{\Delta P}{P} = \frac{(P'-P)}{P} = -K \Delta \sigma \beta L \quad (2.19)$$

Important to note here is that  $K$  is determined for a specific combination of sample, microwave cell and frequency. To illustrate the latter dependency of  $K$ , time-dependent  $\Delta P/P$  traces are measured at different frequencies within the range of 8.2 to 12.2 GHz using a cell filled with nitrogen and a 1 mm thick quartz substrate covered with 250 nm MAPbI<sub>3</sub>. Note that for each frequency, the used laser intensity is the same and hence the  $\Delta G$  is constant. The  $-\Delta P/P$  values are plotted versus frequency in **Figure 2.6**. A clear

broad maximum can be discerned around 8.5 GHz, illustrating that  $K$  is maximum at this frequency. This can be understood from the maximum overlap of the sample with the electric field. At 11 GHz the opposite is true: the electric field strength of the microwaves has a node here so the size of the overlap between field strength and sample is minimal. The full line gives the calculated frequency-dependent  $K$  value for this sample. Note that  $K$  determined using this approach is only valid for thin samples ( $< 1 \mu\text{m}$ ) with low background conductivities, as these barely perturb the microwave pattern.

Once  $K$  is known,  $\Delta G$  can be obtained from the measured  $\Delta P/P$  using **Equation 2.17**. The TRMC signal can then be expressed in the product of the mobility and the charge carrier yield. Assuming that the concentrations of free electrons and holes created by light absorption are initially equal ( $n_e = n_h = n$ ), **Equation 2.16** simplifies to:

$$\sigma = en\Sigma\mu \quad (2.20)$$

in which  $\Sigma\mu = \mu_e + \mu_h$ . The charge carrier generation yield  $\varphi$  is then defined as the fraction of absorbed photons ( $F_A I_0/L$ ) yielding free charges ( $n$ ).

$$\varphi = \frac{Ln}{F_A I_0} \quad (2.21)$$

in which  $I_0$  is the incident intensity of the laser in photons/unit area per pulse and  $F_A$  the fraction of light absorbed at the excitation wavelength.

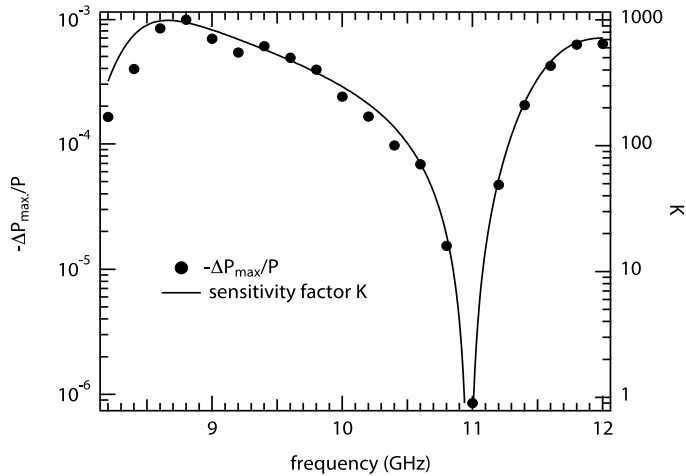


**Figure 2.6:** Dots:  $-\Delta P_{\max}/P$  as function of microwave frequency (8 to 12 GHz) for a 250 nm thin MAPbI<sub>3</sub> film. The solid line represents the frequency-dependent  $K$  factor, obtained from fitting the experimental data points.

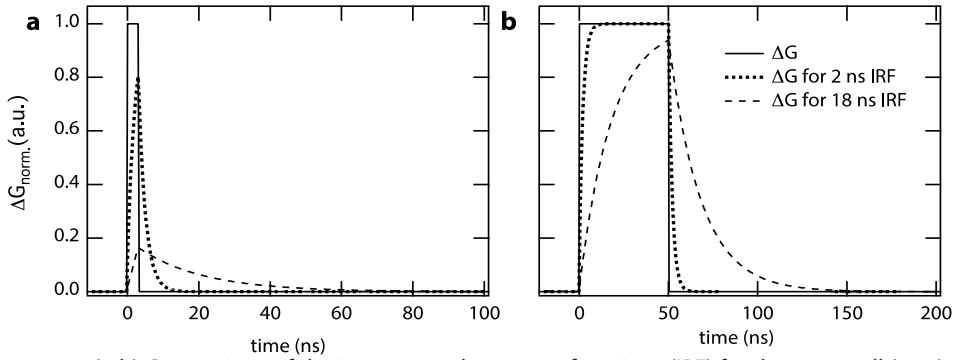


**Figure 2.7:** (a-b) Comparison of the instrumental response functions (IRF) for the open cell (2 ns) and the cavity (18 ns) for (a) a  $\Delta G$  of 3 ns and (b) a  $\Delta G$  of 50 ns.

Combining **Equations 2.19, 2.20 and 2.21**, the product of yield and mobility can be obtained from  $\Delta G_{max}$ :

$$\varphi \Sigma \mu = \frac{Ln}{F_A I_0} \frac{\Delta \sigma}{en} = \frac{L}{F_A I_0} \frac{\Delta G}{e \beta L} = \frac{\Delta G}{\beta e I_0 F_A} \quad (2.22)$$

where the actual thickness of the sample falls out. Importantly, expressing the TRMC signal in the product of  $\varphi \Sigma \mu$  enables direct comparison between TRMC measurements on various types of samples with different compositions, thicknesses and excitation profiles.

The sensitivity of the TRMC set up can be further increased by partially closing the cell using an iris (see **Figure 2.5**). In this case, the cell acts as a resonant cavity for microwaves with wavelength  $\Lambda$ . The standing wave pattern in the cavity leads to more interaction with the sample, thereby enhancing  $K$  and enabling the use of lower photon fluences, however at the expense of the time resolution. For the cavity, the instrumental response time is 18 ns, while this is only 2 ns when a measurement is performed with the so-called open cell. **Figure 2.7** shows the effect of the instrumental response function (IRF) on the measured trace for a mathematically short (a) and long (b) photoconductance signal.<sup>13</sup>

## 2.5 Modelling of Kinetic Data

In order to extract quantitative data out of time-dependent PL and TRMC measurements, we use the following generic kinetic model throughout this thesis, as detailed in **Figure 2.8**, to describe the charge carrier dynamics in MHPs.<sup>14,15</sup> This model accounts for different recombination pathways of photo-excited electrons and holes as function of their densities. This model is based on a homogeneous generation of charges, which can be experimentally realized by using an excitation wavelength close to the absorption

onset (see **Figure 2.3**). Note that only free, mobile charges contribute to the real photoconductance. Considering that the exciton binding energy of MAPbI<sub>3</sub> is only a few meV,<sup>4</sup> the thermal energy at room temperature (*i.e.*  $\sim 26$  meV) is sufficient to dissociate the majority of excitons into free charges (see also **Figure 2.2**). Therefore, it is assumed that at room temperature, every absorbed photon initially leads to one free CB electron and one free VB hole. Since this corresponds to a yield of one (**Equation 2.21**), the initial value of  $n$  is given by:

$$n = \frac{I_0 F_A}{L} \quad (2.23)$$

If the sample is much larger than the penetration depth of light,  $1/\alpha$  can be used instead of  $L$ . This represents the distance at which 63% of the photons is absorbed, *i.e.* where the light intensity is only  $1/e$  of its original value. The time-dependent generation of charge carriers is denoted by  $G_C(t)$ , which takes into account the temporal profile and total light intensity of the laser pulse. The concentration of photo-excited CB electrons ( $\Delta n_{CB} = \Delta n_e$ ) and VB holes ( $-\Delta n_{VB} = \Delta n_h$ ) are initially equal, but can be different as function of time depending on their recombination pathways. For instance, there could be intra-bandgap states acting as electron traps. In this kinetic model, see **Figure 2.8**, the total trap density is represented by  $N_T$ . The concentration of trapped electrons is denoted as  $n_t$ . In a perfectly intrinsic semiconductor, the initial concentrations of CB electrons and VB holes upon photo-excitation are the same. However, in general, impurities in the crystal lattice can result in CB electrons (n-type) or VB holes (p-type) already present before photo-excitation. In **Figure 2.8**, the concentration of thermal equilibrium charges (dark carriers) is represented by  $p_0$ . Note that  $p_0$  does not contribute to the photoconductance. However, the recombination of photo-generated charges is affected by  $p_0$ , because the total concentration of VB holes ( $n_h + p_0$ ) is larger than the concentration of CB electrons ( $n_e$ ).

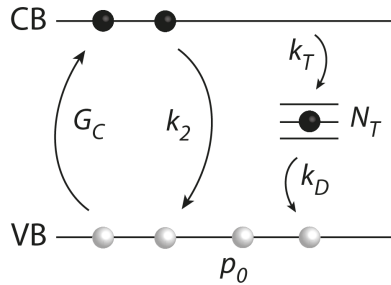


**Figure 2.8:** Kinetic model of processes occurring upon photo-excitation of an MHP, adapted from Stranks *et al.*<sup>14</sup> Here,  $G_C(t)$  represents the photo-excitation of electrons (black spheres) from the valence band (VB) to the conduction band (CB). The electrons in the CB can recombine with holes (white spheres) in the VB via  $k_2$ . In competition with  $k_2$ , electrons can be immobilized in intra-bandgap trap states (total density  $N_T$ ) via  $k_T$ . Finally, the trapped electrons can recombine with holes from the VB via  $k_D$ . In the case of a non-intrinsic MHP, there will be additional holes ( $p_0$ , p-type) on top of the photo-generated holes. Note that this fully mathematical model also holds for the opposite situation, *i.e.* an MHP with trap states for holes and additional dark CB electrons ( $n_0$ , n-type).

The following set of differential equations (**Equations 2.24 to 2.26**) implements **Figure 2.8** and describes  $n_e$  (**2.24**),  $n_h$  (**2.25**) and  $n_t$  (**2.26**) as function of time. The rate constants for band-to-band electron-hole recombination, trap filling and trap depopulation are represented by  $k_2$ ,  $k_T$  and  $k_D$  respectively (**Figure 2.8**). These differential equations are coupled: each photo-excited electron eventually decays back to the ground state.

$$\frac{dn_{CB}}{dt} = \frac{dn_e}{dt} = G_c - k_2 n_e (n_h + p_0) - k_T n_e (N_T - n_t) \quad (2.24)$$

$$\frac{dn_{VB}}{dt} = - \frac{dn_h}{dt} = - G_c + k_2 n_e (n_h + p_0) + k_D n_t (n_h + p_0) \quad (2.25)$$

$$\frac{dn_t}{dt} = k_T n_e (N_T - n_t) - k_D n_t (n_h + p_0) \quad (2.26)$$

As detailed in **Equation 2.24**, the decrease of  $n_e$  over time depends on the recombination rate with VB holes  $k_2 n_e (n_h + p_0)$  and trapping rate  $k_T n_e (N_T - n_t)$ , where  $N_T - n_t$  is the density of available traps. Simultaneously,  $n_t$  increases due to trapping and decreases depending on the recombination rate with holes  $k_D n_t (n_h + p_0)$ . Solving the equations using numerical methods yields the time-dependent concentrations of  $n_e$ ,  $n_h$ , and  $n_t$ . Using **Equations 2.24 to 2.26**, the change in photoconductance as function of time is calculated from the product of charge carrier concentrations and mobilities according to:

$$\Delta G(t) = e\beta L(n_e(t)\mu_e + n_h(t)\mu_h) \quad (2.27)$$

The trapped charge carriers  $n_t$  are immobile and do not contribute to  $\Delta G$ . The mobilities are assumed to be constant within the time window of the measurement and independent of the charge density. Finally, a convolution is applied to take into account the IRF of the set-up and model the experimental TRMC traces.<sup>7,9</sup> Assuming that PL originates only from second-order band-to-band recombination of electrons and holes, the PL lifetime is proportional to the concentration of CB electrons, VB holes and  $k_2$ . The TRPL can then be calculated according to:

$$PL(t) = \frac{k_2 n_e(t)(n_h(t) + p_0)L}{I_0 F_A} \quad (2.28)$$

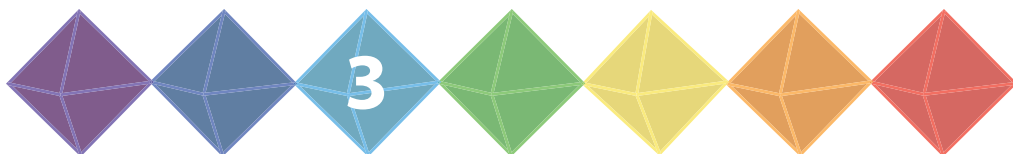
Here, the same set of differential equations is solved, in which only the term  $G_C$  is different due to the fact that another laser was used. This kinetic model can also be used to analyze time-resolved data obtained from different techniques, such as THz or transient absorption (TA) spectroscopy, or describe charge carrier dynamics in other semiconductor materials.

## 2.6 References

1. Shriver & Atkins. *Inorganic Chemistry Fourth Edition*. (2006).
2. Neamen, D. A. *Semiconductor Physics and Devices Fourth Edition*. (2012).
3. D'Innocenzo, V. *et al.* Excitons versus free charges in organo-lead tri-halide perovskites. *Nat. Commun.* **5**, 3586 (2014).
4. Miyata, A. *et al.* Direct measurement of the exciton binding energy and effective masses for charge carriers in organic-inorganic tri-halide perovskites. *Nat. Phys.* **11**, 582–587 (2015).
5. Kroeze, J. E., Savenije, T. J., Vermeulen, M. J. W. & Warman, J. M. Contactless Determination of the Photoconductivity Action Spectrum, Exciton Diffusion Length, and Charge Separation Efficiency in Polythiophene-Sensitized TiO<sub>2</sub> Bilayers. *J. Phys. Chem. B* **107**, 7696–7705 (2003).
6. Sandeep, C. S. S. *et al.* High charge-carrier mobility enables exploitation of carrier multiplication in quantum-dot films. *Nat. Commun.* **4**, 2360 (2013).
7. Savenije, T. J., Ferguson, A. J., Kopidakis, N. & Rumbles, G. Revealing the dynamics of charge carriers in polymer:fullerene blends using photoinduced time-resolved microwave conductivity. *J. Phys. Chem. C* **117**, 24085–24103 (2013).
8. Warman, J. M. *et al.* Charge Mobilities in Organic Semiconducting Materials Determined by Pulse-Radiolysis Time-Resolved Microwave Conductivity:  $\pi$ -Bond-Conjugated Polymers versus  $\pi$ - $\pi$ -Stacked Discotics. *Chem. Mater.* **16**, 4600–4609 (2004).
9. Murthy, D. H. K. *et al.* Origin of reduced bimolecular recombination in blends of conjugated polymers and fullerenes. *Adv. Funct. Mater.* **23**, 4262–4268 (2013).
10. Ponseca Jr, C. S. *et al.* Organometal halide perovskite solar cell materials rationalized: ultrafast charge generation, high and microsecond-long balanced mobilities, and slow recombination. *J. Am. Chem. Soc.* **136**, 5189–5192 (2014).
11. Hutter, E. M., Savenije, T. J. & Ponseca Jr, C.S. in *Perovskite Solar Cells*, 2017, 179-232, *World Scientific Publishing Co*.
12. Wehrenfennig, C., Liu, M., Snaith, H. J., Johnston, M. B. & Herz, L. M. Charge-Carrier Dynamics in Vapour-Deposited Films of the Organolead Halide Perovskite CH<sub>3</sub>NH<sub>3</sub>PbI<sub>3-x</sub>Cl<sub>x</sub>. *Energy Environ. Sci.* **7**, 2269–2275 (2014).
13. Ponseca Jr, C. S. *et al.* Mechanism of Charge Transfer and Recombination Dynamics in Organo Metal Halide Perovskites and Organic Electrodes, PCBM, and Spiro-OMeTAD: Role of Dark Carriers. *J. Am. Chem. Soc.* **137**, 16043–16048 (2015).
14. Stranks, S. D. *et al.* Recombination Kinetics in Organic-Inorganic Perovskites: Excitons, Free Charge, and Subgap States. *Phys. Rev. Appl.* **2**, 34007 (2014).
15. Hutter, E. M., Eperon, G. E., Stranks, S. D. & Savenije, T. J. Charge Carriers in Planar and Meso-Structured Organic-Inorganic Perovskites: Mobilities, Lifetimes and Concentrations of Trap States. *J. Phys. Chem. Lett.* **6**, 3082–3090 (2015).



# Charge Carriers in Thin Films and Macroscopic Crystals of Methylammonium Lead Iodide Perovskites



## ABSTRACT

Although highly efficient solar cells have been obtained using thin films of solution-processed MAPbI<sub>3</sub>, there remains limited knowledge about the relationship between preparation route and optoelectronic properties. In this chapter, we use complementary time-resolved microwave conductivity and photoluminescence to investigate the charge carrier dynamics in thin planar MAPbI<sub>3</sub> films prepared *via* different routes. Mobilities close to 30 cm<sup>2</sup>/(Vs) and microsecond-long lifetimes are found in thin films of MAPbI<sub>3</sub> prepared from a PbCl<sub>2</sub> precursor, compared to lifetimes of only a few hundred nanoseconds in planar MAPbI<sub>3</sub> synthesized from PbI<sub>2</sub>. We describe our TRMC and PL experiments with a global kinetic model, using one set of kinetic parameters characteristic for each sample. We find that the microsecond-long lifetimes found in the MAPbI<sub>3</sub> prepared from PbCl<sub>2</sub> are related to the trap density being as low as 5×10<sup>14</sup> cm<sup>-3</sup>, which is at least one order of magnitude lower than for the other synthesis routes. We attribute the differences in trap density to the film morphology and crystal domain size. Finally, we use single crystals of MAPbI<sub>3</sub> as model systems to study optical absorption, charge carrier generation and recombination lifetimes. Most importantly, we find that for homogeneous excitation throughout the crystal, the lifetime of free charges exceeds 15 μs. This means that the diffusion length in MAPbI<sub>3</sub> can be as large as 50 μm if it is no longer limited by the dimensions of the crystallites.

### Partially based on

Eline M. Hutter, Giles E. Eperon, Samuel D. Stranks, Tom J. Savenije, Charge Carriers in Planar and Meso-Structured Organic–Inorganic Perovskites: Mobilities, Lifetimes, and Concentrations of Trap States, *J. Phys. Chem. Lett.*, 2015, 6, 3082–3090

Yu Bi, Eline M. Hutter, Yanjun Fang, Qingfeng Dong, Jinsong Huang, Tom J. Savenije, Charge Carrier Lifetimes Exceeding 15 Microseconds in Methylammonium Lead Iodide Single Crystals, *J. Phys. Chem. Lett.*, 2016, 7, 923–928

Eline M. Hutter, Tom J. Savenije, and Carlito S. Ponseca Jr., Time-Resolved Photoconductivity Measurements on Organo-Metal Halide Perovskites, *Perovskite Solar Cells*, 2017, 179-232, World Scientific Publishing Co



### 3.1 Introduction

As mentioned in **Chapter 1**, metal halide perovskites (MHPs) are intensively investigated since these materials can be used as photoactive layer in photovoltaic devices yielding highly efficient solar cells.<sup>1–11</sup> Different parameters, *e.g.* the morphology, structure and composition, have been varied in these MHPs to optimize their photovoltaic performance.<sup>12–15</sup> The first embodiments consisted of MAPbI<sub>3</sub> perovskite crystals infiltrated into a meso-structured TiO<sub>2</sub> or insulating alumina (Al<sub>2</sub>O<sub>3</sub>) scaffold.<sup>15</sup> However, the devices with the highest efficiencies to date either have a substantial fraction of MHP capping layer on top of the TiO<sub>2</sub> or Al<sub>2</sub>O<sub>3</sub> scaffold or form planar heterojunction configurations in which a thin perovskite film is sandwiched between n- and p-type contacts.<sup>16</sup> In addition, it was found that using PbCl<sub>2</sub> instead of PbI<sub>2</sub> as the lead precursor for MAPbI<sub>3</sub> significantly improved photovoltaic performance.<sup>2,15,17</sup> Although the first is referred to as MAPbI<sub>3-x</sub>Cl<sub>x</sub>, the fraction of chloride typically appeared not to be more than a few hundred parts per million.<sup>18–21</sup> Many studies have reported that this preparation route leads to enlargement of the crystalline domains as compared to films prepared from a stoichiometric reaction between MAI and PbI<sub>2</sub>.<sup>2,18,22–29</sup> Furthermore, the longer photoluminescence (PL) lifetimes in MAPbI<sub>3-x</sub>Cl<sub>x</sub> with respect to MAPbI<sub>3</sub> suggest that there are fewer non-radiative pathways.<sup>14,30–33</sup> However, there is still little understanding of the relationship between the structure and composition of the MHP absorber layer and its photo-physical properties.

In this chapter, we study the kinetics of charge carriers in solution-processed thin films of MAPbI<sub>3</sub> and MAPbI<sub>3-x</sub>Cl<sub>x</sub> and compare these to their meso-structured analogues (*i.e.*, MHPs infiltrated into an insulating Al<sub>2</sub>O<sub>3</sub> scaffold). The charge carrier dynamics are investigated using the time-resolved microwave conductivity (TRMC) technique.<sup>34,35</sup> Most importantly, with this technique we can measure the charge carrier dynamics at incident light intensities representative for solar radiation. We interpret our results with the kinetic model presented in **Chapter 2**. This enables us to extract the rate constants for second-order recombination and charge carrier trapping. In addition, we can determine for each preparation route the density of trap states<sup>36</sup> and background charges, which most likely result from unintentional doping of the MHPs.<sup>37–40</sup> Complementary time-resolved photoluminescence (TRPL) measurements are then performed to specifically study the kinetics of radiative recombination and the results are included in our model. Based on the electron and hole lifetimes extracted from our kinetic model, we separately determine the electron and hole diffusion lengths. From here, we conclude that diffusion lengths are larger in MAPbI<sub>3-x</sub>Cl<sub>x</sub> than in MAPbI<sub>3</sub>, and in both cases at least 1  $\mu\text{m}$ .

Finally, we perform the same set of experiments and analysis on mm-sized crystals of MAPbI<sub>3</sub>.<sup>41–45</sup> By varying the excitation wavelength, we manipulate the charge carrier generation profile, which allows us to investigate the decay of charges generated close to the surface and compare this to the decay of charges distributed homogeneously throughout the crystal. Importantly, we find that charges deep inside the crystal can have diffusion lengths close to 50  $\mu\text{m}$ , which is one order of magnitude larger than for polycrystalline films.

### 3.2 Thin Film Perovskites

The kinetic model presented in **Chapter 2** was used to describe TRMC and TRPL measurements on solution-processed thin films of  $\text{MAPbI}_3$  and  $\text{MAPbI}_{3-x}\text{Cl}_x$ . Planar thin films were compared to their meso-structured analogues, *i.e.* MHPs infiltrated into an insulating  $\text{Al}_2\text{O}_3$  scaffold, which both have been used to produce state-of-the-art perovskite solar cells.<sup>19,24</sup> We deduced the charge carrier mobilities and lifetimes from the measurements,<sup>10</sup> whereas we obtained the global kinetic parameters from modelling both the TRMC and TRPL data for each sample.

Planar thin films ( $\sim 300$  nm) of  $\text{MAPbI}_3$  and  $\text{MAPbI}_{3-x}\text{Cl}_x$  were spin-coated directly on quartz substrates using  $\text{PbI}_2$  and  $\text{PbCl}_2$  as the lead source, respectively.<sup>47</sup> Although the fraction of chloride ( $x$ ) varies depending on processing conditions, it is not more than a few hundred parts per million.<sup>18–21</sup> Scanning electron microscope (SEM) images showed that in the  $\text{MAPbI}_{3-x}\text{Cl}_x$  thin film, the crystals are micrometer-sized, whereas those in  $\text{MAPbI}_3$  are on the order of only a few hundred nanometers (see **Figure A3.1** in **Appendices**).<sup>46</sup> In addition, mesoporous alumina ( $\text{Al}_2\text{O}_3$ ) scaffolds were infiltrated with MHPs using the same precursor solutions, yielding meso-structured films ( $\sim 400$  nm thick) of  $\text{MAPbI}_3/\text{Al}_2\text{O}_3$  and  $\text{MAPbI}_{3-x}\text{Cl}_x/\text{Al}_2\text{O}_3$ . The concentrations of precursors were such that there was negligible formation of perovskite capping layer on top of the  $\text{Al}_2\text{O}_3$  scaffold, *i.e.* the perovskite is fully contained within the mesoporous layer. The X-Ray Diffraction (XRD) patterns confirmed that all MHP films are highly crystalline, showing strong reflections characteristic for the  $\{110\}$  planes of tetragonal  $\text{MAPbI}_3$  perovskites (see **Figure A3.2** in **Appendices**). Using the Scherrer equation,<sup>47</sup> we estimate that the crystal domain sizes are approximately 50 nm for the meso-structured MHPs.<sup>46</sup> This can be understood considering that the  $\text{Al}_2\text{O}_3$  scaffold limits the growth of MHP crystals and hence, the crystalline domains are of similar size in  $\text{MAPbI}_3/\text{Al}_2\text{O}_3$  and  $\text{MAPbI}_{3-x}\text{Cl}_x/\text{Al}_2\text{O}_3$ .

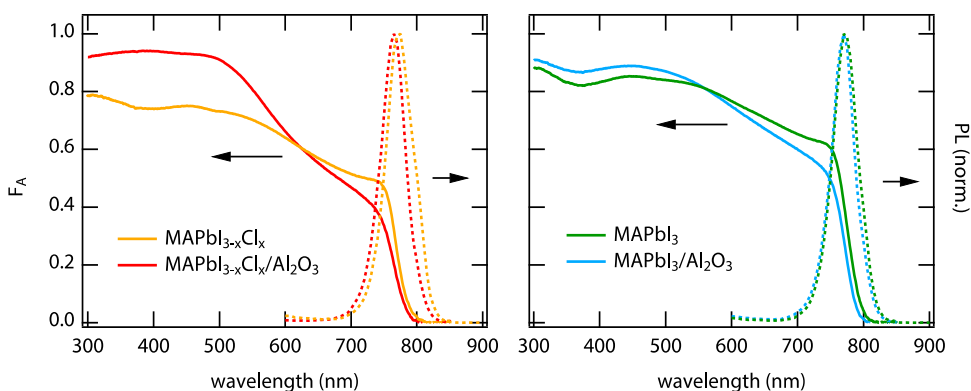


**Figure 3.1:** Fraction of light absorbed ( $F_A$ ) by MHP films with structures as indicated (solid lines) and corresponding photoluminescence (PL) spectra normalized to 1 (dashed lines).

**Figure 3.1** displays the fraction of absorbed light ( $F_A$ , solid lines) and corresponding PL (dashed lines) spectra of the different samples. For all samples, the maximum emission wavelengths are located around  $\lambda = 770$  nm (1.6 eV). We used TRMC technique to measure  $\Delta G$  as function of time after photo-excitation of the different samples at  $\lambda = 600$  nm using incident light intensities ranging over four orders of magnitude: from  $10^9$  to  $10^{13}$  photons/cm<sup>2</sup> ( $3 \times 10^{-4}$  to  $3$   $\mu$ J/cm<sup>2</sup>/pulse). Additionally, TRPL was performed to specifically gain insight in radiative band-to-band recombination ( $k_2$  in **Figure 2.8**). We then used the kinetic model to globally fit the TRMC and TRPL results, using a single set of kinetic parameters for each sample. The traces obtained from fitting the experimental data with the kinetic model introduced in **Paragraph 2.5** are shown in the right panels of **Figure 3.2**. The kinetic parameters that were used to describe the measured TRMC and TRPL data for this specific sample are listed in **Table 3.1**. The left panels in **Figure 3.2** show  $\Delta G$  normalized for the number of absorbed photons as function of time after photo-excitation of MAPbI<sub>3-x</sub>Cl<sub>x</sub> (a), MAPbI<sub>3</sub> (b), MAPbI<sub>3-x</sub>Cl<sub>x</sub>/Al<sub>2</sub>O<sub>3</sub> (c) and MAPbI<sub>3</sub>/Al<sub>2</sub>O<sub>3</sub> (d). The rise of the signal originates from the generation of mobile charges; the maximum signal height represents the product of the charge carrier yield and the sum of their mobilities.<sup>48,49</sup> Assuming that the latter is constant in this time window, the decay of the TRMC signal as function of time after excitation results from a decreasing concentration of mobile carriers. We observe that the sum of the effective electron and hole mobilities (*i.e.*, the maximum TRMC signal) in the planar films is close to 30 cm<sup>2</sup>/(Vs), which is comparable to reported mobilities resulting from THz spectroscopy<sup>50</sup> and photoconductance studies<sup>37,48</sup> on similar types of samples. Based on the effective masses of electrons and holes in MAPbI<sub>3</sub> and the assumption that both have identical scattering times,<sup>51–53</sup> the holes are considered to be twice as mobile as the electrons. This means that the electron and hole mobilities are 10 cm<sup>2</sup>/(Vs) and 20 cm<sup>2</sup>/(Vs), respectively. In contrast, for the meso-structured films the sum of the mobilities is less than 6 cm<sup>2</sup>/(Vs). This lower photoconductance in meso-structured

**Table 3.1:** Overview of kinetic fitting parameters used to fit all TRMC (**Figure 3.2**) and PL (**Figure 3.3**) measurements with the model described by **Equations 2.24** to **2.26** and summarized in **Figure 2.8**.

	MAPbI <sub>3-x</sub> Cl <sub>x</sub>	MAPbI <sub>3</sub>	MAPbI <sub>3-x</sub> Cl <sub>x</sub> /Al <sub>2</sub> O <sub>3</sub>	MAPbI <sub>3</sub> /Al <sub>2</sub> O <sub>3</sub>
Domain size( $\mu$ m)	> 5	$\pm 0.5$	0.05	0.05
$k_2$ ( $\times 10^{-10}$ cm <sup>3</sup> s <sup>-1</sup> )	4.9	3.5	7	6
$k_T$ ( $\times 10^{-10}$ cm <sup>3</sup> s <sup>-1</sup> )	n.a.	1	3.5	2
$k_D$ ( $\times 10^{-10}$ cm <sup>3</sup> s <sup>-1</sup> )	n.a.	0.5	0.5	0.1
$N_T$ ( $\times 10^{15}$ cm <sup>-3</sup> )	< 0.5	60	7	8
$p_0$ ( $\times 10^{15}$ cm <sup>-3</sup> )	1	10	30	35
$\mu_e$ (cm <sup>2</sup> /(Vs))	9	10	2.5	3
$\mu_h$ (cm <sup>2</sup> /(Vs))	18	20	5	6

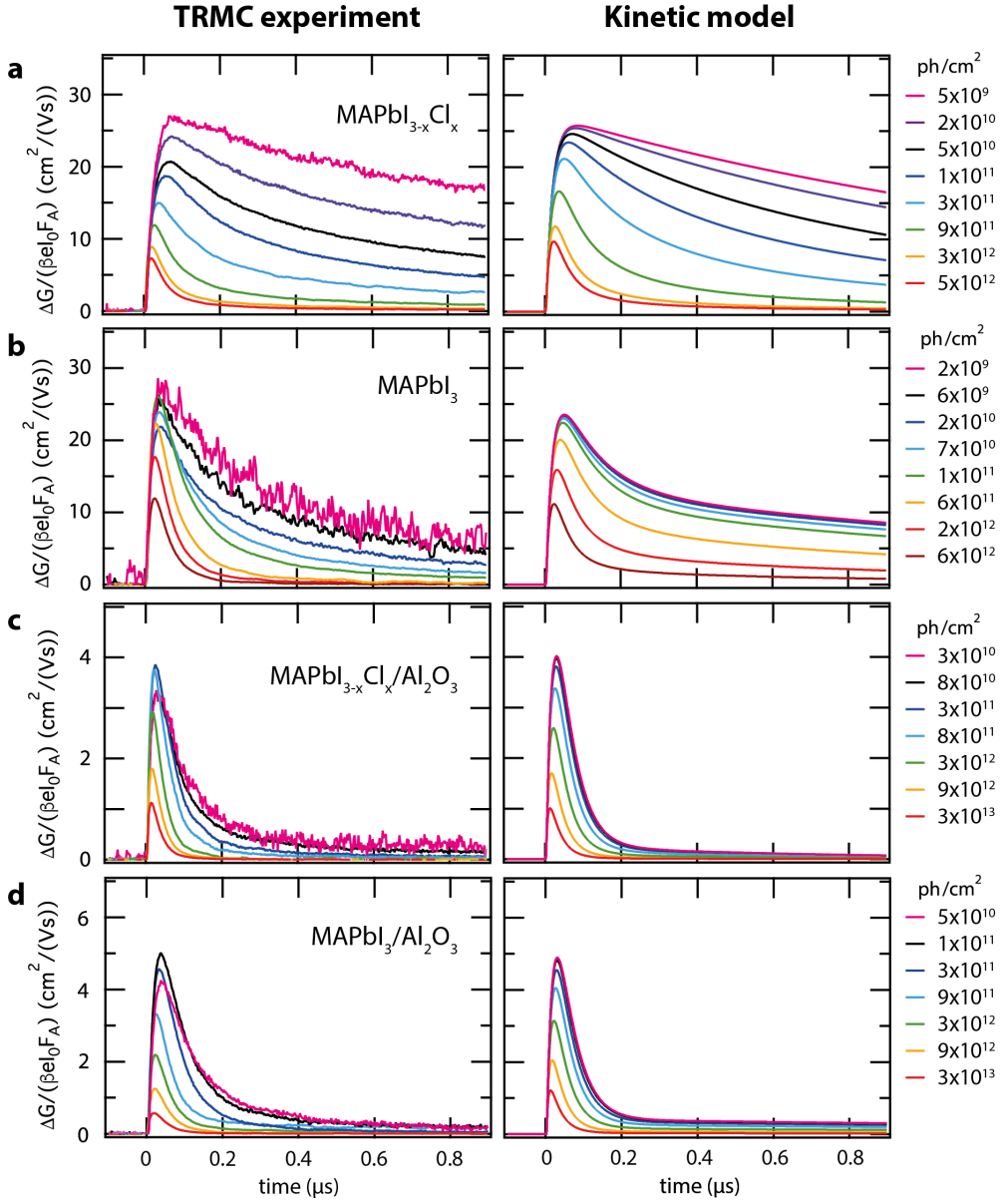


**Figure 3.2:** (a-d) Experimental TRMC traces for (a)  $\text{MAPbI}_{3-x}\text{Cl}_x$ , (b)  $\text{MAPbI}_3$  (c)  $\text{MAPbI}_{3-x}\text{Cl}_x/\text{Al}_2\text{O}_3$  and (d)  $\text{MAPbI}_3/\text{Al}_2\text{O}_3$  recorded at incident light intensities ranging from  $10^9$  to  $10^{13}$  photons/ $\text{cm}^2$  ( $\lambda = 600$  nm, 10 Hz), corresponding to initial charge carrier densities of  $10^{14}$  to  $10^{17}$   $\text{cm}^{-3}$ . The right panels show the traces calculated by solving the differential equations (Equations 2.24 to 2.26) and converting the time-dependent concentration curves to  $\Delta G$  normalized for the number of absorbed photons.

MHPs as compared to planar films has been observed by several groups.<sup>46,54,55</sup> This observation is most likely related to the smaller size of the crystal domains in meso-structured morphologies, which reduces the effective mobilities observed at microwave frequencies (see **Figure A3.3** in **Appendices**).<sup>56–58</sup> At intensities below  $10^{11}$  photons/cm<sup>2</sup>, the lifetimes of mobile carriers are obviously substantially longer in MAPbI<sub>3-x</sub>Cl<sub>x</sub> than in MAPbI<sub>3</sub> and both meso-structured films. The extended charge carrier lifetimes in MAPbI<sub>3-x</sub>Cl<sub>x</sub> are particularly relevant at light intensities below  $5 \times 10^{10}$  photons/cm<sup>2</sup>, since these conditions are representative for illumination by solar radiation.<sup>59</sup> The shorter TRMC lifetimes in MAPbI<sub>3</sub> and the meso-structured films could be attributed to immobilization of charge carriers by trapping or by recombination. For all samples, the maximum signal size lowers and the decay becomes faster with increasing laser intensity, which is indicative of the appearance of decay processes higher than first order.<sup>36,49,50,60</sup> That is, due to the instrumental response time of 18 ns, enhanced recombination results in a decreased intensity-normalized TRMC signal (see also **Figure 2.7**). The charge carrier mobility, on the other hand, is independent of the laser intensity.

Interestingly, we find that this higher order recombination is most pronounced in MAPbI<sub>3-x</sub>Cl<sub>x</sub>, whereas MAPbI<sub>3</sub> and both meso-structured films display semi-first order kinetics at light intensities up to  $10^{11}$  photons/cm<sup>2</sup> (corresponding to  $\sim 10^{15}$  excitations/cm<sup>3</sup>). This absence of higher order decay kinetics in MAPbI<sub>3</sub> and both meso-structured films can be due to *e.g.* trapping of electrons or recombination with dark holes ( $p_0$ , see **Figure 2.8**). That is, second-order electron-hole recombination will start to dominate if the concentration of photo-excited charges exceeds  $N_T$  and  $p_0$ . **Figure 3.3** shows semi-logarithmic time-dependent PL plots for MAPbI<sub>3-x</sub>Cl<sub>x</sub> (a), MAPbI<sub>3</sub> (b), MAPbI<sub>3-x</sub>Cl<sub>x</sub>/Al<sub>2</sub>O<sub>3</sub> (c) and MAPbI<sub>3</sub>/Al<sub>2</sub>O<sub>3</sub> (d), measured at an incident pulsed light intensity of  $4 \times 10^{12}$  photons/cm<sup>2</sup> (2  $\mu$ J/cm<sup>2</sup>) for each pulse at 405 nm and 1 MHz. The calculated traces (black lines) using the kinetic model from **Figure 2.8** and fitting parameters listed in **Table 3.1** are shown together with the experimental TRPL. The PL decay in MAPbI<sub>3-x</sub>Cl<sub>x</sub> (**Figure 3.3a**) exhibits a slower decay at longer times compared to the initial decay. In contrast, the PL transient of MAPbI<sub>3</sub> (see **Figure 3.3b**, green dots) is almost linear in a semi-logarithmic plot, which corresponds to a mono-exponential or pseudo-mono-exponential decay. The PL lifetime is substantially shorter in the meso-structured MHPs (**Figures 3.3c** and **3.3d**) than in their planar analogues.<sup>61</sup> In addition, similar to the TRMC measurements, we observe no obvious difference between the PL lifetime of MAPbI<sub>3-x</sub>Cl<sub>x</sub>/Al<sub>2</sub>O<sub>3</sub> and MAPbI<sub>3</sub>/Al<sub>2</sub>O<sub>3</sub>. The nearly mono-exponential decay in MAPbI<sub>3</sub> could for instance mean that the number of photo-generated electrons is very small compared to the total concentration of holes or vice versa. This could be due to background doping ( $p_0 \gg n_e(t)$ ) and/or photo-doping ( $n_h(t) \gg n_e(t)$ ), the latter arising from trapping of electrons into sub-gap states.<sup>13</sup> In our kinetic model, we account for both background doping and photo-doping. In contrast to MAPbI<sub>3</sub>, the PL decay of the MAPbI<sub>3-x</sub>Cl<sub>x</sub> film in **Figure 3.3a** is initially second-order, which indicates a regime in which electron and hole concentrations are comparable. This means that the initial concentration of photo-excited charge carriers produced by the laser pulse largely

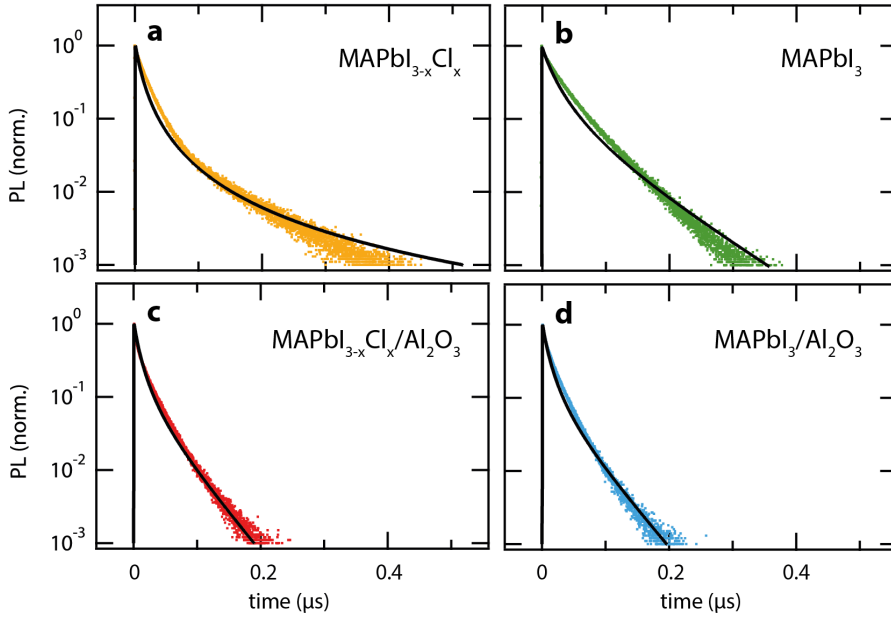


**Figure 3.3:** (a-d) PL lifetimes of photo-excited ( $\lambda = 405$  nm, 1 MHz,  $4 \times 10^{12}$  photons/cm<sup>2</sup>) thin films of MHPs recorded at the maximum emission wavelengths shown in (Figure 3.1). The black lines are the fits from the model.

exceeds the concentration of doping levels arising from photo-doping or background charges, which is consistent with the TRMC results. However, at longer timescales the total charge density drops to reach a mono-exponential decay regime, meaning that there might be a small contribution of background charges. As mentioned before, we included both background carriers ( $p_0$ ) and trap states ( $N_T$ ) to model the experimental TRMC and TRPL results for the planar MAPbI<sub>3</sub> film. This was also the case for the meso-structured films: the model describes the experimental results only if both  $N_T$  and  $p_0$  are included. In contrast, we find that the trap density in the MAPbI<sub>3-x</sub>Cl<sub>x</sub> thin film is too low to significantly contribute to the kinetics in the TRMC experiments. Given that measurements were performed at intensities down to  $5 \times 10^9$  photons/cm<sup>2</sup>, this means that the trap density in MAPbI<sub>3-x</sub>Cl<sub>x</sub> should be less than  $5 \times 10^{14}$  cm<sup>-3</sup>. In both thin films and meso-structured MHPs, we found similar rate constants for band-to-band electron-hole recombination: on the order of  $10^{-10}$  cm<sup>3</sup>s<sup>-1</sup>, which is comparable to earlier reports.<sup>36,62</sup> Furthermore, the rate constants for trap filling are only slightly lower than for band-to-band recombination. This indicates that these are competing processes if the concentration of photo-induced charges is on the same order of magnitude as the trap density. On the other hand, the rate constant for trap depopulation is one order

of magnitude lower, meaning that recombination between a trapped carrier and its counter-charge is relatively slow. This behaviour results in long-lived TRMC signals originating from the mobile counter-charges of the trapped carriers. The trap densities are estimated to be on the order of  $10^{15} \text{ cm}^{-3}$  in  $\text{MAPbI}_{3-x}\text{Cl}_x/\text{Al}_2\text{O}_3$  and  $\text{MAPbI}_3/\text{Al}_2\text{O}_3$  and  $6 \times 10^{16} \text{ cm}^{-3}$  in the  $\text{MAPbI}_3$  thin film. Furthermore, the model suggests a dark carrier concentration of  $10^{15} \text{ cm}^{-3}$  for  $\text{MAPbI}_{3-x}\text{Cl}_x$  and  $> 10^{16} \text{ cm}^{-3}$  for the other MHPs.

Given that both mobile electrons and holes interact with the microwave field, TRMC measurements itself do not enable us to distinguish between the two. However, after applying the kinetic model to the measured data (assuming that electrons are the minority carriers), we can plot the time-dependent concentrations of free electrons, free holes and trapped electrons individually. **Figure 3.4** shows the concentration of electrons in the CB (red), trap states (blue) and VB (black) as function of time after excitation of  $\text{MAPbI}_3$ . Here, the initial concentration of photo-induced electrons and holes is  $2.4 \times 10^{15} \text{ cm}^{-3}$ . As extracted from fitting the experimental photoconductance (**Figure 3.2**), the trap density for this sample is  $6 \times 10^{16} \text{ cm}^{-3}$  and  $p_0$  is  $1 \times 10^{16} \text{ cm}^{-3}$ . Furthermore, the rate constants for electron trapping and second-order recombination are on the same order of magnitude. Therefore, the terms  $k_2 n_e (n_h + p_0)$  and  $k_T n_e (N_T - n_t)$  from **Equations 2.24 to 2.26** are initially comparable for these  $2.4 \times 10^{15}$  photo-induced charge carriers per  $\text{cm}^3$ . This means that electron trapping successively competes with band-to-band recombination, which results in a shorter electron lifetime compared to the holes (as shown in **Figure 3.4a**). Considering that trapped electrons are immobile, the TRMC signal can be separated into the contribution from photo-induced free electrons and holes. **Figure 3.4b** shows a typical example of an experimental TRMC trace (green solid line) together with the calculated traces for electrons (red), holes (black) and the sum of the two (green dotted line) for the planar  $\text{MAPbI}_3$  ( $I_0 = 2 \times 10^9 \text{ photons/cm}^2$ ). For this excitation density of  $7 \times 10^{13} \text{ cm}^{-3}$ , the electron concentration has decreased to half

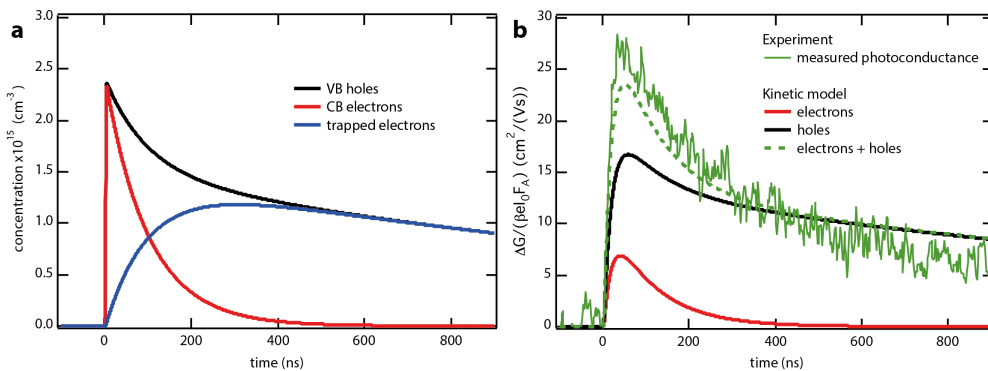


**Figure 3.4:** (a) Time-dependent concentration of  $n_e$  (red),  $n_h$  (black) and  $n_t$  (blue) for  $2.4 \times 10^{15}$  photo-induced charge carriers per  $\text{cm}^3$ . (b) Photoconductance as function of time for a 300 nm  $\text{MAPbI}_3$  film (solid green line), after excitation at 600 nm for an incident fluence of  $2 \times 10^9 \text{ photons/cm}^2$  ( $7 \times 10^{13}$  charge carriers per  $\text{cm}^3$ ), together with a theoretical trace (dotted green line) implementing the kinetic model from **Figure 2.8**. Based on this model, the contributions of electrons (red) and holes (black) to the photoconductance could be separated.



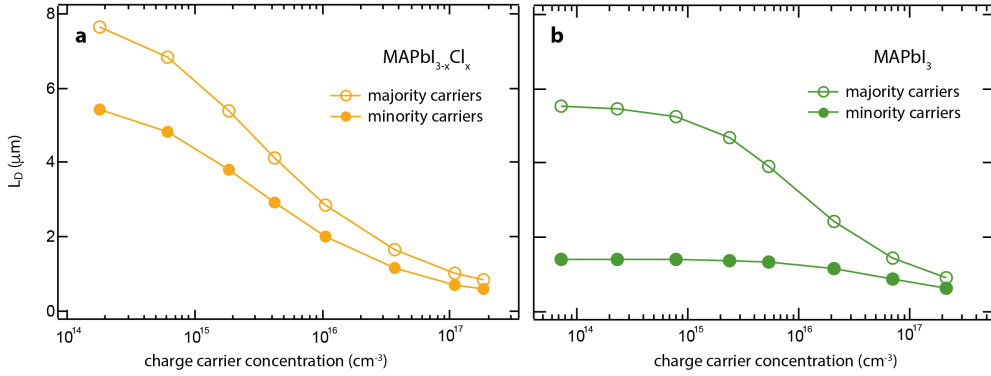


**Figure 3.5:** (a-b) Diffusion length of minority carriers (closed circles) and majority carriers (open circles) as function of initial charge density for  $\text{MAPbI}_{3-x}\text{Cl}_x$  (a) and  $\text{MAPbI}_3$  (b), calculated by **Equation 2.9**. The mobilities and lifetimes were obtained from modelling the experimental data (see **Figure 3.2**).

3

its initial value after  $\sim 80$  ns. We further refer to this as the half lifetime  $\tau_{1/2}$ . Using the electron mobility listed in **Table 3.1**, we calculate the electron diffusion length to be 1.4  $\mu\text{m}$  according to **Equation 2.9**. Similarly, the  $\tau_{1/2}$  of holes is  $\sim 600$  ns, which results in a hole diffusion length of 5.5  $\mu\text{m}$ . Note that the electron and hole lifetimes and thus their diffusion lengths are highly dependent on the initial charge carrier concentration. We used the electron and hole lifetimes that we obtained from applying the kinetic model to the experimental TRMC and TRPL data to calculate the charge-specific  $L_D$  as function of the concentration of photo-induced charges. The results are summarized in **Figure 3.5**. At  $10^{15}$  charge carriers/ $\text{cm}^3$ , which is a typical density for steady-state AM1.5 solar illumination conditions,<sup>59</sup> the longest electron and hole diffusion distances are expected for planar  $\text{MAPbI}_{3-x}\text{Cl}_x$ . This mainly results from the longer lifetimes compared to the other sample types. Additionally, due to the relatively low  $N_T$  and  $p_0$  in  $\text{MAPbI}_{3-x}\text{Cl}_x$ , the lifetimes of electrons and holes are almost the same. As a consequence, assuming that their mobilities differ not more than a factor two, the diffusion lengths of electrons and holes are very close. On the other hand, in planar  $\text{MAPbI}_3$ , the diffusion length is substantially shorter for electrons than holes, especially at excitation densities below  $5 \times 10^{16}$  charge carriers/ $\text{cm}^3$ . This can be explained considering that  $N_T$  and  $p_0$  are both on the order of  $10^{16} \text{ cm}^{-3}$ , resulting in a shorter electron lifetime with respect to the holes. However, the electron diffusion length in excess of 1  $\mu\text{m}$  is larger than the film thickness required to absorb most of the visible light and thus sufficient to enable efficient electron collection in a solar cell device.<sup>14</sup>

For all samples, second-order electron-hole recombination is the dominant recombination pathway at charge carrier densities of  $10^{17} \text{ cm}^{-3}$ , resulting in nearly equal lifetimes for electrons and holes. If their mobilities are also comparable, the electron



and hole diffusion lengths will be similar. Both meso-structured films show comparable TRMC and TRPL decay kinetics. Thus, it seems that using either  $\text{PbCl}_2$  or  $\text{PbI}_2$  as the precursor does not affect the electronic properties of the resulting perovskite film when this is grown within a mesoporous alumina scaffold. In contrast, the charge carrier dynamics in the  $\text{MAPbI}_3$  thin film are obviously different from  $\text{MAPbI}_{3-x}\text{Cl}_x$ . Hence, for the planar thin films, we conclude that  $\text{PbCl}_2$  instead of  $\text{PbI}_2$  to solution-process  $\text{MAPbI}_3$  substantially improves the electronic properties of the resulting film. In the kinetic model shown in **Figure 2.8**, the MHPs are p-type semiconductors in which the trap states are electronic in nature.<sup>36,37,63</sup> We note that this purely mathematical model also holds for the opposite situation, *i.e.* an n-type MHP in which the trap-states are hole-selective and the electrons twice as mobile as the holes. Given that TRMC measurements do not provide direct evidence for the type of background charges, we can not conclude whether the films are unintentionally n-type or p-type doped.

In summary, we used complementary TRMC and TRPL measurements to investigate the charge carrier dynamics in planar and mesoporous perovskite films prepared with different precursors. We then applied a kinetic model to describe the experimental data to estimate the concentrations of background charges and trap states. The observation that global fitting could be performed to both TRMC and TRPL measurements suggests that recombination of free mobile charges gives rise to PL in  $\text{MAPbI}_3$  thin films.

### 3.3 Macroscopic Perovskite Crystals

Millimeter-sized MHP crystals are an ideal model system to investigate intrinsic material properties, such as the charge carrier recombination pathways in the absence of grain boundaries.<sup>41–45</sup> TRMC, TRPL and the kinetic model from **Figure 2.8** were used to analyze macroscopic  $\text{MAPbI}_3$  crystals with dimensions of 10 mm by 8 mm by 3 mm.<sup>64</sup> These were grown in a supersaturated  $\text{MAPbI}_3$  precursor solution using the top-seeded-solution-growth method.<sup>33</sup> Different excitation wavelengths were used to manipulate the location of charge carrier generation and study the effect on the recombination dynamics.

As shown in **Figure 2.3b**, the penetration depth ( $1/\alpha$ ) of visible light in  $\text{MAPbI}_3$  is typically a few hundred nanometers: at least three orders of magnitude smaller than the total depth of the crystal. Therefore, visible light can be used to study the dynamics of charge carriers relatively close to the surface. On the other hand, an initially homogeneous charge carrier concentration can only be realized if  $\alpha$  is substantially lower, which is the case for excitation wavelengths close to the absorption onset. We used an integrating sphere to collect both specular and diffuse reflectance of the  $\text{MAPbI}_3$  crystal (**Figure 3.6a**). By subtracting these from the incident light intensity, we obtained the absorption spectrum of the macroscopic crystal. This is displayed in **Figure 3.6b**, where  $\alpha$  is plotted in the inset for excitation wavelengths between 820 and 890 nm. We used the wavelength-dependent absorption coefficients from **Figure 2.3a** and **Figure 3.6b** to calculate the charge carrier generation profile as function of the excitation wavelength. The results are shown on a linear scale in **Figure 3.6c** for 500 nm (2.48 eV), 820 nm (1.51 eV) and 845 nm (1.47 eV) and on a semi-logarithmic scale in **Figure 3.6d**. This visualizes the

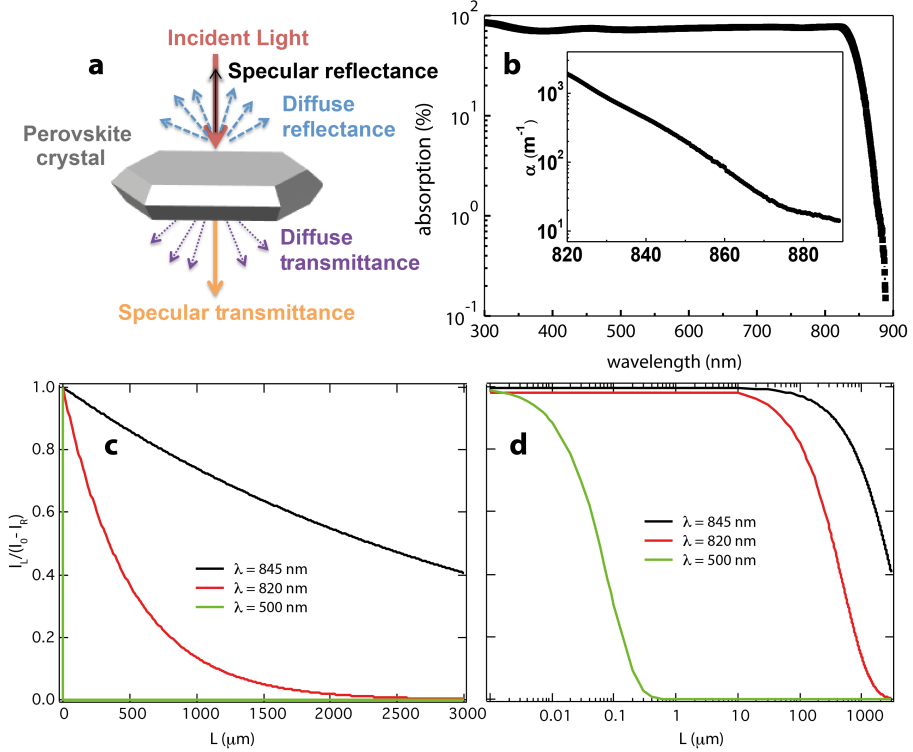


**Figure 3.6:** (a) Overview of absorption measurement on a  $\text{MAPbI}_3$  single crystal. (b) Light absorption (%) and absorption coefficient ( $\text{m}^{-1}$ ) close to the onset of the bandgap. The absorption coefficients at  $\lambda = 820 \text{ nm}$  ( $2 \times 10^3 \text{ m}^{-1}$ ) and  $\lambda = 845 \text{ nm}$  ( $3 \times 10^2 \text{ m}^{-1}$ ) were used to model the excitation profile, see (c-d) where the x-axis corresponds to the total thickness of the single crystal. The excitation profile at 500 nm was calculated using the absorption coefficient from **Figure 2.3**.

extremely different distribution of charge carriers in a 3 mm thick crystal for these excitation wavelengths. With an excitation wavelength of 845 nm, which is close to the absorption, a homogeneous concentration profile can be realized since  $1/\alpha$  is 0.33 cm and thus close to the thickness of the crystal. The  $\text{MAPbI}_3$  crystal was glued on a quartz substrate and mounted in the microwave cell to perform the TRMC measurements. Given that the crystal is extremely large with respect to thin films, the sensitivity factor  $K$  of the microwave cell can no longer be calculated as described in **Paragraph 2.4**. Without accurate determination of  $K$ ,  $\Delta G$  and thus  $\varphi \Sigma \mu$  cannot be calculated from  $\Delta P/P$ . Therefore,  $\Delta P/P$  was only corrected for  $I_0$  to compare the different excitation wavelengths and photon fluences. **Figures 3.7a** and **3.7b** show  $-\Delta P/(PI_0)$  of the  $\text{MAPbI}_3$  crystal as function of time for excitation wavelengths of 845 nm and 500 nm, respectively. **Figure 3.7c** shows the maximum signal sizes as function of the photon fluence at different excitation wavelengths (500 nm, 600 nm, 800 nm and 845 nm), showing

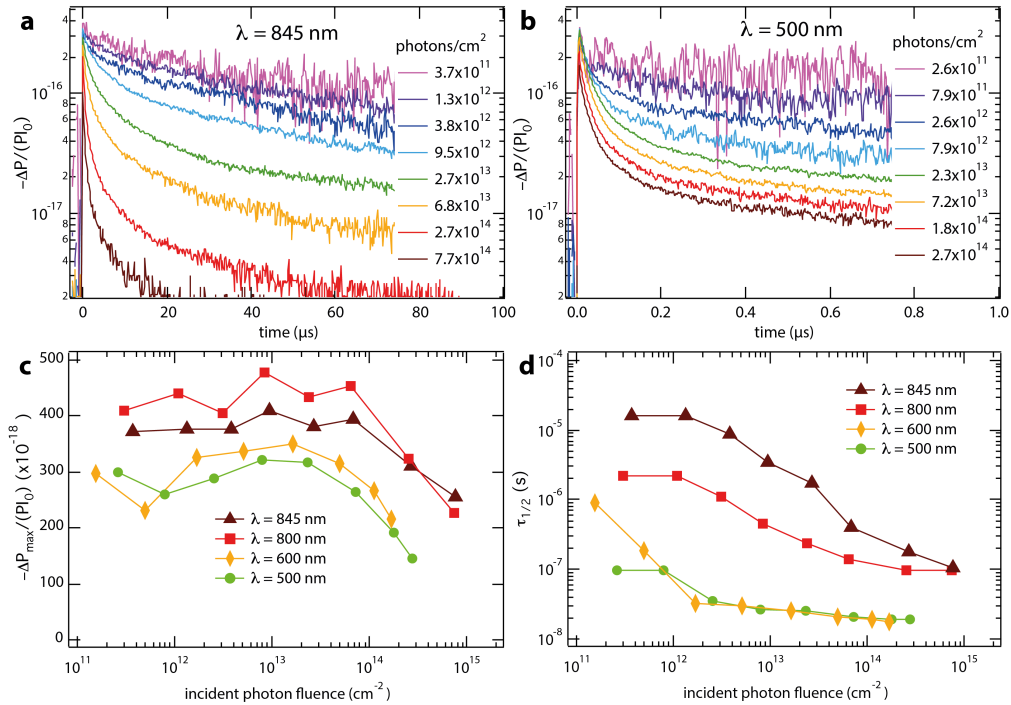


**Figure 3.7:** (a-d) TRMC results under different excitation wavelengths and intensities. TRMC traces normalized to the incident intensity for the MAPbI<sub>3</sub> crystal recorded at excitation wavelengths of (a) 845 nm and (b) 500 nm using different excitation intensities (photons/cm<sup>2</sup>). (c) Maximum change in normalized microwave power corrected for the amount of incident photons and (d) corresponding half lifetimes as function of the photon fluence at indicated wavelengths.

somewhat smaller values for the visible wavelengths (500 nm and 600 nm). In **Figure 3.7d**,  $\tau_{1/2}$  values are plotted for incident intensities ranging from  $10^{11}$  to  $10^{15}$  photons/cm<sup>2</sup>. On excitation at 845 nm, values of  $\tau_{1/2}$  over 15  $\mu$ s are found at low intensities ( $<10^{12}$  photons per cm<sup>2</sup>,  $\sim 10^{12}$  charges/cm<sup>3</sup>). However, if we increase the intensity the  $\tau_{1/2}$  reduces to about 100 ns. For excitation at 500 nm and 600 nm, the  $\tau_{1/2}$  values decrease from a few hundred nanoseconds to about 15 ns on increasing intensities, which is indicative for higher order recombination pathways.<sup>46,49,65,66</sup> The reduction of the maximum signal sizes on higher intensities in **Figure 3.7c** could thus be the result from increased recombination within the response time of the measurements. On close inspection of the TRMC traces recorded on excitation at 500 nm (**Figure 3.7b**), we notice that in particular at higher intensities, a small additional peak can be discerned within the first tens of nanoseconds, which is absent for excitation at 845 nm. This strong decay can be explained in two ways: (i) fast second-order recombination due to

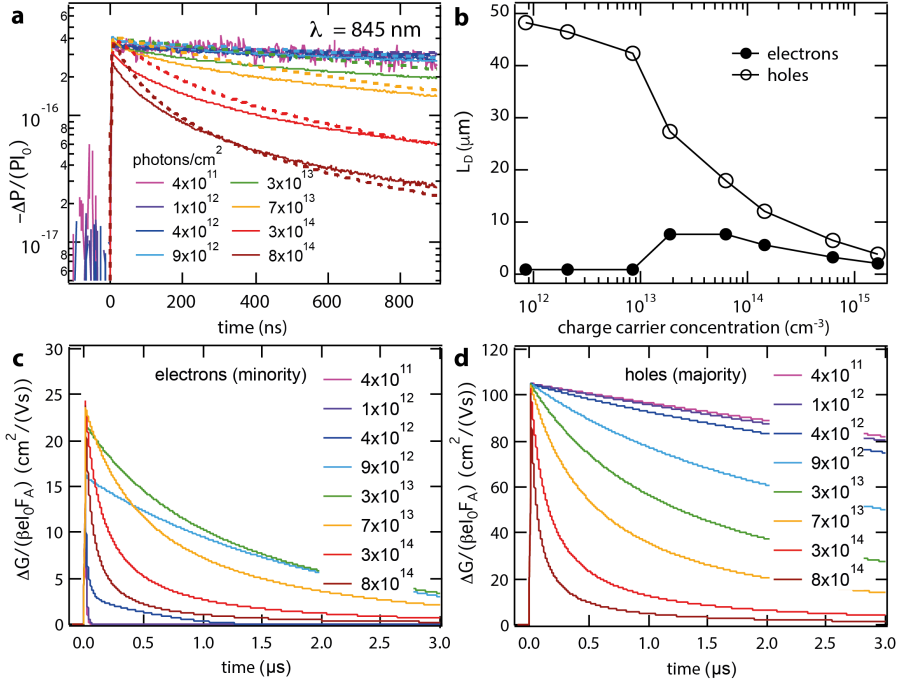


**Figure 3.8:** (a) Fits (dashed lines) to the TRMC traces (full lines) using the model as described in the text for excitation at 845 nm, where charges are generated homogeneously throughout the crystal. (b) Semi-logarithmic plot of the diffusion length for majority carriers (holes, open circles) and minority carriers (electrons, closed circles) as function of the concentration of photo-excited charge carriers. (c-d) Modelled TRMC traces of electrons (c) and holes (d) for  $4 \times 10^{11}$  to  $8 \times 10^{14}$  photons/cm<sup>2</sup> ( $\lambda = 845$  nm). Note that the experimental TRMC traces are always the sum of (c) and (d), as shown in **Figure 3.4b**.

the high local photo-induced charge carrier concentration ( $10^{17}$  cm<sup>-3</sup>) and (ii) in addition, charge recombination might occur at the surface of the crystal. If the surface of the crystal acts as an efficient recombination site, we would expect a smaller signal size on optical excitation at 500 nm and 600 nm. This is in agreement with the observations shown in **Figure 3.7c**. For these wavelengths, the largest part of the charge carriers is generated within 100 nm of the surface. Assuming a modest charge carrier mobility of 10 cm<sup>2</sup>/Vs these carriers have definitely encountered the crystal surface within a few nanoseconds. The absence of this fast initial decay at 800 nm and 845 nm is consistent with the fact that, at these wavelengths, most photo-induced carriers are generated further away from the surface. We applied the kinetic model from **Figure 2.8** to further investigate the charge recombination channels in the macroscopic crystals. We calculated the initial charge carrier concentration using the penetration depth instead of the crystal thickness (see **Equation 2.5**) and the absorption coefficient shown

in **Figure 2.3**. The results are shown in **Figure 3.8a** for the TRMC decay kinetics obtained at 845 nm and the parameters used to fit all the different intensities are listed in **Table 3.2**. Hence, we find an  $N_T$  of  $1.5 \times 10^{13} \text{ cm}^{-3}$ , which is at least one order of magnitude lower than values found in the thin MAPbI<sub>3</sub> films (see also **Table 3.1**).<sup>36,46,50,62</sup> This discrepancy could be attributed to the lack of grain boundaries within the crystal. Furthermore, the  $k_2$  is  $5.5 \times 10^{-9} \text{ cm}^3 \text{ s}^{-1}$ , which is about one order of magnitude higher than reported in several other studies.<sup>36,46,50,62</sup> The higher charge carrier mobility caused by the superior crystallinity in the crystal could result in an enhancement of  $k_2$ . Similar to the analysis performed on the thin films, after fitting the TRMC traces with the kinetic model, we separated the contributions of electrons and holes to the photoconductance. The results are shown in **Figures 3.8c** and **3.8d**, assuming electron and hole mobilities of  $25 \text{ cm}^2/(\text{Vs})$  and  $105 \text{ cm}^2/(\text{Vs})$ , respectively, as reported for this type of crystals.<sup>42</sup> **Figures 3.8c** and **3.8d** show that at light intensities below  $4 \times 10^{12} \text{ photons/cm}^2$ , the hole lifetime (microseconds) is much longer than the electron lifetime ( $< 50 \text{ ns}$ ). On the other hand, when the concentration of photo-excited electrons exceeds the number of trap states (e.g. at  $3 \times 10^{13} \text{ photons/cm}^2$ ), the electron lifetime is also in the order of microseconds. **Figure 3.8b** shows the electron and hole diffusion lengths as function of the initial concentration (calculated from **Equation 2.9**) of photo-generated electron-hole pairs. These results show that below the trap concentration ( $< 1.5 \times 10^{13} \text{ cm}^{-3}$ ), the electron diffusion length is  $0.8 \text{ }\mu\text{m}$ , which increases to  $8 \text{ }\mu\text{m}$  just above the trap concentration. For the holes, the diffusion length reaches a maximum value close to  $50 \text{ }\mu\text{m}$ , which is attributed to the slow recombination with a trapped electron.<sup>36,46</sup> At higher concentrations, the diffusion lengths of both electrons and holes reduce due to increasing second-order electron-hole recombination. These results suggest that the diffusion lengths will be optimal at an electron-hole concentration just above the trap

**Table 3.2:** Kinetic parameters used to model the TRMC measurements (see **Figure 3.8a**). Here,  $k_2$ ,  $k_T$  and  $k_D$  are the rate constants for band-to-band electron-hole recombination, trap filling and trap depopulation, respectively.  $N_T$  denotes the concentration of trap states,  $p_0$  is the background hole concentration at thermal equilibrium. Finally,  $\mu_e$  and  $\mu_h$  are the mobilities of electrons and holes, respectively, obtained from Ref. 42.

	MAPbI <sub>3</sub> crystal
$k_2 (\times 10^{-10} \text{ cm}^3 \text{ s}^{-1})$	55
$k_T (\times 10^{-10} \text{ cm}^3 \text{ s}^{-1})$	90000
$k_D (\times 10^{-10} \text{ cm}^3 \text{ s}^{-1})$	20
$N_T (\times 10^{15} \text{ cm}^{-3})$	0.015
$p_0 (\times 10^{15} \text{ cm}^{-3})$	0.04
$\mu_e (\text{cm}^2/(\text{Vs}))$	25
$\mu_h (\text{cm}^2/(\text{Vs}))$	105

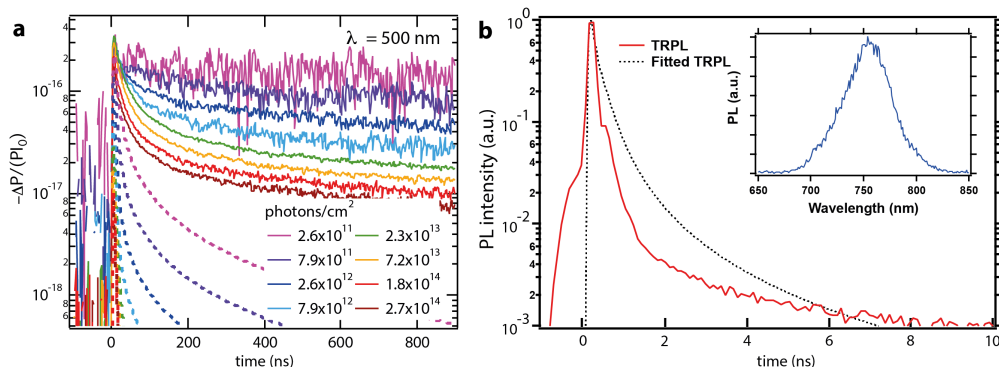


**Figure 3.9:** (a) Modelled TRMC traces (dashed lines) using the kinetic parameters obtained from fitting the data shown in **Figure 3.7a**, see **Table 3.2**, together with the experimental TRMC traces (full lines) recorded at an excitation wavelength of 500 nm (see also **Figure 3.7b**). (b) Time-resolved photoluminescence trace of a mm-sized perovskite crystal on pulsed excitation at 405 nm with an intensity  $4 \times 10^{12}$  photons/cm<sup>2</sup>, detected at 760 nm (red line) and PL trace calculated with the model described in the text (dashed line). The inset shows the emission spectrum of the MAPbI<sub>3</sub> crystal using an excitation wavelength of 405 nm.

density. Note that this model applies to a homogeneous, pulsed excitation profile: additional diffusion resulting from a concentration gradient is not taken into account. The kinetic parameters obtained from fitting the TRMC decay kinetics at  $\lambda = 845$  nm were used to calculate the TRMC traces for excitation at  $\lambda = 500$  nm, using an initial concentration based on a charge carrier generation depth of 85 nm. The fitted traces are plotted together with the experimental TRMC data in **Figure 3.9a**. Considering that initially, the local concentration of electrons and holes is extremely high for excitation at  $\lambda = 500$  nm, the calculated lifetimes are substantially shorter than for  $\lambda = 845$  nm. However, as shown in **Figure 3.9a**, the calculated traces decay much faster than those observed experimentally at  $\lambda = 500$  nm. This means that recombination is slower than we would expect based on the locally high concentration. This suggests that the electron and hole concentrations are lower than calculated based on a generation depth of 85 nm. Most likely, due to the initially large charge carrier concentration gradient, carriers rapidly diffuse towards the bulk of the crystal leading to lowered concentrations and hence longer lifetimes. Therefore, an accurate description of the charge carrier dynamics in macroscopic crystals for  $\lambda < 800$  nm requires an extension of the kinetic model, accounting for diffusion. Finally, PL measurements were performed on the same crystal ( $\lambda = 405$  nm,  $4 \times 10^{12}$  photons/cm<sup>2</sup>). **Figure 3.9b** shows the TRPL with the emission spectrum in the inset. Comparable to previously published values,<sup>65</sup> the PL lifetime is a few ns and hence, much shorter than observed in thin films (see also **Figure 3.3**). Additionally, the PL decay is substantially faster than the TRMC decays: under similar excitation conditions (*i.e.*  $\lambda = 500$  nm,  $2.6 \times 10^{12}$  photons/cm<sup>2</sup>) the lifetime of free mobile

charges is many microseconds as shown in **Figure 3.9**. Using the parameters listed in **Table 3.2**, found for fitting the TRMC traces at 845 nm, and a generation depth of 12.5 nm (*i.e.*  $1/2\alpha$ ) at 405 nm, a TRPL trace is calculated as described above and added in **Figure 3.9b**. The measured PL decay is close to the calculated trace. Considering that the charge carrier concentration was estimated using  $1/2\alpha$ , the model only accounts for the emission of the surface layer with a thickness of half the penetration depth. This corresponds to a very high concentration of charge carriers relatively close to the surface, which undergo rapid band-to-band recombination leading to the fast decay kinetics. PL emitted more in the interior of the crystal is likely to be reabsorbed and will therefore not be probed.<sup>65</sup> Our results show that the short PL lifetimes, as typically observed for mm-sized crystals can be explained by the relatively high recombination rate  $k_2$  in combination with the high local concentration of charge carriers close to the surface of the crystal that recombine radiatively. Another part of the charge carriers diffuses into the crystal, resulting in microsecond lifetimes of free, mobile charges as detected with the TRMC. Hence, the differences observed in the decay kinetics for the macroscopic crystal using PL and TRMC highlight the dissimilarities in measuring techniques. While PL only detects radiative recombination close to the surface, TRMC probes all mobile carriers formed within the crystal. Therefore, we can deduce that for mm-sized crystals, the PL lifetimes are not representative of the lifetime of free mobile charges within the crystal and, therefore, TRPL measurements are not suitable to determine the charge carrier diffusion lengths. That is, instead of  $\tau_{1/2}$  values of several ns as found by TRPL, TRMC reveals that under low excitation energies ( $<10^{12}$  photons per  $\text{cm}^2$ ),  $\tau_{1/2}$  can be as large as 15  $\mu\text{s}$ .

In summary, we performed TRMC measurements on a mm-sized  $\text{MAPbI}_3$  crystal, using different excitation wavelengths to manipulate the initial location of photo-generated charge carriers. For excitation at 845 nm, a homogeneous distribution of charges was realized. From here, using the same approach as for the thin films, we determined the bulk trap density in the  $\text{MAPbI}_3$  crystal to be on the order of  $10^{13} \text{ cm}^{-3}$ . Additionally, our results indicate that the majority and minority carrier diffusion lengths in  $\text{MAPbI}_3$  can be as large as 50 and 10  $\mu\text{m}$ , respectively, if it is no longer limited by the dimensions of the crystallites.

### 3.4 Experimental Methods

#### Thin film preparation

Quartz substrates were cleaned with acetone, propan-2-ol and oxygen plasma-treated immediately prior to film fabrication. Mesoporous alumina layers of  $\sim 400$  nm were formed by spin-coating a solution of  $\sim 20$  nm alumina nanoparticles in propan-2-ol and drying at  $150^\circ\text{C}$ . Fabrication of the organic-inorganic metal halide perovskite layers was carried out in a nitrogen-filled glovebox. Perovskite precursors were spin-coated either directly onto the quartz substrates, for the planar MHPs, or on top of the alumina scaffold, for the meso-structured MHPs.  $\text{MAPbI}_{3-x}\text{Cl}_x$  was deposited by spin-coating a 3:1 molar ratio methylammonium iodide (MAI): lead chloride solution in  $\text{N,N}$ -dimethylformamide. Concentrations of the chloride-based precursor used were 1.98M MAI/0.66M  $\text{PbCl}_2$  for the planar MHPs and 1.32M



MAI /0.44M PbCl<sub>2</sub> for the meso-structured MHPs. Directly after spin-coating, the samples were annealed at 100 °C for 2 hours. The MAPbI<sub>3</sub> perovskite was deposited by spin-coating a 1:1 molar ratio MAI:PbI<sub>2</sub> solution in N,N-dimethylformamide. The concentration used was 0.5M MAI/0.5MPbI<sub>2</sub> for both samples. Directly after spin-coating, the samples were annealed at 100 °C for 5 minutes. To protect the samples, an inert layer of 30 mg/mL polymethylmethacrylate (PMMA) in chlorobenzene was spin-coated on top after annealing the perovskite.

#### Preparation of mm-sized crystals

A mixture of 29.3 g lead (II) acetate trihydrate, 120 mL hydriodic acid (HI) (57% w/w aq. soln.) and 5.97 g methylamine (CH<sub>3</sub>NH<sub>2</sub>) (40% w/w aq. soln.) was heated to 100 °C until the precursors were fully dissolved. Then, it was cooled down to 75 °C for pacification of small MAPbI<sub>3</sub> crystals. The clear blend solution was transferred to a closed container with a silicon substrate, inserted onto top of solution. The small crystals were introduced at the bottom of the container as raw materials for crystal growth. The container was putted in an oil bath of 75 °C, where the bottom was immersed in the oil and the top exposed to air. The MAPbI<sub>3</sub> crystals nucleated on the silicon substrate were used as seeds for further growth to large size crystal. Finally, the as-grown crystals were washed with diethylether and dried in vacuum.

#### Photoconductivity measurements

The TRMC measurements were performed as detailed in **Chapter 2**, using excitation wavelengths of 600 nm. To prevent degradation, the samples were not exposed to moisture and air before and during these experiments.

#### Optical Characterization

Absorption spectra were recorded with a Perkin-Elmer Lambda 900 spectrophotometer equipped with an integrated sphere. The fraction of absorbed light ( $F_A$ ) was then determined as described in **Chapter 2**. Photoluminescence (PL) emission spectra and PL lifetimes were recorded using an Edinburgh LifeSpec spectrometer equipped with a single photon counter. The MHP films were excited at 405 nm with a picosecond pulsed diode laser (Hamamatsu, M8903-01,  $I_0 = 4 \times 10^{12}$  photons/cm<sup>2</sup>).

### 3.5 References

1. Im, J.-H., Jang, I.-H., Pellet, N., Grätzel, M. & Park, N.-G. Growth of CH<sub>3</sub>NH<sub>3</sub>PbI<sub>3</sub> cuboids with controlled size for high-efficiency perovskite solar cells. *Nat. Nanotechnol.* **9**, 927–932 (2014).
2. Zhou, H. *et al.* Interface engineering of highly efficient perovskite solar cells. *Science* **345**, 542–546 (2014).
3. Burschka, J. *et al.* Sequential deposition as a route to high-performance perovskite-sensitized solar cells. *Nature* **499**, 316–319 (2013).
4. <http://www.nrel.gov>.
5. Green, M. A., Ho-Baillie, A. & Snaith, H. J. The emergence of perovskite solar cells. *Nat. Photonics* **8**, 506–514 (2014).
6. McGehee, M. D. Perovskite solar cells: Continuing to Soar. *Nat. Mater.* **13**, 845–846 (2014).
7. Noel, N. K. *et al.* Enhanced Photoluminescence and Solar Cell Performance via Lewis Base Passivation of Organic-Inorganic Lead Halide Perovskites. *ACS Nano* **8**, 9815–9821 (2014).
8. Deng, Y. *et al.* Scalable fabrication of efficient organolead trihalide perovskite solar cells with doctor-bladed. *Energy Environ. Sci.* **8**, 1544–1550 (2015).
9. Jeon, N. J. *et al.* Compositional engineering of perovskite materials for high-performance solar cells. *Nature* **517**, 476–480 (2015).
10. Stranks, S. D. & Snaith, H. J. Metal-halide perovskites for photovoltaic and light-emitting devices. *Nat. Nanotechnol.* **10**, 391–402 (2015).
11. Li, X. *et al.* Improved performance and stability of perovskite solar cells by crystal crosslinking with alkylphosphonic acid w-ammonium chlorides. *Nat. Chem.* **7**, 703–711 (2015).
12. Conings, B. *et al.* Perovskite-based hybrid solar cells exceeding 10% efficiency with high reproducibility using a thin film sandwich approach. *Adv. Mater.* **26**, 2041–2046 (2014).



13. Edri, E. *et al.* Elucidating the charge carrier separation and working mechanism of  $\text{CH}_3\text{NH}_3\text{PbI}_{3-x}\text{Cl}_x$  perovskite solar cells. *Nat. Commun.* **5**, 3461 (2014).
14. Stranks, S. D. *et al.* Electron-hole diffusion lengths exceeding 1 micrometer in an organometal trihalide perovskite absorber. *Science* **342**, 341–344 (2013).
15. Lee, M. M., Teuscher, J., Miyasaka, T., Murakami, T. N. & Snaith, H. J. Efficient hybrid solar cells based on meso-superstructured organometal halide perovskites. *Science* **338**, 643–647 (2012).
16. Ball, J. M. *et al.* Optical properties and limiting photocurrent of thin-film perovskite solar cells. *Energy Environ. Sci.* **8**, 602–609 (2015).
17. Jung, H. S. & Park, N.-G. Perovskite Solar Cells: From Materials to Devices. *Small* **11**, 10–25 (2015).
18. Zhang, W. *et al.* Ultrasoft organic-inorganic perovskite thin-film formation and crystallization for Efficient Planar Heterojunction Solar Cells. *Nat. Commun.* **6**:6142, (2015).
19. Stranks, S. D., Nayak, P. K., Zhang, W., Stergiopoulos, T. & Snaith, H. J. Formation of Thin Films of Organic-Inorganic Perovskites for High-Efficiency Solar Cells. *Angew. Chemie Int. Ed.* **54**, 3288–3297 (2015).
20. Dar, M. I. *et al.* Investigation Regarding the Role of Chloride in Organic – Inorganic Halide Perovskites Obtained from Chloride Containing Precursors. *Nano Lett.* (2014).
21. Unger, E. L. *et al.* Chloride in Lead Chloride-Derived Organo-Metal Halides for Perovskite-Absorber Solar Cells. *Chem. Mater.* **26**, 7158–7165 (2014).
22. Williams, S. T. *et al.* Role of chloride in the morphological evolution of organo-lead halide perovskite thin films. *ACS Nano* **8**, 10640–54 (2014).
23. Edri, E., Kirmayer, S., Kulbak, M., Hodes, G. & Cahen, D. Chloride Inclusion and Hole Transport Material Doping to Improve Methyl Ammonium Lead Bromide Perovskite-Based High Open-Circuit Voltage Solar Cells. *J. Phys. Chem. Lett.* **5**, 429–433 (2014).
24. Eperon, G. E., Burlakov, V. M., Docampo, P., Goriely, A. & Snaith, H. J. Morphological Control for High Performance, Solution-Processed Planar Heterojunction Perovskite Solar Cells. *Adv. Funct. Mater.* **24**, 151–157 (2014).
25. Chen, C.-W. *et al.* Efficient and Uniform Planar-Type Perovskite Solar Cells by Simple Sequential Vacuum Deposition. *Adv. Mater.* **26**, (2014).
26. Tidhar, Y. *et al.* Crystallization of Methyl Ammonium Lead Halide Perovskites: Implications for Photovoltaic Applications. *J. Am. Chem. Soc.* **136**, 13249–13256 (2014).
27. Yu, H. *et al.* The Role of Chlorine in the Formation Process of ' $\text{CH}_3\text{NH}_3\text{PbI}_{3-x}\text{Cl}_x$ ' Perovskite. *Adv. Funct. Mater.* **24**, 7102–7108 (2014).
28. Grancini, G. *et al.* The Impact of the Crystallization Processes on the Structural and Optical Properties of Hybrid Perovskite Films for Photovoltaics. *J. Phys. Chem. Lett.* **5**, 3836–3842 (2014).
29. Raga, S. R. *et al.* Influence of Air Annealing on High Efficiency Planar Structure Perovskite Solar Cells. *Chem. Mater.* **27**, 1597–1603 (2015).
30. Colella, S. *et al.*  $\text{MAPbI}_{3-x}\text{Cl}_x$  Mixed Halide Perovskite for Hybrid Solar Cells: The Role of Chloride as Dopant on the Transport and Structural Properties. *Chem. Mater.* **25**, 4613–4618 (2013).
31. Xing, G. *et al.* Long-range balanced electron- and hole-transport lengths in organic-inorganic  $\text{CH}_3\text{NH}_3\text{PbI}_3$ . *Science* **342**, 344–7 (2013).
32. D'Innocenzo, V., Kandada, A. R. S., Bastiani, M. De, Gandini, M. & Petrozza, A. Tuning the Light Emission Properties by Band Gap Engineering in Hybrid Lead Halide Perovskite. *J. Am. Chem. Soc.* **136**, 17730–17733 (2014).
33. de Quilettes, D. W. *et al.* Impact of microstructure on local carrier lifetime in perovskite solar cells. *Science* **348**, 683–686 (2015).
34. Kroeze, J. E., Savenije, T. J., Vermeulen, M. J. W. & Warman, J. M. Contactless Determination of the Photoconductivity Action Spectrum, Exciton Diffusion Length, and Charge Separation Efficiency in Polythiophene-Sensitized  $\text{TiO}_2$  Bilayers. *J. Phys. Chem. B* **107**, 7696–7705 (2003).
35. Savenije, T. J., Ferguson, A. J., Kopidakis, N. & Rumbles, G. Revealing the dynamics of charge carriers in polymer:fullerene blends using photoinduced time-resolved microwave conductivity. *J. Phys. Chem. C* **117**, 24085–24103 (2013).
36. Stranks, S. D. *et al.* Recombination Kinetics in Organic-Inorganic Perovskites: Excitons, Free Charge, and Subgap States. *Phys. Rev. Appl.* **2**, 34007 (2014).
37. Leijtens, T. *et al.* Electronic Properties of Meso-Superstructured and Planar Organometal Halide Perovskite Films: Charge Trapping, Photodoping, and Carrier Mobility. *ACS Nano* **8**, 7147–7155 (2014).
38. Hao, F., Stoumpos, C. C., Chang, R. P. H. & Kanatzidis, M. G. Anomalous band gap behavior in mixed Sn and Pb perovskites enables broadening of absorption spectrum in solar cells. *J. Am. Chem. Soc.* **136**, 8094–9 (2014).

39. Shi, T., Yin, W.-J. & Yan, Y. Predictions for p-type  $\text{CH}_3\text{NH}_3\text{PbI}_3$  Perovskites. *J. Phys. Chem. C* **118**, 25350–25354 (2014).
40. Stoumpos, C. C., Malliakas, C. D., Kanatzidis, M. G. & G., K. M. Semiconducting tin and lead iodide perovskites with organic cations: phase transitions, high mobilities, and near-infrared photoluminescent properties. *Inorg. Chem.* **52**, 9019–9038 (2013).
41. Dang, Y. *et al.* Bulk crystal growth of hybrid perovskite material  $\text{CH}_3\text{NH}_3\text{PbI}_3$ . *CrystEngComm* **17**, 665–670 (2015).
42. Dong, Q. *et al.* Electron-hole diffusion lengths > 175  $\mu\text{m}$  in solution-grown  $\text{CH}_3\text{NH}_3\text{PbI}_3$  single crystals. *Science* **347**, 967–970 (2015).
43. Saidaminov, M. I. *et al.* High-quality bulk hybrid perovskite single crystals within minutes by inverse temperature crystallization. *Nat. Commun.* **6**, 7586 (2015).
44. Fang, Y., Dong, Q., Shao, Y., Yuan, Y. & Huang, J. Highly narrowband perovskite single-crystal photodetectors enabled by surface-charge recombination. *Nat. Photonics* **9**, 679–686 (2015).
45. Shi, D. *et al.* Low trap-state density and long carrier diffusion in organolead trihalide perovskite single crystals. *Science* **347**, 519–522 (2015).
46. Hutter, E. M., Eperon, G. E., Stranks, S. D. & Savenije, T. J. Charge Carriers in Planar and Meso-Structured Organic-Inorganic Perovskites: Mobilities, Lifetimes and Concentrations of Trap States. *J. Phys. Chem. Lett.* **6**, 3082–3090 (2015).
47. Holzwarth, U. & Gibson, N. The Scherrer equation versus the ‘Debye-Scherrer equation’. *Nat. Nanotechnol.* **6**, (2011).
48. Wojciechowski, K. *et al.* Heterojunction Modification for Highly Efficient Organic-Inorganic Perovskite Solar Cells. *ACS Nano* **8**, 12701–12709 (2014).
49. Ponseca, C. S. *et al.* Organometal halide perovskite solar cell materials rationalized: ultrafast charge generation, high and microsecond-long balanced mobilities, and slow recombination. *J. Am. Chem. Soc.* **136**, 5189–5192 (2014).
50. Wehrenfennig, C., Eperon, G. E., Johnston, M. B., Snaith, H. J. & Herz, L. M. High Charge Carrier Mobilities and Lifetimes in Organolead Trihalide Perovskites. *Adv. Mater.* **26**, 1584–1589 (2014).
51. Chang, Y., Park, C. & Matsuishi, K. First-principles study of the structural and the electronic properties of the lead-halide-based inorganic-organic perovskites  $\text{CH}_3\text{NH}_3\text{PbX}_3$  and  $\text{CsPbX}_3$  (X = Cl, Br, I). *J. Korean Phys. Soc.* **44**, 889–893 (2004).
52. Giorgi, G., Fujisawa, J. I., Segawa, H. & Yamashita, K. Small photocarrier effective masses featuring ambipolar transport in methylammonium lead iodide perovskite: A density functional analysis. *J. Phys. Chem. Lett.* **4**, 4213–4216 (2013).
53. Quarti, C., Mosconi, E. & De Angelis, F. Interplay of Orientational Order and Electronic Structure in Methylammonium Lead Iodide: Implications for Solar Cell Operation. *Chem. Mater.* **26**, 6557–6569 (2014).
54. Pascoe, A. R. *et al.* Planar versus mesoscopic perovskite microstructures: The influence of  $\text{CH}_3\text{NH}_3\text{PbI}_3$  morphology on charge transport and recombination dynamics. *Nano Energy* **22**, 439–452 (2016).
55. Oga, H., Saeki, A., Ogomi, Y., Hayase, S. & Seki, S. Improved Understanding of the Electronic and Energetic Landscapes of Perovskite Solar Cells: High Local Charge Carrier Mobility, Reduced Recombination, and Extremely Shallow Traps. *J. Am. Chem. Soc.* **136**, 13818–13825 (2014).
56. Wang, Y. C., Ahn, H., Chuang, C. H., Ku, Y. P. & Pan, C. L. Grain-size-related transient terahertz mobility of femtosecond-laser-annealed polycrystalline silicon. *Appl. Phys. B* **97**, 181–185 (2009).
57. Katoh, R., Huijser, A., Hara, K., Savenije, T. J. & Siebbeles, L. D. A. Effect of the Particle Size on the Electron Injection Efficiency in Dye-Sensitized Nanocrystalline  $\text{TiO}_2$  Films Studied by Time-Resolved Microwave Conductivity (TRMC) Measurements. *J. Phys. Chem. C* **111**, 10741–10746 (2007).
58. Prins, P., Grozema, F. C. & Siebbeles, L. D. A. Efficient charge transport along phenylene-vinylene molecular wires. *J. Phys. Chem. B* **110**, 14659–14666 (2006).
59. Johnston, M. B. & Herz, L. M. Hybrid Perovskites for Photovoltaics: Charge-Carrier Recombination, Diffusion, and Radiative Efficiencies. *Acc. Chem. Res.* **49**, 146–154 (2016).
60. Manser, J. S. & Kamat, P. V. Band filling with free charge carriers in organometal halide perovskites. *Nat. Photonics* **8**, 737–743 (2014).
61. De Bastiani, M. *et al.* Role of the crystallization substrate on the photoluminescence properties of organo-lead mixed halides perovskites Role of the crystallization substrate on the photoluminescence properties of organo-lead mixed halides perovskites. *APL Mater.* **2**, 81509 (2014).
62. Wehrenfennig, C., Liu, M., Snaith, H. J., Johnston, M. B. & Herz, L. M. Charge-Carrier Dynamics in Vapour-Deposited Films of the Organolead Halide Perovskite  $\text{CH}_3\text{NH}_3\text{PbI}_{3-x}\text{Cl}_x$ . *Energy Environ. Sci.* **7**, 2269–2275 (2014).

63. Wetzelaer, G.-J. A. H. *et al.* Trap-Assisted Non-radiative Recombination in Organic–Inorganic Perovskite Solar Cells. *Adv. Mater.* **27**, 1837–1841 (2015).
64. Bi, Y. *et al.* Charge Carrier Lifetimes Exceeding 15 Microseconds in Methylammonium Lead Iodide Single Crystals. *J. Phys. Chem. Lett.* **7**, 923–928 (2016).
65. Yamada, Y. *et al.* Dynamic Optical Properties of  $\text{CH}_3\text{NH}_3\text{PbI}_3$  Single Crystals as Revealed by One- and Two-photon Excited Photoluminescence Measurements. *J. Am. Chem. Soc.* **137**, 10456–10459 (2015).
66. Savenije, T. J. *et al.* Thermally Activated Exciton Dissociation and Recombination Control the Carrier Dynamics in Organometal Halide Perovskite. *J. Phys. Chem. Lett.* **5**, 2189–2194 (2014).

## Appendices

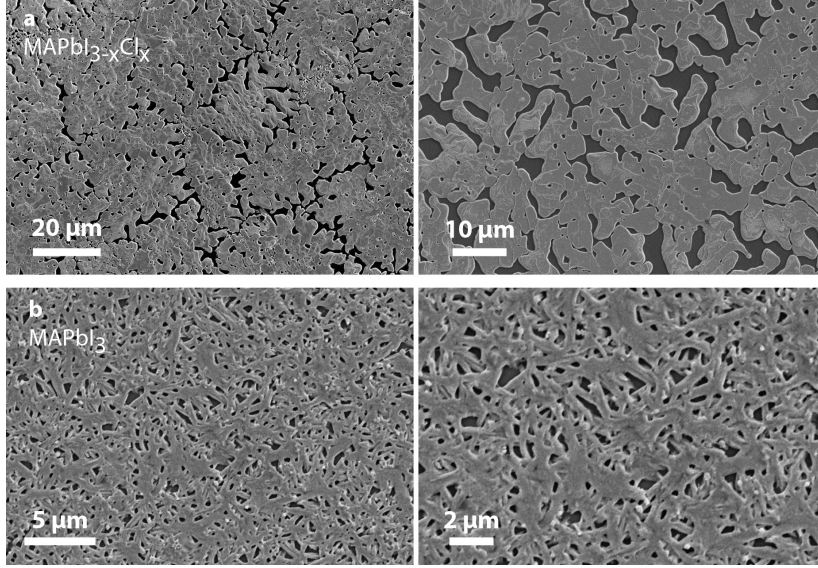


**Figure A3.1:** Top view Scanning Electron Microscopy (SEM) images of thin films of  $\text{MAPbI}_{3-x}\text{Cl}_x$  (a) and  $\text{MAPbI}_3$  (b).

**Figure A3.2** shows X-ray diffraction (XRD) patterns for the different MHP films. The crystal sizes ( $\tau$ ) of the meso-structured MHPs were estimated using the Scherrer equation:

$$\tau = \frac{K\lambda}{\beta \cos \theta} \quad (\text{A3.1})$$

In which  $\lambda$  is the X-ray wavelength ( $1.79 \text{ \AA}$ ),  $\theta$  the Bragg angle,  $\beta$  the full width at half the maximum and  $K$  a shape factor close to unity (we used the approximation  $K = 0.9$ , see Ref. 47 from main text). Note that this represents the crystal size perpendicular to the reflected lattice plane, in this case the (110) direction.

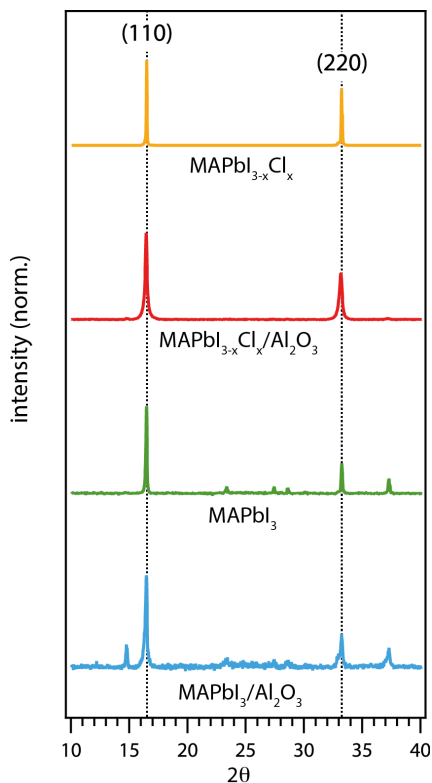


**Figure A3.2:** XRD patterns (Co K $\alpha$  radiation,  $\lambda = 1.79 \text{ \AA}$ ) for MAPbI<sub>3-x</sub>Cl<sub>x</sub>, MAPbI<sub>3-x</sub>Cl<sub>x</sub>/Al<sub>2</sub>O<sub>3</sub>, MAPbI<sub>3</sub> and MAPbI<sub>3</sub>/Al<sub>2</sub>O<sub>3</sub>.

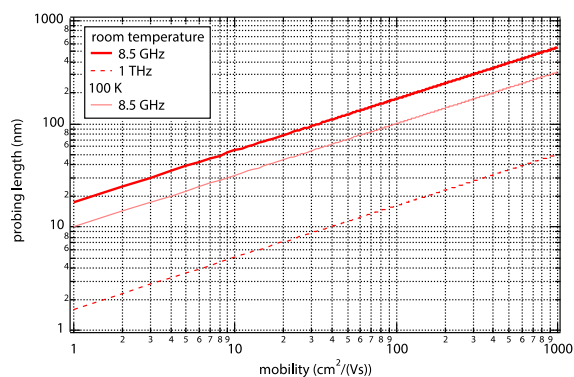


**Figure A3.3:** Relationship between the measured mobility and probing length (nm) of a TRMC experiment. Here, the probing length represents the distance over which charges diffuse in an alternating current (AC) conductivity measurement, using probing frequencies of 8.5 GHz (microwave conductivity) or 1 THz.





# Interfacial Kinetics of Charge Transfer from Methylammonium Lead Iodide Perovskites to Organic Transport Materials



## ABSTRACT

In order to rationally design efficient and stable perovskite solar cells, it is important to understand not only charge trapping and recombination events in the perovskite layer itself, but also processes occurring at the perovskite/transport material (TM) interface, such as charge transfer and interfacial recombination. In this chapter, we use time-resolved microwave conductivity measurements to investigate these interfacial processes for methylammonium lead iodide and various state-of-the-art organic TMs. The global kinetic model introduced in **Chapter 2** is further extended to accurately describe both the dynamics of excess charges in the perovskite layer and transfer to charge-specific TMs. From the obtained charge transfer rates, we are able to deduce the extraction efficiencies. We conclude that for state-of-the-art materials, such as Spiro-OMeTAD and PCBM, the charge extraction efficiency is not significantly affected by intra-band gap traps. That is, for trap densities under  $10^{15} \text{ cm}^{-3}$ , the trapping rates of less than  $10^7 \text{ s}^{-1}$  are substantially lower than the transfer rates (typically  $\sim 10^8 \text{ s}^{-1}$ ). Finally, our results show that transfer rates to C60, PCBM, EDOT-OMeTPA and Spiro-OMeTAD are sufficient to outcompete second-order recombination under excitation densities representative for illumination by AM1.5. These results pave the way for rational design of perovskite-based solar cells with balanced extraction of charges, which essential for avoiding accumulation of charges at one of the electrodes.

### Partially based on

Eline M. Hutter, Jan-Jaap Hofman, Michiel Petrus, Michiel Moes, Ruben D. Abellón, Pablo Docampo, and Tom J. Savenije, Charge Transfer from Methylammonium Lead Iodide Perovskite to Organic Transport Materials: Efficiencies, Transfer Rates and Interfacial Recombination, *Advanced Energy Materials*, 2017, 1602349

Carlito S. Ponseca Jr., Eline M. Hutter, Piotr Piatkowski, Boiko Cohen, Torbjörn Pascher, Abderrazzak Douhal, Arkady Yartsev, Villy Sundström, and Tom J. Savenije, Mechanism of Charge Transfer and Recombination Dynamics in Organo Metal Halide Perovskites and Organic Electrodes, PCBM and Spiro-OMeTAD: Role of Dark Carriers, *J. Am. Chem. Soc.*, 2015, 137, 16043-16048



## 4.1 Introduction

The impressive progress in device efficiency of MHP-based solar cells is mainly due to (i) optimizing experimental procedures to obtain perovskite materials with improved crystallinity, (ii) adjusting the perovskite composition and (iii) investigating different transport materials. However, it remains a major challenge to eliminate the hysteresis in the photovoltaic current-voltage scans, thereby stabilizing perovskite-based solar cells. Recently, it was shown that hysteresis in perovskite-based solar cells is highly dependent on the choice of transport materials (TM), suggesting that device performance is limited by charge accumulation at the interfaces.<sup>1,2</sup> Hence, better understanding of the perovskite/TM interfaces is critical for rational design of stable perovskite-based solar cells with minimum hysteresis and improved device lifetimes.

Interestingly, in contrast to the substantial progress that has been made in understanding the dynamics of photo-generated charges in the photo-active metal halide perovskite,<sup>3,4</sup> there are only a handful of reports investigating the kinetics of charge transfer from perovskite to charge-specific TMs.<sup>5–9</sup> We have previously proposed that injection of charges can be in competition with recombination pathways in the perovskite layer, in particular if the perovskite is unintentionally doped.<sup>6</sup> Other groups have extracted transfer rates<sup>5</sup> or yields<sup>10</sup> from global analysis of spectroscopic data. However, a quantitative description accounting both for the dynamics of charges in the perovskite itself and the transfer to charge-specific electrodes is still lacking.

In this chapter, we use time-resolved microwave conductivity (TRMC) measurements to reveal the charge carrier transfer and recombination pathways in bilayer systems of thin MAPbI<sub>3</sub> films and charge-selective transport materials (TM). First, we prepared smooth, homogeneous MAPbI<sub>3</sub> layers using sequential physical vapour deposition (PVD).<sup>11–13</sup> Via this route, multiple MAPbI<sub>3</sub> films with identical optoelectronic properties can be made, which enables for direct comparison between different samples. Then, various organic electrodes were spin-coated on top of the MAPbI<sub>3</sub> films, so that we could compare the photo-physical processes in a bilayer to those in a neat perovskite.<sup>6</sup> Both the frequently used hole transporting material (HTM) Spiro-OMeTAD and the recently reported low-cost alternatives H101<sup>14</sup> and EDOT-OMeTPA<sup>15</sup> were investigated. Similarly, state-of-the-art PCBM and C<sub>60</sub> were compared to less commonly used electron transport materials (ETM's) such as ICBA<sup>16</sup> and bis-PCBM.

Interestingly, we find that on the timescale of our TRMC experiment, charge transfer of electrons or holes occurs independently of excitation wavelength and illumination side, indicating that this process is not limited by charge diffusion in perovskite films with thicknesses of a few hundred nanometers. We introduce a global kinetic model that implements charge carrier generation, various recombination pathways in the perovskite layers and in addition, the transfer rates to charge-selective TMs. First, the kinetic parameters, including mobilities and rate constants for band-to-band recombination and trapping, are revealed for the neat perovskite layer, using the same approach as in **Chapter 3**.<sup>17</sup> After depositing the TM layer, the same set of kinetic parameters plus an additional rate constant is used to describe the transfer of charges. Hence, we find

the rates of charge transfer and interfacial recombination for a number of different organic TMs. Additionally, this model now enables us to separate the electron and hole mobilities and to deduce the charge collection efficiency as function of charge carrier density (*i.e.*, illumination intensity). We find that at low concentrations, charge transfer can be in competition with charge immobilization due to the presence of traps, whereas second-order recombination in the perovskite dominates over extraction at higher concentrations. Most importantly, these results demonstrate that transfer of charges is optimized when the transfer rates exceed the trapping rates, which is the case for *e.g.* Spiro-OMeTAD and PCBM.

## 4.2 Results and Discussion

To study the transfer of charges from MAPbI<sub>3</sub> to various organic TMs, the charge carrier dynamics in neat perovskite films were directly compared to bilayer systems. The different types of sample configurations are schematically shown in **Figure 4.1**. A 3.5 ns FWHM laser pulse (see also **Paragraph 2.4**) is used to excite the samples through the quartz substrate, thereby generating free charges in the MAPbI<sub>3</sub> layer. As also shown in **Chapter 3**, these charges decay over time by trap-assisted and/or second-order electron-hole recombination.<sup>17-19</sup> When an ETM (or HTM) is deposited on top of the MAPbI<sub>3</sub>, electrons (holes) are extracted and consequently, these can recombine *via* the interface with holes (electrons) that remained in the MAPbI<sub>3</sub>. Using MAPbI<sub>3</sub> layers with identical optoelectronic properties, we can quantitatively investigate the charge carrier dynamics and transfer to the TMs. The initial location of charges was manipulated by varying the excitation wavelength. **Figure 4.2a** shows the charge carrier generation profile in MAPbI<sub>3</sub> for excitation wavelengths of 300 nm (4.14 eV), 600 nm (2.07 eV) and 780 nm (1.59 eV), calculated using the experimentally determined absorption coefficients (see **Figure A4.1** in **Appendices**). At  $\lambda = 300$  nm, the penetration depth ( $1/\alpha$ ) of light is only 30 nm and hence, photo-excitation is concentrated close to the illuminated surface. On

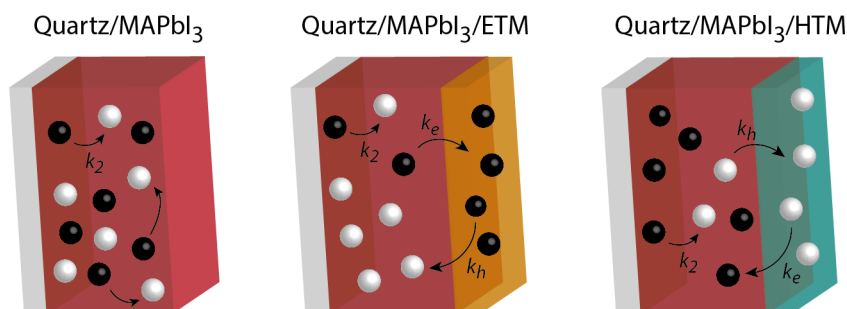


**Figure 4.1:** Schematic overview of the sample configurations investigated. Samples are illuminated with a laser pulse through the quartz, generating free electrons (black spheres) and holes (white spheres). In the neat perovskite (left), their concentration will decrease over time due to second-order ( $k_2$ ) or trap-assisted recombination. In the presence of an electron transport material (ETM, middle), electrons can be extracted ( $k_e$ ) and recombine *via* the interface ( $k_h$ ). Similarly, a hole transport material (HTM, right) extracts the holes ( $k_h$ ) which can recombine *via* the interface ( $k_e$ ) with electrons.

the other hand, at  $\lambda = 780$  nm, the lower absorption coefficient results in a diluted, more homogeneous excitation profile. **Figure 4.2b** shows the normalized photoconductance  $\Delta G$  in a thin ( $\sim 200$  nm) vapour-deposited MAPbI<sub>3</sub> film (see **Figures A4.2 to A4.4** in **Appendices**)<sup>11–13,20</sup> as function of time after pulsed illumination ( $\sim 10^{10}$  absorbed photons/cm<sup>2</sup> per pulse), recorded using the TRMC technique.<sup>21</sup> Given that  $\Delta G$  provides a measure for the concentration of free mobile charges, its initial rise is due to charge generation by the laser pulse, whereas its reduction over time can be directly related to immobilization of charges by *e.g.* trapping or recombination. As shown in **Figure**

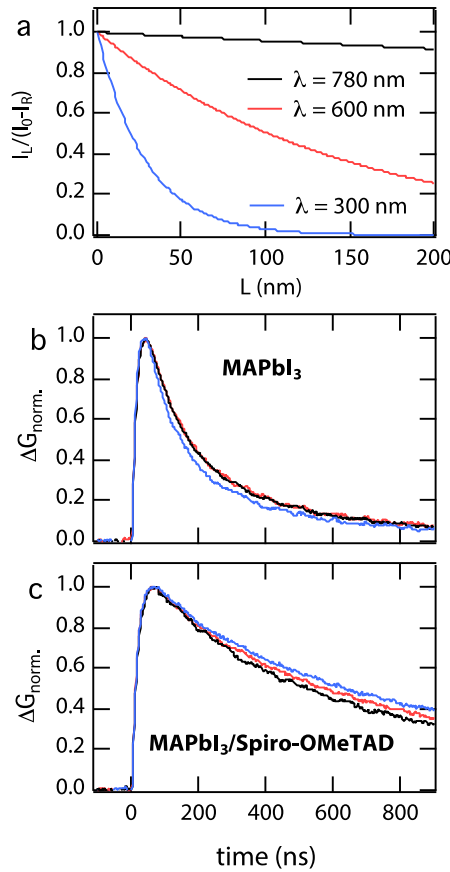


**Figure 4.2:** (a) Charge carrier generation profile as function of excitation wavelength, calculated using the experimentally determined absorption coefficients (see also **Figure A4.1** in **Appendices**). (b-c) Normalized time-resolved photoconductance in a thin ( $\sim 200$  nm) MAPbI<sub>3</sub> film (b) and in a bilayer of MAPbI<sub>3</sub> and Spiro-OMeTAD (c) for a fluence of  $10^{10}$  cm<sup>-2</sup> absorbed photons ( $I_0 F_A$ ) per pulse at excitation wavelengths of 300 nm, 600 nm and 780 nm. Since the fraction of absorbed photons ( $F_A$ ) is wavelength-dependent, the laser intensity  $I_0$  was adjusted in order to obtain the same product of  $I_0 F_A$ . Hence, the total number of photo-excited charges is similar, however their initial distribution differs (see **Figure 4.2a**). Whereas for  $\lambda = 780$  nm, excitation occurs nearly homogeneous throughout the MAPbI<sub>3</sub> layer, for  $\lambda = 300$  nm charges are generated predominantly  $\sim 150$  nm away from the MAPbI<sub>3</sub>/Spiro-OMeTAD interface.

**4.2b**, the signal has reduced to half its initial value within 200 ns for an initial charge carrier concentration of  $5 \times 10^{14} \text{ cm}^{-3}$ . Interestingly, this is independent of the excitation wavelength  $\lambda$ . Similar TRMC results were obtained for excitation from the front side (*i.e.* through the organic layer) and from the back side (see **Figure A4.5** in **Appendices**). Thus, the results in **Figures 4.2b,c** and **A4.5** in **Appendices** show that the timescale for recombination does not depend on the initial distribution of charges, which indicates that transport occurs on a much faster timescale than recombination.

To gain more insight in the charge carrier dynamics in MAPbI<sub>3</sub> and the charge collection by TM layers, we deposited Spiro-OMeTAD on top of the perovskite and repeated the TRMC measurements. The samples were excited through the quartz substrate and thus, in this case, varying the excitation wavelength changes the distance of charge carriers to the MAPbI<sub>3</sub>/Spiro-OMeTAD interface. The change in conductance  $\Delta G$  was determined as explained in **Chapter 2** and the product of the yield of free charges  $\varphi$  and their mobility  $\Sigma\mu$  was calculated from the maximum  $\Delta G$  using **Equation 2.22**. Recall that  $\Sigma\mu$  is the sum of the electron and hole mobilities ( $\mu_e + \mu_h$ ), meaning that all light-induced mobile charges contribute to the TRMC signal, however scaled by their mobility. Since the electron and hole mobilities in organic compounds are much smaller than in MAPbI<sub>3</sub>, we can assume that the charges injected into the TM layers do not contribute significantly to  $\Delta G$ . Thus, the traces in **Figure 4.2c** originate from free charges remaining in the perovskite. On comparison of **Figures 4.2b** and **4.2c**, we find that the lifetime of mobile charges is substantially extended in the bilayer configuration with respect to the neat perovskite. We attribute this to injection of holes into the Spiro-OMeTAD, which reduces the probability of electrons remaining in MAPbI<sub>3</sub> to recombine with holes and consequently, enhances their lifetime. Interestingly, similar to the neat perovskite, we find that the decay in the bilayer hardly changes with the excitation wavelength. In other words, photo-generated holes can diffuse effectively through the perovskite layer over a distance of at least 150 nm and reach Spiro-OMeTAD. Furthermore, the observation that the electron lifetime in MAPbI<sub>3</sub> is shorter in the presence of holes (**Figure 4.2b**) confirms our previous conclusion that higher order electron-hole recombination dominates the decay in the neat perovskite.<sup>18</sup> In an effort to investigate whether the observed results can be generalized to MAPbI<sub>3</sub> films prepared *via* different preparation routes, we repeated the experiments with samples spin-coated from a stoichiometric precursor solution. We find that, although the absolute charge carrier mobilities and lifetimes are different for the latter, the effect of spin-coating the transport layer on top of the spin-coated MAPbI<sub>3</sub> is the same as observed for the vapour-deposited films (see **Figure A4.6** in **Appendices**).

To study the electron-hole recombination pathways in more detail, we performed TRMC measurements as function of the initial charge carrier concentration. **Figures 4.3a** and **4.3b** show  $\Delta G$  normalized for the number of absorbed photons in MAPbI<sub>3</sub> (**Figure 4.3a**) and MAPbI<sub>3</sub>/Spiro-OMeTAD (**Figure 4.3b**) for charge concentrations ranging from  $7 \times 10^{13}$  to  $10^{16} \text{ cm}^{-3}$ . In the neat perovskite, the charge carrier decay becomes faster at higher concentrations, which is due to higher order electron-hole

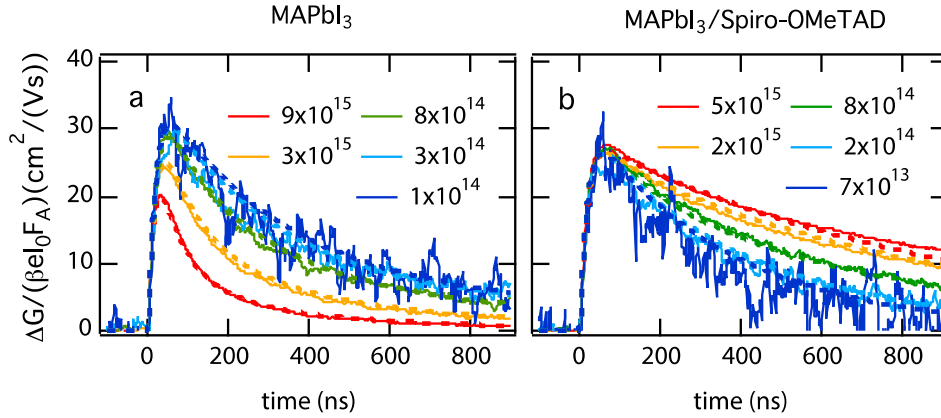


**Figure 4.3:** (a-b) Time-Resolved Microwave Conductivity (TRMC) traces recorded at initial charge carrier densities ranging from  $7 \times 10^{13}$  to  $3 \times 10^{16} \text{ cm}^{-3}$  ( $\lambda = 600$ ) for neat MAPbI<sub>3</sub> (a) and MAPbI<sub>3</sub>/Spiro-OMeTAD illuminated through the perovskite (b).

recombination, as discussed in **Chapter 3**.<sup>17</sup> Importantly, the opposite trend is observed when holes are transferred to Spiro-OMeTAD: the electron lifetime is shorter at low concentrations and *vice versa*. In fact, these results suggest the presence of a limited concentration of electron traps. That is, if the concentration of electron traps exceeds the concentration of free electrons, the latter are likely to be immobilized into trap states resulting in a faster decay. On the other hand, if the electron concentration exceeds the trap density, their lifetime will be enhanced, provided that there are no holes to recombine with (**Figure 4.3b**). Hence, TRMC measurements using extraction layers enables us to identify the nature of trap states (*i.e.* electron or hole traps), which is not possible with *e.g.* photoluminescence (PL) measurements. Finally, considering that the signal in **Figure 4.3b** originates primarily from electrons remaining in MAPbI<sub>3</sub>, we can conclude that the contribution of the electrons ( $\mu_e$ ) to the sum of the mobilities  $\Sigma\mu$  (**Figure 4.3a**) is larger than the contribution of  $\mu_h$ .

Analogous to the previous chapter,<sup>17</sup> we use a kinetic model to obtain quantitative information from the intensity-dependent TRMC traces; see **Figure 4.4**. This model not only includes processes occurring in MAPbI<sub>3</sub> (black, recall **Figure 2.8** and **Equations 2.24 to 2.26**), but is extended to account for the additional pathways introduced by the electron or hole transport material (red).<sup>6</sup> Similar to the previous chapter, the electrons in the MAPbI<sub>3</sub> layer can recombine with holes *via* second-order recombination ( $k_2$ ) or traps ( $k_T$  and  $k_D$ ). However, in the presence of an ETM, electrons can also be extracted ( $k_e$ ) and recombine *via* the interface with holes ( $k_h$ ). *Vice versa*, if the TM is hole-selective,  $k_h \gg k_e$  and thus  $k_h$  represents hole extraction. The time-dependent change in

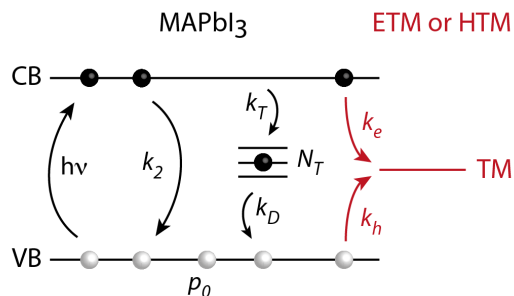


**Figure 4.4:** Kinetic model of processes occurring in a bilayer of MAPbI<sub>3</sub> perovskite and an organic electron transport material (ETM) or hole transport material (HTM). Electrons (black spheres) and holes (white spheres) are selectively generated in the perovskite film upon absorption of light with  $\lambda = 600$  nm. In the neat perovskite, electrons can recombine with holes via second-order band-to-band recombination ( $k_2$ ), or get trapped (trap density  $N_T$ , trapping rate  $k_T$ ) and recombine with holes via  $k_D$ .<sup>17,19</sup> Both  $k_2$  and  $k_D$  are enhanced by the presence of a limited number of dark holes  $p_0$ .<sup>22,23</sup> In the presence of an organic transport layer, electrons and holes can be injected via  $k_e$  and  $k_h$ , respectively, which provides a pathway competitive to recombination in the perovskite.<sup>6</sup> Note that for an ETM,  $k_e \gg k_h$  and vice versa.

the electron concentrations in the CB, VB, trap states ( $N_T$ ) and TM are described by the coupled differential **Equations 4.1 to 4.4**, respectively.

$$\frac{dn_{CB}}{dt} = \frac{dn_e}{dt} = G_c - k_2 n_e (n_h + p_0) - k_T n_e (N_T - n_T) - k_e n_e \quad (4.1)$$

$$\frac{dn_{VB}}{dt} = -\frac{dn_h}{dt} = -G_c + k_2 n_e (n_h + p_0) + k_D n_t (n_h + p_0) + k_h n_h \quad (4.2)$$

$$\frac{dn_t}{dt} = k_T n_e (N_T - n_T) - k_D n_t (n_h + p_0) \quad (4.3)$$

$$\frac{dn_{TM}}{dt} = k_e n_e - k_h n_h \quad (4.4)$$

We used the kinetic model shown in **Figure 4.4** to globally fit the experimental TRMC data,<sup>17</sup> which are added as dotted lines in **Figures 4.3a** and **4.3b**. As shown in **Figure 4.3**, excellent agreement could be obtained between the modelled and the experimental traces. Remarkably, except for hole injection ( $k_h$ ), the same kinetic parameters could be used to describe both the neat perovskite and the MAPbI<sub>3</sub>/Spiro-OMeTAD bilayer (see **Table 4.1**). Most importantly, the concentration-dependent lifetime of

**Table 4.1:** Kinetic parameters for recombination processes in MAPbI<sub>3</sub>; the exact same parameters were used to describe both the neat perovskite (**Figure 4.3a**) and the bilayer systems (**Figure 4.3b** and **Figure 4.5**).

	MAPbI <sub>3</sub>
$k_2 (\times 10^{-10} \text{ cm}^3 \text{ s}^{-1})$	28
$k_T (\times 10^{-10} \text{ cm}^3 \text{ s}^{-1})$	60
$k_D (\times 10^{-10} \text{ cm}^3 \text{ s}^{-1})$	0.5
$N_T (\times 10^{15} \text{ cm}^{-3})$	0.3
$p_0 (\times 10^{15} \text{ cm}^{-3})$	0.4
$\mu_e (\text{cm}^2/(\text{Vs}))$	30.5
$\mu_h (\text{cm}^2/(\text{Vs}))$	6.5

electrons in the absence of holes (MAPbI<sub>3</sub>/Spiro-OMeTAD, **Figure 4.3b**) enables us to accurately determine the trapping parameters  $N_T$  and  $k_T$ . Consequently, we find that  $k_2 = 2.8 \times 10^{-9} \text{ cm}^3 \text{ s}^{-1}$ ,  $k_T = 6 \times 10^{-9} \text{ cm}^3 \text{ s}^{-1}$  and that the trap density is exceptionally low ( $3 \times 10^{14} \text{ cm}^{-3}$ ), similar to spin-coated MAPbI<sub>3</sub> prepared from PbCl<sub>2</sub> (see **Table 3.1**).<sup>17</sup> The concentration of dark holes ( $p_0$ ) is  $4 \times 10^{14} \text{ cm}^{-3}$ , which is in line with experimental findings.<sup>23</sup> Additionally, the only difference between the traces in **Figures 4.3a** and **4.3b** is the injection of holes, from which we deduce that holes are transferred from MAPbI<sub>3</sub> to Spiro-OMeTAD with  $k_h = 8 \times 10^8 \text{ s}^{-1}$ . As there is no signature of interfacial recombination within the timeframe studied, we conclude that  $k_e < 2 \times 10^4 \text{ s}^{-1}$ . In contrast to the present results, we have previously observed little difference between MAPbI<sub>3</sub> and MAPbI<sub>3</sub>/Spiro-OMeTAD (see **Figure A4.7** in **Appendices**).<sup>6</sup> We proposed this was due to the presence of dark holes (with a concentration on the order of  $10^{16} \text{ cm}^{-3}$ ), which completely dominated the decay kinetics in both MAPbI<sub>3</sub> and MAPbI<sub>3</sub>/Spiro-OMeTAD. Considering that the concentration of dark holes is about two orders of magnitude lower in the current study, we can use these data for an extensive quantitative analysis and accurate extraction of the hole transfer rates.

Whereas in **Chapter 3**, we had to assume the relative contributions of electrons and holes to the sum of mobilities on basis of the effective mass, these can now be separately determined. Hence, in contrast to previous assumptions,<sup>17</sup> we find that the electron mobility is  $30.5 \text{ cm}^2/(\text{Vs})$ , while the hole mobility is only  $6.5 \text{ cm}^2/(\text{Vs})$ . In addition, we can now distinguish the electron and hole lifetimes more accurately, which we use to get a better estimate of their diffusion lengths. We find that at a charge density of  $9 \times 10^{15} \text{ cm}^{-3}$ , the electron diffusion length is  $1.8 \text{ } \mu\text{m}$ , and  $0.8 \text{ } \mu\text{m}$  for the holes. Although the electrons are more mobile than the holes, both diffusion lengths are larger than the  $\sim 0.4 \text{ } \mu\text{m}$  MAPbI<sub>3</sub> thickness required for sufficient light absorption and thus, both charges are mobile enough to be efficiently collected in a device. Finally, these mobilities explain the independence of excitation wavelength as presented in **Figures 4.2b** and **4.2c**. That is, it



takes ~3 ns for the holes to diffuse over the 200 nm thickness of the film, which is below the time response of our measurement.

The above approach enabled us to accurately determine the mobilities and recombination pathways of electrons and holes in MAPbI<sub>3</sub>, which we used to obtain transfer rates for the other TMs investigated. **Figure 4.5** shows TRMC traces recorded for bilayers of MAPbI<sub>3</sub> and the HTMs: H101 (a) and EDOT-OMeTPA (b), together with the ETMs: PCBM (c), C<sub>60</sub> (d), ICBA (e) and bis-PCBM (f). The fits to the experimental data as detailed above are added as dotted lines. We note that the perovskite-related mobilities and recombination rates were fixed for all the bilayer systems, leaving  $k_e$  and  $k_h$  as the only variables. The results are listed in **Table 4.2**.

Looking at the experimental data for the HTMs investigated, we observe that lifetimes are extended when H101 is spin-coated on top of MAPbI<sub>3</sub>. In contrast to Spiro-OMeTAD

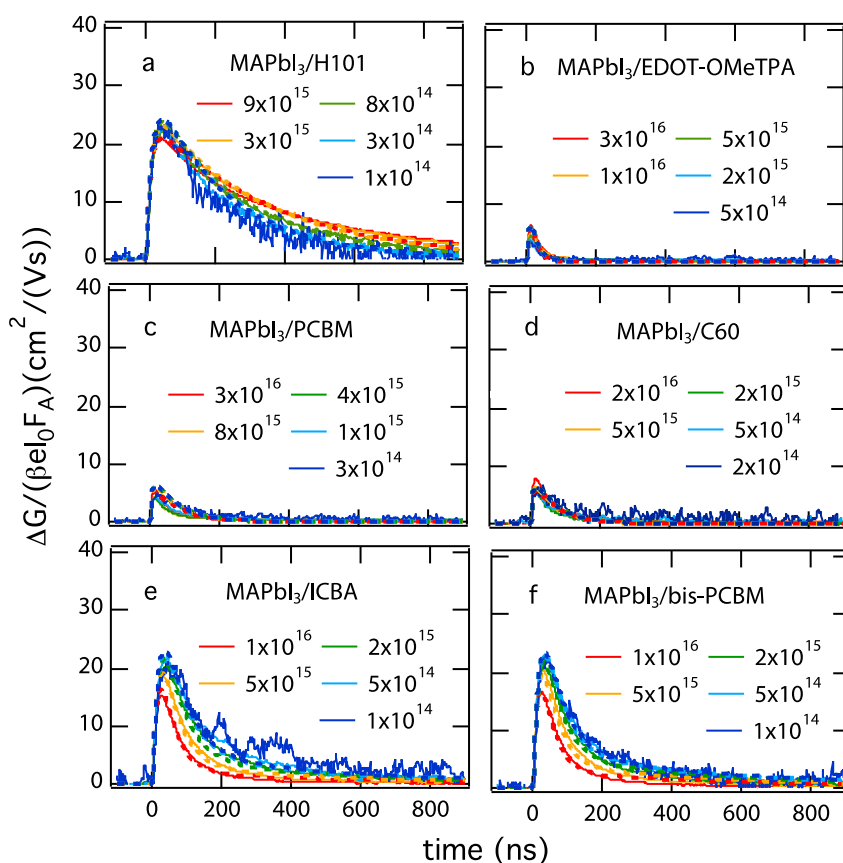


**Figure 4.5:** (a-f) Time-Resolved Microwave Conductivity (TRMC) traces for MAPbI<sub>3</sub>/H101 (a) and MAPbI<sub>3</sub>/EDOT-OMeTPA (b) MAPbI<sub>3</sub>/PCBM (c), MAPbI<sub>3</sub>/C<sub>60</sub> (d), MAPbI<sub>3</sub>/ICBA (e) and MAPbI<sub>3</sub>/bis-PCBM (f) recorded at initial charge carrier densities ranging from 10<sup>14</sup> to 3×10<sup>16</sup> cm<sup>-3</sup> (at λ = 600). The dotted lines are fits to the experimental data (solid lines), using the model shown in **Figure 4.4** and the kinetic parameters listed in **Tables 4.1** and **4.2**.



however, the decay in MAPbI<sub>3</sub>/H101 shows higher order recombination effects within the first 100 ns. This suggests that injection into H101 is slower than for Spiro-OMeTAD and therefore, initially in competition with second-order recombination in MAPbI<sub>3</sub>. At longer timescales however, the holes have transferred to H101 and the lifetime of the remaining electrons follows the same trend as for Spiro-OMeTAD. As shown in **Figure 4.5a**, this behaviour can indeed be modelled using a lower  $k_h$ : both the experimental and fitted traces cross over between 100 and 200 ns (see also **Figure A4.8** in **Appendices**). Additionally, the shorter electron lifetime in MAPbI<sub>3</sub>/H101 suggests a higher value for interfacial recombination  $k_e$  (see **Figure 4.5a** and **Table 4.1**). For MAPbI<sub>3</sub>/EDOT-OMeTPA, as shown in **Figure 4.5b**, the decay is substantially faster than in the neat perovskite, *i.e.* in this bilayer configuration both electrons and holes have recombined within a few nanoseconds. Consequently, we find that holes are transferred with a rate constant of  $8 \times 10^8 \text{ s}^{-1}$ , followed by electron immobilization with  $k_e = 1.5 \times 10^8 \text{ s}^{-1}$ . This rapid quenching of mobile electrons at the MAPbI<sub>3</sub>/EDOT-OMeTPA interface could be due to recombination with injected holes and/or trapping of electrons at the interface. Similarly, we find that for all the ETMs shown in **Figures 4.5c** to **4.5f**, electron injection is followed by rapid immobilization of holes, as already reported for MAPbI<sub>3</sub>/PCBM before.<sup>6,24</sup> This is characteristic of the interface between MAPbI<sub>3</sub> and all the fullerene-related ETMs studied, since we observed this independently of the MAPbI<sub>3</sub> preparation method and the thickness of the ETM (**Figure A4.9a** in **Appendices**). Using the kinetic model from **Figure 4.4**, we find interfacial recombination rates in the order of  $10^6 - 10^7 \text{ s}^{-1}$ . However, we cannot exclude that this represents trapping of holes at the MAPbI<sub>3</sub>/ETM interface rather than recombination with injected electrons (**Figure**

**Table 4.2:** Rate constants for electron ( $k_e$ ) and hole ( $k_h$ ) transfer from MAPbI<sub>3</sub> to different HTMs and ETMs. Note that for the HTMs,  $k_h$  describes extraction and  $k_e$  represents interfacial recombination, while the opposite is valid for the ETMs.

	hole transfer rate $k_h$ ( $\times 10^7 \text{ s}^{-1}$ )	electron transfer rate $k_e$ ( $\times 10^7 \text{ s}^{-1}$ )
MAPbI <sub>3</sub>	0	0
<b>HTMs</b>	<i>extraction</i>	<i>interfacial recombination</i>
MAPbI <sub>3</sub> /EDOT-OMeTPA	80	15
MAPbI <sub>3</sub> /Spiro-OMeTAD	40	< 0.002
MAPbI <sub>3</sub> /H101	10	0.18
<b>ETMs</b>	<i>interfacial recombination</i>	<i>extraction</i>
MAPbI <sub>3</sub> /C <sub>60</sub>	1.2	30
MAPbI <sub>3</sub> /PCBM	1.5	30
MAPbI <sub>3</sub> /bis-PCBM	0.18	1.5
MAPbI <sub>3</sub> /ICBA	0.2	1.2

**A4.9b in Appendices**). We note that interfacial recombination at the ETM interface is not necessarily a limiting factor for photovoltaic performance, as long as the holes are efficiently collected at the other TM. However, in the case of comparable rate constants for injection and interfacial recombination, as for *e.g.* EDOT-OMeTPA, we expect this to be detrimental for device performance.

Interestingly, comparing the injection rates listed in **Table 4.2**, we find that electron transfer from MAPbI<sub>3</sub> to ICBA or bis-PCBM is one order of magnitude slower than injection into the other ETMs investigated. This can be understood considering that the lowest unoccupied molecular orbitals of ICBA and bis-PCBM are probably located at higher energies than the CB of MAPbI<sub>3</sub>, since their electron affinities are 0.2 eV lower than that for PCBM.<sup>25</sup> Although this could result in a higher open-circuit voltage ( $V_{OC}$ ),<sup>16</sup> its band alignment might not favor electron extraction, which explains the relatively low transfer rate in MAPbI<sub>3</sub>/ICBA. These results suggest that other electron recombination pathways such as trapping or recombination with holes could be competing with injection into ICBA. That is, if the trapping rate ( $\sim k_T N_T$ ) and/or the higher order recombination rate ( $\sim k_2 n_e n_h$ ) is in excess of the injection rate of ( $1.2 \times 10^7 \text{ s}^{-1}$ ), this will dominate over injection. However, in high quality films the trapping rate ( $\sim k_T N_T$ ) is on the order of  $10^6 \text{ s}^{-1}$  and hence, too small to impede injection.

Using the rate constants for injection as well as the additional recombination pathways in the perovskite, we can now quantify the yield of electron extraction  $\varphi_e$  as function of  $n_e$ :

$$\varphi_e = \frac{k_e n_e}{k_e n_e + k_2 n_e (n_h + p_0) + k_T n_e (N_T - n_t)} \quad (4.5)$$

which is defined as the ratio between the electron injection rate and the total recombination rate for electrons. Similarly, the hole extraction yield  $\varphi_h$  is given by:

$$\varphi_h = \frac{k_h n_h}{k_h n_h + k_2 n_e (n_h + p_0) + k_R n_t (n_h + p_0)} \quad (4.6)$$

**Figures 4.6a** and **4.6b** show  $\varphi_e$  and  $\varphi_h$ , respectively, as function of the excitation density, using the kinetic parameters listed in **Tables 4.1** and **4.2**. Note that AM1.5 illumination under open circuit conditions leads to charge carrier densities on the order of  $10^{15} \text{ cm}^{-3}$ .<sup>26</sup> **Figure 4.6a** shows that at low charge carrier concentrations,  $\varphi_e$  is close to unity for PCBM and C<sub>60</sub>, which can be understood considering that the injection is fast enough to overcome trapping (*i.e.*,  $k_e \gg k_T N_T$ ). On the other hand, in view of the lower injection rates, electron injection into ICBA and bis-PCBM is in competition both with trapping and second-order recombination. Therefore, the transfer yield will always be less than 0.8 even if all trap-assisted recombination is eliminated (*i.e.* for  $k_e \sim 10^7 \text{ s}^{-1}$  and  $k_2 \sim 10^{-9} \text{ cm}^3 \text{ s}^{-1}$ ). Finally, for all ETMs,  $\varphi_e$  drops down when the concentration increases.

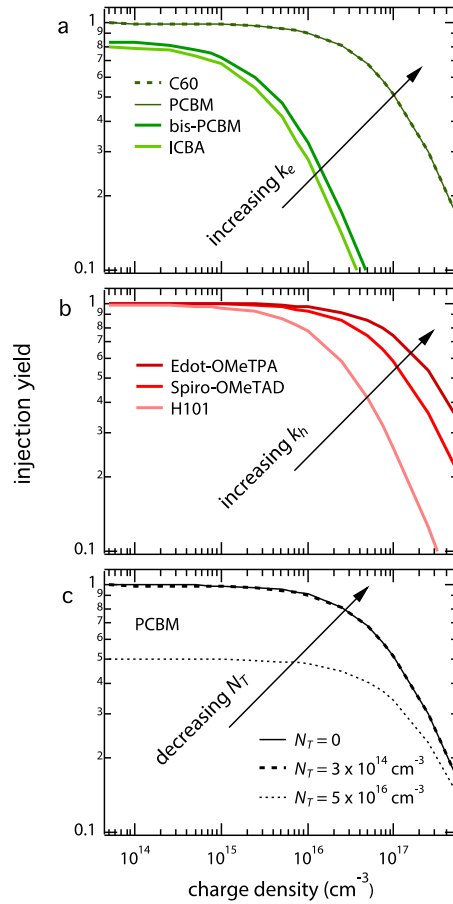


**Figure 4.6:** (a-b) Injection yield as function of charge carrier density for different ETMs (a) and HTMs (b), using **Equations 4.5** (a) and **4.6** (b) and the kinetic parameters from **Tables 4.1** and **4.2**. As we extracted from the TRMC measurements, trapping of electrons ( $\sim k_T N_T$ ) is in competition with extraction ( $k_e$ ), which can lower the extraction yield. This is especially relevant for ETMs with relatively low injection rates such as ICBA. In general, both  $\varphi_e$  and  $\varphi_h$  decrease when the charge carrier concentration increases ( $> 10^{16} \text{ cm}^{-3}$ ), since higher order recombination starts to dominate over injection. (c) Electron transfer yield from MAPbI<sub>3</sub> to PCBM as function of the concentration of electron traps ( $N_T$ ).

This decrease in  $\varphi_e$  is due to second-order recombination effects ( $\sim k_2 n_e n_h$ ), which start to dominate over injection at high charge carrier concentrations. The same trends are observed for the HTMs (**Figure 4.6b**):  $\varphi_h$  is close to unity at low concentrations and decreases at increasing concentrations. Furthermore,  $\varphi_h$  remains higher for Spiro-OMeTAD than for H101, which can be understood considering that  $k_h$  is lower for the latter.

Obviously, electron injection into PCBM could also be impeded by the presence of

traps, but only if the trap densities are much higher, *e.g.* less than 50% of the electrons are injected if  $N_T$  would be  $5 \times 10^{16} \text{ cm}^{-3}$  (see **Figure 4.6c**).<sup>17</sup> Similarly, in samples prepared *via* different routes, the traps could be hole-selective and  $\varphi_h$  could be lower since trapping of holes competes with transfer to the HTM. Finally, considering that illumination with AM1.5 results in charge concentrations in the order of  $10^{15} - 10^{16} \text{ cm}^{-3}$ , these results show that transfer rates to C<sub>60</sub>, PCBM, EDOT-OMeTPA and Spiro-OMeTAD are high enough to outcompete second-order recombination.

### 4.3 Conclusions

In this chapter, we investigated the transfer of optically excited charge carriers from MAPbI<sub>3</sub> to different organic TMs. The TRMC technique was used to study the charge carrier dynamics both in neat MAPbI<sub>3</sub> and bilayers of MAPbI<sub>3</sub> with an ETM or HTM on top. We proposed a global kinetic model, which we used to quantify the recombination dynamics in the MAPbI<sub>3</sub> as well as the additional pathways introduced by the presence of an ETM or HTM. Hence, we were able to deduce rate constants for extraction and interfacial recombination for several organic TMs. Interestingly, we find that both for the state-of-the-art HTM Spiro-OMeTAD and the low-cost alternatives H101 and EDOT-OMeTPA, holes are efficiently collected. However, for the latter this is followed by rapid recombination at the MAPbI<sub>3</sub>/EDOT-OMeTPA interface, which is expected to limit device performance. For the ETMs, we find that injection into PCBM and C60 is substantially more efficient than into ICBA and bis-PCBM, which might be due to the lower electron affinity of the latter two. Finally, we find that intra-bandgap traps do barely affect injection, as long as the trapping rate ( $\sim k_T N_T$ ) is substantially lower than the transfer rates (typically  $\sim 10^8 \text{ s}^{-1}$ ), which is the case for trap densities less than  $10^{15} \text{ cm}^{-3}$ .

### 4.4 Experimental Methods

#### Sample preparation

Thin films (200 nm) of MAPbI<sub>3</sub> on quartz substrates were prepared by sequential physical vapour deposition of the precursors PbI<sub>2</sub> and MAI in a stoichiometric ratio. Therefore, an adapted evaporation machine (ATC Orion 4 – AJA International, Inc.) with Deposition Controller (SQC-310 Inficon) and Thermal Evaporation Controller (TEC-15A) was used. MAI synthesized using standard procedures and commercially available lead iodide (PbI<sub>2</sub>  $\geq 99\%$ , Sigma Aldrich) were put into quartz crucibles, which were positioned in the vacuum chamber after which the pressure was reduced to  $10^{-5}$ - $10^{-6}$  mbar. For each deposition, eight plasma-cleaned quartz substrates were introduced in the vacuum chamber. Consequently, the crucible containing the PbI<sub>2</sub> precursor was heated to 220 - 240 °C until the desired deposition rate of 0.5 Å/s was reached, as indicated by a quartz microbalance. The MAI was heated to 60 - 80 °C to reach a rate of 1.3 Å/s. Then, MAPbI<sub>3</sub> was obtained by alternating deposition of 1 nm PbI<sub>2</sub> and 2 nm MAI (with 16 seconds in between), which was repeated until a total thickness of 200 nm was reached. Finally, the films were annealed at 100 °C for 1 hour. Spin-coated MAPbI<sub>3</sub> films were prepared from a solution consisting of PbI<sub>2</sub> (1.25 M, TCI chemicals) and MAI (1.25 M, Dyesol) in DMF, which was spin-coated dynamically (at 5000 rpm, total 15 sec) onto the quartz substrate. After 5 seconds 75  $\mu\text{L}$  of chlorobenzene was added on top of the spinning substrate and afterwards the substrates were placed on a hotplate (100 °C for 10 minutes). The bilayers were prepared by spin-coating the HTMs and ETMs on top of the vapour-deposited MAPbI<sub>3</sub> films. EDOT-OMeTPA was synthesized according to previously reported procedures,<sup>15</sup>

while H101 and Spiro-OMeTAD were obtained from commercial sources. EDOT-OMeTPA was spin coated from a 15 mg/mL chlorobenzene solution. A 75 mg/mL chlorobenzene solution was prepared for H101 and Spiro-OMeTAD. Dopants were added to all HTM solutions: 4-*tert*-butylpyridine (t-BP) (10  $\mu$ L/mL) and of a lithium bistrifluoromethylsulfonamide (Li-TFSI) (30  $\mu$ L/mL) solution (173 mg/mL Li-TFSI in acetonitrile solution). While rotating the sample at a speed of 150 rpm, an EDOT-OMeTPA solution (100  $\mu$ L) was deposited on top of the thin film MAPbI<sub>3</sub>, after which the rotational speed was increased to 1200 rpm (45 s). H101 and Spiro-OMeTAD were spincoated by depositing the solution (60  $\mu$ L) while rotating the sample at 1500 rpm (45 s). This resulted in HTM thicknesses of 40 nm for EDOT-OMeTPA and 250 nm for Spiro and H101.<sup>15</sup> MAPbI<sub>3</sub>/HTM bilayers were stored overnight with 30% relative humidity in order to let the HTM oxidize. For the ETMs, PCBM, bis-PCBM and ICBA, ETM/chlorobenzene (35 mg/mL) solutions were prepared. From these solutions, 60  $\mu$ L was deposited on the sample while rotating at 3000 rpm (45 s). The thickness of the PCBM layer was found to be around 70 nm. Layers of the other ETMs were estimated to have similar thickness.

### Optical Characterization

Absorption and transmission spectra were recorded with a Perkin-Elmer Lambda 1050 spectrophotometer equipped with an integrated sphere. The thin films were placed in front of the sphere to measure the fraction of transmitted light ( $F_T$ ) and under an angle of 10° inside the sphere to detect the total fraction of reflected and transmitted photons ( $F_{R+T}$ ). The fraction of absorbed light ( $F_A$ ) and charge carrier generation profiles were calculated as described in Chapter 2. The TRMC and PL measurements were performed using the same set-ups as in Chapter 3.

## 4.5 References

1. Wu, B. *et al.* Charge Accumulation and Hysteresis in Perovskite-Based Solar Cells: An Electro-Optical Analysis. *Adv. Energy Mater.* **5**, 1500829 (2015).
2. Calado, P. *et al.* Evidence for ion migration in hybrid perovskite solar cells with minimal hysteresis. *Nat. Commun.* **7**, 13831 (2016).
3. Brenner, T. M., Egger, D. A., Kronik, L., Hodes, G. & Cahen, D. Hybrid organic-inorganic perovskites: low-cost semiconductors with intriguing charge-transport properties. *Nat. Rev. Mater.* **1**, 15007 (2016).
4. Manser, J. S., Christians, J. A. & Kamat, P. V. Intriguing Optoelectronic Properties of Metal Halide Perovskites. *Chem. Rev.* **116**, 12956–13008 (2016).
5. Pydzińska, K. *et al.* Determination of Interfacial Charge-Transfer Rate Constants in Perovskite Solar Cells. *ChemSusChem* **9**, 1647–1659 (2016).
6. Ponseca Jr, C. S. *et al.* Mechanism of Charge Transfer and Recombination Dynamics in Organo Metal Halide Perovskites and Organic Electrodes, PCBM, and Spiro-OMeTAD: Role of Dark Carriers. *J. Am. Chem. Soc.* **137**, 16043–16048 (2015).
7. Makuta, S. *et al.* Photo-excitation intensity dependent electron and hole injections from lead iodide perovskite to nanocrystalline TiO<sub>2</sub> and spiro-OMeTAD. *Chem. Commun.* **52**, 673–676 (2015).
8. Piatkowski, P. *et al.* Direct Monitoring of Ultrafast Electron and Hole Dynamics in Perovskite Solar Cells. *Phys. Chem. Chem. Phys.* **17**, 14674–14684 (2015).
9. Brauer, J. C., Lee, Y. H., Mohammad K., N. & Banerji, N. Ultrafast Charge Carrier Dynamics in CH<sub>3</sub>NH<sub>3</sub>PbI<sub>3</sub>: Evidence for Hot Hole Injection into Spiro-OMeTAD. *J. Mater. Chem. C* **4**, 5922–5931 (2016).
10. Ishida, N., Wakamiya, A. & Saeki, A. Quantifying Hole Transfer Yield from Perovskite to Polymer Layer: Statistical Correlation of Solar Cell Outputs with Kinetic and Energetic Properties. *ACS Photonics* **3**, 1678–1688 (2016).
11. Malinkiewicz, O. *et al.* Perovskite solar cells employing organic charge-transport layers. *Nat. Photonics* **8**, 128–132 (2013).
12. Liu, M., Johnston, M. B. & Snaith, H. J. Efficient planar heterojunction perovskite solar cells by vapour deposition. *Nature* **501**, 395–398 (2013).
13. Momblona, C. *et al.* Efficient vacuum deposited p-i-n and n-i-p perovskite solar cells employing doped

- charge transport layers. *Energy Environ. Sci.* **9**, 3456–3463 (2016).
14. Li, H. *et al.* A simple 3,4-ethylenedioxythiophene based hole-transporting material for perovskite solar cells. *Angew. Chemie - Int. Ed.* **53**, 4085–4088 (2014).
15. Petrus, M. L., Bein, T., Dingemans, T. J. & Docampo, P. A low cost azomethine-based hole transporting material for perovskite photovoltaics. *J. Mater. Chem. A* **3**, 12159–12162 (2015).
16. Jeng, J. Y. *et al.* CH<sub>3</sub>NH<sub>3</sub>PbI<sub>3</sub> perovskite/fullerene planar-heterojunction hybrid solar cells. *Adv. Mater.* **25**, 3727–3732 (2013).
17. Hutter, E. M., Eperon, G. E., Stranks, S. D. & Savenije, T. J. Charge Carriers in Planar and Meso-Structured Organic-Inorganic Perovskites: Mobilities, Lifetimes and Concentrations of Trap States. *J. Phys. Chem. Lett.* **6**, 3082–3090 (2015).
18. Hutter, E. M. *et al.* Direct–indirect character of the bandgap in methylammonium lead iodide perovskite. *Nat. Mater.* **16**, 115–120 (2017).
19. Stranks, S. D. *et al.* Recombination Kinetics in Organic-Inorganic Perovskites: Excitons, Free Charge, and Subgap States. *Phys. Rev. Appl.* **2**, 34007 (2014).
20. Wetzelaer, G.-J. A. H. *et al.* Trap-Assisted Non-radiative Recombination in Organic–Inorganic Perovskite Solar Cells. *Adv. Mater.* **27**, 1837–1841 (2015).
21. Savenije, T. J., Ferguson, A. J., Kopidakis, N. & Rumbles, G. Revealing the dynamics of charge carriers in polymer:fullerene blends using photoinduced time-resolved microwave conductivity. *J. Phys. Chem. C* **117**, 24085–24103 (2013).
22. Wang, Q. *et al.* Qualifying composition dependent p and n self-doping in CH<sub>3</sub>NH<sub>3</sub>PbI<sub>3</sub>. *Appl. Phys. Lett.* **105**, 15–20 (2014).
23. Bi, C. *et al.* Understanding the formation and evolution of interdiffusion grown organolead halide perovskite thin films by thermal annealing. *J. Mater. Chem. A* **2**, 18508–18514 (2014).
24. Wojciechowski, K. *et al.* Heterojunction Modification for Highly Efficient Organic-Inorganic Perovskite Solar Cells. *ACS Nano* **8**, 12701–12709 (2014).
25. Wu, C.-G., Chiang, C.-H. & Chang, S. H. A perovskite cell with a record-high-Voc of 1.61 V based on solvent annealed CH<sub>3</sub>NH<sub>3</sub>PbBr<sub>3</sub>/ICBA active layer. *Nanoscale* **8**, 4077–4085 (2016).
26. Johnston, M. B. & Herz, L. M. Hybrid Perovskites for Photovoltaics: Charge-Carrier Recombination, Diffusion, and Radiative Efficiencies. *Acc. Chem. Res.* **49**, 146–154 (2016).

## Appendices

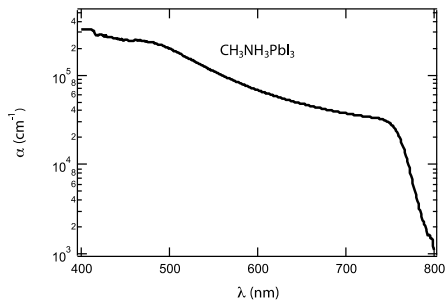


**Figure A4.1:** Semi-logarithmic plot of the absorption coefficient of MAPbI<sub>3</sub>.

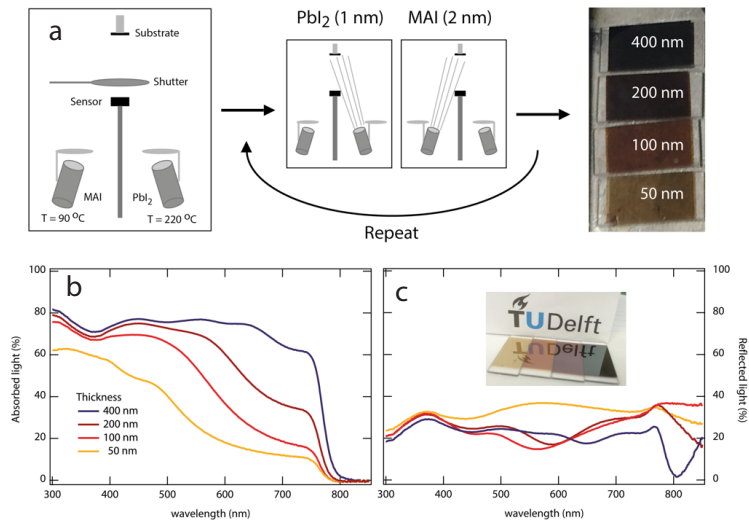


**Figure A4.2:** (a) Schematic representation of sequential physical vapour deposition from MAI and PbI<sub>2</sub> powders (see experimental methods). The MAI powder is heated to 60-90 °C, while the PbI<sub>2</sub> is heated to 220-240 °C. Then, MAPbI<sub>3</sub> is obtained by alternating deposition of 1 nm PbI<sub>2</sub> and 2 nm MAI until the desired thickness is obtained. (b-c) Fraction of light absorbed (b) and reflected (c) as function of thickness.



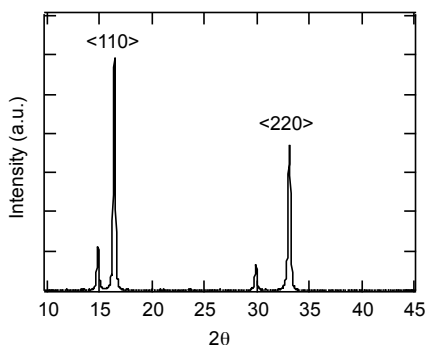


**Figure A4.3:** X-Ray Diffraction (XRD) pattern using Co-K $\alpha$  radiation ( $\lambda = 1.79 \text{ \AA}$ ) for a 200 nm thick vapour-deposited MAPbI<sub>3</sub> film. The primary reflections are the <110> and <220>, showing that the films are highly oriented. A slight excess of PbI<sub>2</sub> was found to be present, as indicated by the reflection at 14.2°.

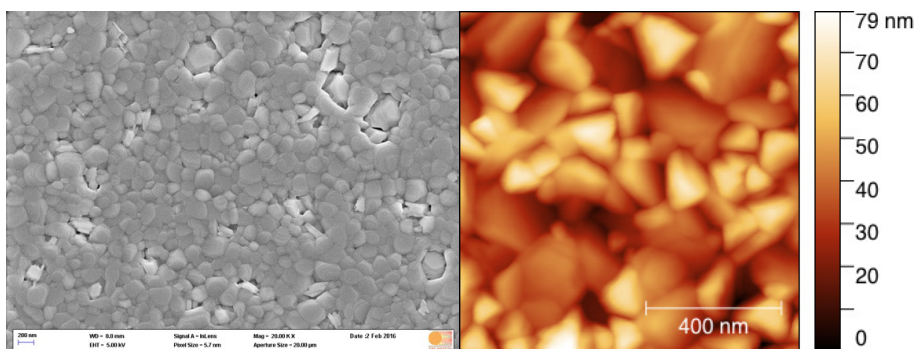


**Figure A4.4:** Scanning Electron Microscopy (a) and Atomic Force Microscopy (b) image of a vapour-deposited MAPbI<sub>3</sub> film, showing that the size of crystalline domains is on the order of several hundred nanometers.

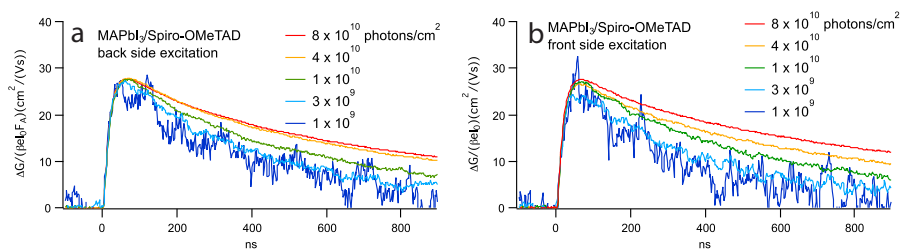


**Figure A4.5:** Photoconductance as function of time after excitation from the back side (through the quartz) (a) and the front side (through the Spiro-OMeTAD) (b) for  $10^9$  to  $8 \times 10^{10}$  photons/cm<sup>2</sup> ( $\lambda = 600 \text{ nm}$ ).



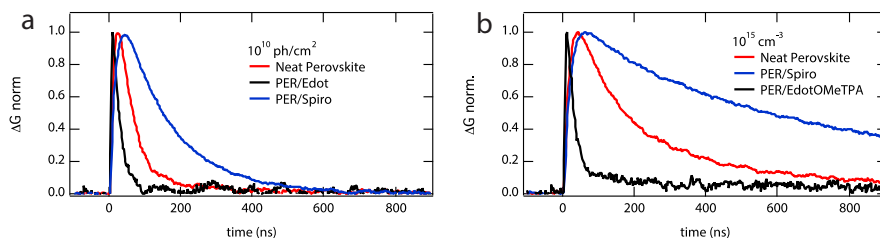


**Figure A4.6:** Normalized photoconductance as function of time after excitation for neat MAPbI<sub>3</sub> (red), MAPbI<sub>3</sub>/EDOT-OMeTPA (black) and MAPbI<sub>3</sub>/Spiro-OMeTAD (blue) for spin-coated (a) and vapour-deposited (b) MAPbI<sub>3</sub> films. Although the spin-coated MAPbI<sub>3</sub> shows a different lifetime than the vapour-deposited perovskite, the same trends are observed. That is, the lifetime of the electrons remaining in MAPbI<sub>3</sub> is extended when the holes are transferred to Spiro-OMeTAD, whereas this is substantially reduced in the case of EDOT-OMeTPA. Note that the traces in (b) correspond to the results shown in the main text.

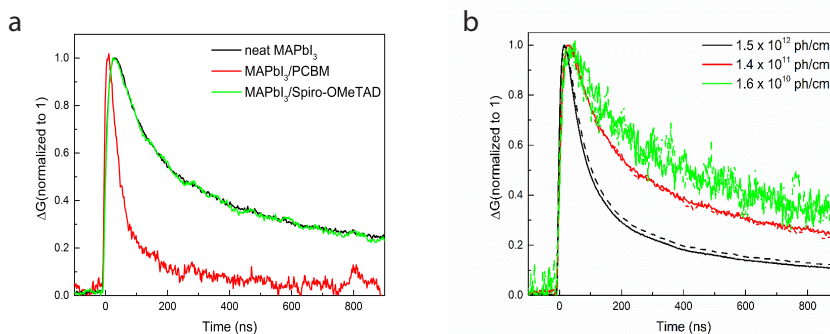


**Figure A4.7:** (a) TRMC traces for spin-coated MAPbI<sub>3</sub>, MAPbI<sub>3</sub>/PCBM and MAPbI<sub>3</sub>/Spiro-OMeTAD recorded at an excitation intensity of  $1.0 \times 10^{11}$  photons/cm<sup>2</sup> per pulse ( $\lambda = 600$  nm) and normalized to unity.<sup>6</sup> (b) Direct comparison of  $\Delta G(t)$  for MAPbI<sub>3</sub> (full lines) and MAPbI<sub>3</sub>/Spiro-OMeTAD bilayer (dashed lines) recorded at indicated intensities expressed in photons/cm<sup>2</sup> per pulse ( $\lambda = 600$  nm).

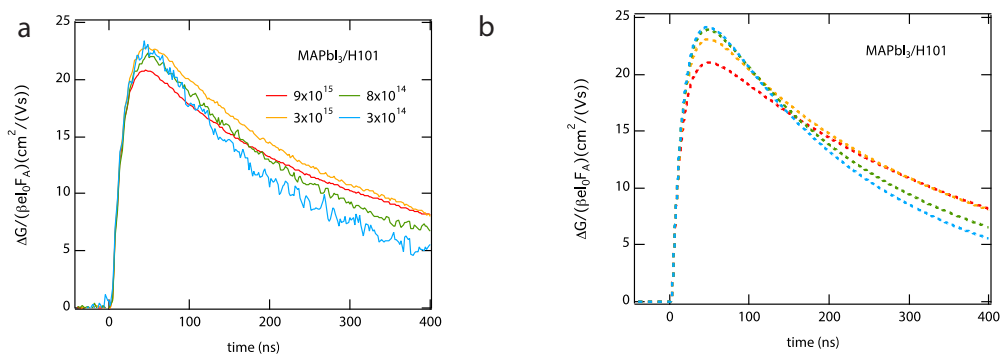


**Figure A4.8:** Magnification of the experimental (a) and modelled (b) TRMC traces for MAPbI<sub>3</sub>/H101 as shown in **Figure 4.5a** of the main text.

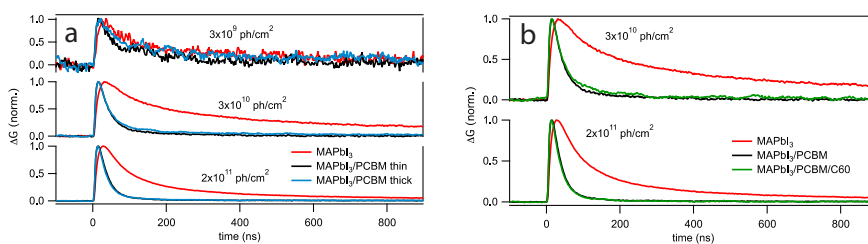


**Figure A4.9:** Normalized TRMC traces for neat MAPbI<sub>3</sub> and bilayers of MAPbI<sub>3</sub>/PCBM with different PCBM thickness (a) and trilayers of MAPbI<sub>3</sub>/PCBM/C<sub>60</sub>, where C<sub>60</sub> has a higher electron affinity than PCBM ( $\lambda = 600$  nm, front side illuminated).

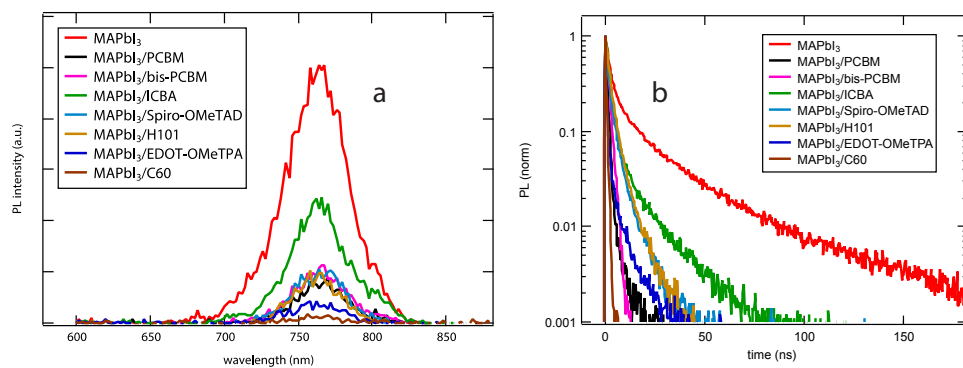
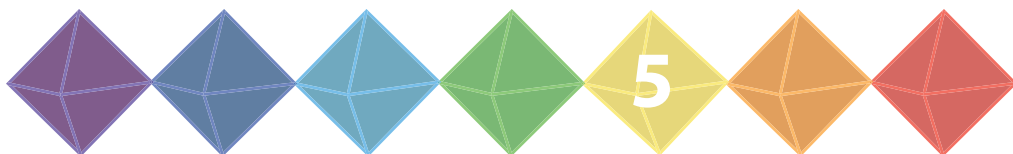


**Figure A4.10:** Photoluminescence emission scans (a) and lifetimes (b) for the neat MAPbI<sub>3</sub> and bilayer samples shown in the main text.





# Temperature-Dependent Recombination Pathways in Tetragonal and Orthorhombic Phases of Methylammonium Lead Iodide Perovskites



## ABSTRACT

Currently, there is debate over what drives the second-order electron–hole recombination in methylammonium lead iodide perovskites. Here, we propose that the bandgap in MAPbI<sub>3</sub> has a direct–indirect character. Time-resolved photoconductivity measurements show that generation of free mobile charges is maximized for excitation energies just above the indirect bandgap. Furthermore, we find that second-order electron–hole recombination of photo-excited charges is retarded at lower temperature. These observations are consistent with a slow phonon-assisted recombination pathway *via* the indirect bandgap. Interestingly, in the low-temperature orthorhombic phase, fast quenching of mobile charges occurs independent of the temperature and photon excitation energy. This chapter provides a new framework to understand the optoelectronic properties of metal halide perovskites and analyse spectroscopic data.

### Partially based on

Eline M. Hutter, María Gélvez-Rueda, Anna Osherov, Vladimir Bulović, Ferdinand C. Grozema, Samuel D. Stranks, Tom J. Savenije, Direct-Indirect Character of the Band Gap in Methylammonium Lead Iodide Perovskite, *Nature Materials*, 2017, 16, 115-120.

Anna Osherov, Eline M. Hutter, Krzysztof Galkowski, Roberto Brenes, Duncan K. Maude, Robin J. Nicholas, Paulina Plochocka, Vladimir Bulović, Tom J. Savenije, Samuel D. Stranks, The Impact of Phase Retention on the Structural and Optoelectronic Properties of Metal Halide Perovskites, *Advanced Materials*, 2016, 28, 10757-10763.

## 5.1 Introduction

Currently, the conventional idea is that MAPbI<sub>3</sub> behaves as a direct bandgap semiconductor, where the absorption and emission of photons occur via allowed transitions. This is fundamentally different from indirect bandgap semiconductors such as silicon in which both absorption and recombination involve not only photons, but also phonons. This results in lower absorption coefficients than in direct semiconductors,<sup>1</sup> but at the same time recombination is much slower.<sup>2</sup> Recent theoretical calculations of the band structure of MAPbI<sub>3</sub> suggest that preferential orientation of the organic cations in the [011] crystallographic direction induces an indirect bandgap in MAPbI<sub>3</sub> perovskites.<sup>3,4</sup> Other theoretical work has predicted that the Rashba effect results in splitting of the conduction band, making the fundamental bandgap indirect.<sup>5,6</sup> In both cases, relaxation of excited electrons (direct excitation) into the conduction band minimum (CBM) corresponding to an indirect bandgap would result in relatively slow recombination. Nevertheless, to date, there are no reports of experimental evidence for the presence of an indirect bandgap in MAPbI<sub>3</sub> or in any other metal halide perovskite. Furthermore, it remains controversial to what extent the crystal phase affects the photo-physics in MAPbI<sub>3</sub>.<sup>7–9</sup> Some groups have suggested that in the orthorhombic phase ( $T < 160$  K), excitons dominate over free charges.<sup>9</sup> However, others have reported an exciton binding energy of only 16 meV in the orthorhombic phase,<sup>10,11</sup> which would yield only a small population of excitons. Finally, most temperature-dependent spectroscopic studies monitor the charge carrier dynamics at relatively high excitation fluences (*i.e.*, in excess of  $1 \mu\text{J}/\text{cm}^2$ ),<sup>8</sup> whereas most processes relevant to solar cell operation happen at much lower illumination intensities. In this chapter, we use temperature-dependent TRPL and complementary TRMC techniques to study the dynamics of optically-excited charge carriers in MAPbI<sub>3</sub> at charge densities comparable to AM 1.5 excitation. At 300 K, the generation yield of free charges is maximized for excitation energies close to 1.7 eV ( $\lambda = 730$  nm). In addition, temperature-dependent TRPL and TRMC measurements both show that second-order electron-hole recombination is a thermally-activated process for  $T > 160$  K.<sup>12,13</sup> These results are explained by proposing that photo-excited carriers undergo slow phonon-assisted recombination from the CBM, which is shifted in  $k$ -space with respect to the valence band maximum (VBM). In the orthorhombic phase ( $T < 160$  K), fast quenching of mobile charges is observed independent of the temperature and excitation energy.<sup>8</sup> Finally, we find that this behaviour is general for solution-processed perovskite films with a planar or meso-structured morphology and independent of the lead precursor used in the fabrication.

## 5.2 Results

Thin ( $\sim 250$  nm) MAPbI<sub>3</sub> films were solution-processed on quartz substrates using an acetate-based precursor solution.<sup>14</sup> **Figures 5.1a** and **5.1c** show the photoconductance  $\Delta G$ , as function of time after excitation at 1.7 and 2.0 eV at  $T = 300$  K and  $T = 120$  K, respectively.<sup>15</sup> X-ray diffraction (XRD) patterns indicate a tetragonal MAPbI<sub>3</sub> phase at 300 K, while at 120 K the material is in the orthorhombic phase (see **Figure A5.1** in

**Appendices).** Interestingly, in the tetragonal phase at  $T = 300$  K, the signal observed on excitation at 1.65 eV is significantly higher than at 2.00 eV, while the opposite is true in the orthorhombic phase at  $T = 120$  K. Furthermore, the signal sizes at 120 K, which are normalized for the number of absorbed photons, are almost an order of magnitude smaller than at 300 K. The incident yield,  $\eta$ , defines the ratio between the number of light-induced carriers over the number of incident photons. The product of  $\eta$  and the summation of the electron and hole mobilities,  $\Sigma\mu$ , can be calculated from the maximum value of the photoconductance  $\Delta G_{max}$  according to:

$$\eta\Sigma\mu = \frac{\Delta G_{max}}{I_0\beta e} \quad (5.1)$$

Note that this equation is similar to **Equation 2.22**: the only difference is that the photoconductance is not corrected for the absorbed photon fraction  $F_A$ . If  $\eta$  and  $\Sigma\mu$  are independent of the excitation wavelength, a wavelength-dependent spectrum of  $\eta\Sigma\mu$  (action spectrum) should thus exactly match the absorbance ( $F_A$ ) spectrum.<sup>16,17</sup> **Figures**

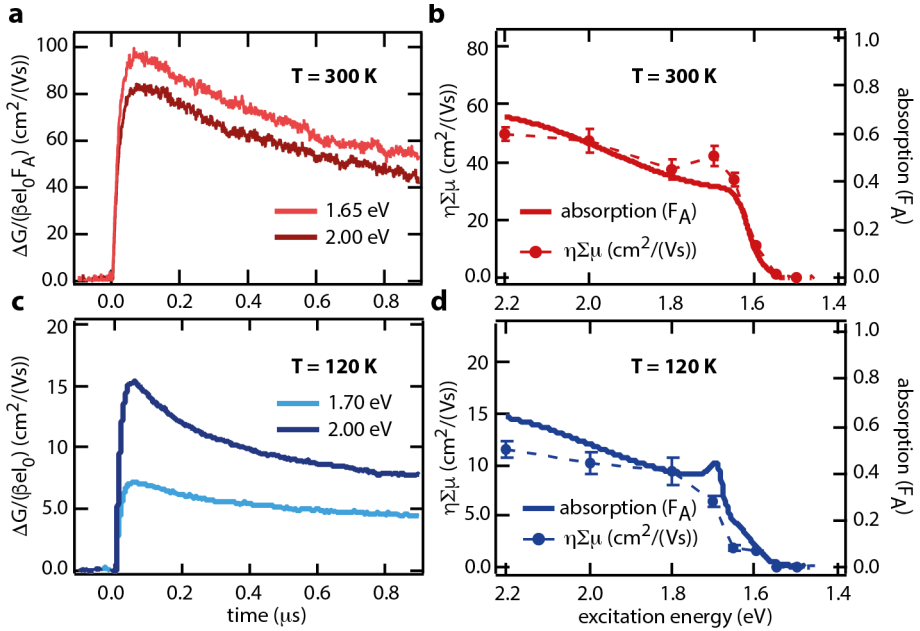


**Figure 5.1:** (a) Photoconductance as function of time after excitation at 1.65 eV ( $\lambda = 753$  nm) and 2.00 eV ( $\lambda = 621$  nm) for the tetragonal phase at 300 K for an absorbed photon fluence of  $8 \times 10^8$  cm<sup>-2</sup> per pulse. (c) Photoconductance as function of time after excitation at 1.70 eV ( $\lambda = 730$  nm) and 2.00 eV ( $\lambda = 621$  nm) for the orthorhombic phase at 120 K for an incident photon fluence of  $2 \times 10^{10}$  cm<sup>-2</sup> per pulse. Comparison of maximum photoconductance ( $\eta\Sigma\mu$ , circles) to fraction of absorbed photons at 300 K (b) and 120 K (d), where the absorbed photon fluences are  $8 \times 10^8$  cm<sup>-2</sup> per pulse for  $T = 300$  K and on the order of  $10^9$  cm<sup>-2</sup> per pulse for 120 K. For each excitation wavelength, the photoconductance was averaged over at least 200 laser pulses and error bars were calculated based on the inaccuracy in the laser intensity  $I_0$ .



**5.1b** and **1d** (dashed lines) show the action spectra for a MAPbI<sub>3</sub> thin film at 300 K (**Figure 5.1b**) and at 120 K (**Figure 5.1d**), together with the temperature-dependent  $F_A$  spectra (solid lines). Strikingly, for both temperatures the action spectra do not match the  $F_A$  spectra. For tetragonal MAPbI<sub>3</sub> (**Figure 5.1b**), the product  $\eta\Sigma\mu$  reaches a local maximum value at excitation energies close to 1.7 eV ( $\lambda = 730$  nm). By normalizing  $\eta\Sigma\mu$  to  $F_A$ , we obtain the product of the charge carrier generation yield  $\phi$  and the mobility  $\Sigma\mu$ , (*i.e.*  $\phi\Sigma\mu$ ). Considering that the thermal energy at 300 K ( $k_B T = 25.9$  meV) is much higher than the exciton binding energy of a few millielectronvolts,<sup>10</sup> most of the excitons will dissociate into free charges and  $\phi$  is close to unity (recall **Figure 2.2**).<sup>7</sup> Therefore,  $\Sigma\mu$  amounts to at least 100 cm<sup>2</sup>/(Vs) for charges excited at 1.7 eV, which is comparable to mobilities reported for single MAPbI<sub>3</sub> crystals and thus indicative of the high quality of the polycrystalline films fabricated from the acetate-based precursors.<sup>18</sup> Exciting above 1.8 eV results in  $\phi\Sigma\mu$  values of 80 cm<sup>2</sup>/(Vs), indicating that  $\phi$  is approximately 20% lower. Here, we assume that  $\Sigma\mu$  is independent of excitation wavelength, which is reasonable in view of the similar decay kinetics (**Figure A5.2** in **Appendices**). This local maximum in the action spectrum around 1.7 eV is also observed at higher excitation densities, and becomes even more pronounced at lower excitation densities (see **Figures A5.3** and **A5.4** in **Appendices**).<sup>19</sup>

For orthorhombic MAPbI<sub>3</sub>, the action spectrum only matches the  $F_A$  spectrum for excitation energies above 1.7 eV (see **Figure 5.1d**). In contrast with the tetragonal phase, the  $\phi\Sigma\mu$  values in the orthorhombic phase using excitation energies close to 1.7 eV are relatively low (see **Figures 5.1b** and **5.1d**). To understand this, we note that at 120 K, the  $F_A$  spectrum is comprised of the band-to-band continuum and a sharp transition peaking at 1.7 eV that has been attributed to an excitonic feature.<sup>7,20,21</sup> Hence we conclude that, for excitation wavelengths that coincide with the excitonic transition (1.7 eV), the generation yield of free charges is much lower than for the band-to-band continuum ( $\geq 1.8$  eV). This implies that in the orthorhombic phase, excitons are less likely to dissociate into free charges than in the tetragonal phase. This observation can be understood from the exciton binding energy being at least 16 meV in orthorhombic MAPbI<sub>3</sub>,<sup>10</sup> which is higher than the thermal energy of 10 meV at 120 K.

To further investigate the generation and recombination pathways of free charges in the different crystal phases, we measured  $\phi\Sigma\mu$  for temperatures ranging from 80 to 340 K using an excitation energy of 2.0 eV, which corresponds to band-to-band excitations in both phases. In the tetragonal ( $\beta$ ) phase down to 150 K,  $\phi\Sigma\mu$  is enhanced upon cooling (**Figure 5.2a**). In contrast, if the temperature is further reduced to 90 K and the crystal structure changes from tetragonal to orthorhombic ( $\gamma$ ),  $\phi\Sigma\mu$  decreases substantially. These changes in  $\phi\Sigma\mu$  could be due to a variation of  $\phi$  and/or  $\Sigma\mu$  with temperature. To unravel this, we performed complementary temperature-dependent pulse-radiolysis TRMC (PR-TRMC) experiments, where free electrons and holes are generated by a high-energy electron pulse instead of a laser. The samples were prepared in the same way as for the photoconductivity experiments.<sup>22</sup> Similar to the photoconductivity experiments, the initial pulse-induced change in conductivity in PR-TRMC is determined by the

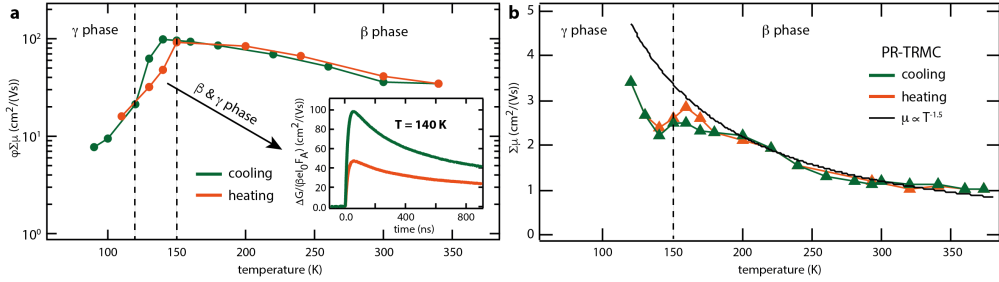


**Figure 5.2:** (a) Product of generation yield  $\phi$  ( $\leq 1$ ) and mobility  $\Sigma\mu$  as a function of temperature in a MAPbI<sub>3</sub> thin film. The film is photo-excited at 2.0 eV ( $10^{10}$  absorbed photons/cm<sup>2</sup>) and the results are shown for cooling (green) and heating (orange) the film. The time-dependent photoconductance at 140 K is shown in the inset. (b) Temperature-dependent mobility measured with pulse-radiolysis TRMC (PR-TRMC) measurements. Note that the absolute values obtained with the PR-TRMC technique (b) are lower than those obtained with the photoconductivity measurements, which could stem from an overestimation of the number of charge carriers (see also experimental section). Nevertheless, this does not affect the temperature-dependent mobility trend.

concentration and mobility of the charge carriers. However, the concentration is now tuned by the duration of the accelerator pulse and free charges are generated instead of excitons. Therefore, PR-TRMC can be used to determine the temperature-dependent mobility.<sup>23</sup> Similar to previous studies,<sup>8,12,23</sup> these measurements confirm that in our MAPbI<sub>3</sub> thin films, the mobility increases when the temperature is lowered (see **Figure 5.2b**).

For these samples  $\Sigma\mu$  is proportional to  $T^{-1.5}$  down to the phase transition and,<sup>8,12,23</sup> apart from small deviations, no abrupt decrease in the mobility is observed below the phase transition. In other words, the increasing  $\phi\Sigma\mu$  values upon cooling the MAPbI<sub>3</sub> thin film down to 150 K are due to an analogous rise in  $\Sigma\mu$ , whereas the reduced  $\phi\Sigma\mu$  values found for temperatures below 150 K can thus only be attributed to a substantial reduction in  $\phi$ . Interestingly, different trends in  $\phi\Sigma\mu$  are found for cooling and heating over the orthorhombic-tetragonal phase transition (see also inset in **Figure 5.2a**). We note that this observation is not an effect of the cooling and/or heating rate, since we made sure that the samples are in thermal equilibrium before we start the photoconductivity measurements. Similar to the different  $\phi\Sigma\mu$  values, we observe differences in the photoluminescence between cooling and heating at temperatures near the phase transition (120 - 150 K).<sup>24,25</sup> For instance, at 130 K, we find lower emission intensities peaking at larger energies in the photoluminescence spectra recorded on heating, see **Figure 5.3a**. Therefore, it seems likely that the tetragonal and orthorhombic phases co-exist in the above mentioned regime, where the ratio between the two phases differs between cooling and heating. Since  $\phi\Sigma\mu$  is substantially lower in the orthorhombic phase ( $T < 120$  K) than in the tetragonal phase, the lower photoconductance at 130 and 140 K upon heating may be associated with a

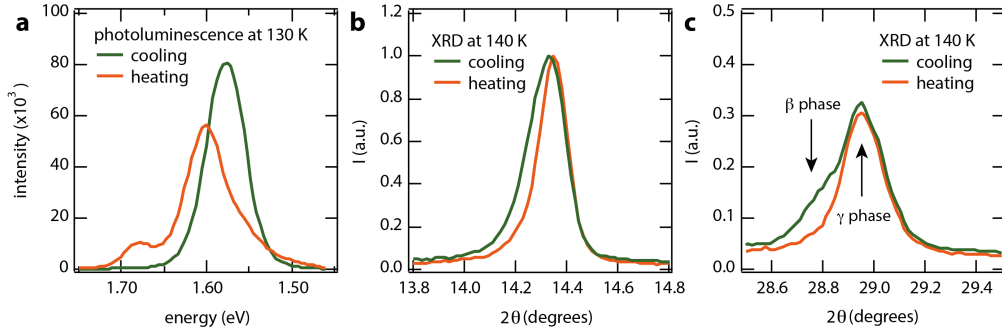


**Figure 5.3:** (a) Photoluminescence emission spectra recorded at 130 K and (b) (110) and (c) (220) reflections from the XRD patterns obtained at 140 K for cooling (green) and heating (orange) MAPbI<sub>3</sub>, confirming the co-existence of the orthorhombic and tetragonal phases.

larger concentration of orthorhombic MAPbI<sub>3</sub> domains than upon cooling. Comparing the XRD patterns recorded at  $T = 140$  K upon both cooling and heating, we find that this is indeed the case. In **Figures 5.3b** and **5.3c**, the reflections centered at  $2\theta$  values of  $14.38^\circ$  and  $28.95^\circ$  represent the (110) and (220) reflections of the orthorhombic ( $\gamma$ ) phase, respectively. These are present both on heating and cooling the sample. In addition, we find at slightly lower angles the (110) (**Figure 5.3b**) and (220) (**Figure 5.3c**) reflections of the tetragonal ( $\beta$ ) phase, however only upon cooling. Altogether, these results thus show that the phase transition itself is different for cooling and heating, and further confirm that the low  $\phi$  is characteristic of the orthorhombic phase.

In order to understand the drastic reduction in  $\phi$ , it is important to consider that the exciton binding energy in the orthorhombic phase is about 16 meV.<sup>10,11</sup> According to the Saha equation (**Equation 2.3**), this binding energy would result in an exciton population of less than 10% of the photo-excited species for an excitation density of  $10^{15} \text{ cm}^{-3}$  (as used in **Figure 5.2a**).<sup>26</sup> Although higher values for the exciton binding energy in the orthorhombic phase have been reported,<sup>27</sup> temperature-dependent THz spectroscopy studies have confirmed that the majority of excitations results in Drude-like free charges down to 77 K.<sup>8,28</sup> Therefore, given that  $\phi$  is at least an order of magnitude lower in the orthorhombic phase than in the tetragonal phase, this can only to a small extent be attributed to the presence of excitons. Instead, the low value of  $\phi$  might be due to the occurrence of (sub)-nanosecond decay of mobile electrons and holes, which is below the temporal resolution of our photon-induced TRMC measurements (see also **Figure 2.7**). To further investigate the phase-specific recombination pathways, we carried out temperature-dependent TRPL measurements at the maximum emission wavelength (**Figure A5.5** in **Appendices**), which depends both on temperature and the crystal structure.<sup>13,25,29</sup> **Figures 5.4a** and **5.4b** show TRPL intensities and TRMC traces

for tetragonal MAPbI<sub>3</sub> recorded between 260 K and 180 K.

Most interestingly, both TRPL and TRMC show the same trends; the lifetime is extended on lowering the temperature.<sup>12,13</sup> Furthermore, at 180 K, both  $\phi$  and the PL quantum efficiency (PLQE) are close to unity.<sup>13</sup> This means that at this temperature, the radiative recombination (PL) originates primarily from recombination between free mobile electrons and holes. In **Chapter 3**, we have shown that TRPL and TRMC lifetimes in MAPbI<sub>3</sub> can be modelled using the same set of kinetic parameters.<sup>30,31</sup> In other words, even at room temperature where the PLQE is typically less than 0.1,<sup>13</sup> second-order band-to-band recombination of mobile charges partially leads to PL.

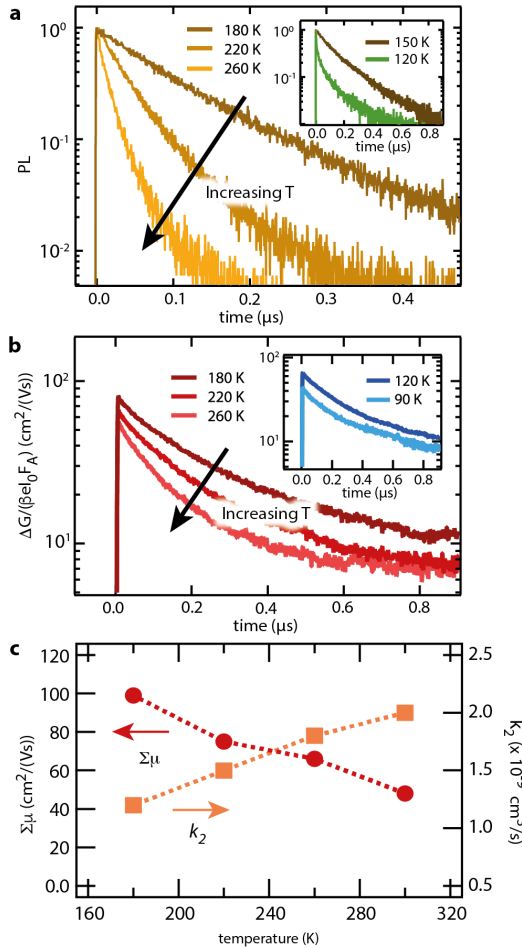


**Figure 5.4:** (a) PL lifetimes recorded at  $180 < T < 260$  K and 120 K (orthorhombic phase, at 1.67 eV, inset) for  $\lambda = 405$  nm (3.1 eV),  $I_0 = 4 \times 10^{12}$  photons/cm<sup>2</sup> per pulse: excitation density of  $10^{17}$  cm<sup>-3</sup>. (b) Temperature-dependent photoconductance in the tetragonal phase for  $180 < T < 260$  K and the orthorhombic phase (inset) for an excitation energy of 2.0 eV,  $I_0 = 9 \times 10^{10}$  photons/cm<sup>2</sup> per pulse: excitation density of  $3 \times 10^{15}$  cm<sup>-3</sup>. (c) Mobility (circles, left axis) and rate constant  $k_2$  (squares, right axis) for second-order electron-hole recombination, obtained from fitting the temperature-dependent TRMC traces.

**Table 5.1:** Kinetic parameters used to fit the experimental temperature-dependent TRMC data.

	180 K	220 K	260 K	300 K
$k_2$ ( $\times 10^{-10} \text{ cm}^3\text{s}^{-1}$ )	12	15	18	21
$k_T$ ( $\times 10^{-10} \text{ cm}^3\text{s}^{-1}$ )	0.6	0.75	0.9	1
$k_D$ ( $\times 10^{-10} \text{ cm}^3\text{s}^{-1}$ )	0.5	0.5	0.5	0.5
$N_T$ ( $\times 10^{15} \text{ cm}^{-3}$ )	1.5	2	5	7
$\mu_e$ ( $\text{cm}^2/(\text{Vs})$ )	66	50	44	32
$\mu_h$ ( $\text{cm}^2/(\text{Vs})$ )	33	25	22	16

The kinetic model introduced in **Chapter 2** was used to describe the temperature-dependent measurements displayed in **Figure 5.4b**. The modelled traces are added as solid lines to **Figure 5.4b** and fitting parameters are listed in **Table 5.1** (see also **Figure A5.6** in **Appendices**). We find that the initial decay is characterized by second-order recombination, while recombination between trapped charges and their mobile counter-charge dominates at longer timescales (*i.e.* lower concentrations).<sup>30</sup> **Figure 5.4c** shows the temperature-dependent mobility and the rate constant  $k_2$ , for second-order band-to-band electron-hole recombination. Interestingly, the temperature dependence of  $k_2$  indicates that electron-hole recombination is retarded when the temperature is lowered. This was observed to be general for solution-processed perovskite thin films, although we note that the absolute values of  $k_2$  differ for each processing route (see **Figures A5.7** and **A5.8** in **Appendices**). Thus, the second-order band-to-band recombination in tetragonal MAPbI<sub>3</sub> is a thermally-activated process under illumination intensities equivalent to 1 sun AM 1.5, implying that there is an energetic barrier for decay.<sup>12,13</sup> This is in contrast with typical direct bandgap bulk semiconductors such as GaAs,<sup>32</sup> where recombination becomes faster at lower temperature.

The inset in **Figure 5.4a** shows the PL decay for MAPbI<sub>3</sub> at 120 K, for the emission peak centered at 740 nm (see **Figure A5.9** in **Appendices**). The PL decay of the tetragonal phase ( $T = 150 \text{ K}$ ) is plotted in the same graph to enable direct comparison, which allows us to visualize that the PL lifetime at 120 K is much shorter than at 150 K. The same trend was observed with the PR-TRMC experiments, where at least half of the free charges is immobilized within 6 ns (**Figure A5.10** in **Appendices**). Clearly, the majority of photo-physical products in the orthorhombic phase decay much faster than those in the tetragonal phase. Furthermore, the emission spectra recorded at 90 K and 120 K comprise multiple peaks with different lifetimes (**Figure A5.9** in **Appendices**), indicating the presence of additional recombination pathways specific for the orthorhombic phase. Finally, the total integrated intensity of emitted photons at 90 K is lower than at 150 K (**Figure A5.9** in **Appendices**), which suggests that non-radiative recombination is

in competition with radiative events. Altogether, the above TRPL results show that in the orthorhombic phase, electron-hole recombination occurs on the (sub-)nanosecond timescale, explaining the extremely low yields of mobile charges detected with TRMC.

### 5.3 Discussion

To briefly summarize our results: at 300 K, the generation yield of free charge carriers in MAPbI<sub>3</sub> is 20% higher for excitation just above the band-gap (at 1.7 eV) than further above the bandgap (> 1.8 eV). Furthermore, in the tetragonal phase, an energetic barrier exists for second-order band-to-band recombination between mobile CB electrons and VB holes. In the orthorhombic phase on the other hand, both excitons and free charges decay via fast non-radiative recombination pathways, which competes effectively with charge carrier generation.

In order to explain all of these findings, we propose that in the tetragonal phase, additional dark states are present, which are located below the optically-accessible conduction band edge. These states are different from shallow traps. That is, if for instance electrons were immobilized in shallow traps, the generation yield of free mobile CB electrons should be enhanced with (i) increasing temperature and (ii) increasing charge carrier concentration. This should lead to a higher  $\phi\Sigma\mu$  with enhanced temperatures (i) and with increasing photon flux (ii). However, as shown in **Figures 5.3a** and in **Figures A5.4b** and **A5.8** in **Appendices**, the opposite trends are observed. Finally, as also shown in **Chapter 4**,<sup>33,34</sup> both electrons and holes are separately mobile under similar excitation conditions. Hence, although we do not rule out the presence of shallow trap states, these alone cannot explain the observations reported here. Instead, we propose that these dark states form band-like structures. Excited electrons thermally relax into these bands, yielding highly mobile carriers. Recombination of these electrons back to the ground-state is forbidden, resulting in long charge carrier lifetimes. This model is reminiscent of a semiconductor with an indirect bandgap, where the CBM is shifted in  $k$ -space with respect to the VBM so that recombination is momentum-forbidden (see also **Paragraph 2.1**). This explanation is corroborated by theoretical work claiming that the fundamental bandgap in MAPbI<sub>3</sub> is indirect.<sup>4-6,35,36</sup> This has been attributed to collective orientations of the organic cations, which is possible in the tetragonal and cubic crystal phases due to the rotational freedom of the organic cations.<sup>4</sup> However, recent calculations of the band structure of MAPbI<sub>3</sub> have shown that Pb spin-orbit coupling results in an indirect bandgap, which is therefore also present in systems with random orientations of the organic cation.<sup>35</sup>

To further investigate these indirect transitions and to elucidate whether their origin is related to the Pb spin-orbit coupling<sup>35</sup> or the dipole moment of the organic cation,<sup>4</sup> it will be important both theoretically and experimentally to replace methylammonium with, for example, Cs<sup>+</sup>, which does not have a dipole moment. In any case, in both theoretical scenarios, the band diagrams suggest that the CBM is only slightly shifted in  $k$ -space, resulting in a manifold of momentum-allowed (direct) transitions for excitation energies close to the absorption onset. Due to the limited density of states at the CBM,<sup>35</sup>



direct transitions might dominate over indirect transitions at excitation densities higher than used in this chapter ( $> 10^{17} \text{ cm}^{-3}$ ).<sup>8</sup> To investigate whether direct or momentum-forbidden transitions dominate the absorption onset, rigorous analysis of absorption spectra, accounting for reflections and excitonic contributions,<sup>21</sup> should be performed. The direct-indirect nature of the bandgap is schematically depicted in **Figure 5.5a**. Here, the local minimum in the CB corresponding to a direct transition is denoted by  $\text{CB}_D$ . We recall here that  $\varphi\Sigma\mu$  is larger at 1.7 eV than at 2.0 eV (**Figure 5.1b**). We propose that, at an excitation energy of 1.7 eV, thermal relaxation of electrons (direct excitation) into the CBM, which forms an indirect bandgap with the VBM, is optimized with respect to relaxation in  $\text{CB}_D$ . We expect that a fraction of the electrons in  $\text{CB}_D$  ( $> 1.8 \text{ eV}$ ) recombines rapidly with VBM holes via direct (radiative) or trap-assisted recombination, resulting in a smaller  $\varphi$  than at 1.7 eV. However, a substantial fraction of electrons excited at  $> 1.8 \text{ eV}$  still relaxes into the CBM.

The direct-indirect nature of the bandgap in tetragonal  $\text{MAPbI}_3$  explains why the recombination is enhanced with increasing temperature. This is in contrast with *e.g.* GaAs with a direct bandgap,<sup>32</sup> where the second-order recombination rate is proportional to  $T^{-1.7}$ . Recombination via an indirect transition however, is assisted by phonons. As a consequence, given that there are more phonons when the temperature is raised, indirect recombination is enhanced by increasing the temperature. For direct bandgap semiconductors, the second-order recombination rate constant  $B(T)$  is proportional to  $E_g^2/(k_B T^{3/2})$ .<sup>37</sup> Thus, if  $\text{MAPbI}_3$  were a direct semiconductor, its room temperature second-order recombination rate constant of  $2.1 \times 10^{-9} \text{ cm}^3 \text{ s}^{-1}$  should actually increase to  $4.3 \times 10^{-9} \text{ cm}^3 \text{ s}^{-1}$  at 180 K instead of decreasing by almost a factor two. To further investigate the barrier for second-order recombination in  $\text{MAPbI}_3$ , we used the Arrhenius formula:

$$k = A e^{-E_{act}/k_B T} \quad (5.2)$$

to calculate the thermal activation energy  $E_{act}$  from the rate constant  $k$  and a reaction constant  $A$ . In this case, we use  $k_2(T)$  and  $E_g^2/(k_B T^{3/2})$  for  $k$  and  $A$ , respectively. We then define the ratio between  $k_2(T)$  and  $E_g^2/(k_B T^{3/2})$  as  $\zeta(T)$ , which is plotted against  $1/T$  in **Figure 5.5b**. From the linear slope of  $\ln(\zeta(T))$  versus reciprocal temperature, we obtained an activation energy of  $47.0 \pm 1.2 \text{ meV}$  for second-order electron-hole recombination. Interestingly, this is on the same order of magnitude as the  $20 \text{ meV}^4$  to  $75 \text{ meV}^{35}$  difference between the direct and indirect bandgaps predicted from theoretical calculations of the band structure. Therefore, thermal energy might assist the release of electrons back into the  $\text{CB}_D$  where these undergo rapid recombination with holes in the VBM.

Finally, considering the fast decay of mobile charges in the orthorhombic phase, it is clear that the dominant recombination pathways are different from the tetragonal phase. A possible scenario for explaining the rapid immobilization of charges in the

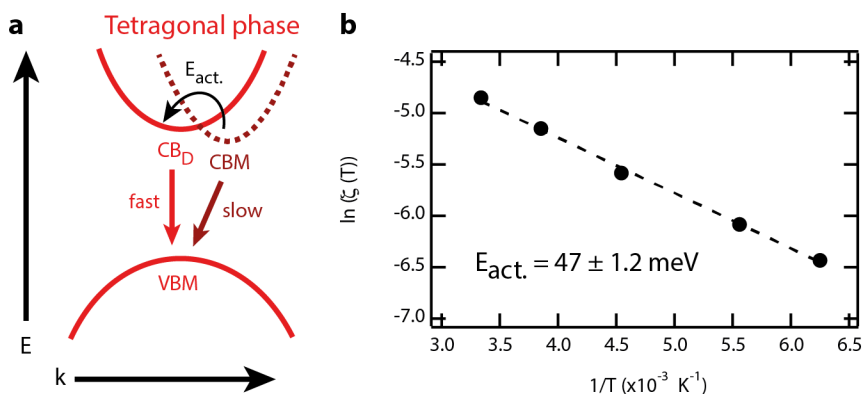


**Figure 5.5.** (a) Proposed band diagram for the tetragonal phase. Here, the conduction band minimum (CBM) is slightly shifted in  $k$ -space with respect to the valence band maximum (VBM), making the fundamental band gap indirect. The local minimum in the CB corresponding to a direct transition is denoted by  $CB_D$ . (b) Arrhenius plot of the pre-factor  $\xi(T)$ <sup>39</sup> defined as the ratio between the  $k_2(T)$ , obtained from fitting the experimental TRMC traces for  $160\text{ K} < T < 300\text{ K}$  (see **Figure A5.12** in **Appendices**), and the theoretical second-order recombination rate  $B(T)$ .<sup>37</sup> The slope of the linear fit (dotted line) indicates that the activation energy for second-order recombination is  $47 \pm 1.2\text{ meV}$ . Therefore, thermal energy ( $k_B T$ ) might assist in the release of electrons from CBM to  $CB_D$ , which is schematically depicted in (a).

orthorhombic phase is the presence of domains that remain in the tetragonal phase even at low temperature, which could act as efficient recombination centers due to the smaller bandgap.<sup>38</sup> Finally, it is also possible that the orthorhombic lattice does not allow for the formation of an indirect bandgap, if the latter is related to orientational freedom of the organic cations.<sup>4</sup>

## 5.4 Conclusions

In this chapter, we used TRMC and PL to investigate the charge carrier dynamics in tetragonal and orthorhombic MAPbI<sub>3</sub>. Most importantly, we find that in the tetragonal phase, second-order recombination of mobile electrons and holes occurs via a non-allowed transition, reminiscent of a semiconductor with an indirect bandgap. An activation energy of  $47.0 \pm 1.2\text{ meV}$  was found, which is on the same order of magnitude as the difference between the direct and indirect bandgaps predicted from theoretical calculations of the band structure. Additionally, we find that the photoconductance, reaches maximum values upon excitation at  $1.7\text{ eV}$ . This is attributed to direct excitation from the VB into the CBM, which forms an indirect bandgap with the VBM. This model also explains why second-order recombination is enhanced with temperature, which is in contrast with other bulk semiconductors such as GaAs.<sup>32</sup> These effects are not observed in the orthorhombic phase of MAPbI<sub>3</sub>, in which the majority of the carriers decays rapidly.



## 5.5 Experimental Methods

### Film preparation

Glass substrates were washed sequentially with soap, de-ionized water, isopropanol, acetone and finally treated under oxygen plasma for 10 minutes. Thin films of MAPbI<sub>3</sub> were solution-processed by employing a methylammonium iodide (MAI) and lead acetate Pb(Ac)<sub>2</sub>·3H<sub>2</sub>O precursor mixture. MAI (Dyesol) and Pb(Ac)<sub>2</sub>·3H<sub>2</sub>O (Sigma-Aldrich) were dissolved in anhydrous *N,N*-dimethylformamide at a 3:1 molar ratio with final concentration of 37 wt%. The precursor solution was spin-coated at 2000 rpm for 45 seconds in a nitrogen-filled glovebox, and the substrates were then dried at room temperature for 10 minutes before annealing at 100°C for 5 minutes. For the meso-structured samples, mesoporous alumina layers of ~400 nm were formed by spin-coating a solution of ~20 nm alumina nanoparticles in propan-2-ol on glass and drying at 150 °C. A diluted version (30 wt%) of the same acetate precursor solution was then spin-coated onto the mesoporous film at 2000 rpm for 45 seconds in a nitrogen-filled glovebox and the film dried at room temperature for 10 minutes before annealing at 100°C for 5 minutes. For the PbI<sub>2</sub>-based samples, the ‘dripping’ technique was employed. Here, an equimolar (0.75 M, total 45 wt%) solution of MAI (Dyesol) and PbI<sub>2</sub> (Alfa Aesar) was prepared in DMF and spin-cast at 5000 rpm for 35 s. After 6 s, 150 µL chlorobenzene was deposited on the spinning sample in order to induce rapid crystallization. After spinning, the samples were immediately heated at 100 °C for 10 minutes. All samples were then stored in a nitrogen-filled glovebox until used.

### X-Ray Diffraction

X-Ray Diffractograms were collected from MAPbI<sub>3</sub> thin films on boron-doped Si(100) substrates using PANalytical X’Pert Pro Multi-Purpose Diffractometer operated at 40 kV and 40 mA (Cu K-alpha radiation- 1.5418 Å) in Bragg-Brentano geometry. An Oxford Cryosystems PheniX Cryostat was employed for low temperature measurements.

### Optical Characterization

Absorption and transmission spectra were recorded according to the methods described in **Chapter 3**. To obtain the low-temperature absorption spectrum, the MAPbI<sub>3</sub> film was placed in a cryostat and the transmission was measured using an Ocean Optics USB2000+ spectrometer.  $F_A$  was calculated from **Equation 2.6**, thereby neglecting possible temperature dependence of  $F_R$ . For the temperature-dependent TRPL measurements the samples were placed in a nitrogen-filled cryostat, and PL emission spectra and PL lifetimes at the maximum emission wavelength were recorded as described in **Chapter 3**.

### Photoconductivity measurements

The TRMC technique was used to the photoconductance as function of temperature for excitation wavelengths from 518 nm (2.4 eV) to 828 nm (1.5 eV), as described in **Chapters 2 and 3**. The laser intensity,  $I_0$ , was determined using a Coherent power meter with an adjustable detection range. The inaccuracy of determination of  $I_0$  due to fluctuations of the laser is approximately  $\pm 0.1$  mJ, which is taken into account in the error analysis of the data.

### Pulse-radiolysis TRMC measurements

Four substrates each covered with ~75 cm<sup>2</sup> MAPbI<sub>3</sub> (thickness ~ 250 nm) were used to scratch off 35 mg of material, which was placed in a polyether ether ketone (PEEK) holder. To protect the MAPbI<sub>3</sub> from moisture and air, it was covered with poly-methyl-methacrylate (PMMA), drop-casted from a 10 mg/mL PMMA/chlorobenzene solution. Pulse-radiolysis TRMC (PR-TRMC) measurements involve the generation of charge carriers through irradiation by a short pulse of high-energy electrons (3 MeV) and the monitoring of the changes in conductivity due to mobile charge carriers using high frequency microwaves (28-38 GHz).<sup>22,40</sup> The conductivity transients shown were obtained at 32 GHz. Similar to the photon-induced TRMC, the change of conductivity is proportional to the absorbed microwave power:

$$\frac{\Delta P}{P} = A \Delta \sigma \quad (5.3)$$

The experimental frequency dependence of  $\Delta P/P$  can be fitted with an analytical expression to determine the dielectric constant,  $\epsilon$ , and change in conductivity,  $\Delta \sigma$ .<sup>40</sup> The mobility is then calculated by:

$$\Delta \sigma = e \sum N_p(0) \mu \quad (5.4)$$

Where  $N_p(0)$  is the initial concentration of charge carriers at the end of the pulse and  $\mu$  the sum of the mobilities for electrons and holes.  $N_p(0)$  is a function of the mass of material ( $m$ ), volume of the sample holder ( $V_{sh}$ ), irradiation energy deposited in the sample ( $D$ ) and of the radiation-ionization energy required for the generation of an electron-hole pair ( $E_p$ ):

$$N_p(0) = \frac{D}{E_p * 1.6 * 10^{-19} \frac{J}{eV}} \frac{m}{V_{sh}} \quad (5.5)$$

$D$  is proportional to the electron density of the material and for perovskites has been determined to be  $\sim 1$  J/Kg/nC.<sup>23</sup> The latter is derived from previous radiation dosimetry experiments.  $E_p$  has been determined according to Klein's theoretical model<sup>41</sup> and Alig's equation<sup>42</sup> for semiconductor materials, which relates it to the bandgap of the material, phonon losses and the residual kinetic energy:

$$E_p = 2.73 E_g + 0.55 [eV] \quad (5.6)$$

In the PR-TRMC set up, the cell is contained in a cryostat in which the temperature can be varied between  $-150^\circ\text{C}$  and  $200^\circ\text{C}$ . The temperature was maintained for  $\sim 15$  min before doing the actual measurement in order to assure the equilibrium of the system. The overall time response of the set-up is limited by the rise time of the detector diode and the length of the excitation pulse ( $\sim 1$  ns). The frequency scans (28-38 GHz) were measured at a pulse length of 200 ps, corresponding to an initial charge carrier concentration of  $4.7 \times 10^{14} \text{ cm}^{-3}$ .

## 5.6 References

1. Green, M. A., Ho-Baillie, A. & Snaith, H. J. The emergence of perovskite solar cells. *Nat. Photonics* **8**, 506–514 (2014).
2. Grundmann, M. *The Physics of Semiconductors: An Introduction Including Devices and Nanophysics*. Springer (2006).
3. Even, J., Pedesseau, L., Jancu, J. M. & Katan, C. DFT and k p modelling of the phase transitions of lead and tin halide perovskites for photovoltaic cells. *Phys. Status Solidi - Rapid Res. Lett.* **8**, 31–35 (2014).
4. Motta, C. *et al.* Revealing the role of organic cations in hybrid halide perovskite  $\text{CH}_3\text{NH}_3\text{PbI}_3$ . *Nat. Commun.* **6**, 7026 (2015).
5. Zheng, F., Tan, L. Z., Liu, S. & Rappe, A. M. Rashba spin-orbit coupling enhanced carrier lifetime in  $\text{CH}_3\text{NH}_3\text{PbI}_3$ . *Nano Lett.* **15**, 7794–7800 (2015).
6. Etienne, T., Mosconi, E. & De Angelis, F. Dynamical Origin of the Rashba Effect in Organohalide Lead

- Perovskites: A Key to Suppressed Carrier Recombination in Perovskite Solar Cells? *J. Phys. Chem. Lett.* **7**, 1638–1645 (2016).
7. D’Innocenzo, V. *et al.* Excitons versus free charges in organo-lead tri-halide perovskites. *Nat. Commun.* **5**, 3586 (2014).
  8. Milot, R. L., Eperon, G. E., Snaith, H. J., Johnston, M. B. & Herz, L. M. Temperature-Dependent Charge-Carrier Dynamics in  $\text{CH}_3\text{NH}_3\text{PbI}_3$  Perovskite Thin Films. *Adv. Funct. Mater.* **25**, 6218–6227 (2015).
  9. Wang, H., Whittaker-Brooks, L. & Fleming, G. R. Exciton and Free Charge Dynamics of Methylammonium Lead Iodide Perovskites Are Different in the Tetragonal and Orthorhombic Phases. *J. Phys. Chem. C* **119**, 19590–19595 (2015).
  10. Miyata, A. *et al.* Direct measurement of the exciton binding energy and effective masses for charge carriers in organic-inorganic tri-halide perovskites. *Nat. Phys.* **11**, 582–587 (2015).
  11. Even, J., Pedesseau, L., Jancu, J.-M. & Katan, C. Importance of Spin–Orbit Coupling in Hybrid Organic/Inorganic Perovskites for Photovoltaic Applications. *J. Phys. Chem. Lett.* **4**, 2999–3005 (2013).
  12. Savenije, T. J. *et al.* Thermally Activated Exciton Dissociation and Recombination Control the Carrier Dynamics in Organometal Halide Perovskite. *J. Phys. Chem. Lett.* **5**, 2189–2194 (2014).
  13. Stranks, S. D. *et al.* Recombination Kinetics in Organic-Inorganic Perovskites: Excitons, Free Charge, and Subgap States. *Phys. Rev. Appl.* **2**, 34007 (2014).
  14. Zhang, W. *et al.* Ultrasoft organic-inorganic perovskite thin-film formation and crystallization for Efficient Planar Heterojunction Solar Cells. *Nat. Commun.* **6**:6142, (2015).
  15. Savenije, T. J., Ferguson, A. J., Kopidakis, N. & Rumbles, G. Revealing the dynamics of charge carriers in polymer:fullerene blends using photoinduced time-resolved microwave conductivity. *J. Phys. Chem. C* **117**, 24085–24103 (2013).
  16. Park, J., Reid, O. G., Blackburn, J. L. & Rumbles, G. Photoinduced spontaneous free-carrier generation in semiconducting single-walled carbon nanotubes. *Nat. Commun.* **6**, 8809 (2015).
  17. Kroeze, J. E., Savenije, T. J., Vermeulen, M. J. W. & Warman, J. M. Contactless Determination of the Photoconductivity Action Spectrum, Exciton Diffusion Length, and Charge Separation Efficiency in Polythiophene-Sensitized  $\text{TiO}_2$  Bilayers. *J. Phys. Chem. B* **107**, 7696–7705 (2003).
  18. Dong, Q. *et al.* Electron-hole diffusion lengths > 175  $\mu\text{m}$  in solution-grown  $\text{CH}_3\text{NH}_3\text{PbI}_3$  single crystals. *Science* **347**, 967–970 (2015).
  19. Guse, J. A. *et al.* Spectral Dependence of Direct and Trap-Mediated Recombination Processes in Lead Halide Perovskites using Time Resolved Microwave Conductivity. *Phys. Chem. Chem. Phys.* **18**, 12043–12049 (2016).
  20. Saba, M. *et al.* Correlated electron–hole plasma in organometal perovskites. *Nat. Commun.* **5**:5049, (2014).
  21. Saba, M., Quochi, F., Mura, A. & Bongiovanni, G. Excited State Properties of Hybrid Perovskites. *Acc. Chem. Res.* **49**, 166–173 (2016).
  22. Grozema, F. C. & Siebbeles, L. D. A. Charge mobilities in conjugated polymers measured by pulse radiolysis time-resolved microwave conductivity: From single chains to solids. *J. Phys. Chem. Lett.* **2**, 2951–2958 (2011).
  23. Gélvez-Rueda, M. C. *et al.* Effect of Cation Rotation on Charge Dynamics in Hybrid Lead Halide Perovskites. *J. Phys. Chem. C* **120**, 16577–16585 (2016).
  24. Osherov, A. *et al.* The Impact of Phase Retention on the Structural and Optoelectronic Properties of Metal Halide Perovskites. *Adv. Mater.* **28**, 10757–10763 (2016).
  25. Wehrenfennig, C., Liu, M., Snaith, H. J., Johnston, M. B. & Herz, L. M. Charge carrier recombination channels in the low-temperature phase of organic-inorganic lead halide perovskite thin films. *APL Mater.* **2**, 81513 (2014).
  26. Johnston, M. B. & Herz, L. M. Hybrid Perovskites for Photovoltaics: Charge-Carrier Recombination, Diffusion, and Radiative Efficiencies. *Acc. Chem. Res.* **49**, 146–154 (2016).
  27. Fang, H. H. *et al.* Photophysics of organic-inorganic hybrid lead iodide perovskite single crystals. *Adv. Funct. Mater.* **25**, 2378–2385 (2015).
  28. Karakus, M. *et al.* Phonon-Electron Scattering Limits Free Charge Mobility in Methylammonium Lead Iodide Perovskites. *J. Phys. Chem. Lett.* **6**, 4991–4996 (2015).
  29. Wu, K. *et al.* Temperature-dependent excitonic photoluminescence of hybrid organometal halide perovskite films. *Phys. Chem. Chem. Phys.* **16**, 22476–22481 (2014).
  30. Hutter, E. M., Eperon, G. E., Stranks, S. D. & Savenije, T. J. Charge Carriers in Planar and Meso-Structured Organic-Inorganic Perovskites: Mobilities, Lifetimes and Concentrations of Trap States. *J. Phys. Chem. Lett.* **6**, 3082–3090 (2015).
  31. Bi, Y. *et al.* Charge Carrier Lifetimes Exceeding 15 Microseconds in Methylammonium Lead Iodide Single Crystals. *J. Phys. Chem. Lett.* **7**, 923–928 (2016).
  32. ’t Hooft, G. W. & van Opdorp, C. Temperature dependence of interface recombination and radiative

- recombination in (Al, Ga)As heterostructures. *Appl. Phys. Lett.* **42**, 813–815 (1983).
33. Ponceca Jr, C. S. *et al.* Mechanism of Charge Transfer and Recombination Dynamics in Organo Metal Halide Perovskites and Organic Electrodes, PCBM, and Spiro-OMeTAD: Role of Dark Carriers. *J. Am. Chem. Soc.* **137**, 16043–16048 (2015).
34. Hutter, E. M. *et al.* Charge Transfer from Methylammonium Lead Iodide Perovskite to Organic Transport Materials: Efficiencies, Transfer Rates, and Interfacial Recombination. *Adv. Energy Mater.* **7**, 1602349 (2017).
35. Azarhoosh, P. *et al.* Relativistic origin of slow electron-hole recombination in hybrid halide perovskite solar cells. *APL Mater.* **4**, 91501 (2016).
36. Wang, T. *et al.* Indirect to direct bandgap transition in methylammonium lead halide perovskite. *Energy Environ. Sci.* **10**, 509–515 (2017).
37. Gfroerer, T. H., Priestley, L. P., Weindruch, F. E. & Wanlass, M. W. Defect-related density of states in low-band gap In<sub>x</sub>Ga<sub>1-x</sub>As/InAs<sub>y</sub>P<sub>1-y</sub> double heterostructures grown on InP substrates. *J. Appl. Phys.* **94**, 1738–1743 (2003).
38. Kong, W. *et al.* Characterization of an abnormal photoluminescence behavior upon crystal-phase transition of perovskite CH<sub>3</sub>NH<sub>3</sub>PbI<sub>3</sub>. *Phys. Chem. Chem. Phys.* **17**, 16405–16411 (2015).
39. Ferguson, A. J., Kopidakis, N., Shaheen, S. E. & Rumbles, G. Dark carriers, trapping, and activation control of carrier recombination in Neat P3HT and P3HT:PCBM blends. *J. Phys. Chem. C* **115**, 23134–23148 (2011).
40. Warman, J. M. *et al.* Charge Mobilities in Organic Semiconducting Materials Determined by Pulse-Radiolysis Time-Resolved Microwave Conductivity:  $\pi$ -Bond-Conjugated Polymers versus  $\pi$ - $\pi$ -Stacked Discotics. *Chem. Mater.* **16**, 4600–4609 (2004).
41. Klein, C. A. Bandgap Dependence and Related Features of Radiation Ionization Energies in Semiconductors. *J. Appl. Phys.* **39**, 2029–2038 (1968).
42. Alig, R. C. & Bloom, S. Electron-hole-pair creation energies in semiconductors. *Phys. Rev. Lett.* **35**, 1522–1525 (1975).

## Appendices

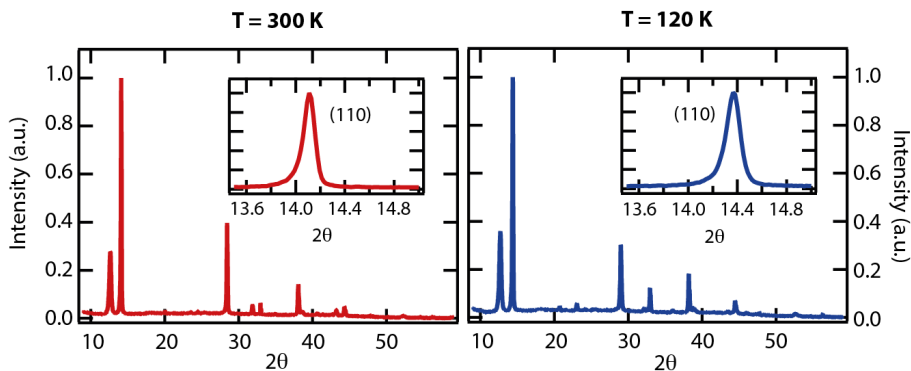


**Figure A5.1:** X-ray diffraction (XRD) patterns of a MAPbI<sub>3</sub> thin film deposited on boron-doped Si(100) substrates, recorded at 300 K (left) and 120 K (right). The (110) reflections are magnified in the inset.

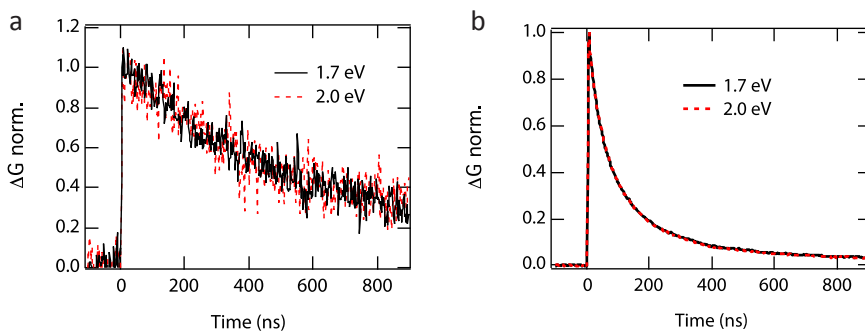


**Figure A5.2:** Normalized photoconductance as function of time after excitation at 2.0 eV (red) and 1.7 eV (black) at  $T = 300 \text{ K}$  for an absorbed photon fluence of  $1.1 \times 10^{10} \text{ cm}^{-2}$  (a) and  $1.6 \times 10^{12} \text{ cm}^{-2}$  (b) per pulse. Note that this photon fluences are respectively one and three orders of magnitude higher than for the traces shown in **Figure 5.1** in the main text.

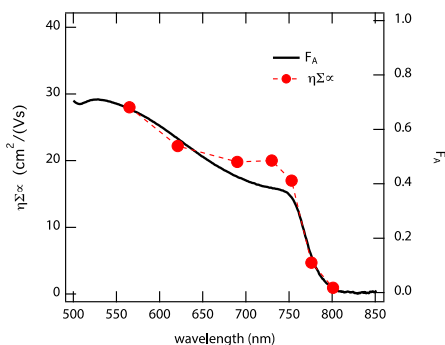


**Figure A5.3:** Excitation-dependent photoconductance for  $2 \times 10^{10}$  absorbed photons/ $\text{cm}^2$  per pulse, which corresponds to a charge carrier density of  $8 \times 10^{14} \text{ cm}^{-3}$ . This is higher than the fluence of  $8 \times 10^8$  absorbed photons/ $\text{cm}^2$  per pulse shown in **Figure 5.1b** in the main text.

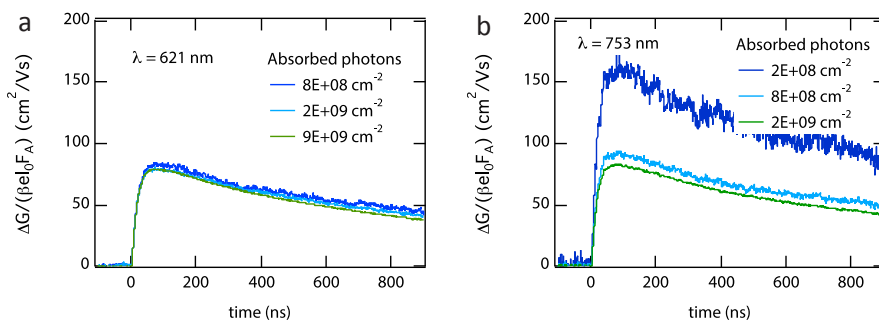


**Figure A5.4:** Photoconductance as function of time after excitation at 753 nm (1.65 eV) for different fluences of absorbed photons, where  $8 \times 10^8$  absorbed photons/ $\text{cm}^2$  per pulse corresponds to the data presented in **Figure 5.1**. The maximum height of the signals represents  $\phi \Sigma \mu$ , the product of generation yield and mobility (sum of electrons and holes). These results show that the peaking  $\phi \Sigma \mu$  for exciting at 1.65 eV is even more pronounced at a fluence of  $2 \times 10^8$  absorbed photons/ $\text{cm}^2$  ( $8 \times 10^{12}$  charge carriers  $\text{cm}^{-3}$ ) per pulse. At this density, the effective mobility is in excess of  $150 \text{ cm}^2/(\text{Vs})$ .

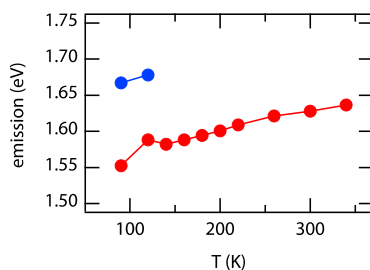


**Figure A5.5:** Maximum emission wavelength as function of temperature for tetragonal (red) and orthorhombic (blue) MAPbI<sub>3</sub>.

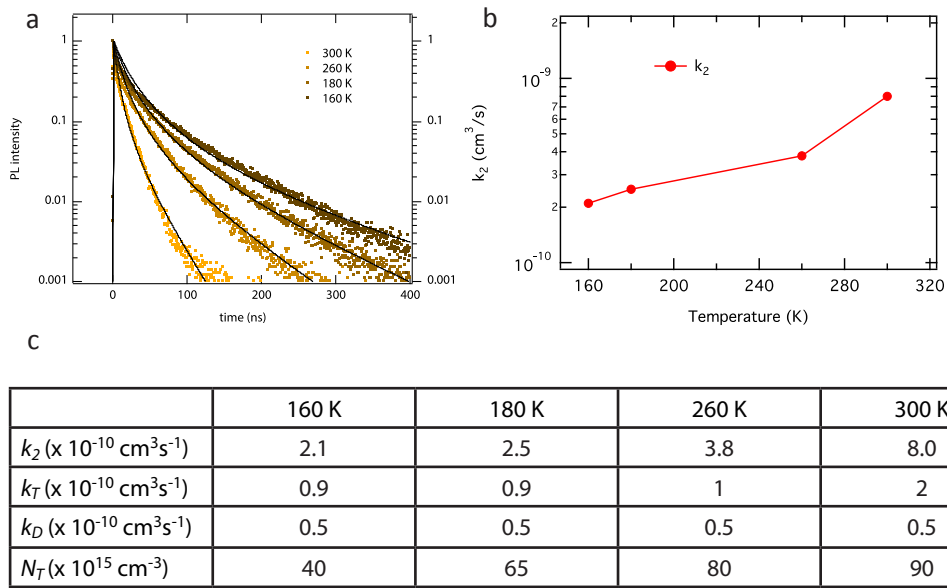


**Figure A5.6:** (a) Temperature-dependent TRPL for a MAPbI<sub>3</sub> film prepared from PbI<sub>2</sub>. (b)  $k_2$  obtained from fitting the data from (a). (c) Kinetic parameters obtained from fitting the data shown in (a).

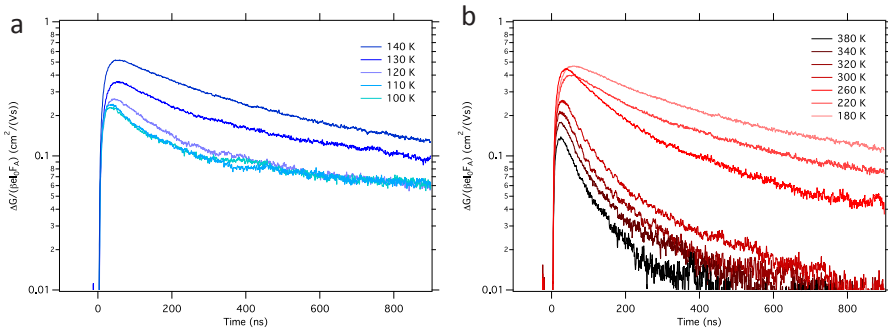


**Figure A5.7:** Temperature-dependent photoconductance in meso-structured MAPbI<sub>3</sub> prepared from PbAc<sub>2</sub> for the orthorhombic (a) and tetragonal (b) phase.

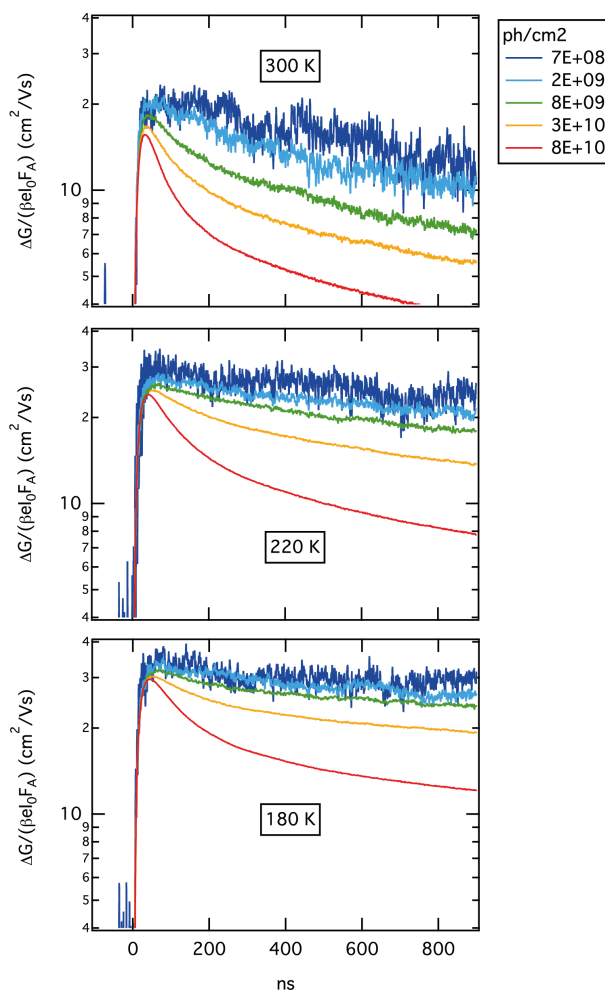


**Figure A5.8:** Photoconductance at 300 K, 220 K and 180 K in a MAPbI<sub>3</sub> film prepared from PbI<sub>2</sub> for various incident photon fluences.



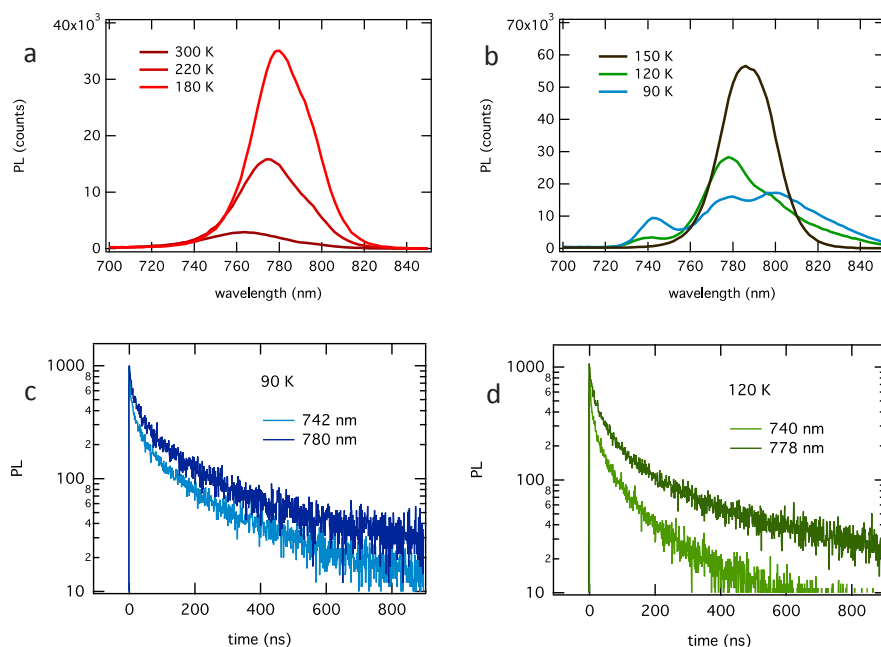


**Figure A5.9:** Emission spectra at 180, 220 and 300 K (a) and 150, 120 and 90 K (b). TRPL decays recorded at the wavelengths corresponding to the emission peaks centered at 742 and 780 nm (90 K, c) and 740 nm (120 K, d).

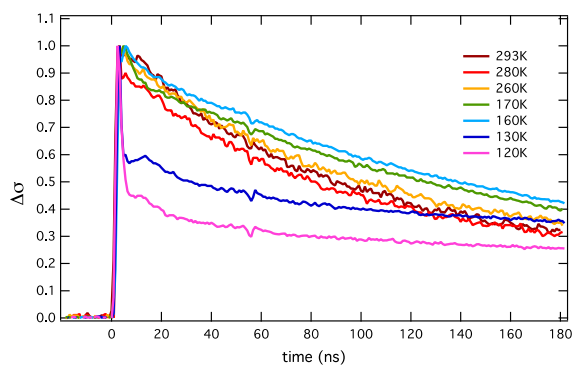


**Figure A5.10:** Pulse-radiolysis TRMC lifetimes for tetragonal (160 to 293 K) and orthorhombic (120 and 130 K) MAPbI<sub>3</sub>.

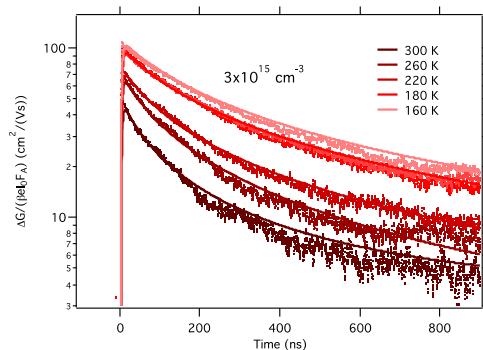


**Figure A5.11:** Experimental temperature-dependent photoconductance, together with the fits (solid lines) obtained by using the kinetic model detailed in **Chapter 2**, using the parameters listed in **Table 5.1** and  $k_2 = 1 \times 10^{-9} \text{ cm}^3 \text{ s}^{-1}$ ,  $k_T = 3 \times 10^{-10} \text{ cm}^3 \text{ s}^{-1}$ ,  $k_D = 5 \times 10^{-11} \text{ cm}^3 \text{ s}^{-1}$ ,  $N_T = 1.5 \times 10^{15} \text{ cm}^{-3}$  for  $T = 160 \text{ K}$ .

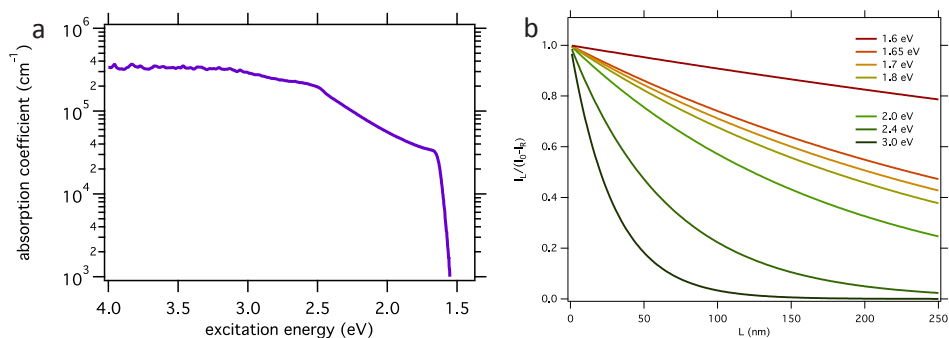
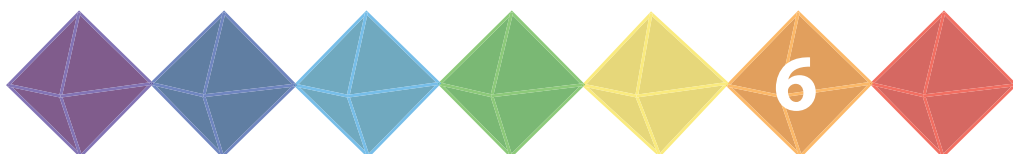


**Figure A5.12:** (a) Absorption coefficient ( $\text{cm}^{-1}$ ) as function of excitation energy. (b) Light absorption profile as function of excitation energy, showing that the homogeneity of the initial charge distribution is not the origin of the peak at 1.7 eV since the penetration depth is similar to 1.8 and 1.65 eV.



# The Role of the Monovalent Cation on the Recombination Kinetics in Lead Iodide Perovskites



## ABSTRACT

The relationship between the organic nature of the cation and the optoelectronic quality of MAPbI<sub>3</sub> has remained debated. In this chapter, we investigate the optoelectronic properties of fully inorganic vapour-deposited and spin-coated black phase CsPbI<sub>3</sub> thin films. Using the TRMC technique, we measure charge carrier mobilities up to 25 cm<sup>2</sup>/(Vs) and charge carrier lifetimes exceeding 10 μs for vapour-deposited CsPbI<sub>3</sub>, while the carrier lifetime reaches less than 0.2 μs in the spin-coated samples. Additionally, for the high quality vapour-deposited CsPbI<sub>3</sub> films, we find that the second-order recombination is retarded on lowering the temperature, similar as we observed for MAPbI<sub>3</sub>. Altogether, these results suggest that charge carrier mobility and recombination lifetime are mainly dictated by the inorganic framework rather than the organic nature of the cation. Finally, on studying a number of mixed-cation perovskites, we find that in fact, the charge carrier mobilities and lifetimes are favorably tuned by adding controlled amounts of inorganic cations, such as Cs and Rb, to metal halide perovskites with organic cations.

### Partially based on

Eline M. Hutter, Rebecca J. Sutton, Sanjana Chandrashekar, Mojtaba Abdi-Jalebi, Samuel D. Stranks, Henry J. Snaith and Tom J. Savenije, Vapour-Deposited Cesium Lead Iodide Perovskites: Microsecond Charge Carrier Lifetimes and Enhanced Photovoltaic Performance, *ACS Energy Letters*, 2017, 2, 1901-1908

Yinghong Hu, Eline M. Hutter, Philipp Rieder, Irene Grill, Meltem F. Aygüler, Alexander G. Hufnagel, Matthias Handloser, Thomas Bein, Achim Hartschuh, Kristofer Tvingstedt, Vladimir Dyakonov, Andreas Baumann, Tom J. Savenije, Michiel L. Petrus, Pablo Docampo, Understanding the Role of Cesium and Rubidium Additives in Perovskite Solar Cells: Trap states, Charge Transport and Recombination, *Advanced Energy Materials*, 2018, 1703057

## 6.1 Introduction

The rotational freedom of the dipolar organic cation in MAPbI<sub>3</sub> has been a topic of interest,<sup>1,2</sup> and was proposed to play a key role in properties of MHPs.<sup>2–5</sup> For instance, it was suggested that electron mobility is driven by dynamic disorder of the MA,<sup>3</sup> and that MHPs owe their unique band structure to collective orientations of MA.<sup>2,4,5</sup> Although optoelectronic properties have been correlated to the orientation of the organic cation,<sup>6</sup> there has still been a lack of experimental work truly revealing the interplay between the organic cation and the fundamental properties of MHPs.<sup>7,8</sup> To this end, replacement of MA with inorganic cesium (Cs) ions is crucial to separate the role of the cation's dipole moment from that of the lead iodide framework.<sup>9</sup> Although mixed-cation perovskites comprising multiple cations can be easily made,<sup>10,11</sup> fully replacing the organic cation with Cs<sup>+</sup> has been experimentally challenging because Cs-based precursors are only poorly soluble in solvents typically used for solution-processing. Additionally, a yellow non-perovskite structure is the stable phase of CsPbI<sub>3</sub> at room temperature.<sup>12–14</sup> However, it was shown that the black perovskite phase of CsPbI<sub>3</sub> can be obtained as a metastable phase at room temperature,<sup>12,13</sup> and that solar cells with efficiencies close to 10% can be obtained using CsPbI<sub>3</sub> produced by co-evaporation of its precursors under vacuum.<sup>15</sup> This improved quality of bulk CsPbI<sub>3</sub> perovskites has opened up the possibility to study their optoelectronic properties and finally enables a rational comparison to their MA-containing analogues.

In this chapter, we use TRMC measurements to investigate the charge carrier dynamics in polycrystalline CsPbI<sub>3</sub> thin films prepared using vapour deposition and different solution-based routes. As shown in **Chapter 4**, vapour deposition is an ideal method to prepare model systems of lead halide perovskites,<sup>16–18</sup> since the film thickness can be precisely tuned and the resulting samples show reproducible quality. We find that the charge carrier mobilities in vapour-deposited polycrystalline CsPbI<sub>3</sub> films reach values around 25 cm<sup>2</sup>/(Vs), which is very similar to values of lead iodide perovskites containing an organic cation such as MA or formamidinium (FA).<sup>16,19</sup> Furthermore, we observe charge carrier lifetimes of several  $\mu$ s in the vapour-deposited CsPbI<sub>3</sub> films, while both electrons and holes are immobilized within tens of ns for their spin-coated analogues. We attribute this difference to a significantly higher defect density of the latter, acting as traps to mobile charge carriers. The extended charge carrier lifetime of vapour-deposited CsPbI<sub>3</sub> is further reflected in enhanced photovoltaic performance with respect to their spin-coated analogues. Importantly, the improved quality of these CsPbI<sub>3</sub> perovskites prepared by physical vapour deposition enabled us to study the second-order recombination as function of temperature. Interestingly, we find that also in fully inorganic CsPbI<sub>3</sub>, second-order recombination is thermally activated, which suggests that the direct-indirect character of the bandgap is not unique to MA-based perovskites, but rather related to the lead iodide framework.

In spite of its promising optoelectronic properties and enhanced thermal stability, fully inorganic CsPbI<sub>3</sub> perovskites suffer from inferior crystal-phase stability and thus, the presence of organic cations might still be required for production of stable,

high-efficiency solar cells. A possible route towards thermally and crystal-structure stable perovskites are MHPs comprising a mixture of different organic and inorganic cations, taking advantage of each of the cations. Starting from the mixed-organic-cation  $\text{FA}_{0.83}\text{MA}_{0.17}\text{Pb}(\text{I}_{0.83}\text{Br}_{0.17})_3$  perovskite, we find that the addition of  $\text{Cs}^+$  and rubidium ( $\text{Rb}^+$ ) actually improves both the charge carrier mobility and lifetime. From here, we conclude that although the presence of organic cations in MHPs improves its phase-stability, it might not necessarily be beneficial for charge carrier transport.

## 6.2 Fully inorganic $\text{CsPbI}_3$ perovskites

Thin  $\text{CsPbI}_3$  films of varying thicknesses were prepared using vapour deposition of its precursors. Specifically,  $\text{CsI}$  and  $\text{PbI}_2$  powders were heated to their sublimation temperatures under vacuum (see experimental section for more details). Although our approach is similar to previously reported co-evaporation methods,<sup>15,17,18</sup> we build up the  $\text{CsPbI}_3$  film in a very controlled fashion by alternating the deposition of thin  $\text{CsI}$  ( $\sim 2$  nm) and  $\text{PbI}_2$  ( $\sim 2.5$  nm) layers until the desired thickness is obtained.<sup>16</sup> The absorption spectrum of an as-deposited film on quartz is shown in **Figure 6.1a**. A relatively weak onset is found below 750 nm (1.66 eV), with a steep rise in absorption at 520 nm (2.39 eV). These results suggest that a mixture of yellow (non-perovskite) and black (perovskite)  $\text{CsPbI}_3$  has formed during the deposition. That is, while its yellow phase is most stable up to 310 °C,<sup>12</sup> the black perovskite phase of  $\text{CsPbI}_3$  is only metastable at room temperature.<sup>13</sup> In order to induce the yellow-to-black phase transition, the as-deposited films were annealed to 310 °C in a nitrogen-filled glovebox until these turned black. Then, the  $\text{CsPbI}_3$  films were rapidly cooled to room temperature on a metal surface to ‘freeze’ the crystals in the black phase. We note that while this black phase is highly unstable under ambient conditions, it can be maintained for at least a few days under nitrogen. Therefore, to prevent conversion back to the yellow non-perovskite phase, the samples were not exposed to air at any time before and during the optoelectronic characterization.

The red line in **Figure 6.1a** shows the absorption spectrum of the  $\text{CsPbI}_3$  film after annealing, which shows a sharp onset around 730 nm (1.70 eV), consistent with conversion to the black phase. The annealed films show an emission peak centered at 727 nm (1.71 eV), see dotted lines in **Figure 6.1a**. Initially, the as-deposited layers are composed of relatively small grains ( $< 50$  nm), which increase in size up to a few microns upon annealing (**Figure A6.1**). We used the absorption and transmission spectra, recorded using an integrating sphere, of the 260-nm thick  $\text{CsPbI}_3$  film to determine its wavelength-dependent absorption coefficient  $\alpha$  (see also **Chapter 2**). The results are shown in **Figure 6.1b**, in which the  $\alpha$  of  $\text{MAPbI}_3$  is added for comparison. This shows that the  $\alpha$  of  $\text{CsPbI}_3$  steeply rises below 730 nm until a value of  $4 \times 10^4 \text{ cm}^{-1}$  is reached, after which it increases gradually to  $2 \times 10^5 \text{ cm}^{-1}$  at 400 nm (3.11 eV). Similar to  $\text{MAPbI}_3$ , these values are relatively high,<sup>20</sup> so that thin ( $\sim 300$  nm) layers of  $\text{CsPbI}_3$  are already sufficient to absorb most of the visible light at wavelengths shorter than the excitonic absorption peak.

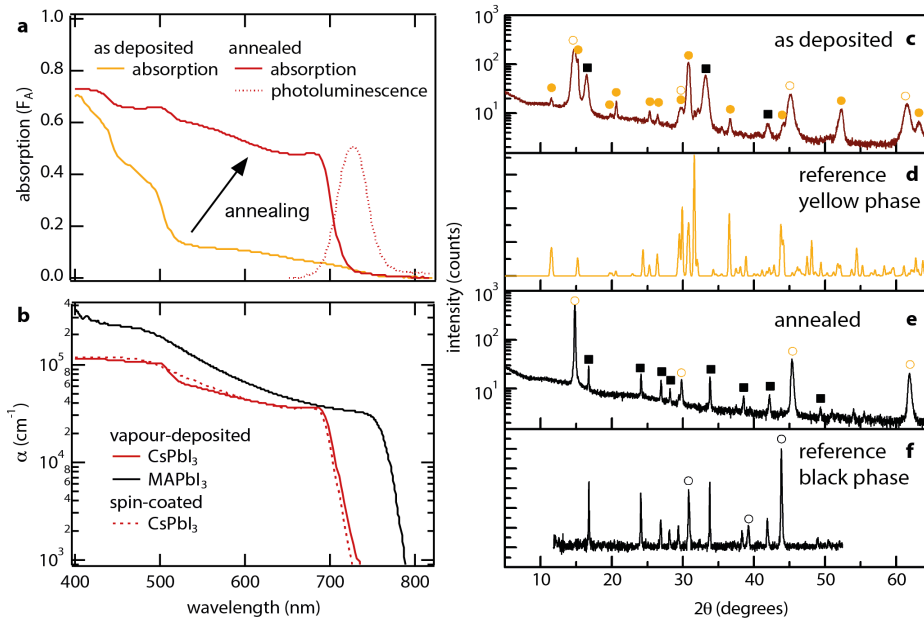


**Figure 6.1:** (a) Fraction of absorbed photons ( $F_A$ ) as function of excitation wavelength for a thin (260 nm) vapour-deposited  $\text{CsPbI}_3$  film before (yellow) annealing and absorption (red, solid line) and emission spectra (red, dotted line) after annealing. (b) Wavelength-dependent absorption coefficient (red) of  $\text{CsPbI}_3$ , calculated using the transmission and absorption spectra for a vapour-deposited (solid line) and spin-coated (dotted line) film. The absorption coefficient of vapour-deposited  $\text{MAPbI}_3$  (black line, data from Ref. 16) is added for comparison. (c-f) Background-subtracted X-ray (Co- $K\alpha$  radiation,  $\lambda = 1.79 \text{ \AA}$ ) diffraction (XRD) patterns of vapour-deposited  $\text{CsPbI}_3$  films before (c) and after (e) annealing, taken at room temperature using an air-tight sample holder. XRD patterns of the yellow non-perovskite phase at 298 K taken from Ref. 21, (d) and black perovskite phase taken from Ref. 12 (f), both simulated for a  $1.79 \text{ \AA}$  Co X-ray source. The closed yellow circles denote the yellow phase, the black squares denote the black phase, the open yellow circles denote  $\text{PbI}_2$ , the open black circles denote  $\text{SnO}_2$ .

The small absorption feature around 500 nm (2.48 eV) hints toward the presence of either  $\text{PbI}_2$  or yellow-phase  $\text{CsPbI}_3$  being left in the film after annealing. To further investigate the crystal structure and phase purity of the films, we measured X-Ray Diffraction (XRD) patterns of the films as deposited (**Figure 6.1c**) and after annealing (**Figure 6.1e**), using an airtight sample holder. The reference patterns of the yellow non-perovskite (**Figure 6.1d**)<sup>21</sup> and black perovskite (**Figure 6.1f**)<sup>12</sup> phases are added for comparison. We observe that the as-deposited film (**Figure 6.1c**) shows reflections corresponding to the black phase (denoted by squares) as well as reflections characteristic of the yellow non-perovskite phase (denoted by closed yellow circles), confirming that the absorption spectrum (**Figure 6.1a**) represents a mixture of yellow and black  $\text{CsPbI}_3$ . After annealing, the reflections corresponding to the yellow non-perovskite phase

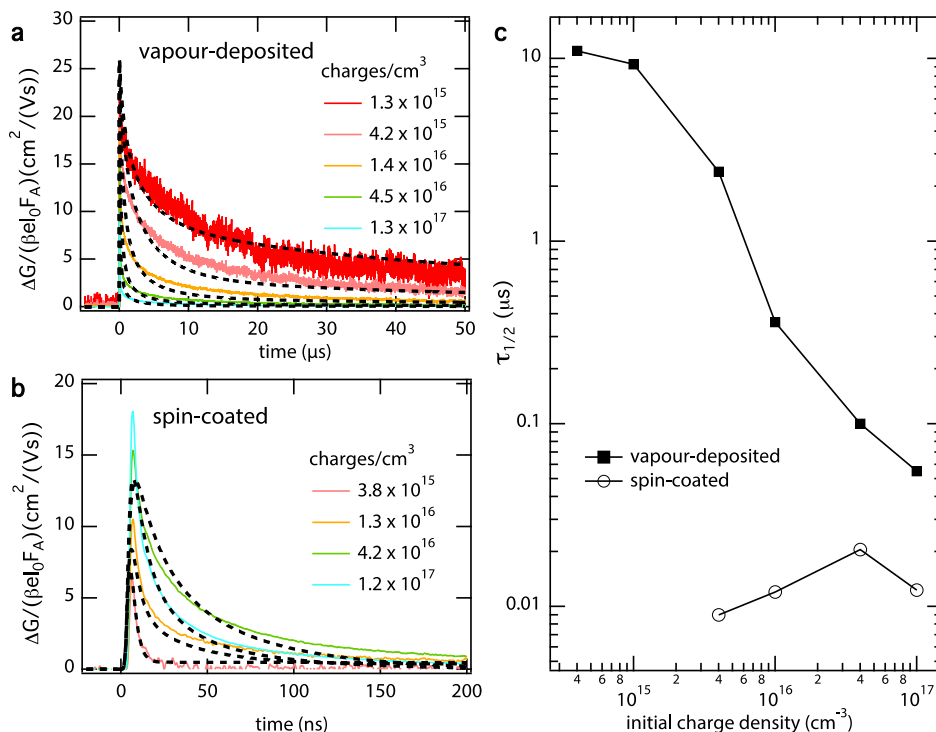


**Figure 6.2:** (a-b) Time-Resolved Microwave Conductivity (TRMC) traces for (a) a vapour-deposited CsPbI<sub>3</sub> thin film with thickness of 260 nm and (b) a 350 nm CsPbI<sub>3</sub> film spin-coated from a DMF:DMSO solution. Note that the horizontal timescales of (a) and (b) are different. An excitation wavelength of 600 nm was used, and the laser intensity was varied to generate initial charge carrier densities ranging from  $10^{15}$  to  $10^{17} \text{ cm}^{-3}$ . The dotted lines are fits to the experimental data (solid lines). (c) Half lifetime as function of the initial charge carrier density, corresponding to the CsPbI<sub>3</sub> thin films shown in (a) and (b).

are no longer present and the XRD pattern matches those reported in the literature (Figure 6.1e).<sup>12,22</sup> Additionally, we observe that in general, the reflections are much broader in the as-deposited film (Figure 6.1c) than after annealing (Figure 6.1e). This is consistent with the enlargement of the crystalline domains as observed with Atomic Force Microscopy (see Figure A6.1 in Appendices). Both before and after annealing, we observe reflections indicative of PbI<sub>2</sub> (diamonds) (see also Figure A6.2 in Appendices), which is most likely the origin of the absorption feature around 500 nm in the black CsPbI<sub>3</sub> (Figure 6.1b).

The TRMC technique<sup>23</sup> was used to investigate the mobilities and recombination dynamics of photo-excited charge carriers in CsPbI<sub>3</sub> thin films frozen in the black phase. Figure 6.2a shows the intensity-normalized photoconductance ( $\Delta G$ ) of a 260



nm thick CsPbI<sub>3</sub> film, as function of time after pulsed excitation at 600 nm. The initial rise of  $\Delta G$  is attributed to the generation of mobile charges, while the decay represents their immobilization due to trapping or recombination. The product of charge carrier generation yield and the sum of their mobilities  $\varphi\Sigma\mu$  is obtained from the maximum signal height. In view of the low exciton binding energy of  $\sim 15$  meV compared to the thermal energy at room temperature,<sup>24</sup> we assume that  $\varphi$  is close to unity (recall **Figure 2.2**). Thus, as clearly shown in **Figure 6.2a**, the sum of electron and hole mobilities in the vapour-deposited CsPbI<sub>3</sub> film is  $\sim 25$  cm<sup>2</sup>/(Vs). Interestingly, this  $\varphi\Sigma\mu$  is very comparable to what we and others have measured in planar MAPbI<sub>3</sub> and FAPbI<sub>3</sub> films using similar techniques.<sup>16,19,25</sup> Therefore, this observation suggests that the mobility in metal halide perovskites is mainly dictated by the inorganic framework rather than the nature of the monovalent cation. As clearly visible from **Figure 6.2a**, the charge carrier lifetimes in the annealed vapour-deposited CsPbI<sub>3</sub> film reach values in the order of tens of microseconds at a charge carrier density of  $10^{15}$  cm<sup>-3</sup>. This is exceptionally long, and only comparable to high quality MAPbI<sub>3</sub>, see **Figure 3.7**.<sup>26</sup> On increasing the initial charge carrier density to  $10^{17}$  cm<sup>-3</sup>, the lifetime gradually decreases. This trend is characteristic for higher order recombination between electrons and holes, for instance second-order band-to-band recombination.<sup>25</sup> On increasing the thickness of the vapour-deposited films, both the mobility and lifetime remain constant, see **Figure A6.3** in **Appendices**. This suggests that the optoelectronic quality of vapour-deposited polycrystalline CsPbI<sub>3</sub> films is not dependent on their thickness, which enables us to prepare electronically homogeneous layers with various thicknesses. To investigate whether the mobilities and lifetimes observed in the vapour-deposited samples could be generalized to polycrystalline CsPbI<sub>3</sub> films, we repeated the TRMC measurements on spin-coated layers (see XRD patterns in **Figure A6.2** in **Appendices**).

**Figure 6.2b** shows the result for a ( $\sim 350$  nm) film, spin-coated using a stoichiometric precursor solution in a mixture of N,N-dimethylformamide (DMF) and dimethyl sulfoxide (DMSO), and annealed to 310 °C to convert to the black phase, see experimental methods for further details. We find that the mobilities in these spin-coated CsPbI<sub>3</sub> layers are close to 20 cm<sup>2</sup>/(Vs), which is very similar to the vapour-deposited CsPbI<sub>3</sub> (**Figure 6.2a**). The charge carrier lifetimes on the other hand, are significantly shorter in the spin-coated samples for equivalent excitation densities, reaching maximum values of 0.2  $\mu$ s. These observations suggest that all mobile charges are rapidly immobilized in trap states, indicating a relatively high trap density for these type of solution-processed CsPbI<sub>3</sub> films. Most importantly, an increasing lifetime with increasing charge carrier densities is observed up to  $4 \times 10^{16}$  cm<sup>-3</sup> (**Figure 6.2b**), while the lifetime decreases again when the number of charge carriers is further increased. We interpret this as filling of trap states until these are saturated, resulting in an enhancement of the lifetime with increasing charge carrier densities.<sup>16</sup>

To further visualize these observations, we have plotted the time at which the signal has reduced to half its initial value (*i.e.*, the half lifetime  $\tau_{1/2}$ ) against excitation density in **Figure 6.2c**. This clearly shows the decrease in lifetime with increasing charge densities

**Table 6.1:** Kinetic parameters used to fit the experimental TRMC data shown in **Figure 6.2**, listing rate constants for second-order recombination ( $k_2$ ), trap filling ( $k_T$ ), trap depopulation ( $k_D$ ), the trap density ( $N_T$ ) and mobilities for electrons ( $\mu_e$ ) and holes ( $\mu_h$ ) for CsPbI<sub>3</sub> thin films prepared *via* different routes.

	vapour-deposited	spin-coated
$k_2$ ( $\times 10^{-10} \text{ cm}^3 \text{ s}^{-1}$ )	1.3	12
$k_T$ ( $\times 10^{-10} \text{ cm}^3 \text{ s}^{-1}$ )	10	600
$k_D$ ( $\times 10^{-10} \text{ cm}^3 \text{ s}^{-1}$ )	0.25	0.9
$N_T$ ( $\times 10^{15} \text{ cm}^{-3}$ )	0.9	11
$\mu_e$ ( $\text{cm}^2/(\text{Vs})$ )	13	22
$\mu_h$ ( $\text{cm}^2/(\text{Vs})$ )	13	1

for the vapour-deposited films (squares), which is typically observed in regimes where higher order recombination dominates. In contrast, in the spin-coated CsPbI<sub>3</sub> (open circles) the lifetime of free charges initially increases ( $< 4 \times 10^{16} \text{ cm}^{-3}$ ), which we attribute to gradual saturation of trap states on increasing the charge carrier density. Then, only when the latter starts exceeding the trap density ( $> 4 \times 10^{16} \text{ cm}^{-3}$ ), higher order recombination will dominate. Considering that for the spin-coated samples, free charges are rapidly immobilized into trap states, the electron and hole diffusion lengths are expected to be significantly shorter than in the vapour-deposited films, for which long-lived free charges are generated.

In order to quantify processes such as charge carrier trapping and second-order band-to-band recombination, we use the global kinetic model introduced in **Chapter 2** to fit the experimental TRMC data.<sup>25,27</sup> Since these measurements do not enable us to separate the contributions of electrons and holes, we initially assumed that the traps are electron-selective and that free electrons and holes have balanced mobilities based on their similar effective masses.<sup>28</sup> The fits are added as dotted lines in **Figure 6.2**, using the kinetic parameters listed in **Table 6.1**. As shown in **Figures 6.2a** and **6.2b**, this relatively simple kinetic model gives an excellent description of the basic features observed in the experimental decays over a wide range of excitation densities. By using a single set of kinetic parameters characteristic for each sample, we can accurately determine the rate constants for second-order recombination and trap-assisted recombination. From here, we extract that the trap densities ( $N_T$ ) in the spin-coated films are on the order of  $10^{16} \text{ cm}^{-3}$ , while these are only  $9 \times 10^{14} \text{ cm}^{-3}$  for the vapour-deposited CsPbI<sub>3</sub> layers. Furthermore, the trapping rate ( $k_T = 10^{-9} \text{ cm}^3 \text{ s}^{-1}$ ) is much higher than the trap depopulation rate ( $k_D = 2.5 \times 10^{-11} \text{ cm}^3 \text{ s}^{-1}$ ), so that at low charge carrier densities electrons get relatively rapidly trapped and subsequently slowly recombine with the free holes (see also **Figure A6.4** in **Appendices**). At charge carrier densities above  $\sim 10^{15} \text{ cm}^{-3}$ , their decay is dominated

by band-to-band recombination, for which we find a second-order recombination rate constant ( $k_2$ ) as low as  $1.3 \times 10^{-10} \text{ cm}^3 \text{ s}^{-1}$ . From here, we conclude that the relatively long lifetimes are a combination of slow recombination of free holes with trapped electrons (at charge densities  $< 10^{15} \text{ cm}^{-3}$ , see also **Figure A6.4** in **Appendices**) and slow second-order recombination between free electrons and holes (charge densities  $< 10^{17} \text{ cm}^{-3}$ ). Interestingly, the rate constants for both second-order recombination and trapping are on the same order of magnitude as for  $\text{MAPbI}_3$ ,<sup>25,29</sup> once again suggesting that the cation actually plays a minor role in the charge carrier dynamics at room temperature.

In contrast with the vapour-deposited layers, the experimental data for the spin-coated sample could only be fitted with the current model assuming one of the charge carriers (for instance the hole) is already immobilized within the instrumental response time of 3 ns. Then, its counter-charge (*i.e.* electron) gets trapped within the timeframe shown in **Figure 6.2b** ( $\sim 200 \text{ ns}$ ). To further investigate the relationship between the preparation route of  $\text{CsPbI}_3$  and their optoelectronic quality, we constructed planar solar cell devices in the configuration of  $\text{FTO}/\text{SnO}_2/\text{CsPbI}_3/\text{HTM}/\text{Ag}$ . This results in

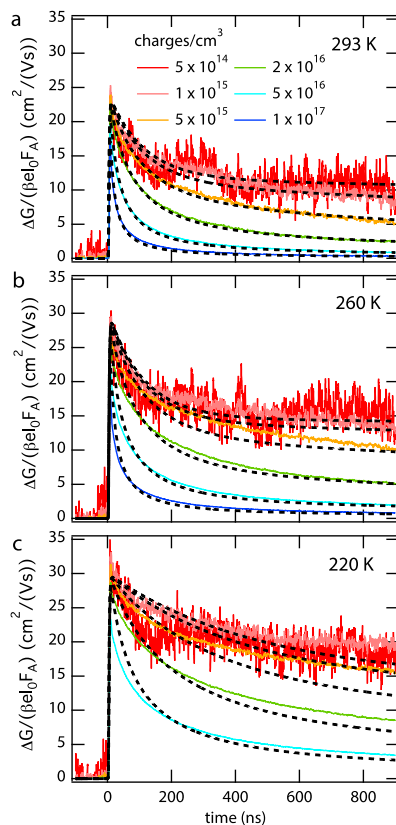


**Figure 6.3:** (a-c) Photoconductance as function of time for vapour-deposited  $\text{CsPbI}_3$ , recorded at 293 K (a), 260 K (b) and 220 K (c) for initial charge carrier densities of  $5 \times 10^{14}$  to  $10^{17} \text{ cm}^{-3}$ . The modelled traces are added as black dotted lines.

power conversion efficiencies (PCE) close to 9% with a highest stabilized power output of 7.8% (see **Figure A6.5c** in **Appendices**) for the vapour-deposited CsPbI<sub>3</sub>, while spin-coated CsPbI<sub>3</sub> devices gave PCEs of less than 6.4%, which stabilized at 4.3%. In view of its lower PCE, it seems likely that indeed, both electrons and holes are rapidly trapped in the spin-coated samples, which makes it challenging to collect both charges efficiently when used in a device configuration. In line with these higher trap densities, we find a substantial reduction in the PL emission intensity as compared to the vapour-deposited samples (see **Figure A6.6** in **Appendices**). Interestingly, the presence of PbI<sub>2</sub> in the vapour-deposited CsPbI<sub>3</sub> does not seem to harm its overall performance, and might even turn out to be beneficial as previously observed for MAPbI<sub>3</sub>.<sup>30</sup> Since the decay in the spin-coated CsPbI<sub>3</sub> films is fully dominated by trap-assisted recombination up to 10<sup>17</sup> charges/cm<sup>3</sup>, these samples are not suitable to gain insight in the temperature dependence of the band-to-band recombination. For the vapour-deposited CsPbI<sub>3</sub> on the other hand, the regime between 10<sup>15</sup> and 10<sup>17</sup> charges/cm<sup>3</sup> is characterized by second-order recombination. As mentioned in **Chapter 5**, the indirect character of the bandgap has previously been attributed to the presence of an electric field caused by collective orientations of the dipolar MA cations. If this is indeed the case, there should be no indirect bandgap for CsPbI<sub>3</sub>. To further investigate this, we performed TRMC measurements at different temperatures for vapour-deposited CsPbI<sub>3</sub> films (thickness 260 nm). **Figure 6.3** shows the photoconductance at 293 K (a), 260 K (b) and 220 K (c), recorded at a timescale of 1  $\mu$ s. Consistent with the sample shown in **Figure 6.2a**, the room temperature mobility is around 25 cm<sup>2</sup>/(Vs). Interestingly, on decreasing the temperature, the mobility in CsPbI<sub>3</sub> gradually increases, following a similar temperature-dependent trend as observed for MAPbI<sub>3</sub>, see **Figure 6.4a** and **Figures A6.7** and **A6.8** in **Appendices**. Therefore, these observations suggest that the charge carrier mobility in lead iodide perovskites is mainly limited by phonon scattering, see **Equation 2.13**, independent of the monovalent cation. Interestingly, not only the mobility but also the lifetime follows the same temperature dependence as for MAPbI<sub>3</sub>.

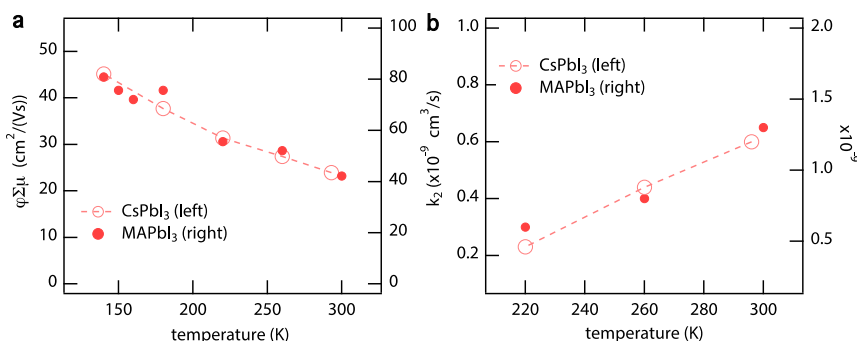


**Figure 6.4:** (a-b) Effective mobility  $\varphi\Sigma\mu$  (a) and  $k_2$  (b) as function of temperature for CsPbI<sub>3</sub> (open circles, left axis) and MAPbI<sub>3</sub> (closed circles, right axis). The dotted lines between the open circles are added to guide the eye.

That is, on lowering the temperature the lifetime increases, which is most pronounced for excitation densities in between  $5 \times 10^{15}$  and  $10^{17} \text{ cm}^{-3}$ . Since this corresponds to a regime in which the lifetime is highly dependent on the initial charge carrier concentration, we can conclude from here that higher order recombination is retarded with decreasing temperatures. For temperatures between 293 K and 220 K, we could fit the experimental data to our kinetic model and extract the temperature-dependent  $k_2$  for CsPbI<sub>3</sub>, which we compare directly to  $k_2(T)$  for MAPbI<sub>3</sub> samples in **Figure 6.4b** (see also **Figure A6.8** in **Appendices**). Importantly, although the absolute values are different, in both cases the  $k_2$  at 220 K is less than half its room temperature value. At and below 180 K, we could not obtain satisfactorily fits for CsPbI<sub>3</sub> (see **Figure A6.7** in **Appendices**), which might be due to processes unaccounted for in our model, such as third-order (Auger) recombination. Still, our results confirm that for both MAPbI<sub>3</sub> and CsPbI<sub>3</sub>, second-order recombination is a thermally activated process for  $220 \text{ K} < T < 300 \text{ K}$ . This suggests that the indirect recombination pathway of free charges is not unique to MA-based perovskites and hence, not related to collective orientations of MA cations. We should note that in general, the extracted  $k_2$  depends on the timeframe studied. For instance, for the vapour-deposited CsPbI<sub>3</sub>, a time window of 1  $\mu\text{s}$  (**Figure 6.3**) yields a  $k_2$  of  $6 \times 10^{-10} \text{ cm}^3/\text{s}$ , while a  $k_2$  of  $1.3 \times 10^{-10} \text{ cm}^3/\text{s}$  leads to better fits if timeframes up to 50  $\mu\text{s}$  are considered. This mismatch at different timescales further illustrates the complexity of the second-order recombination rate in metal halide perovskites and requires further investigation.

### 6.3 Mixed-cation mixed-halide perovskites

In view of its promising optoelectronic properties, it seems likely that optimizing the device configuration and fabrication together with the quality of vapour-deposited CsPbI<sub>3</sub> itself could result in devices with much higher efficiencies. However, without post-synthetic treatments, bulk CsPbI<sub>3</sub> perovskites still suffer from poor phase stability. In addition, their bandgap is slightly increased with respect to MAPbI<sub>3</sub>, which is undesirable for a single-junction solar cell. On the other hand, while fully replacing the MA with the organic cation formamidinium (FA:  $\text{CH}(\text{NH}_2)_2^+$ ) is favorable for light absorption in view of its smaller bandgap (1.48 eV),<sup>31</sup> also FAPbI<sub>3</sub> undergoes a phase transition to a yellow non-perovskite phase at room temperature. Interestingly, mixing MA and FA was found to be a successful strategy to resolve these issues.<sup>10,11</sup> For instance, the perovskite  $\text{FA}_{0.83}\text{MA}_{0.17}\text{Pb}(\text{I}_{0.83}\text{Br}_{0.17})_3$  takes advantage of both the bandgap of FAPbI<sub>3</sub> and the phase-stability of MAPbI<sub>3</sub>.<sup>32</sup> A small amount of bromide is then added to improve the crystal-phase stability, and increases the open-circuit voltage ( $V_{oc}$ ) in photovoltaic devices. These compounds have been used as absorber layers in devices, yielding devices with efficiencies higher than 20%.<sup>11</sup> Interestingly, further improvements in device performance were found on adding small amounts of inorganic cations to the  $\text{FA}_{0.83}\text{MA}_{0.17}\text{Pb}(\text{I}_{0.83}\text{Br}_{0.17})_3$  perovskite (FAMA).<sup>11,33,34</sup> In this section, we investigate the role of the addition of Cs and/or Rb to the charge carrier mobilities and recombination kinetics in FAMA. These samples were prepared according to a

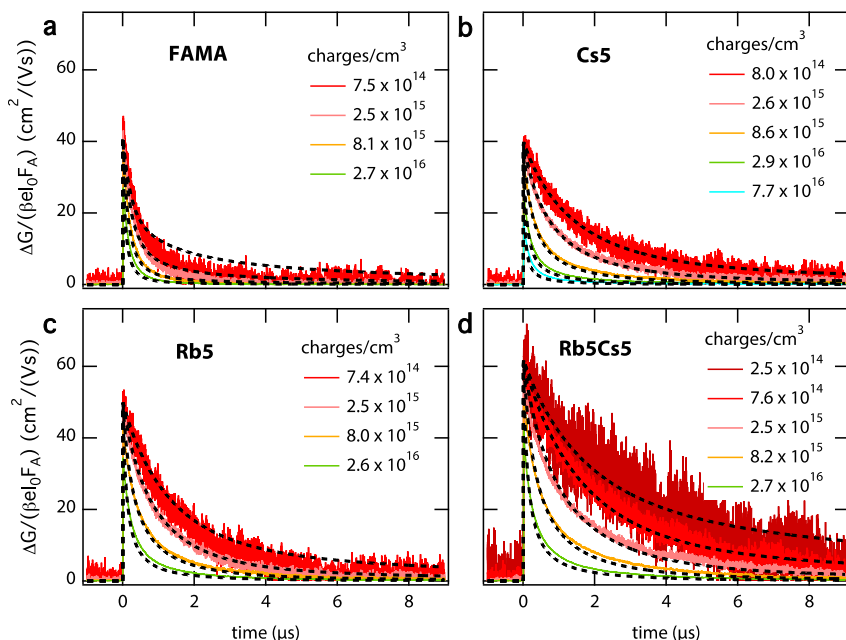


**Figure 6.5:** (a-d) Time-resolved microwave conductivity (TRMC) traces recorded for (a) FAMA, (b) Cs5, (c) Rb5 and (d) Rb5Cs5. The dotted black lines indicate the corresponding fits to the TRMC traces according to our kinetic model.

previously reported protocol for the FAMA perovskite and approximately 5 mol% of RbI, CsI or a combination of both were added to the precursor solution.<sup>34</sup> From previous XRD results,<sup>33</sup> we know that the Cs is fully incorporated into the perovskite lattice, while the Rb is partially present in the form of the  $\text{RbPb}(\text{I}_{1-x}\text{Br}_x)_3$  side phase. In **Figure 6.5**, the intensity-normalized TRMC data are plotted for FAMA (**Figure 6.5a**) and FAMA with 5% Cs (Cs5, **Figure 6.5b**), 5% Rb (Rb5, **Figure 6.5c**) and both of these (Rb5Cs5, **Figure 6.5d**). The modelled traces are added as dotted lines, showing excellent agreement with the experimental TRMC traces. The extracted mobilities, trap densities and rate constants for trap-assisted and second-order recombination are summarized in **Table 6.2**. For both the FAMA and Cs5 perovskite films, the sum of electron and hole mobilities exceeds  $40 \text{ cm}^2/(\text{Vs})$ , which increases to  $60 \text{ cm}^2/(\text{Vs})$  on the addition of Cs in combination with Rb (**Figure 6.5d**). Furthermore, our results indicate a trap density of  $2.5 \times 10^{15} \text{ cm}^{-3}$  in the FAMA sample, which is substantially reduced to  $8.0 \times 10^{14} \text{ cm}^{-3}$  on the addition of Cs. This could be one of the explanations for the observed enhancement in the device performance reported for Cs5.<sup>33</sup> When only Rb is added to the perovskite precursor solution, the resulting Rb5 film also reveals a lower trap density as compared to FAMA ( $N_T = 1.0 \times 10^{15} \text{ cm}^{-3}$ ), but the effect is smaller than if Cs is added. For each

**Table 6.2:** Kinetic parameters for the samples shown in **Figure 6.5**.

	FAMA	Cs5	Rb5	Rb5Cs5
$k_2$ ( $\times 10^{-10} \text{ cm}^3\text{s}^{-1}$ )	6	4.2	3.5	3.0
$k_T$ ( $\times 10^{-10} \text{ cm}^3\text{s}^{-1}$ )	10	10	10	10
$k_D$ ( $\times 10^{-10} \text{ cm}^3\text{s}^{-1}$ )	9	9	9	9
$N_T$ ( $\times 10^{15} \text{ cm}^{-3}$ )	2.5	0.8	1	0.8
$\mu_e$ ( $\text{cm}^2/(\text{Vs})$ )	21	20	25	31
$\mu_h$ ( $\text{cm}^2/(\text{Vs})$ )	21	20	25	31

sample, we find a trap filling rate constant of  $k_T = 1 \times 10^{-9} \text{ cm}^3\text{s}^{-1}$  and a depopulation rate constant of  $k_D = 9 \times 10^{-10} \text{ cm}^3\text{s}^{-1}$ , suggesting that the chemical origin of the trap states is the same for each sample.

Importantly, we find that the presence of the inorganic cations Rb and Cs also reduces the second-order recombination rate. Similar to the improvement of charge carrier mobility, the reduction of the second-order recombination rate constant is most pronounced in Rb5Cs5 and thus significantly extends the charge carrier lifetimes throughout the full range of excitation densities shown in **Figure 6.5**. Both the changes in  $k_2$  and in  $\varphi\Sigma\mu$  might be linked to alterations in the band structure of the perovskite compound. That is, since changing the cations locally affects the distances between the lead halide octahedra and their tilting angles, the retarded second-order recombination in the presence of Rb and/or Cs could be due to changes in the band structure.

## 6.4 Conclusions

To summarize, we have investigated the optoelectronic properties of fully inorganic CsPbI<sub>3</sub> perovskite thin films, prepared using vapour-deposited and solution-based methods. To obtain the CsPbI<sub>3</sub> crystals in their black perovskite phase, the films were heated to 310 °C followed by rapid cooling. Then, the charge carrier mobilities and recombination lifetimes were analyzed using the TRMC technique. We find that the mobilities are around 25 cm<sup>2</sup>/(Vs), both in vapour-deposited and spin-coated CsPbI<sub>3</sub> films. Furthermore, in vapour-deposited CsPbI<sub>3</sub>, we observe lifetimes in the order of tens of microseconds, which is exceptionally long for an MHP thin film. For the spin-coated CsPbI<sub>3</sub>, we find that all free charges are immobilized within 200 ns after pulsed illumination, which we interpret as rapid trapping of electrons and holes. On fitting the experimental TRMC data to a previously reported kinetic model,<sup>25,27</sup> we extract a trap density of  $1.1 \times 10^{16} \text{ cm}^{-3}$  for spin-coated films and  $9 \times 10^{14} \text{ cm}^{-3}$  for vapour-deposited CsPbI<sub>3</sub>. Additionally, for the latter we find that the rate constant for second-order recombination is  $1.3 \times 10^{-10} \text{ cm}^3\text{s}^{-1}$  and hence, comparable to both MA- and FAPbI<sub>3</sub>.<sup>19,29</sup> Finally, we find that the temperature dependence of both the mobility and second-order



recombination rates in CsPbI<sub>3</sub> follow the exact same trends as in MAPbI<sub>3</sub>. Importantly, these observations suggest that the organic or dipolar nature of the cation actually plays a minor role in both the mobility and band-to-band recombination of free charges in metal halide perovskites. Although substantially lower trap densities and superior phase-stability are obtained using a combination of organic and inorganic cations (such as Cs) and a mixture of halides, it seems likely that post-synthetic treatments could improve the optoelectronic quality and phase-stability of CsPbI<sub>3</sub>. We suspect that the relatively low PCE's of CsPbI<sub>3</sub>-based photovoltaic devices compared to MAPbI<sub>3</sub> and mixed-cation lead mixed-halide perovskites are related to poor structural stability of black CsPbI<sub>3</sub> in combination with the limited effort on optimizing the quality of the inorganic perovskite absorber layer and devices, rather than an intrinsic limitation of fully inorganic metal halide perovskites.

## 6.5 Experimental Methods

### Vapour deposition of CsPbI<sub>3</sub>

Thin films of CsPbI<sub>3</sub> on quartz substrates were prepared by sequential physical vapour deposition of the precursors PbI<sub>2</sub> ( $\geq 99\%$ , Sigma Aldrich) and CsI ( $\geq 99.999\%$ , Sigma Aldrich) in a stoichiometric ratio. Therefore, an adapted evaporation machine (ATC Orion 4 - AJA International, Inc.) with Deposition Controller (SQC-310 Inficon) and Thermal Evaporation Controller (TEC-15A) was used. The PbI<sub>2</sub> and CsI powders were put into quartz crucibles and positioned in the vacuum chamber. After the pressure was reduced to  $10^{-5}$ - $10^{-6}$  mbar, the substrates (plasma-cleaned quartz for the optical and structural characterization and SnO<sub>2</sub> on ITO glass for the device fabrication) were introduced in the vacuum chamber. Then, the crucible containing the PbI<sub>2</sub> precursor was heated to 240 – 260 °C until a deposition rate of  $\sim 0.8$  Å/s was reached, as indicated by a quartz microbalance. The CsI was heated to 390 – 400 °C to reach a rate of  $\sim 0.9$  Å/s. CsPbI<sub>3</sub> was then obtained by alternating deposition of 2.5 nm PbI<sub>2</sub> and 2 nm CsI (with 5 seconds in between), which was repeated until the desired total thickness was reached. Finally, the films were annealed at 300 °C until these turned black. This was followed by rapid cooling on a cold metal surface.

### Spin-coating of CsPbI<sub>3</sub>

Substrates were cleaned by sequential sonication in Hellmanex, deionised water, acetone, and isopropanol, and dried with nitrogen. Immediately before spincoating the substrates were treated with oxygen plasma for 10 minutes. Solution preparation, film formation and annealing were carried out in a nitrogen-filled glovebox. The solutions were stirred until dissolved and filtered with a 2.7 µm GF filter before spincoating. The precursors were dissolved in a mixture of 0.65:0.35 DMF:DMSO at 0.8 M (1:1 CsI (Alfa Aesar) + PbI<sub>2</sub> (TCI)). Films were formed by spincoating the precursor solution dynamically using a two-step program: 1000 rpm followed by 2000 rpm, with anisole solvent quenching after 30 s. The films were then dried at 45 °C for 10 minutes. The films were heated at 310-320 °C until black and cooled rapidly on a cold metal surface. The precursors were dissolved in DMF at 0.5 M (1:1 CsI (Alfa Aesar) + PbI<sub>2</sub> (TCI)). Hydriodic acid was added at 35 µL per mL solution prior to spincoating. Films were formed by spincoating the precursor solution dynamically using a two-step program: 1000 rpm followed by 2000 rpm. The films were then annealed at 100 °C for 10 minutes.

### Mixed-cation mixed-halide perovskites

FAI and MABr were purchased from Dyesol. PbI<sub>2</sub> and PbBr<sub>2</sub> (99%) were purchased from TCI. CsI (99.9%) and all anhydrous solvents (DMSO, DMF, chlorobenzene) were purchased from Sigma-Aldrich and RbI from abcr GmbH. All chemicals were used without further purification. Perovskite precursor solutions for FAMA, Cs5, Rb5 and Rb5Cs5 were fabricated according



to a previous report.<sup>33,34</sup> 75  $\mu\text{L}$  of the perovskite precursor solution was spin-coated inside a nitrogen-filled glovebox at 1000 rpm and 4000 rpm for 10 s and 30 s, respectively. Approximately 20 s before the end of spinning, 500  $\mu\text{L}$  of chlorobenzene was added to the film. The perovskite film formation was completed by annealing at 100  $^{\circ}\text{C}$  for 60 min on a hotplate.

#### Solar cell device fabrication

Fluorine doped tin oxide (FTO)-coated glass substrates (Pilkington,  $7\ \Omega\ \square^{-1}$ ) were patterned using etching by 2M HCl and Zn powder. The etched substrates were cleaned by sequential sonication in Hellmanex, deionised water, acetone, and isopropanol, and dried with nitrogen. The clean substrates were then treated with oxygen plasma for 5 minutes before depositing the electron transport layer (ETL). The ETL was prepared by spincoating at 3000 rpm (200 rpm/s acceleration) a solution of  $\text{SnCl}_4 \cdot 5\text{H}_2\text{O}$  (0.05 M in IPA) that had been stirred for 30 minutes. The  $\text{SnCl}_4 \cdot 5\text{H}_2\text{O}$  layer was then dried at 100  $^{\circ}\text{C}$  for 10 minutes and annealed at 180  $^{\circ}\text{C}$  for 60 minutes to form a compact layer of  $\text{SnO}_2$ . Perovskite layers were then deposited and annealed as for optical measurements. The hole transport layers (HTL) were prepared by spincoating 200  $\mu\text{L}$  of a solution of polymer-wrapped single-walled carbon nanotubes dropwise at 3000 rpm.<sup>35</sup> Once dry, this was infiltrated with undoped Spiro-OMeTAD by spincoating a solution of Spiro-OMeTAD (LumTec, 85 mg/mL in chlorobenzene, with 33  $\mu\text{L}$ /mL tert-Butylpyridine additive) at 2000 rpm. The HTL and the active layer at the bottom of the device were removed before deposition of the bottom and top electrodes. Silver electrodes (80 nm) were deposited by thermal evaporation in an evaporator which opens to air.

#### Solar cell device characterization

The performance of the solar cell devices was measured under simulated AM 1.5 sunlight generated with a class AAB ABET solar simulator calibrated to give simulated AM 1.5 of 100.0  $\text{mW cm}^{-2}$  equivalent irradiance, using an NREL-calibrated KG5 filtered silicon reference cell. The mismatch factor was calculated to be 1.02 between 300 to 900 nm for  $\text{MAPbI}_3$ . The current-voltage curves were recorded with a sourcemeter (Keithley 2400, USA). The devices were masked with a metal aperture defining the active area (0.092  $\text{cm}^2$ ) of the device and measured in a light-tight sample holder to minimize any edge effects and to ensure that the reference cell and test cell are located during measurement in the same spot under the solar simulator. To avoid cross-talk between devices on the same substrate, the active material was removed between devices before measurement. The devices were not encapsulated and therefore exposed to ambient conditions during the measurement.

#### Optical Characterization

The absorption and TRMC measurements were performed as described in **Chapters 2 and 3**. For the photoluminescence quantum efficiency (PLQE) measurements, the films were placed in an integrating sphere and were photo-excited using a 532 nm continuous-wave laser. The laser and the emission signals were measured and quantified using a calibrated Andor iDus DU490A InGaAs detector for the determination of PL quantum efficiency. The PLQE was calculated as described in Ref. 36.

## 6.6 References

1. Gélvez-Rueda, M. C. *et al.* Effect of Cation Rotation on Charge Dynamics in Hybrid Lead Halide Perovskites. *J. Phys. Chem. C* **120**, 16577–16585 (2016).
2. Motta, C. *et al.* Revealing the role of organic cations in hybrid halide perovskite  $\text{CH}_3\text{NH}_3\text{PbI}_3$ . *Nat. Commun.* **6**, 7026 (2015).
3. Ma, J. & Wang, L.-W. The nature of electron mobility in hybrid perovskite  $\text{CH}_3\text{NH}_3\text{PbI}_3$ . *Nano Lett.* **17**, 3646–3654 (2017).
4. Azarhoosh, P. *et al.* Relativistic origin of slow electron-hole recombination in hybrid halide perovskite solar cells. *APL Mater.* **4**, 91501 (2016).
5. Etienne, T., Mosconi, E. & De Angelis, F. Dynamical Origin of the Rashba Effect in Organohalide Lead

- Perovskites: A Key to Suppressed Carrier Recombination in Perovskite Solar Cells? *J. Phys. Chem. Lett.* **7**, 1638–1645 (2016).
6. Park, M. *et al.* Critical Role of Methylammonium Librational Motion in Methylammonium Lead Iodide ( $\text{CH}_3\text{NH}_3\text{PbI}_3$ ) Perovskite Photochemistry. *Nano Lett.* **17**, 4145–4157 (2017).
7. Fabini, D. H. *et al.* Main-Group Halide Semiconductors Derived from Perovskite: Distinguishing Chemical, Structural, and Electronic Aspects. *Inorg. Chem.* **56**, 11–25 (2017).
8. Hutter, E. M. *et al.* Direct–indirect character of the bandgap in methylammonium lead iodide perovskite. *Nat. Mater.* **16**, 115–120 (2017).
9. Zhu, H. *et al.* Organic Cations Might Not Be Essential to the Remarkable Properties of Band Edge Carriers in Lead Halide Perovskites. *Adv. Mater.* **29**, 1–6 (2017).
10. McMeekin, D. P. *et al.* A mixed-cation lead mixed-halide perovskite absorber for tandem solar cells. *Science* **351**, 151–155 (2016).
11. Saliba, M. *et al.* Cesium-containing Triple Cation Perovskite Solar Cells: Improved Stability, Reproducibility and High Efficiency. *Energy Environ. Sci.* **9**, 1989 (2016).
12. Eperon, G. E. *et al.* Inorganic caesium lead iodide perovskite solar cells. *J. Mater. Chem. A* **3**, 19688–19695 (2015).
13. Dastidar, S. *et al.* Quantitative Phase-Change Thermodynamics and Metastability of Perovskite-Phase Cesium Lead Iodide. *J. Phys. Chem. Lett.* **8**, 1278–1282 (2017).
14. Sutton, R. J. *et al.* Bandgap-Tunable Cesium Lead Halide Perovskites with High Thermal Stability for Efficient Solar Cells. *Adv. Energy Mater.* **6**, 1–6 (2016).
15. Frolova, L. A. *et al.* Highly efficient all-inorganic planar heterojunction perovskite solar cells produced by thermal coevaporation of CsI and  $\text{PbI}_2$ . *J. Phys. Chem. Lett.* **8**, 67–72 (2017).
16. Hutter, E. M. *et al.* Charge Transfer from Methylammonium Lead Iodide Perovskite to Organic Transport Materials: Efficiencies, Transfer Rates, and Interfacial Recombination. *Adv. Energy Mater.* 1602349 (2017). doi:10.1002/aenm.201602349
17. Liu, M., Johnston, M. B. & Snaith, H. J. Efficient planar heterojunction perovskite solar cells by vapour deposition. *Nature* **501**, 395–398 (2013).
18. Momblona, C. *et al.* Efficient vacuum deposited p-i-n and n-i-p perovskite solar cells employing doped charge transport layers. *Energy Environ. Sci.* **9**, 3456–3463 (2016).
19. Rehman, W. *et al.* Charge-Carrier Dynamics and Mobilities in Formamidinium Lead Mixed-Halide Perovskites. *Adv. Mater.* **27**, 7938–7944 (2015).
20. Green, M. A., Ho-Baillie, A. & Snaith, H. J. The emergence of perovskite solar cells. *Nat. Photonics* **8**, 506–514 (2014).
21. Trots, D. M. & Myagkota, S. V. High-temperature structural evolution of caesium and rubidium triiodoplumbates. *J. Phys. Chem. Solids* **69**, 2520–2526 (2008).
22. Ripolles, T. S., Nishinaka, K., Ogomi, Y., Miyata, Y. & Hayase, S. Efficiency enhancement by changing perovskite crystal phase and adding a charge extraction interlayer in organic amine free-perovskite solar cells based on cesium. *Sol. Energy Mater. Sol. Cells* **144**, 532–536 (2014).
23. Savenije, T. J., Ferguson, A. J., Kopidakis, N. & Rumbles, G. Revealing the dynamics of charge carriers in polymer:fullerene blends using photoinduced time-resolved microwave conductivity. *J. Phys. Chem. C* **117**, 24085–24103 (2013).
24. Yang, Z. *et al.* The Impact of the Halide Cage on the Electronic Properties of Fully Inorganic Caesium Lead Halide Perovskites. *ACS Energy Lett.* **2**, 1621–1627 (2017).
25. Hutter, E. M., Eperon, G. E., Stranks, S. D. & Savenije, T. J. Charge Carriers in Planar and Meso-Structured Organic-Inorganic Perovskites: Mobilities, Lifetimes and Concentrations of Trap States. *J. Phys. Chem. Lett.* **6**, 3082–3090 (2015).
26. Bi, Y. *et al.* Charge Carrier Lifetimes Exceeding 15  $\mu\text{s}$  in Methylammonium Lead Iodide Single Crystals. *J. Phys. Chem. Lett.* **7**, 923–928 (2016).
27. Stranks, S. D. *et al.* Recombination Kinetics in Organic-Inorganic Perovskites: Excitons, Free Charge, and Subgap States. *Phys. Rev. Appl.* **2**, 34007 (2014).
28. Amat, A. *et al.* Cation-induced band-gap tuning in organohalide perovskites: Interplay of spin-orbit coupling and octahedra tilting. *Nano Lett.* **14**, 3608–3616 (2014).
29. Wehrenfennig, C., Eperon, G. E., Johnston, M. B., Snaith, H. J. & Herz, L. M. High Charge Carrier Mobilities and Lifetimes in Organolead Trihalide Perovskites. *Adv. Mater.* **26**, 1584–1589 (2014).
30. Jacobsson, T. J. *et al.* Unreacted  $\text{PbI}_2$  as a Double-Edged Sword for Enhancing the Performance of Perovskite Solar Cells. *J. Am. Chem. Soc.* **138**, 10331–10343 (2016).
31. Eperon, G. E. *et al.* Formamidinium lead trihalide: a broadly tunable perovskite for efficient planar

- heterojunction solar cells. *Energy Environ. Sci.* **7**, 982 (2014).
32. Correa Baena, J. P. *et al.* Highly efficient planar perovskite solar cells through band alignment engineering. *Energy Environ. Sci.* **8**, 2928–2934 (2015).
33. Hu, Y. *et al.* Understanding the Role of Cesium and Rubidium Additives in Perovskite Solar Cells: Trap States, Charge Transport, and Recombination. *Adv. Energy Mater.* 1703057 (2018).
34. Saliba, M. *et al.* Incorporation of rubidium cations into perovskite solar cells improves photovoltaic performance. *Science* **354**, 206–209 (2016).
35. Habisreutinger, S. N. *et al.* Enhanced hole extraction in perovskite solar cells through carbon nanotubes. *J. Phys. Chem. Lett.* **5**, 4207–4212 (2014).
36. Mello, J. C. de, Wittmann, H. F. & Friend, R. H. An improved experimental determination of external photoluminescence quantum efficiency. *Adv. Mater.* **9**, 230–232 (1997).
37. Abate, A. *et al.* Lithium salts as ‘redox active’ p-type dopants for organic semiconductors and their impact in solid-state dye-sensitized solar cells. *Phys. Chem. Chem. Phys.* **15**, 2572 (2013).

## Appendices

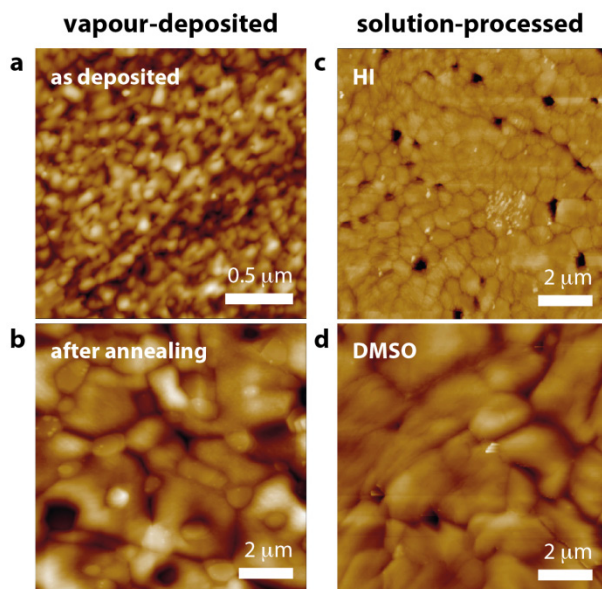


**Figure A6.1:** Atomic Force Microscopy (AFM) images of (a-b) vapour-deposited  $\text{CsPbI}_3$  before (a) and after (b) annealing and (c-d) spin-coated  $\text{CsPbI}_3$ , using HI (c) or DMSO (d) additives in the precursor solution.

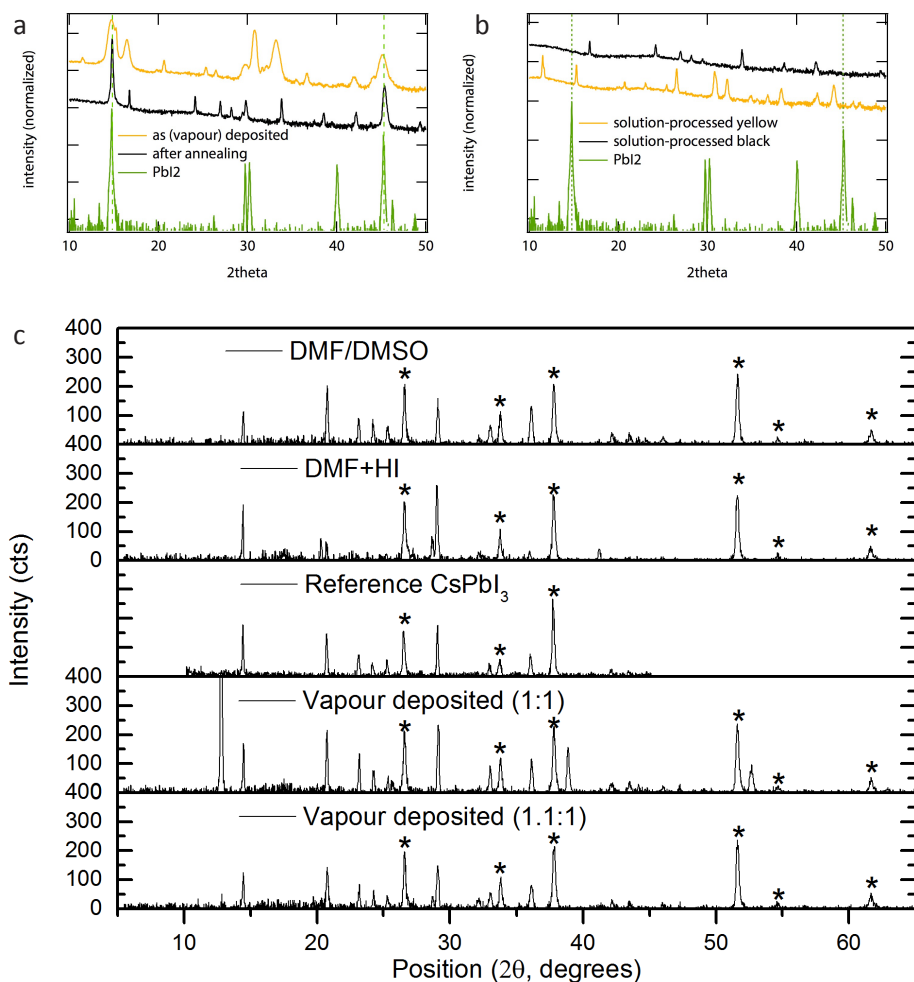


**Figure A6.2:** (a) Background-subtracted X-ray (Co K $\alpha$  radiation,  $\lambda = 1.79 \text{ \AA}$ ) diffraction (XRD) patterns of vapour-deposited CsPbI<sub>3</sub> films (left) before and after annealing and solution-processed CsPbI<sub>3</sub> (right) in the yellow and the black phase. The XRD pattern of vapour-deposited Pbl<sub>2</sub> is added for comparison: the dotted lines are added to guide the eye. This clearly indicates the presence of Pbl<sub>2</sub> in the vapour-deposited samples, while this is not observed for the spin-coated samples. (b) Background-subtracted X-ray (Cu K $\alpha$  radiation,  $\lambda = 1.54 \text{ \AA}$ ) diffraction (XRD) patterns of CsPbI<sub>3</sub> prepared through several different routes and annealed under nitrogen to gain the black phase. We observe reflections from the presence of Pbl<sub>2</sub> in the stoichiometric (1:1) vapour-deposited samples, which are reduced with an excess of CsI (1.1:1). These Pbl<sub>2</sub> reflections are not observed for the spin-coated samples. \* denotes peaks from the SnO<sub>2</sub> substrate.

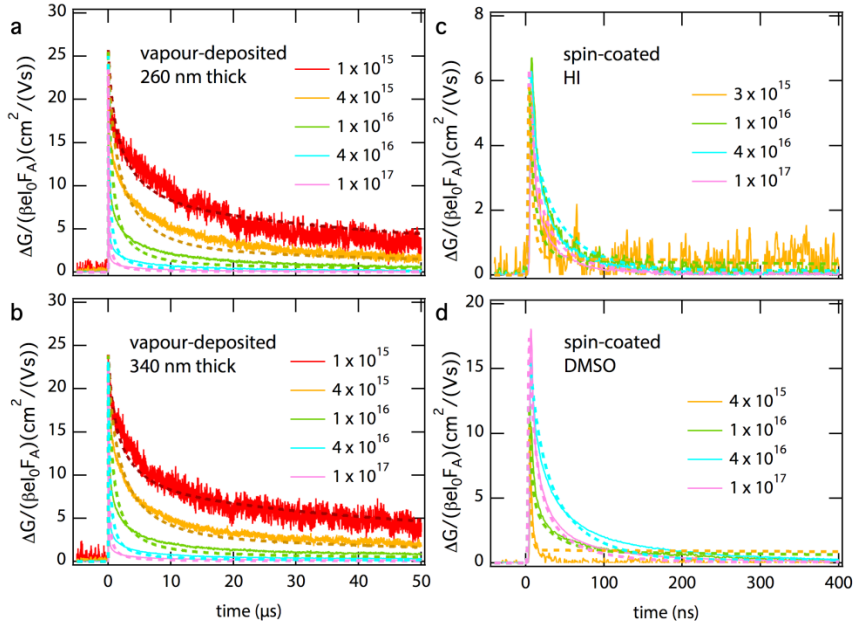


**Figure A6.3:** Time-Resolved Microwave Conductivity (TRMC) traces for (a-b) vapour-deposited CsPbI<sub>3</sub> thin films with thickness of 260 nm (a) and 340 nm (b) and (c-d) CsPbI<sub>3</sub> films spin-coated from solutions in DMF containing HI (c) and DMSO (d). An excitation wavelength of 600 nm was used, and the laser intensity was varied to generate initial charge carrier densities ranging from  $10^{15}$  to  $10^{17}$  cm<sup>-3</sup>.

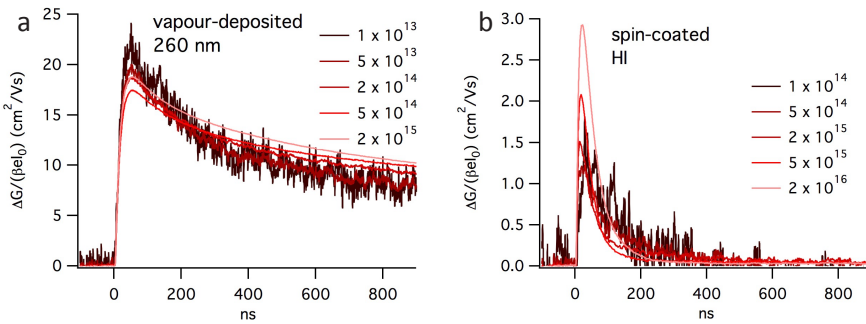


**Figure A6.4:** TRMC traces for a 260 nm vapour-deposited (a) and spin-coated (b) CsPbI<sub>3</sub> thin film, recorded at initial charge carrier densities ranging from  $10^{13}$  to  $10^{15}$  cm<sup>-3</sup>. For these measurements, the samples were put in a resonant cavity which increases the sensitivity and enables us to measure at lower charge carrier densities, however at the cost of the experimental response time (18 ns for these measurements as compared to a few nanoseconds for the data shown in **Figure A6.3** and the main text).

The HTM used to prepare the devices is a composite of polymer-wrapped single-walled carbon nanotubes and Spiro-OMeTAD (see experimental details),<sup>35</sup> which enables good hole extraction without oxidation steps that require air exposure of the solar cell,<sup>37</sup> and temporarily helps to inhibit moisture and air ingress during cell characterization in air. The results for the best performing devices with vapour-deposited and with spin-coated CsPbI<sub>3</sub> are shown in **Figure A6.5**, and the statistics of 20 devices for each preparation route are summarized in **Table A6.1**. Consistent with their superior charge carrier lifetimes, the devices based on vapour-deposited CsPbI<sub>3</sub> (260 nm) show significantly enhanced photovoltaic performance with respect to the spin-coated layers. Additionally, we note that the devices were exposed to air during deposition of the electrodes and the J-V scans, so these may have suffered from a slight loss of black phase CsPbI<sub>3</sub>. However, as these devices are already comparable in efficiency to CsPbI<sub>3</sub> devices in the literature,<sup>15</sup> our results emphasize conclusively that vapour-deposition yields a higher quality inorganic perovskite material than solution-based processing methods.

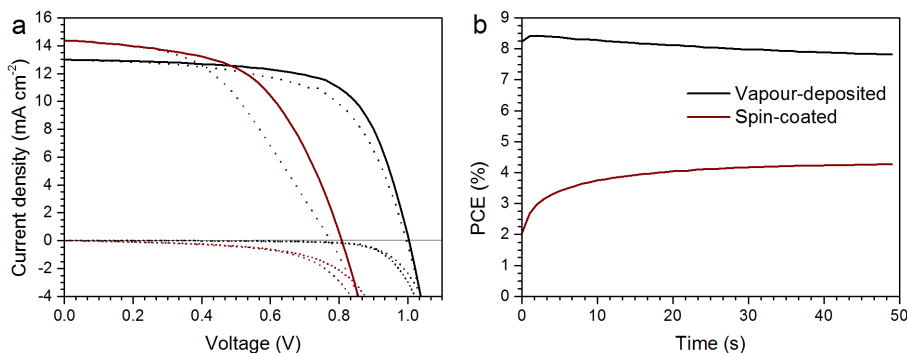


**Figure A6.5:** a) Current-voltage (J-V) scans for the highest efficiency spin-coated (in red) and vapour-deposited (in black) devices. Reverse scans ( $V_{OC}$  to  $J_{SC}$ ) are shown with solid lines and forward scans ( $J_{SC}$  to  $V_{OC}$ ) with dotted lines. Dark J-V scans are added as dotted lines. b) Stabilized power output (SPO) of power conversion efficiency (PCE) measurements for the same devices, measured at constant voltage.

**Table A6.1:** Statistics from J-V data from reverse scans of 20 devices from each preparation method (8 devices for SPO); 's.d.' is the standard deviation; 'SPO Ratio' is the ratio of the SPO with the reverse J-V scan for the same device.

parameter		best cell	mean $\pm$ s.d.		best cell	mean $\pm$ s.d.
$J_{SC}$ (mA cm <sup>-2</sup> )	Vapour-deposited	13.0	12.6 $\pm$ 1.2	Spin-coated	14.4	11.6 $\pm$ 2.6
$V_{OC}$ (V)		1.00	0.95 $\pm$ 0.06		0.80	0.74 $\pm$ 0.13
FF		0.68	0.61 $\pm$ 0.05		0.56	0.51 $\pm$ 0.07
PCE (%)		8.80	7.27 $\pm$ 0.96		6.40	4.4 $\pm$ 1.5
SPO (%)		7.8	6.0 $\pm$ 1.3		4.3	2.5 $\pm$ 1.1
SPO Ratio		0.89	0.82 $\pm$ 0.09		0.67	0.56 $\pm$ 0.14

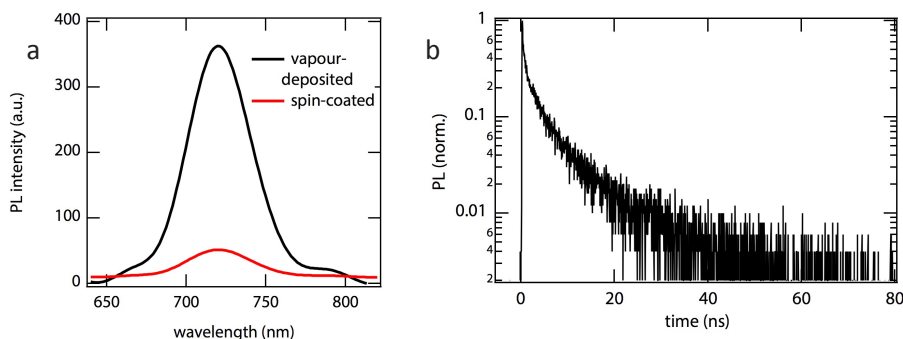


**Figure A6.6:** (a) Photoluminescence (PL) emission spectra for vapour-deposited (black) and spin-coated (red) CsPbI<sub>3</sub>, recorded in an integrating sphere using a 532 nm continuous-wave laser. b) Time-resolved PL intensity (normalized) of a vapour-deposited CsPbI<sub>3</sub> (260 nm) using pulsed excitation at 405 nm (1 MHz,  $4 \times 10^{12}$  ph./cm<sup>2</sup> per pulse). Note that, in both cases, even at charge densities above the trap density, the external photoluminescence quantum efficiencies (PLQE) are very low ( $< 1\%$ ) and the PL lifetime (b) is relatively short compared to the TRMC lifetimes.

**Table A6.2:** Kinetic parameters used to fit the experimental TRMC data shown in **Figure A6.3**, listing rate constants for second-order recombination ( $k_2$ ), trapping ( $k_T$ ), detrapping ( $k_D$ ), the trap density ( $N_T$ ) and mobilities for electrons ( $\mu_e$ ) and holes ( $\mu_h$ ) for CsPbI<sub>3</sub> thin films prepared via different routes.

	vapour-deposited 260 nm	vapour-deposited 340 nm	spin-coated DMF/ DMSO	spin-coated DMF/ HI
$k_2$ ( $\times 10^{-10}$ cm <sup>3</sup> s <sup>-1</sup> )	1.3	1.3	12	12
$k_T$ ( $\times 10^{-10}$ cm <sup>3</sup> s <sup>-1</sup> )	10	10	600	200
$k_D$ ( $\times 10^{-10}$ cm <sup>3</sup> s <sup>-1</sup> )	0.25	0.25	0.9	0.8
$N_T$ ( $\times 10^{15}$ cm <sup>-3</sup> )	0.9	0.85	11	13
$\mu_e$ (cm <sup>2</sup> /(Vs))	13	12	22	8
$\mu_h$ (cm <sup>2</sup> /(Vs))	13	12	1	0.5



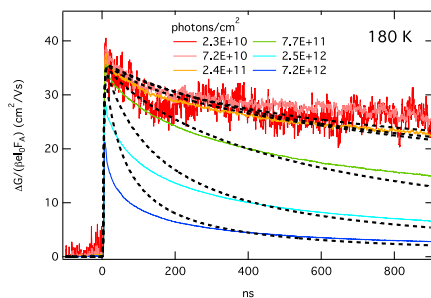


**Figure A6.7:** Experimental and modelled TRMC data for CsPbI<sub>3</sub> at 180 K.

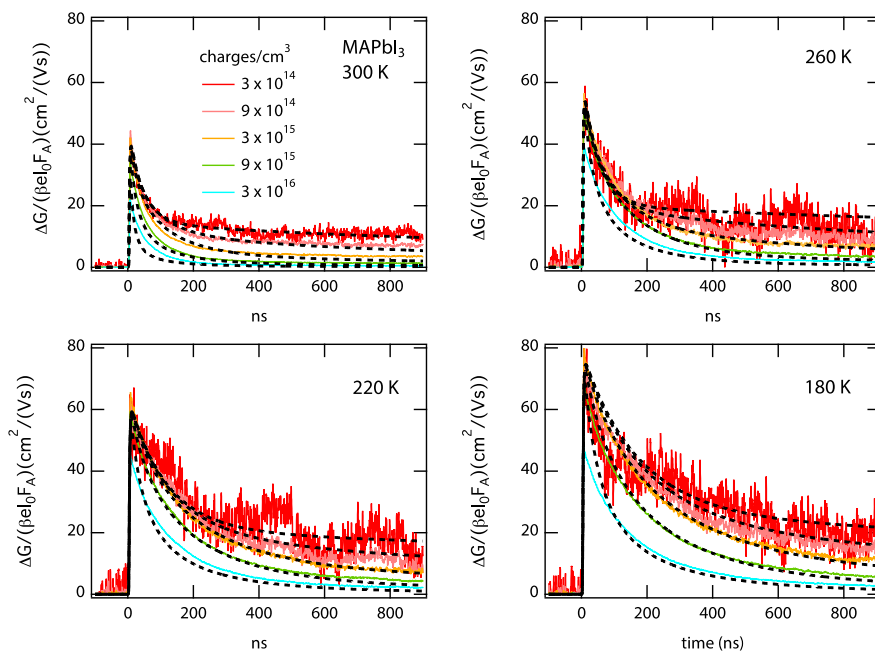
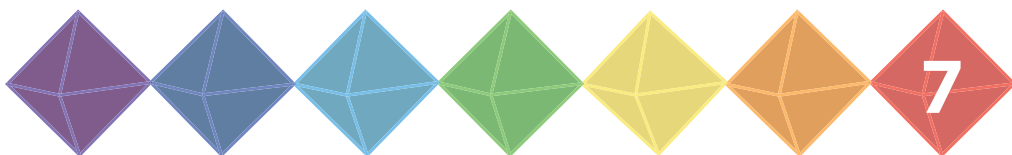


**Figure A6.8:** Temperature-dependent TRMC results for spin-coated MAPbI<sub>3</sub>, prepared from PbAc<sub>2</sub> precursor (see also **Chapter 5**), together with fitted data (dotted lines).





# Band-Like Charge Transport in Antimony-Bismuth Alloyed $\text{Cs}_2\text{AgBi}_{1-x}\text{Sb}_x\text{Br}_6$ Halide Double Perovskites



## ABSTRACT

The toxicity of lead is one of the major drawbacks that hampers commercialization of perovskite-based solar cells. Recently, halide double perovskites, such as  $\text{Cs}_2\text{AgBiBr}_6$ , have been reported as promising lead-free alternatives. However, it remains unclear whether the charge transport properties of these materials are as favorable as for lead-based perovskites. In this chapter, we study the charge transport properties of  $\text{Cs}_2\text{AgBiBr}_6$  and antimony-bismuth alloyed  $\text{Cs}_2\text{AgBi}_{1-x}\text{Sb}_x\text{Br}_6$ , with bandgaps tunable from 2.0 to 1.6 eV. Using temperature-dependent PR-TRMC, we find that the mobility is proportional to  $T^p$  (with  $p \sim 1.5$ ). This indicates that phonon scattering is the dominant scattering mechanism determining charge carrier mobility in these HDPs, similar to state-of-the-art lead-based perovskites. In addition, we show that wet chemical processing of  $\text{Cs}_2\text{AgBi}_{1-x}\text{Sb}_x\text{Br}_6$  powders is a successful route to prepare thin films of these materials, which paves the way toward photovoltaic devices based on non-toxic HDPs with tunable bandgaps.

### Based on

Eline M. Hutter, María Gélvez-Rueda, Davide Bartesaghi, Ferdinand C. Grozema, Tom J. Savenije, Band-Like Charge Transport in Antimony-Bismuth Alloyed  $\text{Cs}_2\text{AgBi}_{1-x}\text{Sb}_x\text{Br}_6$  Halide Double Perovskites (submitted)

*This project was funded by a Fulbright Scholarship and partially conducted in the group of dr. Hemamala Karunadasa at Stanford University.*

## 7.1 Introduction

Metal halide perovskites have not only yielded highly efficient single junction photovoltaic devices,<sup>1–3</sup> but were also successfully used as top cells in two-cell configurations with Si-based bottom cells, having the potential to further boost the efficiencies of commercial Si solar cells.<sup>4</sup> As mentioned in **Chapter 1**, the highest performances so far have been obtained using lead-based perovskites, as these show excellent light absorption and charge transport properties (as elaborated in **Chapters 2 to 6**).<sup>5</sup> However, one of the major drawbacks that hampers commercialization of metal halide perovskite-based solar cells is the toxicity of lead, which is specifically harmful in view of its relatively higher water-solubility in its 2+ oxidation state.<sup>6</sup> Therefore, lead should ideally be replaced with a less toxic alternative, while preserving the favorable properties found in lead-based perovskites. One of the approaches towards lead-free perovskites are halide double perovskites (HDPs), which adapt the elpasolite crystal structure.<sup>7</sup> Here, the  $\text{Pb}^{2+}$  is replaced with a 1-to-1 mixture of monovalent and trivalent metal ions, such as  $\text{Ag}^+$  and  $\text{Bi}^{3+}$ , which are incorporated in the lattice in an alternating fashion.<sup>8–10</sup> The recently reported HDPs  $\text{Cs}_2\text{AgBiBr}_6$  and  $\text{Cs}_2\text{AgBiCl}_6$  are indirect semiconductors with bandgaps of 2.19 and 2.77 eV, respectively,<sup>8</sup> and have reduced light absorption compared to lead iodide perovskites. However, it was also shown that alloying  $\text{Tl}^{3+}$  or  $\text{Sb}^{3+}$  can be used as a strategy to decrease the bandgap of  $\text{Cs}_2\text{AgBiBr}_6$  toward values more relevant for single-junction solar cells.<sup>11,12</sup> Here, the  $\text{Tl}^{3+}$  or  $\text{Sb}^{3+}$  is thought to substitute for  $\text{Bi}^{3+}$ .<sup>11,12</sup> Although HDPs of various compositions have been designed,<sup>11–15</sup> it remains unclear whether the transport properties of these HDPs are as favorable as for their lead-based analogues. Additionally, there have been no reports presenting the synthesis and characterization of thin films of alloyed HDPs, which is a crucial step toward devices of these materials.

In this chapter, we study the optoelectronic properties of  $\text{Cs}_2\text{AgBiBr}_6$  and investigate the effect of partially replacing  $\text{Bi}^{3+}$  with the non-toxic  $\text{Sb}^{3+}$ , yielding HDPs with the general formula  $\text{Cs}_2\text{AgBi}_{1-x}\text{Sb}_x\text{Br}_6$ . As reported previously, powders of these materials show an absorption red-shift with increasing  $x$ , reaching  $\sim 1.6$  eV upon replacing 40% of the  $\text{Bi}^{3+}$  with  $\text{Sb}^{3+}$  (*i.e.*  $x = 0.4$ ).<sup>12</sup> Then, we use Pulse-Radiolysis Time-Resolved Microwave Conductivity (PR-TRMC) measurements to gain insight in the mobility of free charges generated by an electron pulse as a function of  $x$  and temperature.<sup>16–18</sup> Interestingly, we find that the charge carrier mobility decreases only marginally on increasing the fraction of Sb. Furthermore, we observe that, independent of the Sb content, the mobility decreases with increasing temperature in between 140 and 420 K. Importantly, these results indicate band-like transport of charges in  $\text{Cs}_2\text{AgBiBr}_6$  and antimony-bismuth alloyed analogues, in which the mobility is limited by phonon scattering. The observation that the charge transport mechanism is very similar to lead-based perovskites<sup>19–21</sup> highlights the great potential of these materials as non-toxic alternatives. Finally, we find that dissolving the  $\text{Cs}_2\text{AgBi}_{1-x}\text{Sb}_x\text{Br}_6$  powders in DMSO is a successful route to spin-coat thin films of HDPs with mixed trivalent metals. Also in these thin films, the bandgap gradually reduces on increasing the Sb content, which paves the way toward photovoltaic devices based on HDPs with tunable bandgaps.

## 7.2 Powders of $\text{Cs}_2\text{AgBi}_{1-x}\text{Sb}_x\text{Br}_6$

Powders of  $\text{Cs}_2\text{AgBi}_{1-x}\text{Sb}_x\text{Br}_6$ , with  $x$  values ranging from 0 to 0.4, were prepared from stoichiometric mixtures of the precursors  $\text{CsBr}$ ,  $\text{AgBr}$ ,  $\text{BiBr}_3$  and  $\text{SbBr}_3$  following previously reported procedures.<sup>12</sup> The powders were ground, sealed in tubes under vacuum and then heated to 320 °C for 3 days.<sup>12</sup> We used X-ray photoelectron spectroscopy (XPS) to investigate the content of Sb in each sample (see **Table A7.1** in **Appendices**), and find that the Sb-to-Bi ratio follows the expected trend based on the stoichiometry of the precursor mixtures. **Figure 7.1a** shows the absorption spectra, measured using an integrating sphere, of  $\text{Cs}_2\text{AgBi}_{1-x}\text{Sb}_x\text{Br}_6$  powders with  $x = 0, 0.05, 0.1$  and 0.4, attached to quartz substrates using optically clear adhesive. These spectra show that increasing the Sb content gradually reduces the bandgap, resulting in absorption onset values as low as 1.6 eV ( $\sim 775$  nm) for  $x = 0.4$ . Although these absolute values are different from those derived using reflection measurements,<sup>12</sup> the bandgap reduction on alloying Bi with Sb is consistent with previous reports.<sup>12,13</sup> Furthermore, all of the samples show X-ray reflections characteristic of the double perovskite structure, see **Figure 7.1b**, which monotonically shift to larger angles on increasing  $x$  (see also **Figure A7.1** in **Appendices**). These results indicate that the lattice is contracted while the overall crystal structure is preserved, supporting the replacement of  $\text{Bi}^{3+}$  with the smaller  $\text{Sb}^{3+}$ .

To investigate the suitability of  $\text{Cs}_2\text{AgBiBr}_6$  and mixed antimony-bismuth HDPs for photovoltaic applications, we studied the transport of free charges in powders of these materials using the PR-TRMC technique.<sup>16,17</sup> With this technique, free charges are homogeneously generated throughout the sample by irradiation with a high-energy electron pulse. The primary electrons from the pulse are not injected but lose part of their energy by ionizing the sample, resulting in a uniform distribution of electrons and holes. The density of charges initially generated by each high energy electron from the

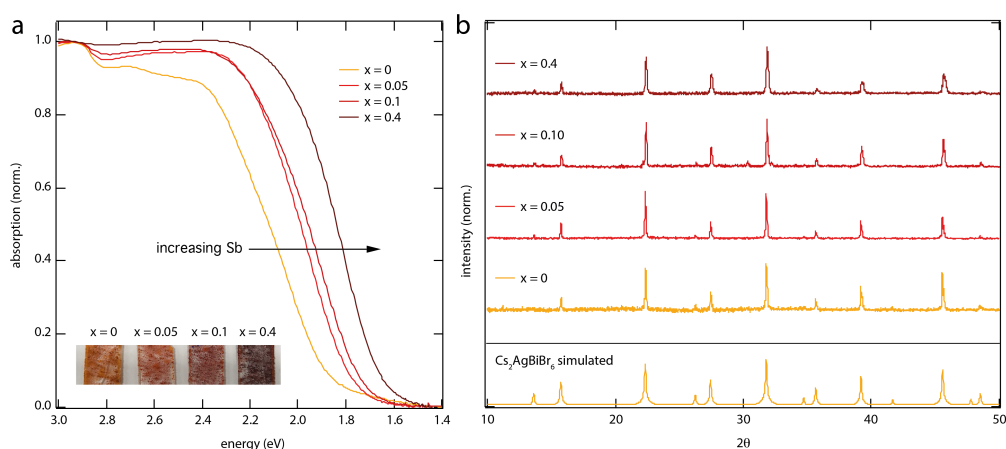


**Figure 7.1:** (a) Absorption spectra and (b) powder X-ray diffraction (XRD) patterns (Cu  $K\alpha$  radiation,  $\lambda = 1.54$  Å) of mixed antimony-bismuth halide double perovskites with the general formula  $\text{Cs}_2\text{AgBi}_{1-x}\text{Sb}_x\text{Br}_6$ .

pulse can be calculated using previously reported procedures (see experimental section). The total density of free charges  $n_0$  created by the electron pulse can be varied by changing its duration. Similar to the laser-induced TRMC measurements (see **Paragraph 2.4**), a microwave probe is then used to measure the change in conductivity on the generation of free charges, which scales with the number and mobility of charge carriers.<sup>16,18</sup> Importantly, since the initial density of free charges can be tuned independently of the exciton binding energy, the PR-TRMC technique is very suitable to determine the temperature-dependent mobility. Similar to the more widely used laser-induced TRMC,<sup>22,23</sup> the end-of-pulse charge density  $n$  can however still be affected by fast trapping or recombination of mobile charges within the instrumental response time of 1 ns (see also **Figure 2.7**). Therefore, we choose a pulse length at which losses are minimized so that  $n/n_0$  is closest to unity. **Figure 7.2a** shows the sum of electron and hole mobility  $\Sigma\mu$  for  $\text{Cs}_2\text{AgBi}_{1-x}\text{Sb}_x\text{Br}_6$  with  $x = 0, 0.05, 0.1$  and  $0.4$  at temperatures ranging from 140 to 420 K. From here, we find that at room temperature,  $\Sigma\mu$  is at least  $0.3 \text{ cm}^2/(\text{Vs})$  for  $\text{Cs}_2\text{AgBiBr}_6$  ( $x = 0$ ) powders, which is only about four times lower than the mobility observed in  $\text{CsPbBr}_3$  crystals using the same technique.<sup>17,22</sup> Considering that the effective mass of holes in  $\text{Cs}_2\text{AgBiBr}_6$  is calculated to be smaller than for its lead-based analogue (*i.e.*  $\text{CsPbBr}_3$ ) and the effective electron masses are calculated to be nearly the same,<sup>8</sup> the mobilities are actually expected to be somewhat higher in  $\text{Cs}_2\text{AgBiBr}_6$ . Therefore, this lower mobility observed in  $\text{Cs}_2\text{AgBiBr}_6$  could result from shorter scattering times, due to enhanced scattering with phonons or defects. On partially replacing the  $\text{Bi}^{3+}$  with  $\text{Sb}^{3+}$ , slightly reduced mobilities are observed, although at each temperature the absolute values stay within the same order of magnitude. Furthermore, independent of  $x$ , the mobility decreases with rising temperatures in between 140 and 420 K. On further analysis of the data, we find that  $\Sigma\mu$  scales with  $T^{-1.15}$  for  $x = 0$ ,  $T^{-1.62}$  ( $x = 0.05$ ),  $T^{-1.19}$  ( $x = 0.1$ ) and  $T^{-1.34}$  ( $x = 0.4$ ). Importantly, these negative powers indicate that phonon scattering (*i.e.*  $\mu \propto T^{-1.5}$ ) is the dominant scattering mechanism determining charge carrier mobility in these HDPs (**Equation 2.13**). These powers are within the same range as state-of-the-art lead-based perovskites, for which values in between -1.2 and -1.6 have been reported.<sup>19,21,24,25</sup> Additionally, the observation that these negative powers are very similar for the different  $x$  values suggests that the charge transport mechanism is not substantially disturbed on alloying bismuth with antimony. This means that independent of the  $\text{Sb}^{3+}$  content in the  $\text{Cs}_2\text{AgBiBr}_6$  lattice, there is band-like transport of charges with no indication of major defect scattering. As mentioned above, charge carrier losses within the instrumental response time leads to a reduction of  $n/n_0$ . Therefore, to get insight into sub-ns recombination processes, we can plot  $(n/n_0)\Sigma\mu$  as a function of  $n_0$  ( $\text{cm}^{-3}$ ). This is shown in **Figure 7.2b** for  $\text{Cs}_2\text{AgBiBr}_6$  (upper panel) and  $\text{Cs}_2\text{AgBi}_{0.9}\text{Sb}_{0.1}\text{Br}_6$  (lower panel) for temperatures ranging from 140 to 420 K. At each temperature,  $(n/n_0)\Sigma\mu$  initially rises on increasing charge carrier densities. We attribute this to sub-ns charge carrier trapping, leading to low yields if the trap density is higher than the charge carrier density.<sup>26,27</sup> Gradual saturation of these traps then results in increased  $n$  values for higher  $n_0$  and thus, an enhancement of  $n/n_0$

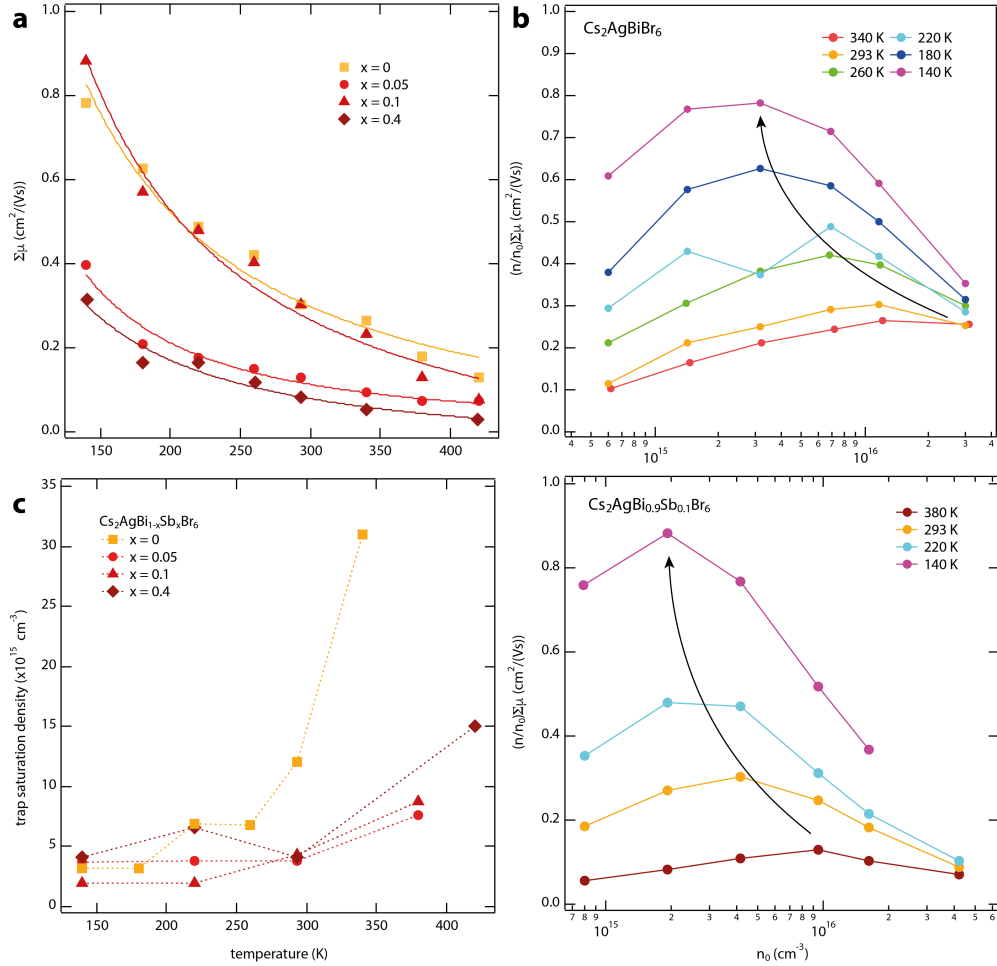


**Figure 7.2:** (a) Dots: mobility  $\Sigma\mu$  as function of temperature for  $x = 0$  (squares),  $x = 0.05$  (spheres),  $x = 0.1$  (triangles) and  $x = 0.4$  (diamonds), determined using the PR-TRMC technique. On fitting these mobilities to  $\mu(T) \propto T^{-p}$ , added as solid lines, we obtained  $p$ -values of -1.15 ( $x = 0$ ), -1.62 ( $x = 0.05$ ), -1.19 ( $x = 0.1$ ) and -1.34 ( $x = 0.4$ ). (b)  $(n/n_0)\Sigma\mu$  as function of  $n_0$  and temperature for  $x = 0$  (top) and  $x = 0.1$  (bottom). (c) Trap saturation density as function of temperature for  $x = 0$  (squares),  $x = 0.05$  (spheres),  $x = 0.1$  (triangles) and  $x = 0.4$  (diamonds), obtained from the maximum  $n/n_0$ .

(similar to the data shown in **Figure 6.2b**). On further increasing  $n_0$ ,  $n/n_0$  decreases again, which is typically observed if higher order recombination starts to dominate.<sup>28,29</sup> Therefore, the charge carrier concentration at which  $(n/n_0)\Sigma\mu$  reaches maximum values represents the regime in which band-to-band recombination is in competition with trap-assisted recombination, and can thus be used as an indication of the trap saturation density ( $\text{cm}^{-3}$ ). **Figure 7.2c** displays the densities at which the traps are saturated as



function of temperature for the sample with ( $x > 0$ ) and without ( $x = 0$ ) antimony. For  $\text{Cs}_2\text{AgBiBr}_6$ , this shows a clear increase from  $3 \times 10^{15} \text{ cm}^{-3}$  at 140 K to more than  $3 \times 10^{16} \text{ cm}^{-3}$  for  $T > 340 \text{ K}$ . The room-temperature value of  $1.2 \times 10^{16} \text{ cm}^{-3}$  is close to the previously suggested upper limit of  $10^{16} \text{ cm}^{-3}$  for a  $\text{Cs}_2\text{AgBiBr}_6$  single crystal.<sup>30</sup> Interestingly, the temperature dependence of  $(n/n_0)_{\text{max}}$  suggests that the trap density is enhanced with increasing temperatures, which could be due to the origin of the traps being related to vacancies or interstitials resulting from thermal displacement of ions. Alternatively, it might be that trap states originate from thermal ionization of defects, which also results in increased trap densities at higher temperatures. For the Sb-containing HDPs, the trap saturation densities at 140 K are 2 to  $4 \times 10^{15} \text{ cm}^{-3}$  and thus, close to the antimony-free  $\text{Cs}_2\text{AgBiBr}_6$ . Also here, an enhancement is observed as the temperature rises, with  $(n/n_0)$  reaching a maximum just below  $10^{16} \text{ cm}^{-3}$  at 380 K for  $\text{Cs}_2\text{AgBi}_{0.9}\text{Sb}_{0.1}\text{Br}_6$  (see bottom panel in **Figure 7.2b**) and the other antimony-bismuth alloyed HDP powders (see also **Figure A7.2** in **Appendices**). Most importantly, at and above room temperature, the trap saturation densities for  $x > 0$  are about a factor three lower than for  $x = 0$ , see **Figure 7.2c**. If indeed the trap states in  $\text{Cs}_2\text{AgBiBr}_6$  are related to thermal ionic motion, these results would mean that this can be partially suppressed by replacing some of the  $\text{Bi}^{3+}$  with  $\text{Sb}^{3+}$ .

We note that in general, the charge carrier lifetimes in these HDP powders are a few hundred nanoseconds and thus, relatively short compared to fully optimized state-of-the-art lead-based MHPs (see **Figure A7.3** in **Appendices**), which might be due to the trap densities being two orders of magnitude lower for the latter.<sup>17,28</sup> However, the above results at least suggest that the combination of decent charge carrier mobilities and tunable bandgaps is feasible in HDPs, which highlights their potential as non-toxic alternatives to lead-based perovskites.

### 7.3 Thin films of $\text{Cs}_2\text{AgBi}_{1-x}\text{Sb}_x\text{Br}_6$

The preparation of thin films is a crucial step toward devices employing HDPs with tunable bandgaps, and also important to further investigate their optoelectronic properties using spectroscopic techniques. Although it was recently shown that  $\text{Cs}_2\text{AgBiBr}_6$  films can be spin-coated from a solution of its precursors in DMSO,<sup>31</sup> there have been no reports on mixed trivalent metal HDP films. Here, we used the products of the solid-state synthesis to prepare thin films of  $\text{Cs}_2\text{AgBi}_{1-x}\text{Sb}_x\text{Br}_6$ , see also experimental methods. These powders were dissolved in DMSO at 0.5 M, yielding clear solutions with yellow to orange colour (depending on  $x$ ). The solutions, preheated to 75 °C, were then spin-coated on quartz substrates, followed by annealing at 200 °C ( $x = 0$ )<sup>31</sup> or 90 °C (for  $x > 0$ , to prevent the formation of undesired side phases).

**Figure 7.3a** shows the XRD pattern of the resulting films with  $x = 0, 0.05, 0.1$ , and  $0.4$ , showing all of the reflections characteristic of the HDP crystal structure. The shift to higher angles (see also **Figure A7.4** in **Appendices**) shows that the lattice parameters are reduced on addition of Sb, consistent with  $\text{Sb}^{3+}$  replacing the larger  $\text{Bi}^{3+}$  in these HDP thin films. Note that the different relative intensities of the reflections compared to the

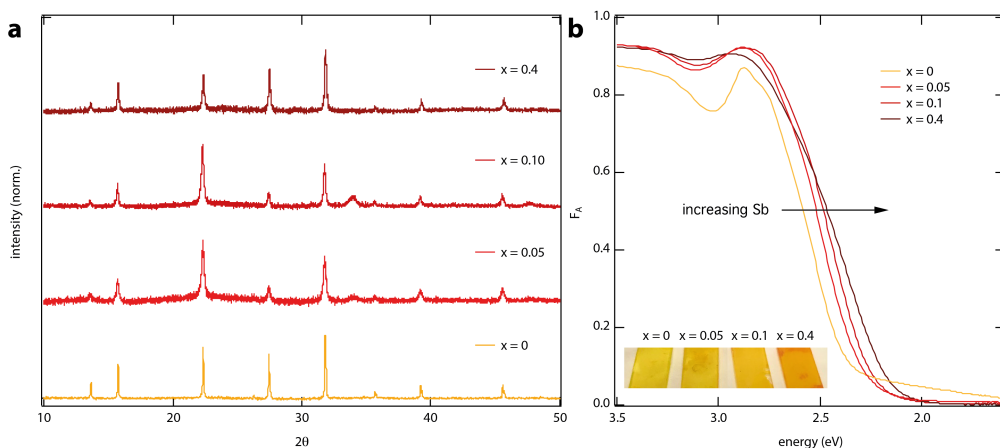


**Figure 7.3:** (a) X-Ray Diffraction patterns and (b) absorption spectra of thin  $\text{Cs}_2\text{AgBi}_{1-x}\text{Sb}_x\text{Br}_6$  films, spin-coated from solutions of the powders (0.5 M) in DMSO.

corresponding powders (**Figure 7.1c**) most likely result from preferential orientations of the crystalline domains with respect to the substrate. In addition, XPS analysis (**Figure A7.5** and **Table A2** in **Appendices**) of the thin films indicates higher Sb fractions for increasing  $x$ , which we find to be homogeneously distributed according to SEM-EDS analysis (**Figure A7.6** in **Appendices**). Altogether, the above results suggest that the overall stoichiometries of the powders are well preserved in the thin films.

**Figure 7.3b** shows the absorption spectra of the films. In general, the observed absorption onsets are different for the films than for the corresponding powders. This can be understood from the low absorption coefficients around the onset due to the indirect bandgap so that the absorption is very sensitive for the sample thickness (see **Figure A7.7** in **Appendices**).<sup>9,12</sup> However, consistent with the  $\text{Cs}_2\text{AgBi}_{1-x}\text{Sb}_x\text{Br}_6$  powders, the absorption onset of the films is red-shifted on increasing  $x$ , indicating that alloying  $\text{Bi}^{3+}$  and  $\text{Sb}^{3+}$  is an effective strategy to manipulate the bandgap in thin HDP films. To investigate to what extent the PR-TRMC results of the antimony-bismuth alloyed HDP powders (**Figure 7.2**) are representative for light-generated charges in the thin  $\text{Cs}_2\text{AgBi}_{1-x}\text{Sb}_x\text{Br}_6$  films, we recorded the photo-conductance using laser-induced TRMC measurements.<sup>22,23</sup> **Figure 7.4** shows the photo-conductance as function of time for the  $\text{Cs}_2\text{AgBiBr}_6$  (**Figure 7.4a**) and  $\text{Cs}_2\text{AgBi}_{0.6}\text{Sb}_{0.4}\text{Br}_6$  (**Figure 7.4b**) films, using an excitation energy of 2.8 eV (445 nm). Here, the maximum signal height represents the yield-mobility product  $\varphi\Sigma\mu$ , in which the yield  $\varphi$  represents the ratio between free charges and absorbed photons.<sup>23</sup> For  $\text{Cs}_2\text{AgBiBr}_6$  (**Figure 7.4a**), consistent with the PR-TRMC measurements, we initially observe an enhancement of the maximum signal height (i.e.  $\varphi\Sigma\mu$ ), followed by a decrease on further increasing the excitation density in  $\text{Cs}_2\text{AgBiBr}_6$  (**Figure 7.4a**). Interestingly, the maximum  $\varphi\Sigma\mu$  is found at a charge

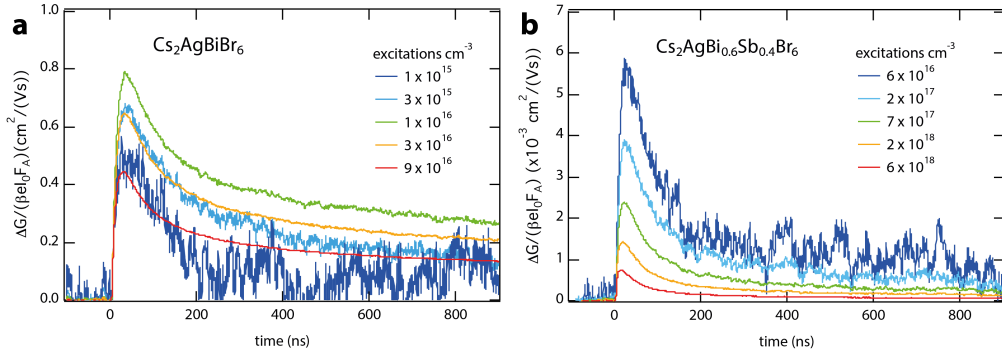


**Figure 7.4:** (a-b) Photo-conductance as function of time after excitation at 2.8 eV ( $\lambda = 445$  nm) for  $\text{Cs}_2\text{AgBiBr}_6$  (a) and  $\text{Cs}_2\text{AgBi}_{0.6}\text{Sb}_{0.4}\text{Br}_6$  (b).

density  $1 \times 10^{16} \text{ cm}^{-3}$ , meaning that the density at which higher order recombination starts to compete with trap filling in these thin films is nearly identical to that of the corresponding powders (*i.e.*  $1.2 \times 10^{16} \text{ cm}^{-3}$  at room temperature, recall **Figure 7.2c**). We can further conclude from the maximum  $\varphi \Sigma \mu$  that the sum of electron and hole mobilities amounts to at least  $0.8 \text{ cm}^2 / (\text{Vs})$  for the non-alloyed HDP (**Figure 7.4a**,  $x = 0$ ), similar to previously reported values for a  $\text{Cs}_2\text{AgBiBr}_6$  thin film.<sup>30</sup> The photo-conductance signals decay at timescales on the order of a microsecond. This observation is in contrast with previous work, which showed that all mobile charges recombine within several nanoseconds after exciting a  $\text{Cs}_2\text{AgBiBr}_6$  film synthesized under ambient conditions at 2.5 eV.<sup>30</sup> We suspect that the longer recombination lifetimes in the films in this chapter are due to the fact that all of these samples were synthesized under inert conditions and not exposed to air at any time before or during the measurements. The microsecond lifetimes in  $\text{Cs}_2\text{AgBiBr}_6$  films synthesized under inert conditions (**Figure 7.4a**) suggest that at least one of the charges remains free, and that the decay represents the recombination between a free charge and its trapped counter-charge.

For the  $\text{Cs}_2\text{AgBi}_{0.6}\text{Sb}_{0.4}\text{Br}_6$  (**Figure 7.4b**) thin film, the  $\varphi \Sigma \mu$  decreases on increasing the charge density from  $6 \times 10^{16}$  to  $6 \times 10^{18} \text{ cm}^{-3}$ , indicating that higher order recombination processes dominate in this regime.<sup>29</sup> Additionally, the maximum  $\varphi \Sigma \mu$  is two orders of magnitude smaller than for the antimony-free HDP film (**Figure 7.4a**). On measuring the corresponding powders with laser-induced TRMC, we also obtained lower photo-conductance signals for the Sb-containing HDPs (**Figure A7.8** in **Appendices**). Considering that the charge carrier mobilities are only slightly lowered on replacing Bi with Sb (**Figure 7.2a**), the reduced  $\varphi \Sigma \mu$  in the photo-conductance measurements probably results from a low yield due to sub-ns recombination. However, it seems likely that further optimizing the synthesis procedure and annealing conditions will improve

the sample quality and hence, increase both mobilities and lifetimes in thin films of Sb-containing HDPs.

## 7.4 Conclusions

In this chapter, we have investigated the optoelectronic properties of the double perovskite  $\text{Cs}_2\text{AgBiBr}_6$ , in which controlled amounts of  $\text{Bi}^{3+}$  have been replaced with  $\text{Sb}^{3+}$  to yield perovskites with the general formula  $\text{Cs}_2\text{AgBi}_{1-x}\text{Sb}_x\text{Br}_6$ , showing a bandgap red-shift with increasing Sb content down to 1.6 eV for  $x = 0.4$ . With pulse-radiolysis TRMC measurements on  $\text{Cs}_2\text{AgBi}_{1-x}\text{Sb}_x\text{Br}_6$  powders, we observe that for all  $x$ -values, the charge carrier mobility increases on decreasing temperature. Importantly, the above observations suggest that replacing bismuth with antimony is a successful strategy to manipulate the absorption onset of  $\text{Cs}_2\text{AgBiBr}_6$ , while preserving band-like transport of free charges. Finally, we demonstrate a route to prepare thin films of  $\text{Cs}_2\text{AgBi}_{1-x}\text{Sb}_x\text{Br}_6$ , showing that incorporation of Sb can red-shift the absorption onset up to a few hundred meV in thin  $\text{Cs}_2\text{AgBiBr}_6$  films. Altogether, these results represent a crucial step toward lead-free perovskite devices implementing antimony-bismuth alloyed HDPs.

## 7.5 Experimental Methods

### $\text{Cs}_2\text{AgBi}_{1-x}\text{Sb}_x\text{Br}_6$ powders

1 mmol CsBr, 0.5 mmol AgBr,  $(1-x)0.5$  mmol  $\text{BiBr}_3$  and  $0.5x$  mmol  $\text{SbBr}_3$  were ground until fine powders were obtained. The mixtures were sealed in glass tubes under vacuum and heated in a box furnace to 320 °C (heating rate of 3 °C/min) and kept at this temperature for three hours.<sup>12</sup> After cooling down to room temperature (cooling rate of 3 °C/min), the closed tubes containing the products were transferred to a nitrogen-filled glovebox.

### $\text{Cs}_2\text{AgBi}_{1-x}\text{Sb}_x\text{Br}_6$ thin films

0.5 mmol of  $\text{Cs}_2\text{AgBi}_{1-x}\text{Sb}_x\text{Br}_6$  was dissolved in 1 mL of DMSO at 75 °C under magnetic stirring in a nitrogen-filled glovebox.<sup>31</sup> Quartz substrates were cleaned with isopropanol and treated with an ozone plasma for 30 minutes. The  $\text{Cs}_2\text{AgBi}_{1-x}\text{Sb}_x\text{Br}_6$ /DMSO solutions were filtered and kept at 75 °C. Then, 100  $\mu\text{L}$  of the filtered solution was spin-coated on a quartz substrate using a two-step procedure starting at 500 rpm for 30 seconds (ramping speed of 100 rpm/s) followed by 60 seconds at 5000 rpm (ramping speed of 5000 rpm/s). The  $\text{Cs}_2\text{AgBiBr}_6$  ( $x = 0$ ) films were annealed at 200 °C for three minutes, and the Sb-containing films were annealed at 90 °C for three minutes.

### X-Ray Diffraction

X-Ray Diffraction patterns were obtained with a Bruker D8 diffractometer in a Bragg-Brentano configuration, using  $\text{Cu-K}\alpha$  ( $\lambda = 1.54 \text{ \AA}$ ) radiation.

### X-Ray Photo-electron Spectroscopy

XPS measurements were performed with a Thermo Scientific K-alpha instrument equipped with an Al K-alpha X-ray Source and a Flood Gun to avoid charging of the sample. For the high-resolution scans of C1s, O1s, Ag3d, Bi4f, Br3d, Sb3d and Cs3d signals the following parameters were used: spot size 400  $\mu\text{m}$ , pass energy 50 eV, energy step size 0.1 eV, dwell time 50 ms, 10 scans. XPS spectra were corrected using the atmospheric carbon C peak position (284.8 eV). Elemental quantification was performed using the Advantage software. High-resolution scans of each element were fit with a mixture of Gaussian and Lorentzian functions; the area under each peak was used to determine the concentration of each element.

### Optical characterization

For the PR-TRMC measurements, about 30 mg of each  $\text{Cs}_2\text{AgBi}_{1-x}\text{Sb}_x\text{Br}_6$  powder was used. For the absorption and photoconductance measurements, the  $\text{Cs}_2\text{AgBi}_{1-x}\text{Sb}_x\text{Br}_6$  powders were attached to quartz substrates using optically clear adhesive tape (Thorlabs). Absorption, photoluminescence and (PR-)TRMC measurements were performed as described in **Chapters 2, 3 and 5**.

### 7.6 Acknowledgments

Hemamala Karunadasa is acknowledged for facilitating this project and for critical reading of this chapter. We thank Adam Slavney for fruitful discussions.

### 7.7 References

1. Kojima, A., Teshima, K., Shirai, Y. & Miyasaka, T. Organometal halide perovskites as visible-light sensitizers for photovoltaic cells. *J. Am. Chem. Soc.* **131**, 6050–6051 (2009).
2. Stranks, S. D. *et al.* Electron-hole diffusion lengths exceeding 1 micrometer in an organometal trihalide perovskite absorber. *Science* **342**, 341–344 (2013).
3. <http://www.nrel.gov>.
4. McMeekin, D. P. *et al.* A mixed-cation lead mixed-halide perovskite absorber for tandem solar cells. *Science* **351**, 151–155 (2016).
5. Saliba, M. *et al.* Cesium-containing Triple Cation Perovskite Solar Cells: Improved Stability, Reproducibility and High Efficiency. *Energy Environ. Sci.* **9**, 1989 (2016).
6. Slavney, A. H. *et al.* Chemical Approaches to Addressing the Instability and Toxicity of Lead-Halide Perovskite Absorbers. *Inorg. Chem.* **56**, 46–55 (2016).
7. Knochenmuss, R., Reber, C., Rajasekharan, M. V. & Güdel, H. U. Broadband near-infrared luminescence of  $\text{Cr}^{+3}$  in the elpasolite lattices  $\text{Cs}_2\text{NaInCl}_6$ ,  $\text{Cs}_2\text{NaYCl}_6$ , and  $\text{Cs}_2\text{NaYBr}_6$ . *J. Chem. Phys.* **85**, 4280–4289 (1986).
8. McClure, E. T., Ball, M. R., Windl, W. & Woodward, P. M.  $\text{Cs}_2\text{AgBiX}_6$  (X = Br, Cl): New Visible Light Absorbing, Lead-Free Halide Perovskite Semiconductors. *Chem. Mater.* **28**, 1348–1354 (2016).
9. Slavney, A. H., Hu, T., Lindenberg, A. M. & Karunadasa, H. I. A Bismuth-Halide Double Perovskite with Long Carrier Recombination Lifetime for Photovoltaic Applications. *J. Am. Chem. Soc.* **138**, 2138–2141 (2016).
10. Filip, M. R., Hillman, S., Haghighirad, A. A., Snaith, H. J. & Giustino, F. Bandgaps of the Lead-Free Halide Double Perovskites  $\text{Cs}_2\text{BiAgCl}_6$  and  $\text{Cs}_2\text{BiAgBr}_6$  from Theory and Experiment. *J. Phys. Chem. Lett.* **7**, 2579–2585 (2016).
11. Slavney, A. H. *et al.* Defect-Induced Band-Edge Reconstruction of a Bismuth-Halide Double Perovskite for Visible-Light Absorption. *J. Am. Chem. Soc.* **139**, 5015–5018 (2017).
12. Du, K. K. Z., Meng, W., Wang, X., Yan, Y. & Mitzi, D. B. Bandgap Engineering of Lead-Free Double Perovskite  $\text{Cs}_2\text{AgBiBr}_6$  through Trivalent Metal Alloying. *Angew. Chemie - Int. Ed.* **56**, 8158–8162 (2017).
13. Tran, T. T., Panella, J. R., Chamorro, J. R., Morey, J. R. & McQueen, T. M. Designing Indirect-Direct Bandgap Transitions in Double Perovskites. *Mater. Horiz.* **4**, 688–693 (2017).
14. Du, K., Wang, X., Han, Q., Yan, Y. & Mitzi, B. Heterovalent B-Site Co-Alloying Approach for Halide Perovskite Bandgap Engineering. *ACS Energy Lett.* **2**, 2486–2490 (2017).
15. Volonakis, G. *et al.*  $\text{Cs}_2\text{InAgCl}_6$ : A New Lead-Free Halide Double Perovskite with Direct Bandgap. *J. Phys. Chem. Lett.* **8**, 772–778 (2017).
16. Warman, J. M. *et al.* Charge Mobilities in Organic Semiconducting Materials Determined by Pulse-Radiolysis Time-Resolved Microwave Conductivity:  $\pi$ -Bond-Conjugated Polymers versus  $\pi$ - $\pi$ -Stacked Discotics. *Chem. Mater.* **16**, 4600–4609 (2004).
17. Gélvez-Rueda, M. C. *et al.* Effect of Cation Rotation on Charge Dynamics in Hybrid Lead Halide Perovskites. *J. Phys. Chem. C* **120**, 16577–16585 (2016).
18. Grozema, F. C. & Siebbeles, L. D. A. Charge mobilities in conjugated polymers measured by pulse radiolysis time-resolved microwave conductivity: From single chains to solids. *J. Phys. Chem. Lett.* **2**, 2951–2958 (2011).
19. Savenije, T. J. *et al.* Thermally Activated Exciton Dissociation and Recombination Control the Carrier Dynamics in Organometal Halide Perovskite. *J. Phys. Chem. Lett.* **5**, 2189–2194 (2014).
20. Rehman, W. *et al.* Charge-Carrier Dynamics and Mobilities in Formamidinium Lead Mixed-Halide

- Perovskites. *Adv. Mater.* **27**, 7938–7944 (2015).
21. Karakus, M. *et al.* Phonon-Electron Scattering Limits Free Charge Mobility in Methylammonium Lead Iodide Perovskites. *J. Phys. Chem. Lett.* **6**, 4991–4996 (2015).
22. Hutter, E. M. *et al.* Direct-indirect character of the bandgap in methylammonium lead iodide perovskite. *Nat. Mater.* **16**, (2017).
23. Savenije, T. J., Ferguson, A. J., Kopidakis, N. & Rumbles, G. Revealing the dynamics of charge carriers in polymer:fullerene blends using photoinduced time-resolved microwave conductivity. *J. Phys. Chem. C* **117**, 24085–24103 (2013).
24. Milot, R. L., Eperon, G. E., Snaith, H. J., Johnston, M. B. & Herz, L. M. Temperature-Dependent Charge-Carrier Dynamics in  $\text{CH}_3\text{NH}_3\text{PbI}_3$  Perovskite Thin Films. *Adv. Funct. Mater.* **25**, 6218–6227 (2015).
25. Oga, H., Saeki, A., Ogomi, Y., Hayase, S. & Seki, S. Improved Understanding of the Electronic and Energetic Landscapes of Perovskite Solar Cells: High Local Charge Carrier Mobility, Reduced Recombination, and Extremely Shallow Traps. *J. Am. Chem. Soc.* **136**, 13818–13825 (2014).
26. Hutter, E. M. *et al.* Vapour-Deposited Cesium Lead Iodide Perovskites: Microsecond Charge Carrier Lifetimes and Enhanced Photovoltaic Performance. *ACS Energy Lett.* **2**, 1901–1908 (2017).
27. Savenije, T. J., Huijser, A., Vermeulen, M. J. W. & Katoh, R. Charge carrier dynamics in  $\text{TiO}_2$  nanoparticles at various temperatures. *Chem. Phys. Lett.* **461**, 93–96 (2008).
28. Hutter, E. M., Eperon, G. E., Stranks, S. D. & Savenije, T. J. Charge Carriers in Planar and Meso-Structured Organic-Inorganic Perovskites: Mobilities, Lifetimes and Concentrations of Trap States. *J. Phys. Chem. Lett.* **6**, 3082–3090 (2015).
29. Labram, J. G. & Chabinyc, M. L. Recombination at high carrier density in methylammonium lead iodide studied using time-resolved microwave conductivity. *J. Appl. Phys.* **122**, 65501 (2017).
30. Bartesaghi, D. *et al.* Charge Carrier Dynamics in  $\text{Cs}_2\text{AgBiBr}_6$  Double Perovskite. *J. Phys. Chem. C* **122**, 4809–4816 (2018).
31. Greul, E., Petrus, M. L., Binek, A., Docampo, P. & Bein, T. Highly stable, phase pure  $\text{Cs}_2\text{AgBiBr}_6$  double perovskite thin films for optoelectronic applications. *J. Mater. Chem. A* **0**, 1–10 (2017).
32. Klein, C. A. Bandgap Dependence and Related Features of Radiation Ionization Energies in Semiconductors. *J. Appl. Phys.* **39**, 2029–2038 (1968).
33. Alig, R. C. & Bloom, S. Electron-hole-pair creation energies in semiconductors. *Phys. Rev. Lett.* **35**, 1522–1525 (1975).

## Appendices

**Table A7.1:** XPS elemental analysis of  $\text{Cs}_2\text{AgBi}_{1-x}\text{Sb}_x\text{Br}_6$  powders.

$x$		% Cs	% Ag	% Bi	% Sb	% Br	Sb/(Sb+Bi)
<b>0</b>	spot 1	34.26	8.67	8.79	0.09	48.20	0.010
	spot 2	26.09	6.06	8.30	0.03	59.52	0.004
	average	30.18	7.37	8.55	0.06	53.86	<b>0.007</b>
<b>0.05</b>	spot 1	24.60	9.14	7.62	0.66	57.97	0.080
	spot 2	25.28	10.21	7.10	0.42	57.00	0.056
	average	24.94	9.68	7.36	0.54	57.49	<b>0.068</b>
<b>0.1</b>	spot 1	25.57	8.91	7.06	1.66	56.80	0.190
	spot 2	26.00	8.85	6.56	1.51	57.09	0.187
	average	25.79	8.88	6.81	1.59	56.95	<b>0.189</b>
<b>0.4</b>	spot 1	24.41	9.32	5.00	3.73	57.54	0.427
	spot 2	25.09	9.11	4.85	3.80	57.15	0.439
	average	24.75	9.22	4.93	3.77	57.35	<b>0.433</b>

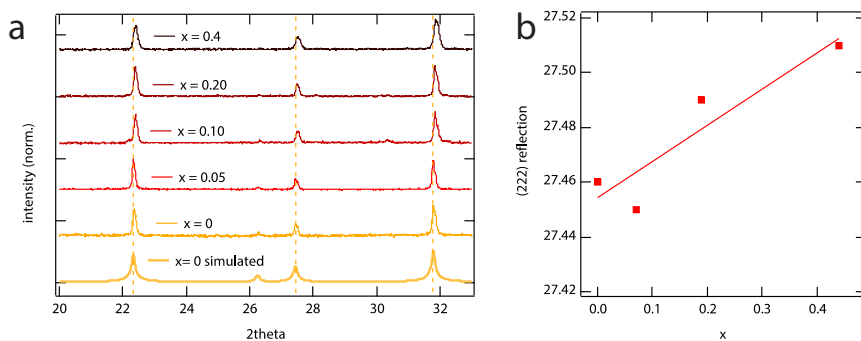


**Figure A7.1:** (a) Zoom-in of the X-Ray Diffraction patterns of  $\text{Cs}_2\text{AgBi}_{1-x}\text{Sb}_x\text{Br}_6$  from **Figure 7.1b**. The yellow dotted lines indicate the positions of the (022), (222) and (004) reflections, respectively, for  $\text{Cs}_2\text{AgBiBr}_6$ , showing that these shift to larger  $2\theta$  values for increasing  $x$ . This confirms that the lattice contracts on replacing Bi with the smaller Sb. (b)  $2\theta$  value of (222) reflection as function of Sb-content (using the  $x$  values from **Table A7.1**).

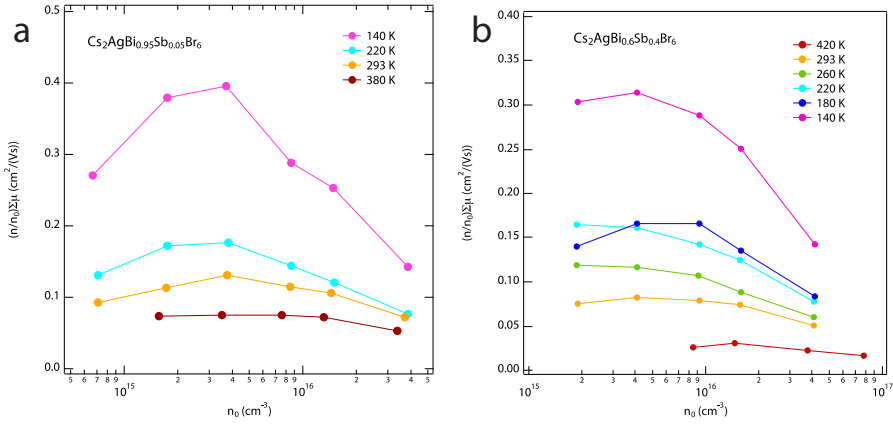


**Figure A7.2:**  $(n/n_0)\Sigma\mu$  as function of  $n_0$  and temperature for  $\text{Cs}_2\text{AgBi}_{1-x}\text{Sb}_x\text{Br}_6$  with  $x = 0.05$  (a) and  $x = 0.4$  (b). Similar to the data shown in **Figure 7.2b** in the main text, we used the maximum  $(n/n_0)\Sigma\mu$  at each temperature to estimate the trap saturation density, which is shown in **Figure 7.2c**. Note that for  $\text{Cs}_2\text{AgBi}_{0.6}\text{Sb}_{0.4}\text{Br}_6$  (b), at 220 K and higher, the  $(n/n_0)\Sigma\mu$  ( $T$ ) is nearly flat up to  $\sim 4 \times 10^{15} \text{ cm}^{-3}$ , suggesting that trap saturation occurs at or below the lowest densities used for the measurements.

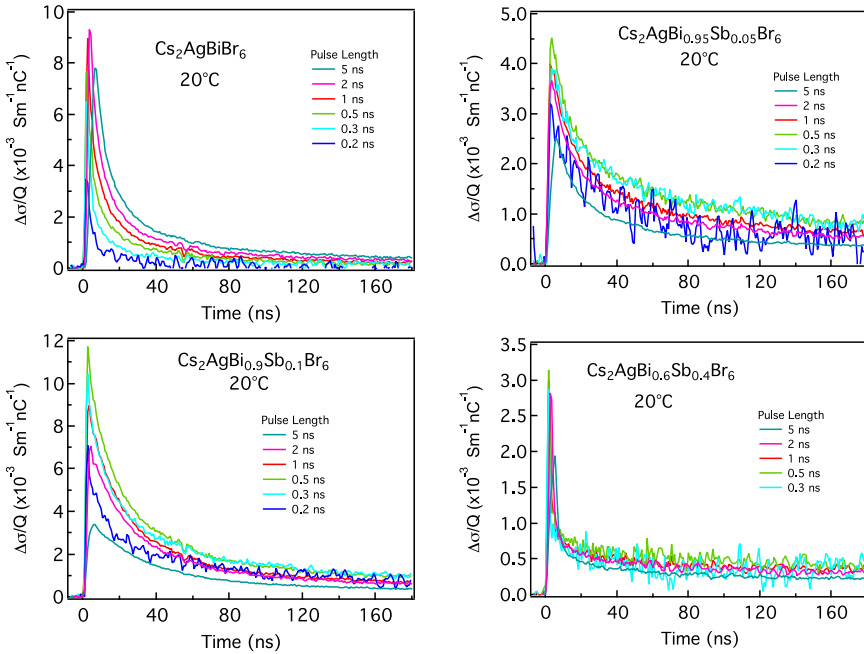


**Figure A7.3:** PR-TRMC lifetimes for the different  $\text{Cs}_2\text{AgBi}_{1-x}\text{Sb}_x\text{Br}_6$  powders at room temperature (293 K).



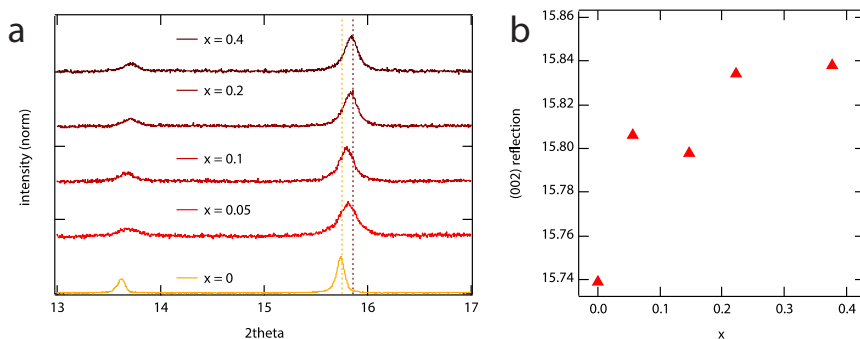


**Figure A7.4:** (a) Zoom-in of the X-Ray Diffraction patterns of  $\text{Cs}_2\text{AgBi}_{1-x}\text{Sb}_x\text{Br}_6$  from Figure 7.3a. The yellow and dark red dotted line indicate the positions of the  $(002)$  reflections for  $\text{Cs}_2\text{AgBiBr}_6$  and  $\text{Cs}_2\text{AgBi}_{0.6}\text{Sb}_{0.4}\text{Br}_6$ , respectively, showing that these shift to larger  $2\theta$  values for increasing  $x$ . This confirms that the lattice contracts on replacing Bi with the smaller Sb. (b)  $2\theta$  value of  $(002)$  reflection as function of  $x$ , using the values from Table A7.2.

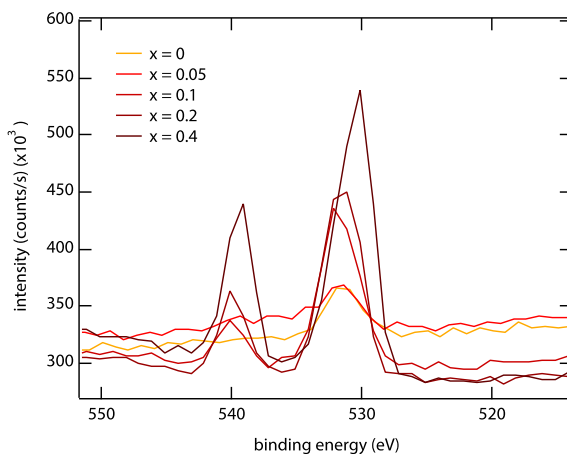


**Figure A7.5:** Zoom-in of X-ray photoelectron spectra of  $\text{Cs}_2\text{AgBi}_{1-x}\text{Sb}_x\text{Br}_6$  thin films, with  $x = 0, 0.05, 0.1, 0.2, 0.4$ . The peaks at 540 eV and 531 eV are characteristic for Sb; the (small) additional peak observed at 531 eV for  $x = 0$  originates from oxygen.

**Table A7.2:** XPS elemental analysis of  $\text{Cs}_2\text{AgBi}_{1-x}\text{Sb}_x\text{Br}_6$  thin films.

<b>x</b>		<b>% Cs</b>	<b>% Ag</b>	<b>% Bi</b>	<b>% Sb</b>	<b>% Br</b>	<b>Sb/(Sb+Bi)</b>
<b>0</b>	<i>spot 1</i>	21.93	6.84	6.81	0.03	64.39	0.004
	<i>spot 2</i>	23.18	7.15	8.39	0.05	61.22	0.006
	<i>average</i>	22.56	7.00	7.60	0.04	62.81	<b>0.005</b>
<b>0.05</b>	<i>spot 1</i>	21.48	9.11	8.69	0.21	60.50	0.024
	<i>spot 2</i>	19.05	12.03	13.73	1.31	53.87	0.087
	<i>average</i>	20.27	10.57	11.21	0.76	57.19	<b>0.055</b>
<b>0.1</b>	<i>spot 1</i>	20.29	9.89	7.27	1.21	61.34	0.143
	<i>spot 2</i>	28.01	10.39	9.20	1.65	50.76	0.152
	<i>average</i>	24.15	10.14	8.24	1.43	56.05	<b>0.147</b>
<b>0.2</b>	<i>spot 1</i>	21.33	7.76	7.24	2.08	61.59	0.223
	<i>spot 2</i>	22.86	9.79	7.88	2.27	57.20	0.224
	<i>average</i>	22.10	8.78	7.56	2.18	59.40	<b>0.223</b>
<b>0.4</b>	<i>spot 1</i>	21.97	8.47	5.51	4.00	60.05	0.421
	<i>spot 2</i>	23.28	15.38	11.37	5.73	44.24	0.335
	<i>average</i>	22.63	11.93	8.44	4.87	52.15	<b>0.378</b>

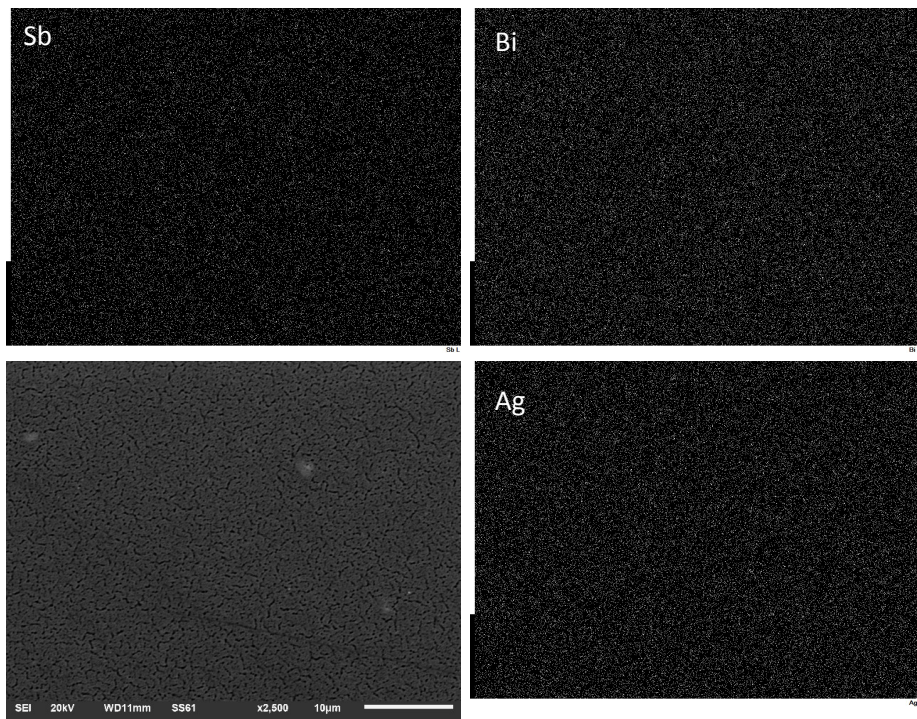


**Figure A7.6:** Scanning Electron Microscopy image of the  $\text{Cs}_2\text{AgBi}_{0.6}\text{Sb}_{0.4}\text{Br}_6$  thin film and corresponding EDS elemental analysis maps for Sb, Bi and Ag.

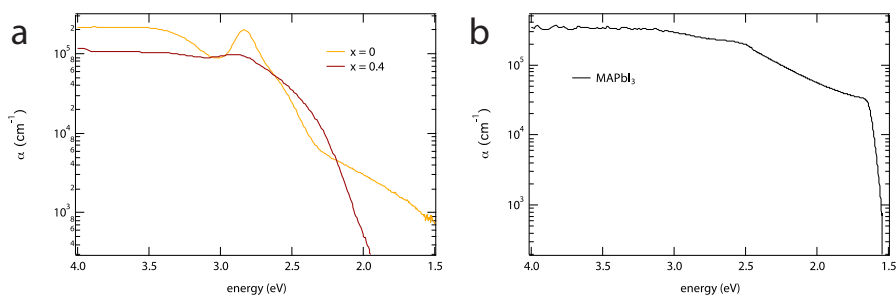


**Figure A7.7:** Energy-dependent absorption coefficient for  $\text{Cs}_2\text{AgBi}_{1-x}\text{Sb}_x\text{Br}_6$  with  $x = 0$  and  $0.4$ , determined from the absorption and transmission spectra of the thin films, recorded using an integrating sphere. The absorption coefficient of methylammonium lead iodide (MAPbI<sub>3</sub>), see also **Figure A5.11**, is shown for comparison.

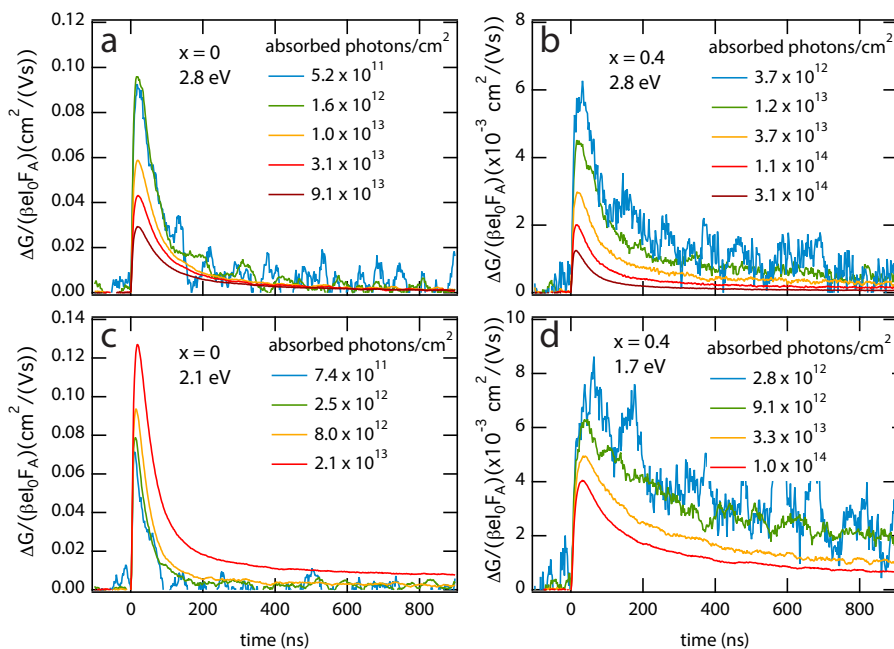


**Figure A7.8:** Intensity-normalized photo-conductance as function of time at an excitation energy of 2.8 eV for the  $\text{Cs}_2\text{AgBi}_{1-x}\text{Sb}_x\text{Br}_6$  powders  $x = 0$  (a) and  $x = 0.4$  (b) and at 2.1 eV for  $x = 0$  (c) and 1.7 eV for  $x = 0.4$  (d).



## Summary

In this thesis, we have investigated the optoelectronic properties of metal halide perovskites with a special focus on their application in solar cells. In less than a decade of development, metal halide perovskites have yielded solar cells with efficiencies comparable to commercialized technologies. However, there has been limited knowledge about the fundamental properties of these materials. As mentioned in the introduction, the efficiency of perovskite-based solar cells is still not at its theoretical limit. In order to rationally design solar cells with maximized efficiencies, we need to understand which factors are currently limiting the performance of perovskite-based solar cells. In general, one of the first important processes in a solar cell is the absorption of light. For metal halide perovskites based on lead iodide, a thickness of 0.3 micrometer is already sufficient to absorb a substantial amount of visible (sun-)light, which makes these materials very suitable for solar cells. Furthermore, it is crucial that this absorbed light is converted into a current of moving charges, also known as electricity. Semiconductor materials such as silicon or metal halide perovskites have the ideal properties to generate a current of charges from light. In order to use this current however, the charges need to be collected. The efficiency with which charges are collected in a solar cell is closely related to its power conversion efficiency.

In this research, we have used a number of spectroscopy techniques to investigate the above-mentioned properties. With these techniques, which are described in detail in **Chapter 2**, we use short laser pulses to illuminate the perovskites, thereby mimicking the processes occurring in a solar cell. Our main analysis method throughout this thesis is referred to as the time-resolved microwave conductivity (TRMC) technique, which we use to study the moving charges that have been generated in the perovskite after absorption of the laser light. From the interaction between these charges and a microwave field, we can get insight in the mobility of charges, which is a measure for the speed at which these move. Additionally, we can detect the lifetime of charges, *i.e.* how long these charges can move freely through the perovskite material. Both a high mobility and a long lifetime increase the probability of a charge to be collected, and therefore these are two crucial parameters governing the efficiency of a solar cell.

In **Chapter 3**, we investigate the mobility and lifetime of charges in lead iodide perovskites prepared *via* different routes. We observe that charges can get trapped in the perovskite layer, which decreases their lifetime and as a consequence, might unfavorably affect their collection probability. We find that trapping of moving charges especially occurs at low light intensities. Importantly however, we also find that the quality of the perovskite layer is highly dependent on both the preparation route and the precursors used. For instance, using a chloride-based lead precursor minimizes the number of trap

states and thus, changing the precursors can be used to optimize the properties of the resulting perovskite layer. On extensive analysis of our TRMC data, we further estimate that charges could move over a distance of about 10 micrometers. This is sufficient to overcome the 0.3 micrometer that is needed to absorb the sunlight. Therefore, these results mean that in principle, it should be feasible to collect the majority of charges from the perovskite layer.

However, we find in **Chapter 4** that this is not necessarily the case. Although the charges move relatively easily throughout the perovskite layer, these are in many cases immobilized at the interface between the perovskite and the material that is supposed to extract these charges in an operating solar cell. From here, we conclude that this is most likely the main obstacle for the collection of moving charges. In other words, to obtain more efficient perovskite-based solar cells, the quality of the interfaces should be substantially improved.

If a negative charge, an electron, is brought into motion by sunlight, a positively charged hole remains behind. When a moving electron passes a hole, it can decay back into the hole after which the electron is no longer moving. This process is called recombination. If the chance of recombination increases, the chance of collection decreases. In **Chapter 5**, we investigate the mechanism of electron-hole recombination in lead iodide perovskites. Importantly, we find that electrons encounter a barrier for recombination, which makes it less likely for electrons to decay into holes. Therefore, the chance of recombination is smaller than initially assumed. Hereby, we have found a unique property of lead iodide perovskites.

The perovskites described in **Chapters 3 to 5** all have the same composition: next to lead and iodide these contain organic molecules. The organic molecules have a dipole moment, meaning these are negatively charged at one side and positively charged at the other side. Considering that moving charges such as electrons are also negatively charged, it has been proposed that the dipole moment affects the movement of charges (**Chapter 3**) and might be responsible for the recombination barrier (**Chapter 5**).

In **Chapter 6**, we test these hypotheses by replacing the organic molecule with cesium, which is an inorganic component without a dipole moment. Interestingly, we find that the movement of charges and their recombination mechanism in these cesium-based perovskites is not very different from the perovskites with the organic cation. From here, we conclude that the properties that we have found in **Chapters 3 and 5** originate from the lead and/or iodide, instead of the dipole moment of the organic cation. Therefore, the exact mechanism behind the recombination barrier has to be further investigated.

As mentioned before, one of the components of perovskite-based solar cells is lead, which is present in a toxic and water-soluble state. From an environmental point of view, it would therefore be favorable if lead could be replaced with less toxic metals, while the properties that make perovskites suitable for high efficiency solar cells are preserved. In **Chapter 7**, we prepare perovskites based on a mixture of silver, bismuth and antimony instead of lead. We observe that the amount of absorbed light depends on the amount of antimony with respect to bismuth. This means that varying the ratio

between antimony and bismuth can be used to manipulate the absorption properties of these perovskites. Additionally, we measure that charges can move freely throughout these materials, which makes them promising candidates for lead-free perovskite solar cells.

Will perovskite-based solar cells ever dominate the market? And which perovskite composition will eventually find a commercial application? Only time will tell. Anyway, with this research we have at least contributed to revealing some of the properties of these fascinating class of semiconductor materials.





## Samenvatting

In dit proefschrift zijn de opto-elektronische eigenschappen onderzocht van metaalhalideperovskieten, met een speciale focus op de toepassing van deze materialen in zonnecellen. Hoewel metaalhalideperovskieten in relatief korte tijd zeer efficiënte zonnecellen hebben opgeleverd, was er bij aanvang van dit onderzoek nog weinig bekend over de fundamentele eigenschappen. Zoals beschreven in de introductie kan in theorie de efficiëntie van dit type zonnecellen nog verbeterd worden. Om dit te kunnen realiseren is het belangrijk om te begrijpen hoe metaalhalideperovskieten stroom opwekken uit zonlicht en wat er vervolgens met deze stroom gebeurt. Oftewel, wat zijn de knelpunten die maken dat de efficiëntie van dit type zonnecellen nog niet optimaal is? Voor het beantwoorden van deze vraag is het belangrijk om te bedenken wat voor eigenschappen een materiaal idealiter zou moeten hebben om er een goede zonnecel van te kunnen maken. Om zo veel mogelijk zonlicht om te zetten in elektriciteit is het ten eerste belangrijk dat er zo veel mogelijk licht geabsorbeerd wordt. De metaalhalideperovskieten die we hebben bestudeerd zijn gebaseerd op loodjodide. Als deze materialen een dikte van slechts een dertigduizendste van een centimeter ( $\sim 0.3$  micrometer) hebben, dan zijn deze al bijna zwart van kleur. Dit komt omdat een substantieel deel van het zichtbare zonlicht geabsorbeerd wordt en hierdoor zijn het gunstige materialen voor zonnecellen. Nu is de volgende cruciale stap dat dit geabsorbeerde zonlicht wordt omgezet in een andere vorm van energie, namelijk een stroom van bewegende elektrische ladingen, ook wel bekend als elektriciteit. Halfgeleidermaterialen zoals silicium, maar ook metaalhalideperovskieten, hebben de juiste eigenschappen om licht om te zetten in bewegende ladingen. Om deze stroom vervolgens te kunnen gebruiken moeten de ladingen die in de zonnecel ontstaan worden gecollecteerd. Hoe meer ladingen er worden gecollecteerd, hoe hoger de efficiëntie van de zonnecel. En hiermee komen we bij een van de grootste uitdagingen als het gaat om het verbeteren van de efficiëntie van perovskiet-zonnecellen: zorgen dat er zo veel mogelijk ladingen gecollecteerd worden.

Om dit te bestuderen hebben wij in dit onderzoek een aantal verschillende spectroscopische technieken gebruikt. Hierbij gebruiken we laserstralen om de perovskieten kort te belichten, waarmee we de processen nabootsen die plaatsvinden in een werkende zonnecel. Een veelvoorkomende term in dit proefschrift is 'time-resolved microwave conductivity' (tijdsopgeloste microgolfsgeleidingsmetingen, afgekort als TRMC): een techniek waarmee we onderzoeken wat er gebeurt met de bewegende ladingen die zijn ontstaan na het absorberen van het laserlicht. Door middel van de interactie tussen de bewegende ladingen en een microgolf-veld kunnen we met de TRMC-techniek vaststellen hoe snel ladingen bewegen: de mobiliteit. Ook meten we

hoe lang de ladingen in beweging blijven: de levensduur. Zowel een hoge mobiliteit als een lange levensduur vergroten de kans dat een lading gecollecteerd wordt.

In hoofdstuk 3 bestuderen we de mobiliteit en levensduur van ladingen in loodjodide perovskieten die op verschillende manieren gemaakt zijn. We observeren dat een deel van de ladingen vast kan komen te zitten in de perovskiet-laag, waardoor collectie van deze ladingen wordt verhinderd. Dit is met name een probleem bij lage lichtintensiteiten, wat het geval is op een dag met weinig zonlicht. Een belangrijke bevinding in hoofdstuk 3 is echter dat het bepalend is welke grondstoffen gebruikt worden voor het maken van de perovskieten. Zo zorgt de aanwezigheid van chloride tijdens de reactie er bijvoorbeeld voor dat de perovskiet van betere kwaliteit is en dat er minder ladingen vast komen te zitten. Uiteindelijk schatten we af dat ladingen in loodjodide perovskieten een afstand van een duizendste van een centimeter ( $\sim 10$  micrometer) kunnen afleggen. Dit is meer dan genoeg om een dertigduizendste centimeter te overbruggen: de dikte van de perovskiet-laag die nodig is om het zonlicht te absorberen. Dit betekent dat in principe het merendeel van de ladingen gecollecteerd moet kunnen worden.

In hoofdstuk 4 vinden we dat dit echter niet het geval is. Hoewel de ladingen relatief makkelijk door de perovskiet zelf bewegen, komen deze in veel gevallen tot stilstand op het grensvlak tussen de perovskiet en de materialen die in een zonnecel de bewegende ladingen af moeten vangen. Hieruit concluderen we dat dit waarschijnlijk een van de belangrijkste belemmeringen is voor de collectie van de bewegende ladingen. Om perovskiet-zonnecellen efficiënter te maken, zal dus onder andere de kwaliteit van de grensvlakken verbeterd moeten worden.

Als een negatieve lading, een elektron, in beweging wordt gebracht blijft er een positief geladen gat over. Wanneer een bewegend elektron een gat passeert, kan het elektron terugvallen in het gat waarna deze niet langer in beweging is. Dit proces heet recombinatie. Hoe groter de kans op recombinatie, hoe kleiner de kans op collectie. In hoofdstuk 5 bestuderen we het mechanisme achter recombinatie in lood jodide perovskieten. Een van de belangrijkste bevindingen is dat elektronen over een barrière heen moeten om terug te vallen in een gat. Dit zorgt ervoor dat de kans op recombinatie kleiner is dan aanvankelijk werd gedacht, waarmee we op een bijzondere eigenschap van perovskieten zijn gestuit.

De perovskieten die beschreven staan in hoofdstuk 3 t/m 5 hebben allemaal dezelfde compositie en bevatten naast lood en jodide nog organische moleculen. Deze organische moleculen hebben een dipoolmoment, wat betekent dat ze aan de ene kant een beetje positief en aan de andere kant een beetje negatief geladen zijn. Omdat elektronen ook negatief geladen zijn, hebben sommige onderzoekers gesuggereerd dat dit dipoolmoment invloed heeft op de bewegingssnelheid van elektronen (hoofdstuk 3) en de oorzaak is van de barrière voor recombinatie (hoofdstuk 5). Om deze hypothesen te testen hebben we in hoofdstuk 6 het organische molecuul vervangen door cesium, een anorganisch component zonder dipoolmoment. Interessant genoeg vinden we dat de kenmerken van deze cesium-houdende perovskieten nagenoeg hetzelfde zijn. Hieruit concluderen we dat de eigenschappen die we in hoofdstuk 3 en 5 hebben gevonden dus voortkomen

uit de lood en/of jodide, en niet veroorzaakt worden door het dipoolmoment van het organische molecuul. Nader onderzoek zal moeten uitwijzen wat dan wel het precieze mechanisme achter de recombinatie-barrière is.

Zoals hierboven genoemd is lood één van de componenten van perovskiet-zonnecellen. Dit lood is aanwezig in een vorm die zowel giftig als wateroplosbaar is. Daarom zou het vanuit milieuoverwegingen gunstig zijn als het lood in metaal halide perovskieten kon worden vervangen door minder giftige metalen, terwijl alle eigenschappen voordelig voor een efficiënte zonnecel behouden blijven. In hoofdstuk 7 maken we perovskieten met een mengeling van zilver, bismut en antimoon in plaats van lood. We observeren dat de hoeveelheid geabsorbeerd licht afhankelijk is van de hoeveelheid antimoon ten opzichte van bismut. Dit betekent dat het variëren van de compositie gebruikt kan worden om de absorptie-eigenschappen te manipuleren. Verder meten we dat ladingen vrij kunnen bewegen in deze materialen, een hoopgevende bevinding voor loodvrije perovskiet-zonnecellen.

Overheersen perovskiet-zonnecellen straks de markt? En welke perovskiet-compositie zal uiteindelijk een commercieel doeleinde vinden? De tijd zal het leren. In ieder geval hebben we met dit onderzoek een klein steentje bijgedragen aan het ontrafelen van de eigenschappen van deze bijzondere halfgeleidermaterialen.



# Dankwoord

*“Als je weet waar je heen gaat, zul je er zeker komen. Als je niet weet waar je heen gaat, zul je zeker ergens anders komen”,*

schreef mijn moeder op een kaart aan mij toen ik in 2008 op het punt stond om een jaar naar de Verenigde Staten te gaan. Door de jaren heen heeft deze spreuk steeds meer betekenis voor mij gekregen. Toen ik een jaar bezig was met mijn promotieonderzoek werd mij gevraagd wat ik aan het einde van mijn promotie zou hebben bijgedragen aan de wetenschap. Ik had hier geen antwoord op. Dat vond ik destijds erg vervelend. Nu, drie jaar later, kan ik vol trots zeggen dat ik meer heb bereikt dan ik me ooit had kunnen voorstellen. En misschien is dat juist wel te danken aan het feit dat ik niet van tevoren wist wat er uit mijn onderzoek zou komen, maar dat ik mij in plaats daarvan heb laten leiden door wat het onderzoek mij bracht. En mij niet te vergeten heb laten inspireren door de talloze discussies met verscheidene wetenschappers, waaronder **alle mede-auteurs** met wie ik de afgelopen jaren in wetenschappelijke tijdschriften heb gepubliceerd en **mijn collega's uit de OM sectie**. Een aantal mensen heeft in het bijzonder bijgedragen aan mijn persoonlijke ontwikkeling en de totstandkoming van dit proefschrift, wie ik bij dezen expliciet hiervoor wil bedanken.

Allereerst, **Tom**. Ik ben me ervan bewust dat ik soms heel erg eigenwijs ben en dat dit voor een begeleider lastig kan zijn. Ik ben je heel erg dankbaar voor hoe je de afgelopen jaren met mij om bent gegaan. Aan de ene kant gaf je mij ongekend veel ruimte en vrijheid, maar tegelijkertijd was je er altijd als ik je nodig had. Daarnaast kijk ik ook met veel plezier terug op alle uren waarin wij samen hebben gefilosofeerd over perovskietjes en van alles en nog wat. Zo zal ik nooit vergeten dat wij na een conferentie in Barcelona bijna het vliegtuig misten omdat we, onder het genot van een karaf Sangria, bandenplaatjes zaten te tekenen op een terras. Ik heb veel bewondering voor jou als begeleider, omdat je voor iedereen een passende manier zoekt om het maximale uit diegene te halen. Bedankt voor je ondersteuning tijdens mijn PhD traject en ik hoop dat we in de toekomst nog vaak samen zullen werken.

Mijn voormalige studenten **Eva, Jan-Jaap, Sanjana** en collega's **Davide, Dengyang, Ferdinand, María**, ook jullie hebben mij allemaal op jullie eigen manier geïnspireerd en gestimuleerd en hiermee een belangrijke bijdrage geleverd aan mijn proefschrift. Bedankt hiervoor.

Ik wil ook graag degenen bedanken die dag in dag uit, weliswaar iets meer vanaf de achtergrond, de faculteit draaiende houden en zodoende, hebben bijgedragen aan de

efficiëntie waarmee ik de afgelopen jaren onderzoek heb kunnen doen. Waaronder: de technici **Martien, Wybe, Jos en Ruben**, de secretaresses **Wil en Heleen**, iedereen werkzaam op de logistiek afdeling en de schoonmakers.

Ik heb niet alleen tijdens werk, maar ook daarbuiten, erg genoten van de afgelopen vier jaar. Zowel **collega's** als mijn (**schoon-**)**familie, vriendinnen** en de meiden van het koor **Cantiamo** hebben hier een belangrijke rol in gehad. Bedankt lieve vriendinnen die altijd voor me klaar staan: **Suus**, die altijd betrokken is bij alles wat ik beleef, **Inge**, die me altijd weet op te vrolijken, **Wendel**, die altijd de juiste adviezen geeft, en **María**, die 'flavour' in mijn leven brengt. **Sólrún, Cansel, María**: I have really enjoyed our dinner nights together, which always started with a general conversation but quickly changed into hours of talking about gender equality.

**Papa, mama en Arne**: jullie zijn onmisbaar in mijn leven. Het is mede dankzij jullie dat ik ben geworden wie ik ben en dat ik nu op het punt sta om te promoveren. Ik weet nog goed dat ik halverwege de middelbare school na één onvoldoende verzuchtte dat ik gewoon niet goed was in wiskunde. Waarop jij, **papa**, zei: 'Dat is onzin. Als jij leert voor je examen, dan haal je gewoon een voldoende.' En zo geschiedde. Jullie hebben me altijd gestimuleerd om mijn vaardigheden optimaal te benutten en me niet te laten leiden door man/vrouw-stereotypen. En **mama**, bedankt dat je mij hebt geleerd om altijd eerlijk te zijn naar mezelf en naar anderen.

Als laatste: mijn geliefde en maatje **Ward**. Al ruim zeven jaar mag ik jou aan mijn zijde hebben. Ik ben je dankbaar voor alle rust die je in mijn leven brengt en dat je me in elke beslissing steunt. Ik geniet van elke dag die wij samen doorbrengen. Over een paar maanden zal ons leven verrijkt worden met het mooist denkbare geschenk dat is voortgekomen uit onze liefde voor elkaar. Vandaag zal deze een slokje vruchtwater drinken, terwijl wij proosten op dit bijzondere moment.

We hebben veel gereisd en zullen misschien nog een aantal keer naar een andere stad moeten verhuizen. Om terug te komen op de eerste twee zinnen van dit dankwoord: ik weet niet precies hoe ons leven eruit zal komen te zien. Ik weet wel, waar het leven ons ook zal brengen, zolang jij bij me bent ben ik 'thuis'.

~ Eline ~







## Curriculum Vitae



Eline Mathilde Hutter was born in Breda, the Netherlands, on the 1<sup>st</sup> of October in 1990. In 2002, she started high school at Hofstad Lyceum in Den Haag. Here, Eline was editor-in-chief of the school paper and a member of the Youth and Technology (Jet-Net) student panel. After finishing high school in 2008, she went to Green River Community College in the USA, where she followed several courses in journalism and philosophy and worked as an editor for *The Current*. After returning to the Netherlands in 2009, she started a bachelor in chemistry at the University of Utrecht.

From 2009 to 2013, Eline was responsible for organizing the student-for-a-day activities and coordinated the open days for the chemistry bachelor together with the communication department. In addition, she was a teaching assistant at Stichting Studiebegeleiding Leiden, where she prepared high school students for their final exams in chemistry. In 2014, Eline graduated from the University of Utrecht with a thesis entitled “Silica-Coated Anisotropic Nanoparticles as Building Blocks for Plastic Crystals” under the supervision of professor Daniël Vanmaekelbergh. She received her MSc degree in chemical sciences *cum laude* (with honours).

Afterwards, Eline started as a PhD student in the group of dr. ir. Tom Savenije at Delft University of Technology, where she specialized in time-resolved spectroscopy techniques. In the past years, she has mainly used time-resolved microwave conductivity and photoluminescence measurements to investigate optoelectronic properties of metal halide perovskites. In addition, she assisted in several bachelor courses and supervised two bachelor and three master students.

In 2017, Eline was awarded with a Fulbright research grant. This allowed her to spend three months in the group of dr. Hemamala Karunadasa at Stanford University in the USA, where she explored the synthesis of non-toxic metal halide perovskites for solar cells. At the moment, Eline is interested in further investigating fundamental properties of metal halide perovskites and she will continue her academic career as a postdoc in the group of dr. Bruno Ehrler at AMOLF, the Netherlands.



# List of Publications

This thesis is partially based on the following publications:

1. **Eline M. Hutter**, María Gélvez-Rueda, Davide Bartesaghi, Ferdinand C. Grozema, Tom J. Savenije, Band-Like Charge Transport in Antimony-Bismuth Alloyed  $\text{Cs}_2\text{AgBi}_{1-x}\text{Sb}_x\text{Br}_6$  Halide Double Perovskites (submitted)
2. Yinghong Hu, **Eline M. Hutter**, Philipp Rieder, Irene Grill, Meltem F. Aygüler, Alexander G. Hufnagel, Matthias Handloser, Thomas Bein, Achim Hartschuh, Kristofer Tvingstedt, Vladimir Dyakonov, Andreas Baumann, Tom J. Savenije, Michiel L. Petrus, and Pablo Docampo, Understanding the Role of Cesium and Rubidium Additives in Perovskite Solar Cells: Trap states, Charge Transport and Recombination, *Advanced Energy Materials*, 2018, 1703057
3. **Eline M. Hutter**, Tom J. Savenije, and Carlito S. Ponseca Jr., Time-Resolved Photoconductivity Measurements on Organo-Metal Halide Perovskites, *Perovskite Solar Cells*, 2017, 179-232, *World Scientific Publishing Co*
4. **Eline M. Hutter**, Rebecca J. Sutton, Sanjana Chandrashekar, Mojtaba Abdi-Jalebi, Samuel D. Stranks, Henry Snaith, and Tom J. Savenije, Vapour-Deposited Cesium Lead Iodide Perovskites: Microsecond Charge Carrier Lifetimes and Enhanced Photovoltaic Performance, *ACS Energy Letters*, 2017, 2, 1901-1908
5. **Eline M. Hutter**, Jan-Jaap Hofman, Michiel Petrus, Michiel Moes, Ruben D. Abellón, Pablo Docampo, and Tom J. Savenije, Charge Transfer from Methylammonium Lead Iodide Perovskite to Organic Transport Materials: Efficiencies, Transfer Rates and Interfacial Recombination, *Advanced Energy Materials*, 2017, 1602349
6. **Eline M. Hutter**, María Gélvez-Rueda, Anna Osherov, Vladimir Bulović, Ferdinand C. Grozema, Samuel D. Stranks, and Tom J. Savenije, Direct-Indirect Character of the Band Gap in Methylammonium Lead Iodide Perovskite, *Nature Materials*, 2017, 16, 115-120
7. Anna Osherov, **Eline M. Hutter**, Krzysztof Galkowski, Roberto Brenes, Duncan K. Maude, Robin J. Nicholas, Paulina Plochocka, Vladimir Bulović, Tom J. Savenije, and Samuel D. Stranks, The Impact of Phase Retention on the Structural and Optoelectronic Properties of Metal Halide Perovskites, *Advanced Materials*, 2016, 28, 10757-10763
8. Yu Bi, **Eline M. Hutter**, Yanjun Fang, Qingfeng Dong, Jinsong Huang, and Tom J. Savenije, Charge Carrier Lifetimes Exceeding 15 Microseconds in Methylammonium Lead Iodide Single Crystals, *J. Phys. Chem. Lett.*, 2016, 7, 923-928
9. Carlito S. Ponseca Jr., **Eline M. Hutter**, Piotr Piatkowski, Boiko Cohen, Torbjörn Pascher, Abderrazzak Douhal, Arkady Yartsev, Villy Sundström, and Tom J. Savenije, Mechanism of Charge Transfer and Recombination Dynamics in Organo Metal Halide Perovskites and Organic Electrodes, PCBM and Spiro-OMeTAD: Role of Dark Carriers, *J. Am. Chem. Soc.*, 2015, 137, 16043-16048
10. **Eline M. Hutter**, Giles E. Eperon, Samuel D. Stranks, and Tom J. Savenije, Charge Carriers in Planar and Meso-Structured Organic-Inorganic Perovskites: Mobilities, Lifetimes, and Concentrations of Trap States, *J. Phys. Chem. Lett.*, 2015, 6, 3082-3090

## Other publications by the author:

11. Michiel L. Petrus, Kelly Schutt, Maximilian T. Sirtl, **Eline M. Hutter**, Anna C. Closs, James M. Ball, Johan C. Bijleveld, Annamaria Petrozza, Thomas Bein, Theo J. Dingemans, Tom J. Savenije, Henry Snaith, and Pablo Docampo, New Generation Hole Transporting Materials for Perovskite Solar Cells: Amide-based Small-Molecules with Non-Conjugated Backbones (submitted)
12. Mojtaba Abdi-Jalebi, Zahra Andaji-Garmaroudi, Stefania Cacovich, Camille Stavrakas, Bertrand Philippe, Johannes M. Richter, Mejd Alsari, Edward P. Booker, **Eline M. Hutter**, Andrew J. Pearson, Samuele Lilliu, Tom J. Savenije, Håkan Rensmo, Giorgio Divitini, Caterina Ducati, Richard H. Friend, and Samuel D. Stranks, Maximising and Stabilising Luminescence in Halide Perovskite Device Structures with Potassium-Halide Passivating Interlayers, *Nature*, 2018, 555, 497-501
13. María Gelvez-Rueda, **Eline M. Hutter**, Duyen H. Cao, Nicolas Renaud, Constantinos C. Stoumpos, Joseph T. Hupp, Tom J. Savenije, Mercouri G. Kanatzidis, and Ferdinand C. Grozema, Interconversion between Free Charges and Bound Excitons in 2D Hybrid Lead Halide Perovskites, *J. Phys. Chem. C*, 2017, 121, 26566-26574
14. Roberto Brenes, Dengyang Guo, Anna Osherov, Nakita K. Noel, Christopher Eames, **Eline M. Hutter**, Sandeep Pathak, Farnaz Niroui, Richard H. Friend, M. Saiful Islam, Henry J. Snaith, Vladimir Bulović, Tom J. Savenije, and Samuel D. Stranks, Metal Halide Perovskite Polycrystalline Films Exhibiting Properties of Single Crystals, *Joule*, 2017, 1, 1-13
15. Dengyang Guo, Davide Bartsaghi, Haotong Wei, **Eline M. Hutter**, Jinsong Huang, and Tom J. Savenije, Photoluminescence from Radiative Surface States and Excitons in Methylammonium Lead Bromide perovskites, *J. Phys. Chem. Lett.*, 2017, 8, 4258-4263
16. Wiebke Albrecht, Bart Goris, Sara Bals, **Eline M. Hutter**, Daniël Vanmaekelbergh, Marijn A. van Huis, and Alfons van Blaaderen, Photostability and morphological transformations of single silica-coated CdSe/CdS nanorods upon fs-laser excitation, *Nanoscale*, 2017, 9, 4810-4818
17. Cristina Momblona, Lidon Gil-Escrig, Enrico Bandiello, **Eline M. Hutter**, Michele Sessolo, Kay Lederer, Jan Blochwitz-Nimoth, and Henk J. Bolink, Efficient vacuum deposited p-i-n and n-i-p perovskite solar cells employing doped charge transport layers, *Energy and Environmental Science*, 2016, 9, 3456-3463
18. Daniel Pérez-del-Rey, Dávid Forgács, **Eline M. Hutter**, Tom J. Savenije, Dennis Nordlund, Philip Schulz, Joseph J. Berry, Michele Sessolo, and Henk J. Bolink, Strontium Insertion in Methylammonium Lead Iodide: Long Charge Carrier Lifetime and High Fill-factor Solar Cells, *Advanced Materials*, 2016, 28, 9839-9845
19. **Eline M. Hutter**, Eva Bladt, Bart Goris, Francesca Pietra, Johanna C. van der Bok, Mark P. Boneschanscher, Celso de Mello Donegá, Sara Bals, and Daniël Vanmaekelbergh, Conformal and Atomic Characterization of Ultrathin CdSe Platelets with a Helical Shape, *Nano Letters*, 2014, 14, 6257-6262
20. **Eline M. Hutter**, Francesca Pietra, Relinde J.A. van Dijk – Moes, Dariusz Mitoraj, Johannes D. Meeldijk, Celso de Mello Donega, and Daniël Vanmaekelbergh, Method to Incorporate Anisotropic Semiconductor Nanocrystals of All Shapes in an Ultrathin and Uniform Silica Shell, *Chemistry of Materials*, 2014, 26, 1905-1911
21. Julius W. J. de Folter, **Eline M. Hutter**, Sonja I. R. Castillo, Kira E. Klop, Albert P. Philipse, and Willem K. Kegel, Particle Shape Anisotropy in Pickering Emulsions: Cubes and Peanuts, *Langmuir*, 2014, 30, 955-964





# List of Presentations

The results described in this thesis were presented at the following meetings:

1. May 2015 (oral) at the International Conference on Hybrid and Organic Photovoltaics in Rome, Italy
2. May 2015 (poster) at the International Conference on Hybrid and Organic Photovoltaics in Rome, Italy
3. June 2015 (oral) at the Applied Sciences Day in Delft, the Netherlands
4. June 2015 (oral) at the Dutch Perovskite Workshop in Delft, the Netherlands
5. Sep 2015 (oral) at the International Conference on Perovskite Solar Cells and Optoelectronics in Lausanne, Switzerland
6. Nov 2015 (poster) at the MRS Fall Meeting in Boston, USA
7. Jan 2016 (oral) in the group of Vladimir Dyakonov at the University of Würzburg, Germany
8. Mar 2016 (oral) at the International Conference on Perovskite Thin Film Photovoltaics in Barcelona, Spain
9. June 2016 (poster) at the Dutch Perovskite Workshop in Delft, the Netherlands
10. Sep 2016 (oral) at the E-MRS Fall Meeting in Warsaw, Poland
11. Nov 2016 (poster) at the MRS Fall Meeting in Boston, USA
12. Jan 2017 (oral) at the Chemical Engineering department colloquium in Delft, the Netherlands
13. Mar 2017 (oral) at the International Conference on Perovskite Thin Film Photovoltaics in Valencia, Spain
14. Mar 2017 (poster) at the International Conference on Perovskite Thin Film Photovoltaics in Valencia, Spain
15. May 2017 (oral) in the Optoelectronics group at the University of Cambridge, United Kingdom
16. Dec 2017 (oral) at the national conference Chains in Veldhoven, the Netherlands
17. Jan 2018 (oral) at the national conference Physics@Veldhoven in Veldhoven, the Netherlands
18. Feb 2018 (oral) at AMOLF in Amsterdam, the Netherlands
19. May 2018 (oral) at the International Conference on Hybrid and Organic Photovoltaics in Benidorm, Spain



